SIMPLIFIED CFD MODELLING OF TIDAL TURBINES FOR EXPLORING ARRAYS OF DEVICES

Submitted by

Mulualem Gebregiorgis Gebreslassie

to the University of Exeter as a thesis for the degree of

Doctor of Philosophy in Engineering

In September 2012

I certify that all material in this thesis which is not my own work has been identified and that no material has previously been submitted and approved for the award of a degree by this or any other University.

Signature:

ABSTRACT

The status of marine current tidal energy technology is currently in the research and development phase, with a few deployments and tests of prototypes under-way in some countries. There is a huge pressure for tidal farms to be of Gigawatt scale in order to have a real, economically viable impact on renewable energy utilization targets outlined for 2020. A route to achieving this is the large scale energy farm philosophy, similar to wind farms, based on very large numbers of unit current tidal stream devices. However, this emerging technology development raises different research questions which lead to further problems in the practical implementation of tidal stream devices. Thus, the aim of this study was: (i) to develop a new, computationally cheap computational fluid dynamics (CFD) based model of the Momentum-Reversal-Lift (MRL) tidal turbine, and (ii) to perform a detailed calculations of the flow field of single and multiple turbines using the developed model to investigate the flow features such as, downstream wake structures, dynamics of the free surface, wake recovery, and the influence of wake interactions on the performance of individual devices.

A new CFD based *Immersed Body Force* (IBF) model has been developed to represent the MRL turbine. The IBF model was developed based on the concept of actuator disc methodology by incorporating additional geometric features that induce energy absorption from the flow which also lead to a downstream wake structure intended to reflect more closely those of the real turbines than simple momentum sink zone models. This turbine model was thoroughly used to investigate the performance of the MRL turbine and the associated flow characteristics and proved its capability in analysing several issues relating to this design of tidal turbines.

Several calculations have been carried out and a full range of operating points of the MRL turbine was formulated. A maximum power coefficient of, $C_p = 0.665$, was obtained with a blockage ratio of, $B = 0.016$. However, the performance of the turbine was improved at a higher blockage ratio both in a single and tidal stream farm investigations. The power coefficient of a single turbine was improved by about 3% when simulated with a blockage ratio of, $B = 0.029$, and even a higher value was obtained in a tidal stream farm containing three turbines configured in the spanwise direction which reached up to, $C_P = 0.761$, with a global blockage ratio of, $B = 0.027$. These power coefficients are higher than the Lanchester-Betz limit of $C_P = 0.593$ obtained at $B = 0$, which is mainly due to the tidal turbine operating in a constrained environment, high blockage ratio, that increases the thrust force on the device. The power coefficient of the IBF model showed consistently higher values compared to experiments and a detailed CFD model results. This indicates that the power coefficient calculated using the IBF model includes some other losses within the turbine region, such as losses due to viscous, shear etc.

Investigations on the influence of closely packed clusters of turbines in a tidal stream

farm showed that a laterally close configuration of turbines improved the performance of individual turbines due to the blockage effect, which is created by the array of turbines in the span-wise direction. In contrast, a small longitudinal spacing between turbines inflicted a massive energy shadowing that affects the performance of downstream turbines. However, a tidal stream farm with a staggered turbine layout can reduce the longitudinal spacing by about 50% with a minimum of 6D lateral spacing compared with a regular turbine layout due to the advantage of using an accelerated bypass flows.

Keywords: MRL, IBF model, Wake interaction, Power extraction, LES

ACKNOWLEDGEMENT

The journey taken in the creation of this thesis has been a long, sometimes difficult, but always enjoyable experience and I would like to personally thank numerous people for their help in making this work possible. Many thanks to Prof. Michael Belmont and Dr. Gavin Tabor, my supervisors, who have been always there during the course of this study and for their valuable and constructive advice, which helps me to develop a solid fundamental engineering thinking. A mention also, for all my friends, who made the whole University of Exeter experience so enjoyable.

Special thanks to my wife, Faley Mekonen , for all those years of unwavering love and support, and to my mother, Etay Weldegebriel, and the rest of my family who I am sure are equally proud of what I have achieved. This thesis would not be possible without funding from the University of Exeter and I am equally grateful for this too.

Contents

DECLARATION

I hereby declare that this PhD thesis report entitled

"SIMPLIFIED CFD AND ANALYTICAL MODELLING OF TIDAL TURBINES FOR EXPLORING ARRAYS OF DEVICES"

is written by me and that all material in this thesis which is not my own work has been identified and properly cited.

Student's Name: Mulualem Gebregiorgis Gebreslassie

Signature _____ Date: _____

ABBREVIATIONS

MRL Momentum−Reversal−Lift 6

THAWT Transverse Horizontal Axis Water Turbine 6

LMADT Linear Momentum Actuator Disc Theory 60

TSR Tip Speed Ratio 79

BSR Blade Speed Ratio 79

COLM Conservation of Linear Momentum 56

CFD Computational Fluid Dynamics 6

GGI General Grid Interface 84

RANS Reynolds-Averaged Navier-Stokes 17

LES Large Eddy Simulation 17

DNS Direct Numerical Simulation 18

VOF Volume of Fluid 19

IBF Immersed Body Force 17

US Upstream Spacing 137

LS Lateral Spacing 138

OS Outlet Spacing 137

NS Navier-Stokes 18

Chapter 1

INTRODUCTION

1.1 General Informal Introduction

The growing of worldwide energy demand together with the unsustainable sources of conventional energy have lead to considerable interest in renewable energy development over many years. However, despite a huge potential of resources, the world is still heavily dependent on fossil fuels such as oil, gas and coal, which supplies 80% of energy needs with the contribution of renewable energy and nuclear power limited to 13.5% and 6.5% respectively [Asif and Muneer, 2007]. Gross et al. [2003] also reported that without large hydro and traditional biomass, renewables contribute less than 3% of global electricity and 2% of primary energy. Biomass, wind energy, solar energy, are the current contenders with tidal energy emerging as a possible source for some countries situated in a better site.

Tidal energy has been used since 787 A.D as explained by Clark et al. [2003] for milling purposes in England and France though in modern times it has been rarely used for power generation due to slow pace of technology developments and other cheap energy source competitors such as fossil fuels. However, due to the fluctuating cost of conventional fuels and their environmental impacts, and a rapid development of new devices for tidal energy exploitation, a considerable number of countries are willing to invest in this energy to increase their share of renewable energy use. The UK is one of those countries which is actively engaged and the phase II UK tidal stream energy resource assessment presented by Andrew [2005] showed that tidal stream energy can contribute a significant fraction of the UK energy needs. Several studies have been carried out on evaluating the environmental impacts and locating potential sites, as documented by [Bedard et al., 2005, Hagerman et al., 2006, Andrew, 2005].

Marine renewables could provide 3% of the total UK electricity demand with proper investment and planning[Callaghan and Boud, 2006], which is a valuable contribution

to the European Union commitment to increase the power generation from renewables to 20% by 2020 [Fouquet and Johansson, 2008]. In order to use this vast, clean and predictable energy resource, the UK is investing a huge amount of money in research and development of new tidal stream devices to make the technology more economically and environmentally feasible and acceptable to society.

Tidal barrages are the first generation and oldest technologies of tidal power. La Rance barrage is the first industrial scale tidal power generation plant constructed in the Rance river in France, which was opened on the 26th November 1966 [Frau, 1993]. However, they have not been widely constructed and are not favoured by private investors, governments, and engineers due to their side effects such as ecological and/or environmental impacts, high construction cost and many years of payback period. This has lead to multi-stockholder initiatives and governments, seeking more ecologically acceptable alternatives that also allow fast revenue from early installation with a subsequent increase in investment and scale. Marine current turbine technologies which use the kinetic energy of tides in a similar manner to wind energy technologies are proving a better choice over the tidal barrages. Turbines may be less intrusive into the local environment, and unlike a barrage can be installed incrementally in a location, half a turbine fan will still generate some power, half a barrage will not.

Several innovations have been made to improve the performance of the technology since its creation to fulfil the demand as discussed in detail by [Fraenkel, 2006, Blunden and Bahaj, 2007]. As a result, a number of designs have been invented and utilized for the exploitation of tidal energy. As the demand and competition increases, the development of new and sophisticated designs has been continuous producing an encouraging improvement of the performance of the tidal turbines. The tidal turbine technologies are often termed as a conventional and new generation tidal turbines based on their maturity. A detailed description of each technology and their working principles are given in the next sections.

1.2 Conventional Tidal Turbines

Conventional tidal turbine technologies are the ones that have been in the market for sometime but not yet reached maturity. Tidal turbine technologies are generally categorised as axial and cross flow turbines [Miller et al., 2011]. Most of those technologies have been utilized for wind energy applications but in recent years they were imparted for tidal applications due to the similarity of their working principle though there are some exceptions such as the difference of the working environment for both technologies.

1.2.1 Axial flow tidal turbines

The shaft of an axial flow tidal turbines rotates parallel to the stream flow. Axial flow tidal turbines operate in a similar fashion to exploit the tidal energy although they may differ in the way they are mounted as shown in Fig. 1.1.

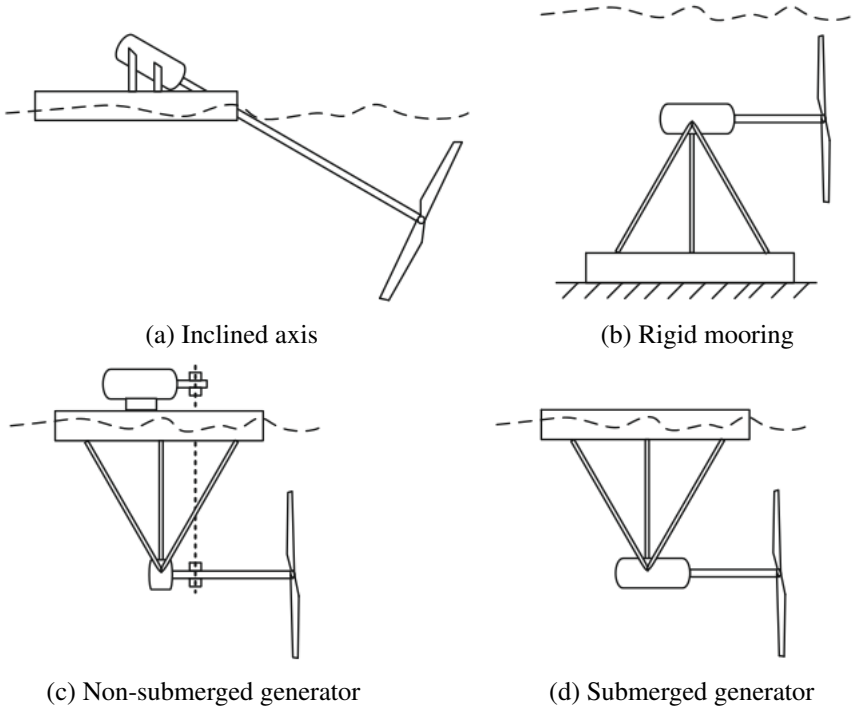

(a) Inclined axis (b) Rigid mooring

(c) Non-submerged generator (d) Submerged generator

Figure 1.1: Axial flow tidal turbines [Khan et al., 2009]

1.2.2 Cross flow tidal turbines

Cross flow turbines are those turbines where their axis of rotation is either vertical or horizontal but perpendicular to the stream flow. The performance of cross flow turbines such as helical turbines and Darrieus turbines (35% and 23.5% respectively) are better than the axial (propeller) turbines because of their better lift extraction mechanisms as documented by Gorlov and Silantyev [2001], Khan et al. [2006], Miller et al. [2011]. There are different types of cross flow turbines as shown in Fig. 1.2. Although the application of all these turbines is to extract energy from the stream flow, the way they exploit the energy is different from one type to another.

The Darrieus turbine was originally developed for power generation in wind energy but recently, it has been used for tidal energy extraction though there were some technical issues in the design and strength [Shiono et al., 2002] due to the differences encountered by the working environment. To address the technical issues, the design of the Darrieus turbine has been subsequently modified as shown in Fig. 1.2c (H-Darrieus turbine) and Fig. 1.2b (Squirrel Cage Darrieus turbine). These two turbines have straight blade shapes compared to the Darrieus turbine [Paraschivoiu, 2002].

Although both the Darrieus turbines have the same type of blades, the H-Darrieus turbine is often used in larger applications where mechanical strength is crucial because as the turbine size decreases, there is a possibility of the influence of high turbulence on the turbine efficiency [Davis, 1997]. This is the reason that the Squirrel Cage Darrieus turbine was developed, which is suited for small scale energy extraction as described by Fo [2003], Shiono et al. [2000], Nilsson et al. [2003]. However, the Darrieus turbines have a self starting problem once they stopped operating due to their small starting torques (they need a high speed flow to produce a high torque), which requires either a motoring technique or forced periodic rotation to re-start it again. There are different efforts to solve the re-start problem such as the study carried out by Kyozuka [2008] using combined Darrieus-savonius turbines, and design modifications such as the Gorlov helical turbine as explained by Shiono et al. [2002].

The Savonius turbine is relatively simple in design, manufacturing and maintenance

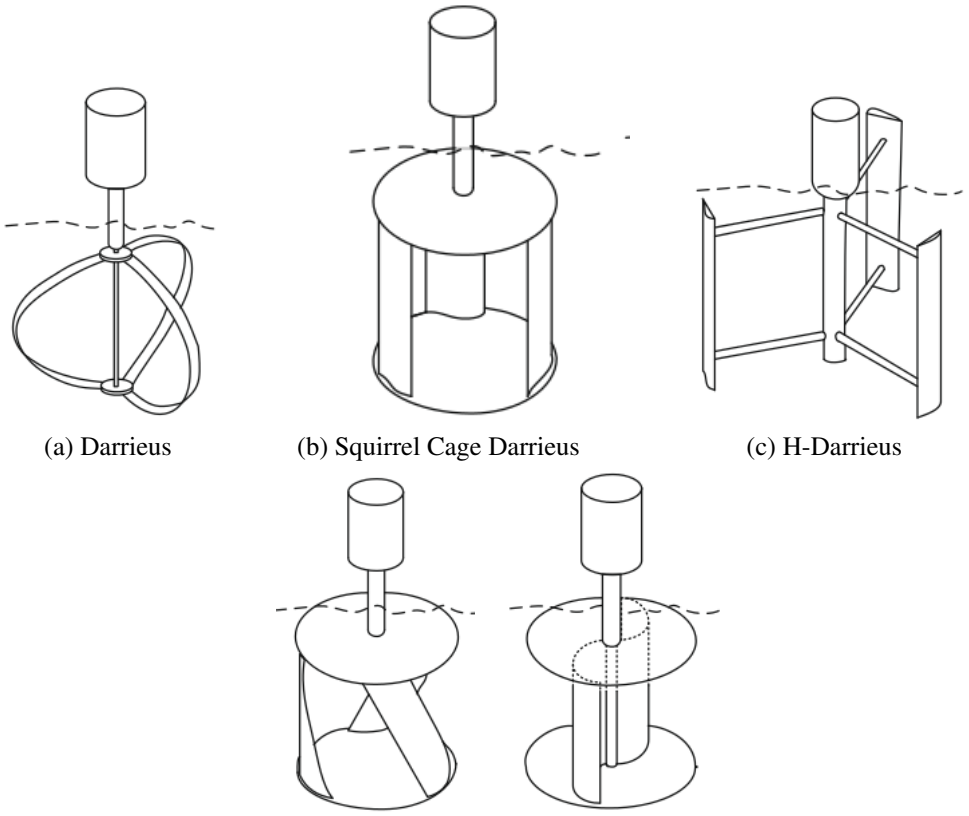

(a) Darrieus (b) Squirrel Cage Darrieus (c) H-Darrieus

(d) Gorlov (e) Savonius

Figure 1.2: Cross flow tidal turbines [Khan et al., 2009]

and is suitable for small scale application but has large starting torque [Grinspan et al., 2001], which enables to use it in low fluid flow. The Savonius turbine is not widely utilized due to its relatively small efficiency of about 15% and the large surface area it employs [Shankar, 1979, Kumar and Grover, 1993], but has a great advantage of being self starting and could be used in places where the tides are small.

The Gorlov Helical turbine is constructed from one or more long helical blades that run along a cylindrical surface as shown in Fig. 1.2d. This turbine was invented between 1993 - 1995 [Gorlov, 2003] to solve the self starting problems occurred in the Darrieus turbines as explained by Shiono et al. [2002]. An experimental study in laboratory and tidal current showed that the helical turbine demonstrated up to 35% efficiency [Gorlov, 2003]. The blades provide a reaction thrust that can rotate the turbine faster than the water flow itself and it always rotates in the same direction even if the tidal currents reverse directions [Ben Elghali et al., 2007]. The helical turbine can extract energy from a stream velocity as low as 1.5 m/s [Ben Elghali et al., 2007].

1.3 New Generation Tidal Turbines

The increase in demand and competition always triggers a new innovation and/or improvement of the conventional technologies to address critical issues that arise during deployment and utilization of those technologies in the practical world. The most influential problems of the technologies in the marine current applications are:

- The performance of the turbine
- The size of the turbine, which often depends on the depth of the fluid flow and the available current of the flow
- The location of the device across the depth of the fluid flow
- To some extent environmental effects such as flooding risks

Several novel designs are being continuously developed in order to address the above problems, such as the Transverse Horizontal Axis Water Turbine (THAWT) developed by Oxford University [McAdam et al., 2010], and the Momentum−Reversal−Lift (MRL) tidal turbine developed by Aquascientific Ltd [Janssen and Belmont, 2009]. These two turbines have a high aspect ratio and they can be deployed in shallow water estuaries due to their suitability of operating near the free surface, which significantly reduces the need to have a significant depth of water. A recent experimental and Computational Fluid Dynamics (CFD) study on these turbines also showed that they might produce better performance compared to the conventional tidal turbines, but they are at an early stage of research and development. Thus, more research is required to fully understand their advantages over conventional turbines.

1.3.1 Transverse Horizontal Axis Water Turbine

The Transverse Horizontal Axis Water Turbine (THAWT) turbine shown in Fig. 1.3 is a cross flow tidal turbines but contains more superior structural characteristics compared to the conventional Darrieus tidal turbines discussed in the previous sections [Houlsby

et al., 2011]. One of the main drawbacks of conventional axial flow tidal turbines is size restrictions as explained by McAdam et al. [2010], which ultimately explains the development of new devices such as the THAWT turbine. The size of conventional axial flow turbines can not be significantly increased due to the restrictions of the depth of flow in some sites. This might lead to the use of several small scale axial flow tidal turbines to produce megawatts of power generation. Therefore, the idea behind the development of the THAWT tidal turbine is to use the advantage of stretching the size of the turbine laterally to avoid the depth problem and to produce more power using large scale THAWT turbines with fewer number of devices [McAdam et al., 2010].

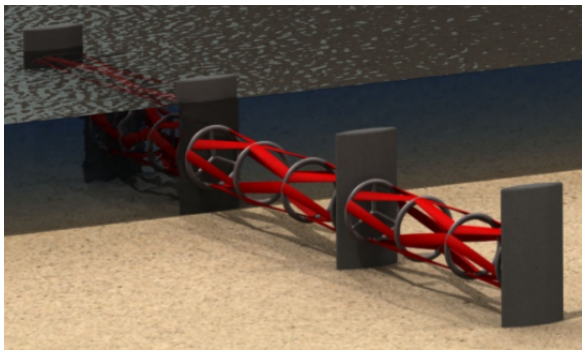

Figure 1.3: THAWT turbine [McAdam et al., 2010]

In addition, the simplicity of design, construction and scalability of the THAWT turbine reduces the requirement of more foundations, bearings and generators compared to conventional cross flow turbines. Experimental tests of scale models showed that the scalability of the device improved the power extraction capability because of the blockage effects that can be imposed due to the stretching of the device across a channel, which helps to extract a large amount of energy from the stream flow [Houlsby et al., 2011].

1.3.2 Momentum Reversal Lift Turbine

The Momentum Reversal Lift (MRL) turbine shown in Fig. 1.5 is another new generation cross flow tidal turbine developed by Aquascientific Ltd. The design is based on a cylindrical cycloidal system where each of three blades rotates 180^0 for every full rotation of the main shaft. This design allows the blades to provide torque through most of the cycle in both lift and drag phases. It is this combination of both lift and drag which gives

the turbine a high conversion efficiency over a wide range of operating fluid velocities. The novel aspect of the device is the combination of lift and momentum reversal (drag) that is utilised to optimise the energy extraction. It has been known since the early days of aerodynamics that the forces on a plate held in a flowing stream consist of two orthogonal components:

1. Lift which acts perpendicularly to the flow direction
2. Drag (momentum reversal)- which acts parallel to the flow direction.

The blade rotation is nominally half that around the central shaft since this condition results in near optimum conditions for both lift and drag forces on each blade [Janssen and Belmont, 2009], but this is still under investigation and the exact details could be subjected to some changes. Fig. 1.4 shows the rotation of the blade around the central axis presenting a variable incident angle to the flow during the rotation cycle. The power is taken off from the central shaft and transferred to a generator.

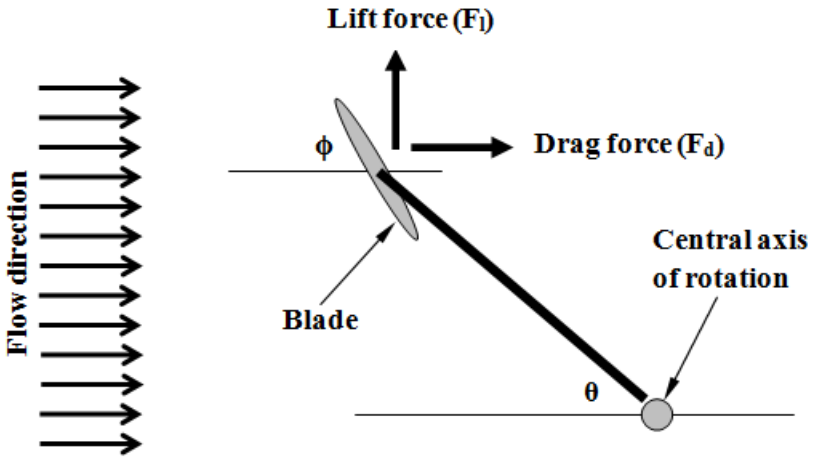

Figure 1.4: Torque on axis as a function of arm angle θ and blade angle ϕ

Since both the drag and lift exert forces, both of these can be used to extract energy from the fluid flow. Of these, lift has been the subject of considerably more attention since it is the basis of winged flight and also the basis for propeller based propulsion, whereas drag has been viewed as a problem to be overcome in this context. Nevertheless, for a given plate area and flow velocity, the drag force generally exceeds the lift force and is much less sensitive to the flow incident angle. The proposed turbine and configuration is capable of taking advantage of both these characteristics through the operating cycle.

This is a novel aspect and together with a body of associated designs form the core of the MRL turbine. The blades are allowed to rotate about their own axis and also about a mutually central axis where the rotation axis is perpendicular to the flow direction in contrast to the better known windmill device. There are several aspects to this configuration which give it potential advantage particularly in water where the flow forces on the blades can be extremely high. Fig. 1.5 shows a schematic of the turbine with three blades.

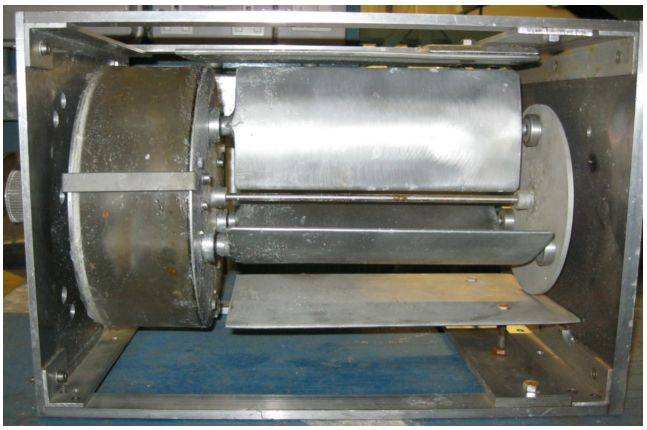

Figure 1.5: MRL turbine

It is surprising that there is a set of blade conditions where both lift and drag forces act uni-rotationally around the main axis such that the torque contribution is positive over the whole cycle. This allows both lift and drag forces to act together to produce a large summed torque as described by Janssen and Belmont [2009]. The MRL turbine is currently under testing with a couple of different size prototypes and an experimental study showed that its efficiency could reach up to 50% [Janssen and Belmont, 2009]. The work described in this report focuses entirely on the MRL turbine because of the involvement of Belmont and Tabor in the development of this turbine in collaboration with Aquascientific Ltd.

1.3.3 Tradewind Turbines

There are new generation of wind turbines developed by Tradewind turbines Ltd and Wollongong University and Voith Turbo as shown in Fig. 1.6a and 1.6b. They are a vertical axis turbines where the blades rotates about their own axis and about a mutually central axis, which is the same working principle as the MRL turbine. Voith Schneider Propellers (Fig. 1.6c) have also a similar working principle but they are mainly used in ships due to

their easiness of thrust adjustment which improves ship handling as explained by Jürgens and Heinke [2009]. Some of the benefits of these novel wind turbines are:

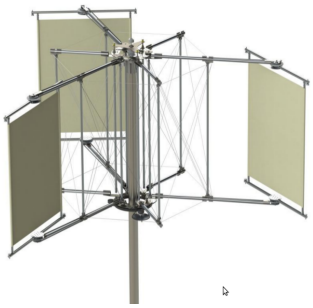

(a) TradeWind turbine

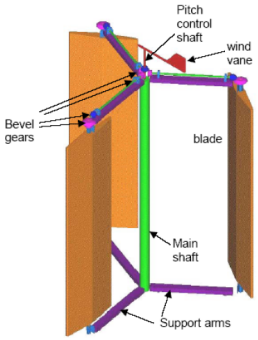

(b) Wollongong turbine

(c) Voith Schneider Propellers

Figure 1.6: Vertical axis wind turbines [Paget, 2012, Cooper and Kennedy, 2004, Jürgens and Heinke, 2009]

- They are easy to install, compact and lightweight.
- They have high levels of reliability in extreme conditions and slow moving enhancing component and product life
- They generate power over wide range of wind speeds.

1.4 Motivation and Significance of the Research Findings

The status of marine current tidal energy technology is currently in the research and development phase, with a few deployments and tests of prototypes under-way in some countries. This emerging technology development raises different research questions which lead to further problems in the practical implementation of tidal stream devices.

There is a huge pressure for tidal farms to be of GW scale in order to have a real, economically viable impact on renewable energy utilization targets outlined for 2020. A route to achieving this is the large scale energy farm philosophy, similar to wind farms, based on very large numbers of unit current tidal stream devices. However, there is still a gap in optimizing tidal stream farm designs to tackle the problem which arises due to the presence of several hundred tidal stream devices which inevitably introduces turbine to turbine interaction.

Marine current turbines use the kinetic energy of the fluid flow in a similar manner to the way in which wind energy technologies do and one might expect that the closely allied offshore wind farm sector would provide a natural jumping off point for the equivalent marine work. Wind farm optimization has been getting much attention for many years, as a result different approaches have been implemented to address the energy re-mixing problem that is central to assigning turbine locations with minimum energy shadowing [Douglas et al., 1998, Elkinton et al., 2008]. However the major issue of turbine to turbine interaction has proved a thorny problem, with highly pragmatic global farm infrastructure approaches, [Elkinton et al., 2008] , tending to neglect interaction or use highly empirical correlations, while some methods even resort to simple geometric interference criteria [Donovan, 2005]. An additional issue is that almost all existing approaches assume that the energy extracted by the farm introduces at most a small perturbation on the energy content of the flow system. Thus even if such methods could be readily transferred to large scale tidal stream farms, they could not be used directly because of the big computational difference between the two technologies as the tidal turbines are operating in constraint environment with a higher density working fluid.

Several methods can be used to study the development of new devices. The most commonly used methods are:

- Small scale experiments
- Analytical techniques
- Computational fluid dynamics

Experimental studies are commonly considered as reliable compared to the analytical and computational methods. However, the use of experiments in a large scale tidal stream farms could inflict huge costs, which is not practical considering the limitation of funds for such huge experimental tests. Thus, analytical and computational techniques have been used for many years to minimise the cost of experiments and have shown good success in supporting the design and development of new devices. The analytical and computational studies are often validated by small scale experiments in order to use them for testing ideas

in a large scale prior to implementation.

Analytical methods have been used in the study of the behaviour of a single and clusters of tidal turbines and to estimate the power potential of tidal currents as documented by Garrett and Cummins [2007], Whelan et al. [2009], Houlsby et al. [2008], Li et al. [2007], Vennell [2012, 2011a,b, 2010], Shives and Crawford [2010]. A theoretical model has been developed by Nishino and Willden [2012b] to explore the efficiency of arrays of turbines partially blocking a wide channel. However, this method is not reliable because of the assumptions made to reduce the number of parameters involved in the development of the analytic models in order to minimise the complexity of the problem but it is still in use because of its simplicity.

CFD is a scientific computing discipline which has a set of methodologies that enable computers to provide numerical simulation of fluid flows [Rizzi and Engquist, 1987, Versteeg and Malalasekera, 2007, Hirsch, 2007, Blazek, 2001]. CFD is a powerful tool and it can be applied in a wide range of areas related to fluid flows, such as in the study of aerodynamics of aircraft and vehicles, hydrodynamics of ships, marine engineering including tidal turbines. In recent years, CFD tools have been commonly used to support the development of tidal turbines by testing new ideas prior to implementation [Bahaj and Myers, 2003]. It is a useful tool for predicting the flow characteristics, the impact of the surrounding environment and the supporting structure on the performance of the device [Williams et al., 2010]. In general, CFD tools can investigate different issues related to tidal turbines with low cost compared to experimental studies [Jo et al., 2012a].

There have been several studies carried out recently using CFD techniques to investigate the performance and wake characteristics of a single turbine and the influence of arrays of turbines as documented by Batten and Bahaj [2006], Bai et al. [2009], Lain and Osorio [2010], MacLeod et al. [2002], Williams et al. [2010], Jo et al. [2012a]. A comparison of CFD and experimental studies has been carried out to investigate the wake states of a single turbine using an actuator disc method, which provides a simplified but encouraging results [Harrison et al., 2010b, Coiro et al., 2006]. A study by ODoherty et al. [2009], Clarke et al. [2007] also investigates the performance of improved tidal stream turbine

using double rows of contra-rotating blades using CFD. Those studies indicates a surge of interest towards the development of efficient tidal turbines and the frequent use of CFD techniques to support this development.

The application focus of this study is the new generation of horizontally operating device, the MRL turbine as mentioned before, aimed at deployment primarily as block farms, rather than fences, in shallow estuaries with medium flow such as the Severn. There are no documented CFD investigations carried out on the MRL turbine to date and most of the aforementioned studies have been focusing on the conventional tidal turbines. Thus a direct use of the methodologies utilized to study the conventional tidal turbines to the MRL turbine is difficult because of the substantial difference of their working principle. In addition, even though some of the impacts of the common parameters such as the blockage effects can be compared, it would be incorrect to directly compare every parameter of the MRL turbine with those employed in conventional turbines.

Detailed CFD models of such machines (including blade geometry and blade motions) can be undertaken using moving reference frame or overset meshing techniques, however the ensuing calculations are computationally unrealistically expensive for all but the very smallest clusters of devices. Therefore, one might expect that trying to compute the performance of several hundred turbines could represent a huge computational cost due to the complexity involved in modelling the individual underwater tidal turbines. Without reliable predictions of farm outputs it is unlikely to be possible to persuade private investors and governments to invest in the exploitation of tidal energy. Beyond the performance estimation, there is also the problem of optimizing the deployment of individual members of large arrays of turbines. Thus, this study endeavours to get satisfactory solutions for the following questions:

1. How to develop computationally realistic semi-empirical turbine models that represents the MRL turbine for use in the CFD modelling of clusters of tidal stream energy capture farms?

2. How to investigate the turbine-to-turbine interactions using such models?

The findings will have significant impact for further research especially to those conducting

multi-objective optimisation of the design of tidal stream farms to minimise investor risk. In addition, the CFD model will help as a guide for the development of analytic models that can be used in determining the performance of several turbines in a tidal stream farm taking into consideration the turbine to turbine interactions. This builds the confidence to implement tidal turbines in a large scale to generate in Gigawatts (GW) of power, which plays an important role in increasing the share of renewable energy supply.

1.5 Research Objectives

This thesis is part of a large project, which aims to develop a methodology for optimizing the design of tidal stream devices in a tidal stream farm taking in to consideration different constraints involved in the determination of their performance. Thus, the main objectives outlined for this thesis work are:

1. The development of a new, computationally cheap CFD based model of the MRL tidal turbine.

2. To perform detailed calculations of the flow field of single and multiple turbines using the developed model to:

    - Understand the downstream wake structure.
    - Calculate the energy that can be extracted from the flow by the turbine.
    - Provide information about dynamics of the free surface.
    - Investigate the turbine to turbine interaction

1.6 Thesis Layout

The thesis is presented in 6 Chapters. Chapter 2 presents a literature review of the computational modelling. This includes details of the governing equations of LES and the source terms such as the newly developed CFD based *Immersed Body Force* (IBF) model, aspects of setting up of the models such as mesh generation, inflow conditions, fluid

properties and wall functions, and the data processing methods such as the post processing tool ParaFoam, and wavelet transforms. Further, it provides a comparison of LES and RANS and the sub Grid scale models of LES.

Chapter 3 presents a detailed analysis of the CFD calculations carried out to measure the performance of the MRL turbine using the IBF model. It also presents details of the experiments of Janssen and Belmont, used here as a validation for the IBF model and a comparison of the performance of the turbine with and without side plates including an investigation of the influence of blade positions on the IBF model results.

Chapter 4 presents a detailed flow field analysis. This includes investigation of the wake characteristics of a single turbine, a detail sensitivity analysis of the wake characteristics to different parameters such as grid size, wall boundary proximity, body force loading, and ambient turbulence intensity, and a comparison of the surface deformation at different turbine positions across the depth of the computational domain.

Chapter 5 presents a detailed investigation of turbine to turbine interactions. It starts with the calculation of the performance of a single turbine and its wake characteristics which is used as a basis for the investigation of the influence of the wake interactions on the downstream turbines. This is followed by the analysis of tidal stream farms containing two, three and seven turbines and provides a detailed investigation of the influence of turbine to turbine interactions both on the flow characteristics and performance of the individual turbines. A discussion of the conclusions and a recommendation for future works is presented in Chapter 6.

Chapter 2

COMPUTATIONAL METHODS

2.1 Introduction

Small scale experimental works have been used for many years to study the design, performance and other related parameters of a new device before the introduction of computational methods. As the devices become sophisticated, the experimental study becomes increasingly expensive and not only this, large scale experimental study is also often prohibitive in terms of time, cost, and deployment. Thus, alternative solutions such as cost effective computational methods have been developed for the study of new large scale designs effectively. However, the computational methods themselves have had their own pitfalls in-terms of effectiveness and their computational power but researchers have developed several methods balancing both the engineering solutions and the computational cost.

In this chapter Large Eddy Simulation (LES) and Reynolds-Averaged Navier-Stokes (RANS), which are commonly used in the study of tidal energy turbines, are presented. In addition, a new tidal turbine modelling method called "*Immersed Body Force (IBF)*" is introduced. The IBF method is used as a forcing function to change the momentum of the fluid flow as it passes through the turbine region. The aim being to develop a simplified turbine modelling method that is a compromise between at one extreme, a full treatment using overset meshing and/or sliding mesh techniques to describe the detailed internal blade motions and at the other, a highly simplified momentum extraction zone such as the actuator disc method. The approach should allow reasonable estimations of the larger length-scale gross effects, such as the turbine to turbine interactions and the depth changes induced by energy extraction linked to flood risk, at moderate computational cost.

The chapter is divided into several sections. Section 2.2 presents a brief introduction of turbulence modelling. The specific turbulence modelling techniques such as LES and

RANS are presented in sections 2.3 and 2.4 respectively. A detailed descriptions of the new IBF turbine modelling approach is presented in section 2.6. In section 2.7 model set-ups such as the mesh generation techniques, the inflow conditions, fluid properties, wall functions and time step control are presented. Section 2.8 presents the data post-processing tools used for analysing the CFD simulation results. 2.9 presents comparison of the computational methods (LES and RANS) and two of the LES sub-grid scale models with an extensive literature review. Finally, the chapter is concluded with a summary.

2.2 Turbulence Modelling

Turbulent flows are characterized as unsteady, three dimensional, fluctuating in a wide range of length scales, and contain vorticity that leads to increased turbulence intensity and energy dissipation and remains the major unresolved problem of classical physics [Tennekes and Lumley, 1972, McDonough, 2004, Celik, 1999, Speziale, 1990]. Most engineering applications including tidal turbines involve turbulent motions. Experiments have been used to study these turbulent flows for many years, but as engineering devices get increasingly sophisticated, the level of detail and accuracy also increase, inflicting massive cost and time constraints [Ferziger and Perić, 1999]. To minimise the cost and time of experiments, other options have been developed in particular numerical methods have been introduced and these methods have become a very popular and cost effective tools for optimising sophisticated devices. The physics of these turbulent flows can in principle be described by the Navier-Stokes (NS) equations however the large number of dynamically significant scales of motion make it impossible for the current computing resources to handle it [Speziale, 1990, Verstappen and Veldman, 1998].

Direct Numerical Simulation (DNS) is the most accurate approach for turbulence simulations because of its capability to solve the NS equations by resolving all the motions without averaging or approximations [Ferziger and Perić, 1999, Eswaran and Pope, 1988a,b, Rogallo and Moin, 1984]. However, the requirements on mesh resolution and time-step size to fully resolve the small scale motions put very high demands on the computer making it extremely computationally expensive. To make the computational cost affordable, efforts

have been made to model the turbulent flows by only resolving a few of the length and time scales of interest although this process makes the physics description less accurate. LES and RANS are the most popular and widely used modelling techniques, and both models have shown great success in replacing the DNS.

Tidal turbines are one of the devices that experience turbulent flows and these modelling techniques have been widely used to understand the physics of the flow surrounding these devices and to calibrate their energy extraction capability from the flow. Some examples of the application of LES and RANS in tidal turbine simulations can be found in [Churchfield et al., 2011, Gant and Stallard, 2008, Sun et al., 2008, Lee et al., 2012, Harrison et al., 2010b, Turnock et al., 2011, Nicholls-Lee et al., 2008, O'Doherty et al., 2009b]. The existing LES and RANS techniques have also been developed for solving two phase incompressible fluids capturing the interface using a Volume of Fluid (VOF) method (refer to section 2.5 for a description of VOF method). LES and RANS are discussed in the subsequent sections. In the present study a new source term, body force (F_b), was added to the NS equations. Detailed explanation about the new source term added is given in section 2.6.

2.3 Large Eddy Simulations

The eddy sizes of a turbulent flows may be represented as shown in Fig. 2.1 because of the wide range of length and time scales available in the flow. The large scale eddy sizes are represented by LES and are most energetic, making them the most effective way of transporting the conserved properties [Ferziger and Perić, 1999]. In contrast, the small scale eddy sizes are weaker in terms of transporting the conserved properties. A spatial filter is applied to separate the large eddies from the smaller eddies in the turbulent flow. The first application of LES was made by Deardorff [1970], who simulated a turbulent channel flow at an indefinitely large Reynolds number. The LES modelling approach resolves the large-scale turbulent motions by solving the 3D time dependent filtered NS equations while modelling the small-scale motions using Sub-Grid Scale (SGS) methods [Moin and Kim, 1982, Givi, 1989, Lesieur and Metais, 1996]. As the mesh gets finer, the

number of scales that require modelling becomes larger, thus approaching the DNS.

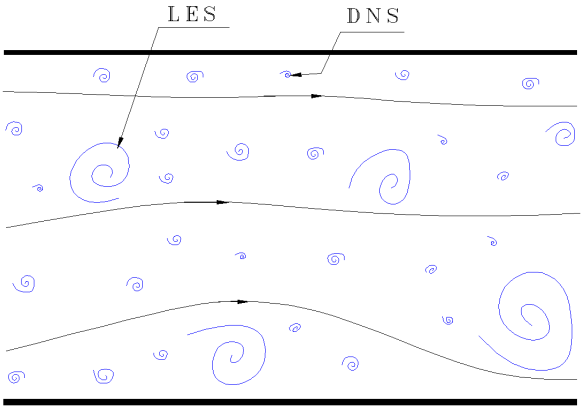

Figure 2.1: Schematic representation of turbulent flows [Ferziger and Perić, 1999]

2.3.1 LES Governing Equations

The LES governing equations utilized for the simulations are a combination of filtered NS equations and source terms. Filtering the NS equations is essential in the LES modelling to separate the velocity field that contains the large scale components of the total field as shown in Fig. 2.1, which is performed by filtering the velocity field [Leonard, 1974]. Using the one-dimensional notation, the filtered velocity is defined as:

$$\overline{u}_i(x) = \int G(x, x')u_i(x')dx' \tag{2.1}$$

Where $G(x, x')$ is the filter kernel, which is a localized function. The eddy sizes are identified using a filter width, Δ. Eddies that are larger than Δ are considered as large eddies, those the ones that are resolved, whilst those which are smaller than Δ , the small eddies, will be replaced by a statistical model. Filtering the NS equations for incompressible flow produces a set of equations [Ferziger and Perić, 1999, Xie and Castro, 2006] that can be written as:

$$\frac{\partial \overline{u}_i}{\partial t} + \frac{\partial}{\partial x_j}\left(\overline{u_i u_j}\right) = -\frac{1}{\rho}\left(\frac{\partial \overline{p}}{\partial x_i} + \delta_{i1}\frac{\partial \langle P \rangle}{\partial x_1}\right) + \nu\frac{\partial}{\partial x_j}\left(\frac{\partial \overline{u}_i}{\partial x_j} + \frac{\partial \overline{u}_j}{\partial x_i}\right) + \rho g_i + \overline{F}_s + \overline{F}_b \tag{2.2}$$

However, the continuity equation does not change in the filtering process because of its linearity and can be written as:

$$\frac{\partial \overline{u}_i}{\partial x_i} = 0 \tag{2.3}$$

Where the bar $\overline{(.)}$ defines the resolved scales; $\overline{u}$ is the filtered velocity; $\overline{p}$ is the filtered pressure; ν is a kinematic viscosity; δ_{i1} is the Kronecker-delta and $\frac{\partial \langle P \rangle}{\partial x_1}$ is the driving force, a constant streamwise pressure gradient.

Since $\overline{u_i u_j} \neq \overline{u}_i \overline{u}_j$, the filtered convection term $\overline{u_i u_j}$ is the cause of difficulty in LES modelling because of its non-linearity causing the interaction of large and small scales making it separation difficult. One of the modelling approximation for the difference of the two inequalities has been introduced by Leonard [1974], which splits them as:

$$\tau_{ij} = \overline{u_i u_i} - \overline{u}_i \overline{u}_i \tag{2.4}$$

Where the new linking term τ_{ij} is the SGS Reynolds stress. Combining Eqns. (2.2) and (2.4), the filtered NS equations can be rewritten as:

$$\begin{aligned} \frac{\partial \overline{u}_i}{\partial t} + \frac{\partial}{\partial x_j}\left(\overline{u}_i \overline{u}_j\right) = -\frac{1}{\rho}\left(\frac{\partial \overline{p}}{\partial x_i} + \delta_{i1}\frac{\partial \langle P \rangle}{\partial x_1}\right) + 2\nu \frac{\partial}{\partial x_j}\overline{S}_{ij} - \frac{\partial \tau_{ij}}{\partial x_j} \\ + \rho g_i + \overline{F}_s + \overline{F}_b \end{aligned} \tag{2.5}$$

where $\overline{S}_{ij}$ is the strain rate of the large scales or resolved scales and is defined as:

$$\overline{S}_{ij} = \frac{1}{2}\left(\frac{\partial \overline{u}_i}{\partial x_j} + \frac{\partial \overline{u}_j}{\partial x_i}\right) \tag{2.6}$$

2.3.2 LES Sub-Grid Scale Models

The resulting SGS stresses from the filtering processes are unknown and need modelling. The stresses are a large scale momentum flux resulting from the unresolved scales. Most of the time, those stresses have been approximated by SGS models based on the eddy viscosity. The most commonly employed hypothesis in the SGS turbulence models is the Boussinesq hypothesis [Boussinesq, 1877] and calculates the SGS stress using a linear

relationship with the rate of strain tensor. The most popular SGS models extensively used for simulations include Smagorinsky, the one equation eddy viscosity, and the dynamic sub-grid scale models, which can be applied to nearly all SGS models. Definition of the former two sub-grid scale models are discussed in the next sections and a comparison of these models is given in section 2.9.2.2 with a sample of tidal turbine simulations.

2.3.2.1 Smagorinsky

The earliest SGS model was the model proposed by [Smagorinsky, 1963], where the SGS stress is related to the rate of strain tensor using the Boussinesq hypothesis, as:

$$\tau_{ij} - \frac{1}{3}\tau_{kk}\delta_{ij} = -2\nu_t \overline{S}_{ij} \tag{2.7}$$

Where: ν_t is the SGS eddy viscosity computed as $\nu_t = C_S^2\overline{\Delta^2}|\overline{S}|$, C_S is the Smagorinsky coefficient, $\overline{\Delta}$ is the length scale, and $|\overline{S}| = (\overline{S}_{ij}\overline{S}_{ij})^{1/2}$. The value of C_S is not constant for any kind of problem because of different reasons (refer to section 2.9.2.2 for detailed discussions).

2.3.2.2 One-equation eddy viscosity

The one-equation eddy viscosity model (*oneEqEddy*) developed by Yoshizawa and Horiuti [1985] has been used in a wide range of turbulent problems. Based on Yoshizawa and Horiuti [1985], the sub-grid stresses are defined as:

$$\tau_{ij} = \frac{2}{3}k_{sgs}\delta_{ij} - 2\nu_t \overline{S}_{ij} \tag{2.8}$$

where ν_t is the SGS eddy viscosity given as:

$$\nu_t = C_k\overline{\Delta}\sqrt{k_{sgs}} \tag{2.9}$$

and the SGS kinetic energy, k_{sgs}, is given as:

$$k_{sgs} = \frac{1}{2}\left(\overline{u_i u_i} - \overline{u}_i \overline{u}_i\right) \tag{2.10}$$

The transport equation for the SGS kinetic energy is defined as [Menon et al., 1996]:

$$\frac{\partial k_{sgs}}{\partial t} + \overline{u}_i \frac{\partial k_{sgs}}{\partial x_i} = -\tau_{ij}\frac{\partial \overline{u}_i}{\partial x_j} - C_c \frac{k_{sgs}^{3/2}}{\overline{\Delta}} + \frac{\partial}{\partial x_i}\left(\frac{\nu_t}{\sigma_k}\frac{\partial k_{sgs}}{\partial x_i}\right) \tag{2.11}$$

where $C_k = 0.05$, $C_c = 1.0$, and $\sigma_k = 1.0$ based on Menon et al. [1996]. However, different values of the the model coefficient C_k have been used in other studies such as $C_k = 0.094$ by Nakayama and Vengadesan [2002], $C_k = 0.1$ by Moeng and Wyngaard [1988].

2.4 Reynolds Averaged Navier-Stokes

The Reynolds-averaged Navier-Stokes equation is obtained by statistical averaging of the equations of motion, where none of the flow structures are resolved, and requires the introduction of turbulence models. These turbulence models are used to model all the large and small scale motions and depend on the average flow quantities or modelled approximations. The modelling approach results in a loss of all spectral effects in the time averaging process [Davidson and Peng, 2003].

2.4.1 RANS Governing Equations

The unsteady RANS modelling approach solves the Reynolds averaged equations of mass and momentum conservation given in Eqns: (2.12) and (2.13) respectively [Harrison et al., 2010a, Sun et al., 2008]

$$\frac{\partial \overline{U}_i}{\partial x_i} = 0 \tag{2.12}$$

$$\frac{\partial \overline{U}_i}{\partial t} + \frac{\partial \overline{U}_i \overline{U}_j}{\partial x_j} = -\frac{1}{\rho}\left(\frac{\partial \overline{P}}{\partial x_i} + \delta_{i1}\frac{\partial \langle P \rangle}{\partial x_1}\right) + \frac{\partial}{\partial x_j}\left(\nu \frac{\partial \overline{U}_i}{\partial x_j} - \overline{u_i' u_i'}\right) + \rho g_i + \overline{F}_s + \overline{F}_b \tag{2.13}$$

Where the bar $\overline{(.)}$ defines the time averaged components; $\overline{U}$ is the Reynolds averaged velocity; $\overline{P}$ is the Reynolds averaged pressure; ν is a kinematic viscosity; δ_{i1} is the Kronecker-delta, $\frac{\partial \langle P \rangle}{\partial x_1}$ is the driving force, a constant streamwise pressure gradient, and $\overline{u_i' u_i'}$ are the Reynolds stresses. The Reynolds stresses are defined as:

$$\overline{u_i' u_i'} = \nu \left(\frac{\partial \overline{U}_i}{\partial x_j} - \frac{\partial \overline{U}_j}{\partial x_i} \right) - \frac{2}{3} k \delta_{ij} \tag{2.14}$$

where $k = \frac{1}{2}\overline{u_i' u_i'}$ is the turbulent kinetic energy.

A set of fairly simple turbulence models can be constructed by utilising the Boussinesq approximation, modelling the effect of the unresolved turbulence as a turbulent viscosity (enhancing or replacing the molecular viscosity). The most commonly used turbulence model, the $k - \epsilon$ model, is of this kind. However, the Boussinesq approximation is an assumption of isotropy in the unresolved turbulence, which is not always appropriate. More sophisticated models include Reynolds stress models, in which algebraic or transport models are developed for all independent components of the unresolved (Reynolds) stress term. The standard $k - \epsilon$ model is used to model the Reynolds stress term, $\overline{u_i' u_i'}$, by utilising the turbulence kinetic energy ,k, and its dissipation rate, ϵ, as [Sun et al., 2008]:

$$\nu_t = C_\mu \frac{k^2}{\epsilon} \tag{2.15}$$

The turbulent kinetic energy and the dissipation rate are derived from two separate transportation equations.

Turbulent kinetic energy:

$$\frac{\partial k}{\partial t} + \frac{\partial \overline{U}_i k}{\partial x_i} = \nu_t S^2 - \epsilon + \frac{\partial}{\partial x_j} \left[\left(\nu + \frac{\nu_t}{\sigma_k} \right) \frac{\partial k}{\partial x_j} \right] \tag{2.16}$$

Dissipation rate:

$$\frac{\partial \epsilon}{\partial t} + \frac{\partial \overline{U}_i \epsilon}{\partial x_i} = C_{\epsilon 1} \frac{\epsilon}{k} \nu_t S^2 - C_{\epsilon 2} \frac{\epsilon^2}{k} + \frac{\partial}{\partial x_j} \left[\left(\nu + \frac{\nu_t}{\sigma_\epsilon} \right) \frac{\partial \epsilon}{\partial x_j} \right] \tag{2.17}$$

where S is the turbulent kinetic energy production, C_μ, σ_k,σ_ϵ, $C_{\epsilon 1}$, $C_{\epsilon 2}$ are model co-

efficients with their values 0.09, 1.0, 1.3, 1.44, and 1.92 respectively [Sun et al., 2008, Santiago et al., 2010, Xie and Castro, 2006, Salim et al., 2011, Dejoan et al., 2010].

2.5 Volume of Fluid Method

The MRL turbine is designed to operate relatively close to the water surface and the dynamics of the free surface will be important to understand the overall behaviour of the turbine. The VOF method has been widely used in the study of floating body applications, breaking waves, non linear free surface flows and other multiphase flows as documented by Yang et al. [2006, 2005], Chen et al. [1999], He et al. [1999]. It is a simple, flexible and efficient method for treating free boundaries as described by Hirt and Nichols [1981] and was used in this study coupled with the governing equations.

The volume of fluid in a cell is calculated as $F_{vol} = \alpha V_{cell}$, where V_{cell} is the volume of a computational cell and α is the fluid fraction of a cell. If the cell is filled with fluid then $\alpha = 1$ and if it is void then its value should be 0. At the interface between the two phases, the value of α is between 0 and 1.

The value of α is calculated from a separate transport equation as:

$$\frac{\partial \alpha}{\partial t} + \bigtriangledown . (\alpha \overline{u}) = 0 \tag{2.18}$$

An extra artificial compression term, which is active only on the interface region, is introduced into Eqn. (2.18) in order to account a surface compression which occurs during the simulations. Therefore, Eqn. (2.18) is re-written as:

$$\frac{\partial \alpha}{\partial t} + \bigtriangledown . (\alpha \overline{u}) + \bigtriangledown . (\alpha (1 - \alpha) u_c) = 0 \tag{2.19}$$

The physical properties (μ and ρ) at any point in the domain are calculated as a weighted averaged of the volume fraction of the two fluids, α , as:

$$\mu = \alpha \mu_f + (1 - \alpha) \mu_g \tag{2.20}$$

$$\rho = \alpha\rho_f + (1-\alpha)\,\rho_g \tag{2.21}$$

2.6 Turbine Modelling

2.6.1 Detailed Modelling Method

The application focus was the new generation of horizontally operating devices aimed at deployment primarily as block farms, rather than fences, in shallow estuaries with medium flow such as the Severn. These devices are typified by: THAWT machine developed at Oxford University, the Momentum Reversal Lift (MRL) turbine produced by Aquascientific Ltd., and the family of devices designed by Natural Currents Ltd.

The focus of this study was particularly on the MRL turbine designed based on a cylindrical cycloidal system where each of three blades rotates 180^0 for every full rotation of the main shaft as discussed in Chapter 1 section 1.3.2. This clearly induces very complex, highly sheared internal flows plus large oval like shaped circulation flows. Detailed CFD models of such machines (including blade geometry and blade motions) can be undertaken using dynamic (sliding) mesh or overset meshing techniques, however the ensuing calculations are computationally unrealistically expensive for all but the very smallest clusters of devices. Given that the long term goal is farm scale array modelling, such methods are untenable to use for arrays of devices. Hence this study aimed at developing moderate cost techniques that have acceptable fidelity.

2.6.2 Actuator Disc Method

The principle of an actuator disc has been frequently utilized for modelling turbines both in experimental and computational studies. It has been widely used for wind turbines as documented by [Mikkelsen, 2003, Sanderse, 2009]. Recently this method has been also used in tidal turbines both in experiments [Harrison et al., 2010b] and using CFD techniques [Belloni and Willden, 2011, MacLeod et al., 2002, Sun et al., 2008]. The disc acts as a momentum sink which is matched to the thrust coefficients of the turbine [Gant and Stallard, 2008, Harrison et al., 2010b]. The pressure drop, S_i, is imposed as a sink term

into the Navier-Stokes flow equations creating a pressure drop across the disc [Harrison et al., 2010b] and is defined as:

$$S_i = \frac{K_L}{\ell}\frac{1}{2}\rho u_{i(d)}|u_{i(d)}| \tag{2.22}$$

where, K_L is the resistance coefficient of the disc, $u_{i(d)}$ is the velocity at the disc, ℓ is the disc thickness.

Examples of the studies carried out using the actuator disc method include the simulation of two dimensional flow past a turbine with a free surface by Draper et al. [2010], simulation of a horizontal axis turbine and comparison of the far wake with experimental data [Harrison et al., 2010b, Myers and Bahaj, 2010], and for the study of close proximity [Gant and Stallard, 2008]. Studies by Harrison et al. [2010b], Sun et al. [2008], Gant and Stallard [2008] indicate that the above method minimizes the requirement of mesh refinement and of modelling the geometry in full, thus reducing the associated computational costs. The technique has shown good agreement with experimental data but Harrison et al. [2010b] acknowledged that the vortex shedding from the edge of the disc is not similar to the real turbines. The study by Gant and Stallard [2008] also indicates that the actuator disc method has no capability of resolving the flow around each blade except by reducing the momentum of the fluid as it passes through the disc.

A laboratory experiment was carried out by Harrison et al. [2010b] using an actuator disc rather than re-creating the turbine blades, which gave realistic results. The actuator disc is chosen for simplification purpose because of the problem of downscaling the turbines involved in laboratory studies. However, Harrison et al. [2010b] noted that the actuator disc did not produce swirl flows like rotating blades do, and the vortices shed from the edges of the disc are different from the bladed turbines. The concerns about downscaling the turbines were supported by the fact that a hydraulic jump was observed during experimental study of a horizontal axis turbine by Myers and Bahaj [2007] which is believed to be due to the constrained experimental conditions. Therefore, a CFD model will be a better choice for resolving the forces around the blades by eliminating the use of large scale experimental works.

Understanding the rotational effects of real turbines is crucial to the study of tidal turbines in order to correctly describe the free surface and the downstream wake structures, which is the main concern when using the actuator disc method as it fails to resolve sufficient detail of the large scale transient flow though it is considerably cheaper to compute. Other methods of modelling the rotational effects were carried out by Mason-Jones et al. [2008], O'Doherty et al. [2009b], using an approach of cutting a cylinder from the channel, to create a rotating inner cylinder (containing the marine current turbine) and a stationary outer cylinder. Similarly, O'Doherty et al. [2009a] used the same approach of the cylinder but this time accommodating the turbine blades. However, the problem with this approach is that any larger cylinders would have the possibility of overlapping.

2.6.3 Immersed Body Force

Most researchers accept that simple momentum sink zone models such as the actuator disc methods are crude and make it difficult to incorporate energy loss processes. However, they are one of the few computationally realistic approaches for gaining insight into the behaviour of substantial clusters of devices. This study builds upon this accepted methodology by incorporating additional geometric features that induce energy absorption from the flow which also lead to a downstream wake structure intended to reflect more closely those of the real turbines than simple momentum sink zone models. In this study, a different tidal turbine modelling method called *Immersed Body Force (IBF)* is therefore introduced. The IBF model must be capable of three roles:

1. Estimating the downstream wake structure.

2. Allowing calculation of the energy that can be extracted from the flow together with a method of relating this to methods of estimating the useful power extracted by the turbine which can be validated against experiments. This typically requires access to a fully detailed CFD model as an intermediate step.

3. Providing information about the free surface interaction. This is important in the class of machines considered here because they are designed to be deployed close to

the surface, often supported by floating pontoons. Thus in principle pitch resonance of the pontoons could occur with undesirable results.

For the IBF approach, a forcing function per unit volume of the blades (F_b) representing the resistance by the turbine against the flow is used to create momentum change. The force function was imposed in the NS equations and a code was developed by considering drag (F_{RD}) and lift (F_{RL}) resistance forces applied by the blades on the fluid flow as shown in Fig. 2.2. The force applied by the vertical blade was considered entirely as a

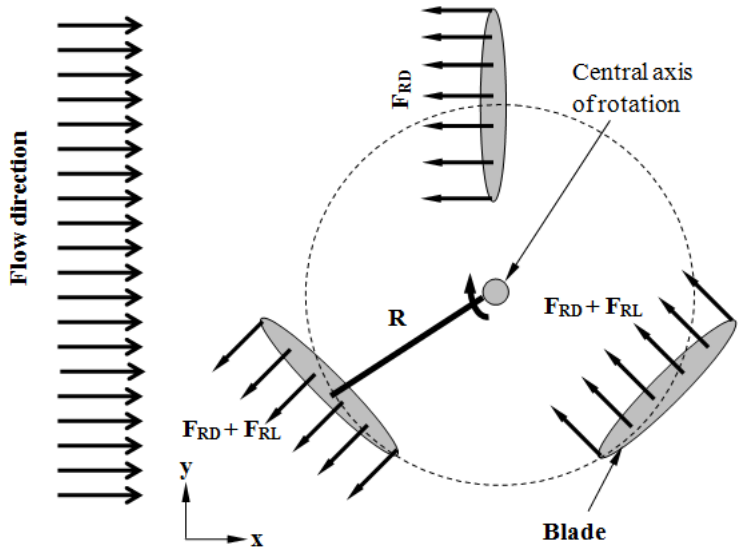

Figure 2.2: Body forces applied by each blade (*blade* method)

drag resistance force while the other two blades have both drag and lift resistance forces. This force is a reaction force to the forces applied by the flow on the blades. The forcing function can be defined as:

$$\overline{F}_b = \overline{F}_{RD} + \overline{F}_{RL} \tag{2.23}$$

The IBF model comprises two parts:

1. A set of resistance forces seated on the cells corresponding to the fixed blade positions as shown in Fig. 2.2.

2. A force ring designed to represent the effect of the main turbine vortex as shown in Fig. 2.3.

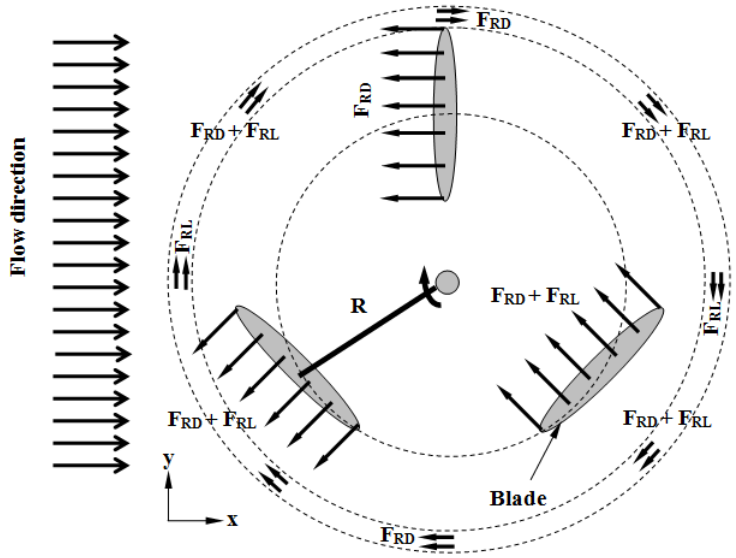

Figure 2.3: Body forces applied by each blade and annular section (*annular* method)

Both 1 and 2 contain the free parameters (F_{RD} and F_{RL}) that define the associated resistances against the incoming flow. This type of representation has several advantages as summarised below:

- It reduces the requirement of mesh resolution at the surface because there is no physical presence of the blades in the model, which minimises the requirement of fine meshing to treat the blade surface and fluid interaction.

- It is applied in a volume which creates complex motions within the turbine housing

- The geometric features lead to downstream wake structures intended to reflect more closely those of the real turbines.

- If the physical blades were to use, they will be simply as solid boundaries imposing blockage but in the case of using the resistance forces, there is a flow of fluid through it similar to the porous region used in the application of actuator disc method. However, if excessive resistance were to be used, it will act as a blockage body similar to the physical body of the blades.

- It allows application of both drag and lift resistances against the flow based on the blade position.

The models described in Figs. 2.2 and 2.3 are denoted *blade* method and *annular* method respectively for subsequent discussions.

2.6.3.1 Limitations of the Immersed Body Force model

Since the IBF model is developed on the notion of non-rotating blades, this clearly has a number of limitations compared to a detailed CFD modelling techniques. Those limitations are mostly related to the way the energy is extracted from the flow plus the swirling type of flows that are produced by rotating turbines. However, despite the limitations of this approach, will be shown that it can still be usefully applied especially for optimisation of arrays of devices where there is a significant computational demand. The following two major limitations are identified in the IBF model approach:

- The shedding of tip vortices and swirling flows from the blades of a rotating turbine can not be replicated.
- The IBF model mathematically extracts power from the flow due to the total change in flux within the finite length of the device, whereas the actual turbine power is calculated using the flow generated torque and angular speed in detailed CFD models and experiments.

2.6.3.2 IBF model parameter

The body force or resistance is the main free parameter required as an input in the IBF model. There are two ways to obtain this free parameter.

1. Using an iteration scheme until a specified power coefficient is achieved
2. From experimental data

The first approach requires a known value of the performance of the turbine in advance which is not the case in this particular study as one of the objectives is to establish the operating point of the novel MRL turbine. While a preliminary experimental work has been undertaken on this device there is no comprehensive parametric exploitation of it either experimentally or using CFD simulations. The experimental data can be used to

fix the power coefficient in advance in cases where there are no other options. However, this is not possible if there are no detailed experimental data for tidal stream devices as the power coefficient of individual devices is unknown in advance before simulations are performed, which is the case in this study.

The second approach can be easily employed to obtain the free parameters/resistance forces using a simple empirical formula by assuming that the blades are at instantaneous positions as if they were rotating. This means if the blades were rotating they are generating torques and at that instant, the resistance forces can be considered equivalent to the thrust force applied by the fluid against the blades. Note that the thrust force must be greater than that exerted on a stationary structure or there would be no rotation. In the present case the initial estimate of the IBF parameter was made from experimental data rather than starting from scratch. This approach can link the resistance forces to the experimentally measured torques and considering the radius from the axis of rotation of the centre of the blades, $R = 0.0525$, the IBF parameter, F_b , can be calculated as:

$$\tau = F_b R \tag{2.24}$$

Thus the second approach has been used to obtain the IBF parameter in most of the single turbine simulations due to the availability of experimentally measured torques. Once the value of F_b is calculated from Eqn. (2.24), it is decomposed into the drag and lift forces based on the chosen position of the blades and is equally divided to the three blades. This decomposition is made within the CFD code.

2.7 Model Set-up

2.7.1 CFD Software Package

There are many CFD packages available for solving complex fluid flows. To name a few, Fluent, OpenFOAM (Open Field Operation And Manipulation), STAR-CCM$^+$ etc. Most of the available CFD packages have their own strengths and weaknesses, in one way or

another, in solving the problems at hand or in their ease of use. Some of the CFD packages, such as OpenFOAM, are open source codes and are free to use, but the others, such as Fluent, are commercial and the codes are not accessible. There are also in-house codes which are either universal or for specific problems developed by individual companies and institutions but are not freely available to the public for use.

OpenFOAM is an open source CFD toolbox produced by OpenCFD Ltd and it is a rapidly expanding software package, with the largest user base in a wide range of engineering applications [Jasak et al., 2007, Jasak, 2006]. The software package includes meshing tools, pre and post-processing tools and accepts meshes developed by a number of other mesh generators and CAD systems. Moreover, the packages give full freedom for users to modify the existing code to extend its functionality to suit their own problem. A combination of all these advantages attracts CFD users to use the OpenFOAM package and it is becoming more popular in recent years. Therefore, it was decided that OpenFOAM would be used for the simulation of the MRL turbine in this study.

2.7.2 Geometry and Mesh Generation

In CFD simulations, mesh generation is as important as the models used for the simulations. The strong effect of the mesh structure on the results has meant that a large number of mesh generation tools have been developed. The smaller the cell size of meshes, the more the model is capable of resolving the flow and capturing the flow characteristics. However, as the cell count increases, the computation time increases rapidly.

OpenFOAM gives great flexibility by supporting unstructured meshes of cells of any shape, allowing mesh generation around more complex geometries. However, the computational domain for the MRL turbine is relatively simple and so it was not necessary to use more complex meshing tools in this study. *blockMesh* is a multi-block mesh generator software included in the OpenFOAM package and is mostly used for simple geometries generating hexahedral meshes. Although orthogonal cells have the capability of reducing errors by avoiding interpolation, hexahedral meshes are more easily controllable by the user, though they are not suitable for complex geometries.

The LES modelling approach requires finer mesh compared to the RANS approach and in general the cell sizes have to be fine enough to capture the flow field around the region of interest, such as around the blades in tidal turbines. Studies by O'Doherty et al. [2009b], Craft et al. [2006], Mccombes et al. [2011] suggest that the tip effects require capturing and need high mesh density. Mccombes et al. [2011] particularly indicated that around two hundred nodes are needed for a blade profile, which could reach millions of cells if all the computational domain were to be meshed with the same cell sizes.

Thus in the study of the MRL turbine, the cell size in the region of interest (turbine housing) was kept as fine as possible for improved capture of the flow characteristics on the surface of the side plates as there are no physical blades present for the reasons discussed previously. The meshing for the rest of the computational domain was coarser when moving away from the turbine, in order to reduce the computational time required. The mesh size used in most of the simulations ranged from 156848 cells for a single small scale MRL turbine simulation to as many as 1.2 million cells for the simulation of tidal device farms containing 7 MRL turbines. However, a sensitivity analysis with different cell sizes have been undertaken to understand its effect on the results.

2.7.3 Inflow Conditions

The inflow conditions are required to be a realistic representation of the practical engineering situation, although sometimes it is difficult to achieve those realistic conditions due to constraints such as time, cost and technology. Based on the way the data is obtained, Gant and Stallard [2008] divided the input data into three major categories as follows:

1. Gathering on-site data measurements.

2. Meta-scale simulations to predict the flow field.

3. Assumption of velocity profiles and turbulence values.

The first approach to obtaining the input data is mostly either site specific or expensive and time consuming but if this approach is used, it is the most reliable data as it often represents the realistic conditions. The second approach is based on a large scale simulation and

requires a detailed geometry over a large region which makes it an unfavourable method. The third approach is the most commonly used, although there is often a risk when using assumed data. In this study, the third approach was used because of the absence of field data and the high cost of the large region approach.

2.7.3.1 Inlet velocity

The channel velocity varies with depth. Thus, at the inlet to the computational domain, a $1/7^{th}$ power law velocity field is applied to account for the flow variation along the depth of the channel. This velocity field has been studied for many years and there are some arguments that say the maximum velocity occurs at the free surface as explained by Fischer [1973], Kirkgoz and Ardiclioglu [1997]. This argument has been challenged by other researchers [Gordon, 1992, Yang et al., 2004, Chaudhry, 2008, Chiu and Tung, 2002] and they have proved that the maximum velocity occurs slightly below the free surface because of the resistance at the interface between the two phases, water and air. Gordon [1992] specifically described that the maximum velocity occurs at one third of the water depth from the free surface.

There have been several efforts to develop an appropriate velocity profile in order to use as an inlet boundary condition in the numerical simulations. Harrison et al. [2010b] has used the Dyer boundary layer model [Dyer, 1986] by comparing with measured inflow data from experiments. It may be necessary to use logarithmic equations that take into account the seabed roughness scales in order to accurately predict the velocity profile for a specific site, but collecting those data takes over a period of months and requires high investment [Batten et al., 2008]. For this reason, most researchers tend to use an approximate tidal velocity profile developed by assuming a power law [Schlichting and Gersten, 2004, White, 1991, Batten et al., 2008]. The power law velocity profile gives good approximations for most tidal current sites and it can be estimated by assuming a power law of the form:

$$u_{(y)} = u_{mean} \left(\frac{y}{0.32h} \right)^{1/7} \tag{2.25}$$

where: u_{mean} is the mean velocity, y is the vertical height, and h is the depth of water

level. This method has been used in the numerical simulation of tidal turbines. Some of the research carried out using the power law velocity profile are given in [Bai et al., 2009, Batten et al., 2008, Bahaj et al., 2012]

The present work was not targeted at any specific site therefore it was appropriate to employ the approximate power law velocity profile for this study. Fig. 2.4 shows a plot of the $1/7^{th}$ power law extracted from the undisturbed tidal turbine simulations. In addition, it shows the position of the MRL turbine relative to the velocity profile that has been used in most of the present CFD simulations. However, in some cases of the CFD simulations a

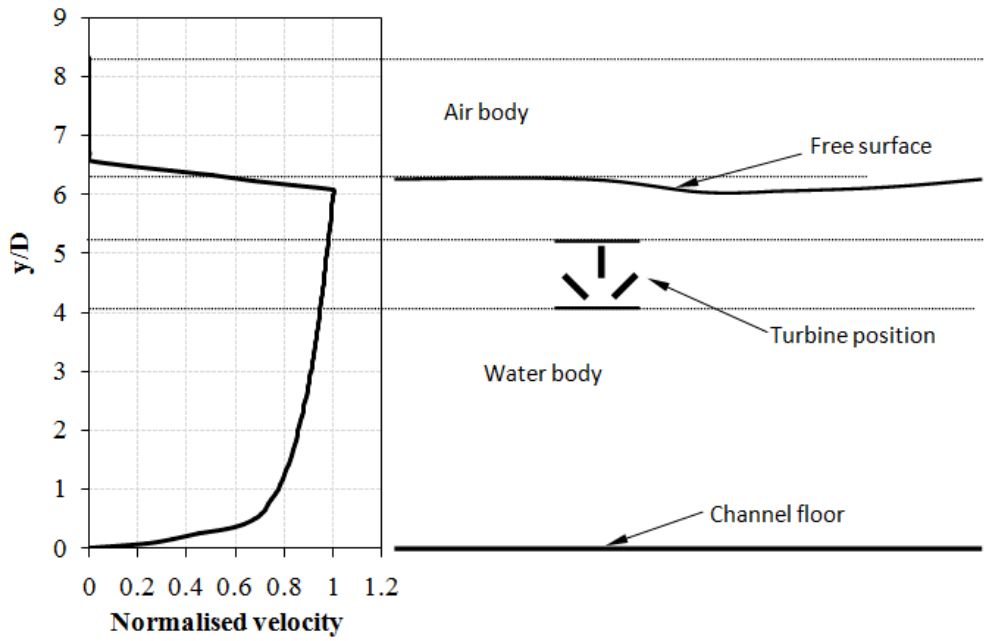

Figure 2.4: Power law turbulent inlet velocity profile

constant velocity across the inlet has been assumed.

2.7.3.2 Turbulent kinetic energy

One of the inlet conditions required in modelling and simulation of turbulent conditions is turbulent kinetic energy (k). This turbulent kinetic energy can be estimated using the equation defined as [Ferziger and Perić, 1999]:

$$k = \frac{1}{2}\overline{u_i' u_i'} = \frac{1}{2}\left(\overline{u_x' u_x'} + \overline{u_y' u_y'} + \overline{u_z' u_z'}\right) \tag{2.26}$$

A turbulence intensity, I, can be defined in-terms of the root-mean-square of the turbulent velocity, u', and the mean velocity, U, as [Myers and Bahaj, 2010]:

$$I = \frac{u'}{U} \tag{2.27}$$

where: $u' = \sqrt{\frac{1}{3}\left(u'_x u'_x + u'_y u'_y + u'_z u'_z\right)}$, $U = \sqrt{u_x^2 + u_y^2 + u_z^2}$. Combining Eqns. (2.26) and (2.27), the turbulent kinetic energy can be estimated as:

$$k = \frac{3}{2} I^2 U^2 \tag{2.28}$$

The value of the turbulence intensity,I, has to be obtained either from measurements or previous experience. There are general guidelines that for high speed flow inside complex geometries and flows inside rotating machinery such as the turbines, the turbulence intensity can be assumed between 5% and 20%. Several Tidal turbine CFD simulations have been carried out using different values of turbulence intensities. A turbulence intensity was estimated by Thomson et al. [2010] ranging from 5% to 50% and recommended 10% for tidal power applications. Lawson et al. [2011] used 5% turbulence intensity in the development and verification of CFD model for horizontal axis tidal turbine. Turbulence intensities ranging from 1% to 20% were also used for tidal turbine simulations by Gant and Stallard [2008], McCann [2007], Shives and Crawford [2011], Egarr et al. [2004]. This shows that there are no clear guidelines on how much inlet turbulence intensity should be used for tidal turbine simulations. Therefore, a turbulence intensity of 5% was assumed and used for the CFD simulations in this study, however a sensitivity analysis was also carried out (see chapter 4 section 4.3.2.4) to investigate the influence of a higher turbulence intensity (15%) on the outcome.

2.7.4 Fluid Properties

The MRL turbine is simulations employed the VOF method described in section 2.5. The properties of the two phases have to be defined in the appropriate directories in the OpenFOAM case and the physical properties used in this study are given in table 2.1.

The surface tension between the two phases is given in the table denoted by sigma. The gravitational acceleration is also required in the simulation and the standard value of 9.81 ms^{-2} is the numerical value used in addition to the physical properties described in table 2.1.

Phase Name	Kinematic viscosity (μ) (m^2s^{-1})	Density(ρ) (kgm^{-3})
Water	1.0×10^{-6}	1.0×10^{3}
Air	1.48×10^{-5}	1.204
Properties of both phases		
Surface tension (Nm^{-1})	Sigma	0.07

Table 2.1: physical properties of the fluid phases

2.7.5 Wall Treatment

The computational geometry includes wall patches on both sides and bottom of the domain. The regions near these walls are highly influential in the presence of turbulent flows because the walls are often subject to a turbulent boundary layer and require a fine mesh to capture the flow characteristics by resolving the turbulence equations up to the wall. A study carried out by Craft et al. [2002] indicates that resolving the flow near the walls could increase the computational time between 3 and 300 times more than the rest of the flow requires, depending on the flow problem, complexity of the mathematical model, and the CFD model adopted. To minimise the high computational cost, wall models have been developed by approximations and assumptions [VAN et al., 1956, Piomelli, 1999, 2008, Moin and Kim, 1982]. Some examples of those wall models are the *van Driest damping* and *wall function* which have been used in this study to model the wall patches to minimise the computational cost.

The *van Driest damping* is a wall damping model which is used to modify and reduce the eddy viscosity near the wall region [VAN et al., 1956, Moin and Kim, 1982, Hughes et al., 2001]. This wall damping model is commonly used for LES modelling technique. The grid length scale, $\overline{\Delta}$, is multiplied by an exponential damping function $1 - exp\left(-\frac{y^+}{A^+}\right)$

where y^+ is the distance from the wall in viscous wall units, $y^+ = yu_\tau/\nu$, u_τ is the friction velocity, and A^+ is a dimensionless constant, $A^+ = 25$.

The *wall function* is developed by describing the effects near to the wall assuming a two-dimensional shear flow in the turbulent boundary layer using several layers and they are commonly employed in the RANS modelling technique. The velocity at the outer layer satisfies the logarithmic law as Piomelli [2008]:

$$u^+ = \frac{1}{\xi} ln(y^+) + B \tag{2.29}$$

Where: $u^+ = \frac{u}{u_\tau}$, $u_\tau = \sqrt{\frac{\tau_w}{\rho}}$, u is the velocity parallel to the wall, τ_w is the wall shear stress, B is a constant ($\approx 5 - 5.5$), ξ is von Karman's constant (≈ 0.41) [Piomelli, 2008]. Close to the wall ($y^+ < 11$) in the viscous sub-layer, the law of the wall can be a linear law as $u^+ = y^+$.

2.7.6 Time Step Control

Time step control is crucial for controlling the computational time and stability, especially on sensitive algorithms such as the surface-tracking of two phase problems. There are two important parameters, namely Courant number and time step which need to be carefully assessed. The maximum Courant number recommended for surface tracking problems is 0.5 in the interface of the two phases. The upper limit of the time step can be set by calculating its value from the maximum Courant number defined for a cell as [Eswaran and Pope, 1988b]:

$$C_o = \frac{\delta t |U|}{\delta x} \tag{2.30}$$

where:δt is the time step; $|U|$ is the magnitude of the velocity through that cell and δx is the cell size in the direction of the velocity.

This upper limit of the time step will keep the Courant number lower than the maximum value during the transient simulation. Automatic time step control can be used to save results at arbitrary times with fixed number of time step intervals but there is also flexibility in OpenFOAM to force the output to be given at fixed times.

2.8 Data Post-processing Methods

Data post-processing is as important as the collection of raw-data from whatever source. Therefore, selecting the correct method of post-processing the data is crucial in order to get the best results out of it. The results obtained from the CFD simulation were processed using different methods such as, graphically using paraFoam, calculation of the power extraction (see Chapter 3 section 3.2 for details), and wavelet transforms.

2.8.1 paraFoam

paraFoam is an open-source data analysis and visualization tool provided with OpenFOAM and runs with ParaView. ParaView is a general scientific visualisation package written using the VTK open source visualisation library. paraFoam is a modified version distributed with the OpenFOAM package which contains a mesh reader module for OpenFOAM file formats. Therefore, this paraFoam tool was used to graphically visualise and analyse the OpenFOAM cases. In addition, data can be extracted from the visualisation tool for further post-processing using other methods.

All the simulations were carried out in 3D but the graphical results demonstrated in the subsequent Chapters are given in 2D, with slices in the three XYZ planes. The slicing methods and the naming used for the three planes are as follows:

- ***Vertical plane*** is sliced with a Z-normal cutting plane through the centre of the turbines.
- ***Horizontal plane*** is sliced with a Y-normal cutting plane through the centre of the turbines.
- ***YZ plane*** is sliced with a X-normal cutting plane through the centre of the turbines.

Some datasets were also extracted from the visualisation tool, often using a line along the centre of the turbines, for further analysis using other methods such as the wavelet transform and analytical calculations. Thus, the velocity and pressure profiles always represent the dataset along the centreline through the turbine unless otherwise described.

2.8.2 Wavelet Transforms

The analysis of the simulated data was mainly carried out by estimating the performance of the turbines and using the velocity graphs. In addition, a wavelet transform method was used to obtain more clear information on the mixing of the wake by using the velocity data extracted from the simulations as a signal. The method helps to transform the velocity signal, one-dimensional data, into another representation which is a more useful and illustrative form [Addison, 2002].

Flow structures such as the wake downstream of the turbine as in a statistical sense are non-stationary. This description is thus best suited to non-stationary representation function such as the wavelets. Statistically stationary representations like Fourier are ill-suited to such situations. The Wavelet transform can be calculated via an inner product between an analysing wavelet at a given scale λ and the signal to be analysed. The wavelet analysis uses multi-scale wavelike functions known as wavelets. There are two types of wavelet transform, a continuous wavelet transform and a discrete wavelet transform [Farge, 1992]. The continuous wavelet transform has been developed by Grossmann and Morlet [1984], whereas the discrete or orthogonal transform was developed by Lemarié-Rieusset and Meyer [1986]. There are several wavelet functions developed for different applications. However, the choice of the function depends on the nature of the data and the kind of information required to be extracted from the signal. In this study, Daubechies orthogonal wavelets were applied to obtain the wavelet coefficients. The analysing wavelet ,ψ, used to investigate the velocity signal is defined as [Addison, 2005]:

$$\psi_{m,n}(x) = \frac{1}{\sqrt{a_0^m}}\psi\left(\frac{x - nb_0a_0^m}{a_0^m}\right) \tag{2.31}$$

Where: a_0 is a fixed dilation step parameter and b_0 is the location parameter. Substituting $a_0 = 2$ and $b_0 = 1$, Eqn. (2.31) can be re-written as [Addison, 2005]:

$$\psi_{m,n}(x) = 2^{-m/2}\psi\left(2^{-m}x - n\right) \tag{2.32}$$

where: m and n controls the dilations and translations respectively. Wavelet coefficients can be obtained from the velocity signals using these equations to better understand the behaviour of the flows. These wavelet coefficients are the relative contributions to the mean square value of a signal from all scales. A discrete wavelet transform was used to compute the wavelet coefficients, $W_{m,n}(x)$, of the velocity signal $u(x)$ using the analysing wavelet as [Tzanetakis et al., 2001]:

$$W_{m,n}(x) = \sum_{m=-\infty}^{+\infty} \sum_{n=-\infty}^{+\infty} u(x)\psi_{m,n}(x) \tag{2.33}$$

2.9 Comparison of the Computational Models

2.9.1 Computational Set-Up

2.9.1.1 Computational domain

The schematic representation shown in Fig. 2.5 gives the dimensions of the geometry used for the computation. To simplify the computational domain and to minimise any bathymetry effect on the simulation results, the bottom of the domain was considered flat. The initial condition of the whole domain is considered to consist of two fluid phase , water

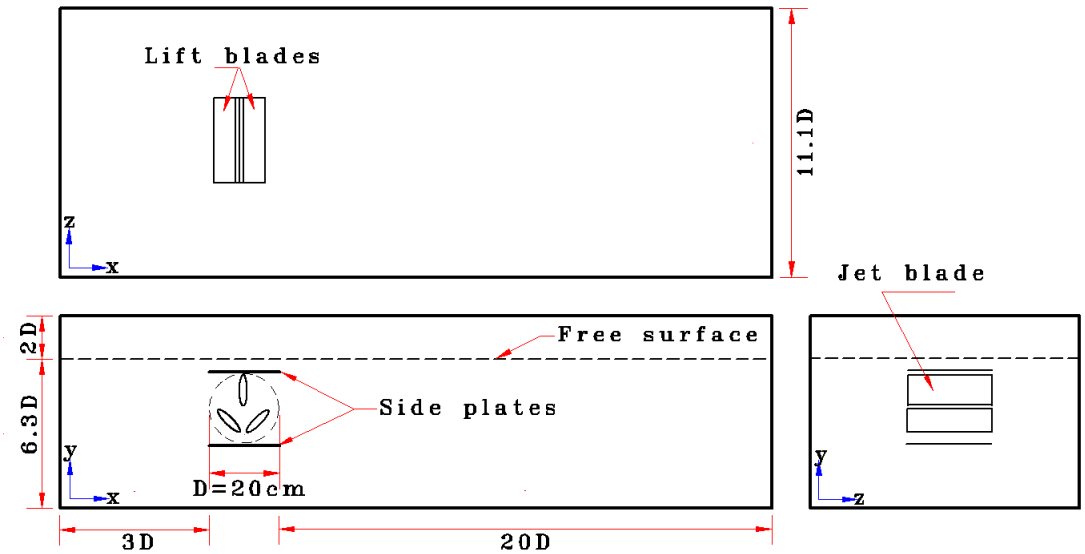

Figure 2.5: Computational domain geometry

and air, as shown in Fig. 2.6. Fig. 2.5 is represented as 3D in Fig. 2.6 in order to show the sharp interface of the two phases where the water level is at 6.3D from the bottom of the domain and the rest of the domain is occupied by air.

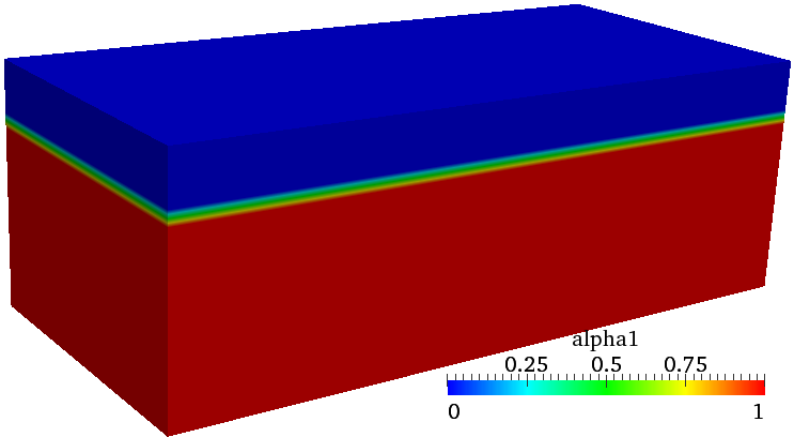

Figure 2.6: Initial Conditions of water and air column

The turbine has an overall diameter of D = 0.20m and a length of L = 0.22m. The blades have maximum thickness and chord length (C) of 1.7cm and 9.5cm respectively. The domain size is 3D upstream of the turbine, 20D downstream, 11.1D laterally and with an overall height of 8.3125D. These dimensions were often used in the simulations but were subjected to some changes based on the requirement of the analysis. The spacing between the turbine and the wall boundary on both sides is 5D. The spacings between the turbine with the bottom wall boundary and the free surface are 4.175D and 1D respectively. The initial conditions for the simulation were $\alpha = 1$ up to 6.3125D, $\alpha = 0$ above this level, representing a water level of 6.3125D from the ground with the rest of the domain occupied by air.

Table 2.2 shows the number of cells used in the computational domain where the cell counts in the horizontal and vertical directions are represented by N_x and N_y respectively and along the span of the domain by N_z. The cell sizes are not equal throughout the domain, in order to reduce the computational cost. The cell sizes were refined in the zone of interest around the turbine region in order to create a uniform computation. The grid topology and mesh are shown in Fig. 2.7. The number of cells given in table 2.2 were used for the computational domain given in Fig. 2.5 but were changed accordingly with the changes of domain dimensions for different analyses. Note that most of the dimensions

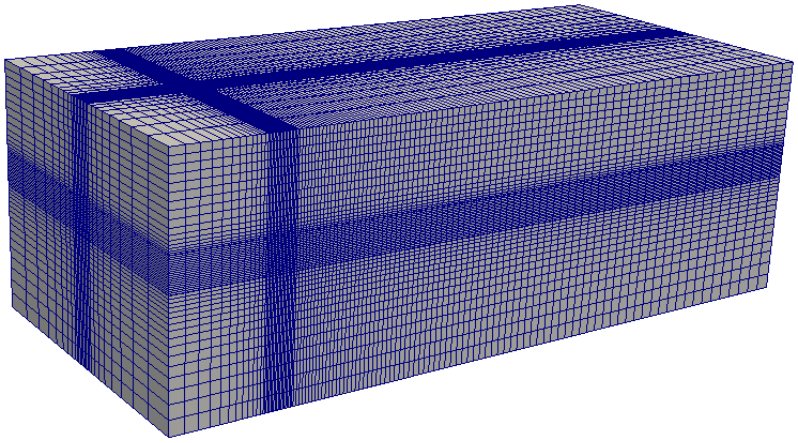

Figure 2.7: Non uniform mesh representation of the domain

Coordinate	Number of cells
X-axis(N_x)	112
Y-axis(N_y)	54
Z-axis(N_z)	26
Total	156848

Table 2.2: Number of cells used for the computational domain

of the computational domains used in this study have been chosen to be arbitrary except dimensions used in the validation with experiments in Chapter 3 section 3.5.1.1. However, there are plans for experimental works to be done in the future in which these computational dimensions could be used as a base to construct the test channel.

2.9.1.2 Implementation of boundary condition

The computational domain contains seven boundary patches, namely *atmosphere*, *seaBed*, *wall*, *waterInlet*, *airInlet*, and *outlet*. The top part of the domain was an atmosphere. This top boundary was free to the atmosphere and allows both outflow and inflow according to the internal flow. *seaBed* and *wall* are the floor and the front and back side of the computational domain respectively and both patches represent wall boundary condition. The *waterInlet* and *airInlet* are the patches where the water and air enter to the computational domain respectively. The *outlet* is the patch where both fluids flow out of the computational domain. The power law approximation discussed previously has been implemented to the inlet to represent the inlet flow conditions with the outlet being a fixed value.

2.9.2 Flow Field Analysis

A preliminary analysis of the flow field simulated using the LES and RANS models was carried out in order to select the appropriate model for the study outlined for this thesis. Although the objective of the thesis is not to compare these models as they require significantly detailed and rigorous analysis, it was important to make a preliminary analysis in terms of the characteristics of the flow field generated by both models. The next two sections compare the two modelling techniques (LES and RANS) and the sub-grid scale models of LES.

2.9.2.1 Comparison of LES and RANS

Several comparisons of the LES and RANS modelling techniques have been reported due to their increased importance in modelling turbulent flows. A detailed comparison of the two techniques was carried out by Rodi [1997], Xie and Castro [2006] to understand the vortex shedding flow past a square cylinder and on a surface mounted cube and the results were compared with detailed experimental data available for those two bluff bodies. The study concluded that the RANS model results with the standard $k - \epsilon$ turbulence model produced poor agreements with the experiments because of excessive turbulence production in the stagnation flow which under-predicted the periodic motion. It was indicated that this problem can be solved by using Reynolds-stress models but even with this modification it was concluded that the RANS model is not sufficient to give better details of the flow compared with the LES although the computational time induced by the use of LES is still noted by the researcher as one of the main challenges. However, Iaccarino et al. [2003], Wegner et al. [2004] have shown that the poor disagreement is due to the assumption of statistical stationarity and proved that unsteady RANS can show good agreement with experiment. In addition, a study by Wegner et al. [2004] in predicting the precessing vortex core phenomenon showed that the unsteady RANS technique can show good agreement with LES and experimental data.

It was also reported by Iaccarino et al. [2003], Lübcke et al. [2001], Churchfield et al. [2011], Schmidt and Thiele [2002], Hamba [2001] that the mesh and time-step requirements

of RANS and LES are quite different. LES resolves the eddies of the turbulence itself which demands a higher spatial and temporal resolution inflicting a huge computational cost but provides more detail of the flow physics, and it places less reliance on turbulence modelling, whereas the more computationally-efficient RANS models model all turbulent scales. Zhang and Chen [2000] also noted that the success of LES in predicting more detailed flow physics is due to the fact that the large-eddy scales make greater contribution to the turbulent transport than the small scale eddies.

A detailed study of the LES and RANS techniques using fully developed flow over a matrix of cubes by Cheng et al. [2003] showed a significant difference between the two techniques. They have used the standard $k - \epsilon$ turbulence model and the findings from the LES approach showed much better agreement with a experiments especially the complex futures such as vortex shedding, large separation zones, topology of the reattachment lines bordering the recirculation regions, fine scale flow structures near the side walls. However it was acknowledged that the computational time was about 100 times higher than the standard $k - \epsilon$ RANS model.

The use of LES and RANS techniques in other applications such pollutant dispersion and pollution transport in buildings, or urban street canyons showed that the LES performs better than the RANS in capturing the spatial distribution of the pollutant and in providing instantaneous fluctuations [Salim et al., 2011, Tominaga and Stathopoulos, 2011, 2010, Gousseau et al., 2011, Santiago et al., 2010, Dejoan et al., 2010]. Although prediction of pollutant dispersion is a different application to the tidal turbines, it clearly shows the extent of their difference when a more detailed physics of the flow is required.

Most of the researchers who conducted a detailed investigation of the differences of RANS and LES techniques agree that RANS is the simplest technique but it lacks accuracy especially in applications where there are more complex flows such as vortex shedding, large separation zones, high streamline curvature etc [Wilcox, 1998, Cheng et al., 2003, Mihaescu et al., 2008, Breuer et al., 2003]. All RANS models suffer from the deficiency that they fail to resolve any of the fluctuating scales in the flow. Mihaescu et al. [2008] and Mongia [2008] noted that the solutions are different for different turbulence models within

the RANS technique, which makes it dependent either on LES results or experiments to choose the proper turbulence model.

Although most of the studies showed that the LES technique is better than the RANS model in many ways, it was important to make a preliminary analysis using the tidal turbine simulations as most of the comparisons made so far were on different applications. This will help to back up the arguments and select the proper technique for the tidal turbine simulations. The standard $k - \epsilon$ turbulence model was used for this single illustration of RANS simulation. Fig. 2.8 show velocity contours of the simulation results using both techniques. It was evident from this single illustration that the flow characteristics especially the downstream vortex structures are different. More detailed information about the vortex shedding was observed from the LES technique given in Fig. 2.8b compared to the results from the RANS (Fig. 2.8a). Better results may be obtained by using different RANS turbulence models but it needs time and effort to obtain and select the best turbulence model. However, even with the appropriate RANS turbulence model there is no guarantee of obtaining detailed flow information as the LES does because of the reasons already discussed above. Thus, it was considered unnecessary to spend much time in finding the proper turbulence model for the RANS technique and the LES modelling technique was been selected for this study.

A strong reason for choosing LES is that because one of the main objectives of this study was to investigate the details of the large scale transient motions within and downstream of the turbines and its importance in the study of wake interactions in the tidal stream farms.

2.9.2.2 Comparison of LES Sub-Grid Scale Models

There are several sub-grid scale models available for different applications. The Smagorinsky is one of the simplest models and it has been commonly used in different applications with the LES technique. However, though it has shown good success, it has several short comings especially if the flow is highly complex and has shear flows as documented by Ferziger and Perić [1999], Murakami [1998]. The most common problems of this sub-grid model are [Murakami, 1998, Speziale, 1998, Bardino et al., 1983]:

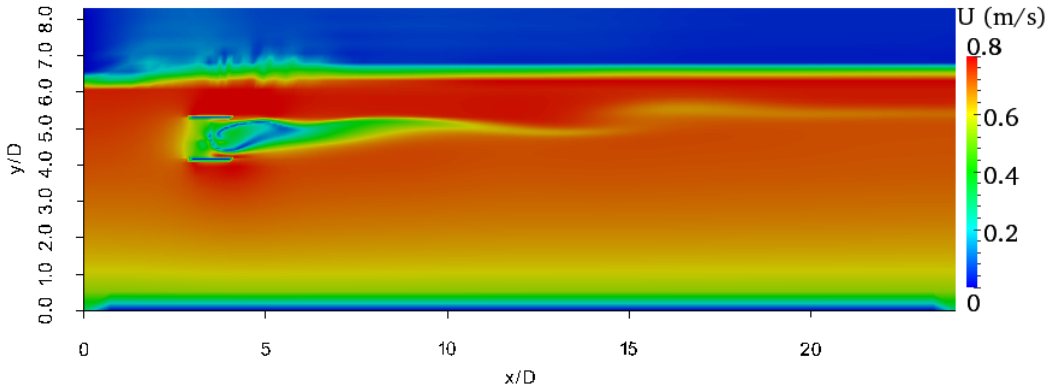

(a) RANS model

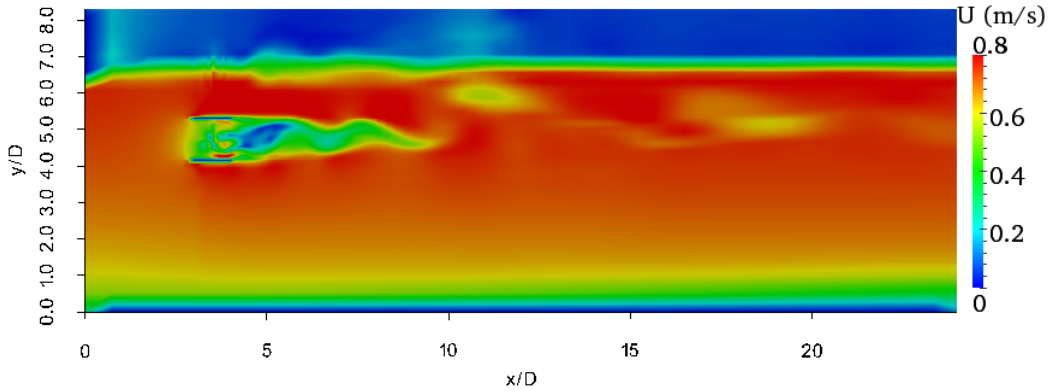

(b) LES Model

Figure 2.8: Snapshots of velocity contours simulated by LES and RANS models

1. The model is over dissipative

2. The model constant C_S has to be optimised based on the flow fields due to its inability to respond to local state of the flow.

3. It exhibits poor correlation with DNS at lower turbulence Reynolds numbers

Since the value of C_S is not constant, although a constant $C_S = 0.2$ can be applied to all isotropic turbulence, this value has to be changed if used for channel flow simulations, as described by [Ferziger and Perić, 1999]. Zhang and Chen [2000] conducted an investigation to understand performance of the standard Smagorinsky model in indoor airflow but failed to give good results. They have proposed a filtered dynamic sub-grid scale model to solve the problem and they argued that this model showed good agreement with experimental data. Menon et al. [1996] also noted that the one-equation eddy viscosity model is much better than the Smagorinsky model because of its weak dependence on the filter width and Reynolds number and therefore is suited for applications in coarse grid LES.

Studies by Germano et al. [1991], Lesieur [1997], Yoshizawa [1991] also pointed out that one of the major drawbacks of the Smagorinsky model is the lack of having a single universal model constant that can be used in different turbulent flow fields and concluded that a dynamic sub-grid scale eddy viscosity model can solve this problem. The dynamic scale model is developed in a way that it locally calculates the eddy viscosity coefficient by sampling the smallest resolved scales to model the sub-grid scale and they argued that this can reflect closely the condition of the flow. However, Johnson [1998] indicated that although the dynamic sub-grid scale model shows some success, it is not suitable for turbulent flows in complex geometries because of uncertainty of the effect of the filter and the difficult of reliable de-filtering.

It should be always noted that the claims of drawbacks and improvements of the different sub-grid scale models are based on comparisons set-up by each developer. For this reason, it is better to select the SGS models by testing them on the same problem of interest. Fig. 2.9 shows a plot of the velocity contours simulated using the two sub-grid scale models tested. The model coefficients of $C_S = 0.2$ and $C_k = 0.094$ were used for the Smagorinsky and one-equation eddy viscosity model respectively. This result shows no significant difference between the two sub-grid scale models. One of the possible reasons for this similarity is that the small scale motions modelled using the SGS model may have little impact on the description of the flow physics surrounding the tidal turbine device compared to the resolved large scale motions. This is an indication that the CFD simulations of the MRL turbine may be independent of the details of the SGS models. Thus it was decided to use the one-equation eddy viscosity in order to avoid any chance of affecting the results due to the drawbacks of the Smagorinsky model discussed from the literature review. Two other values of $C_k = 0.05$ and $C_k = 0.1$ from different literatures were also tested but the results showed no difference and $C_k = 0.094$ was used for the rest of the simulations.

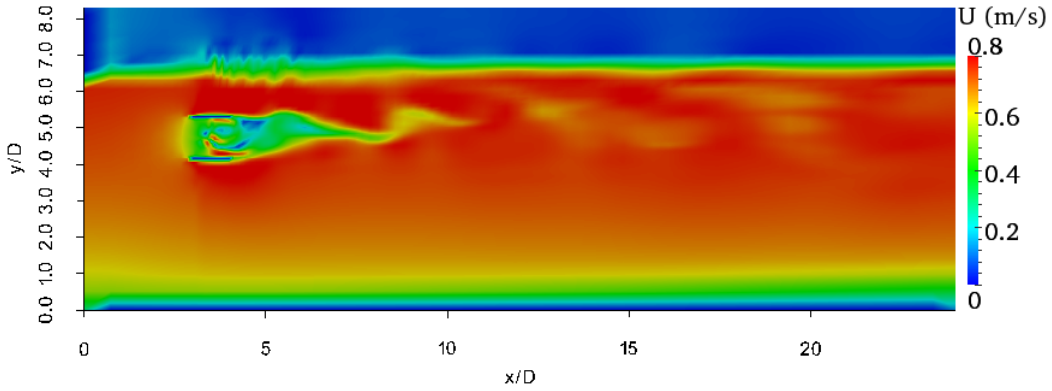

(a) Smagorinsky

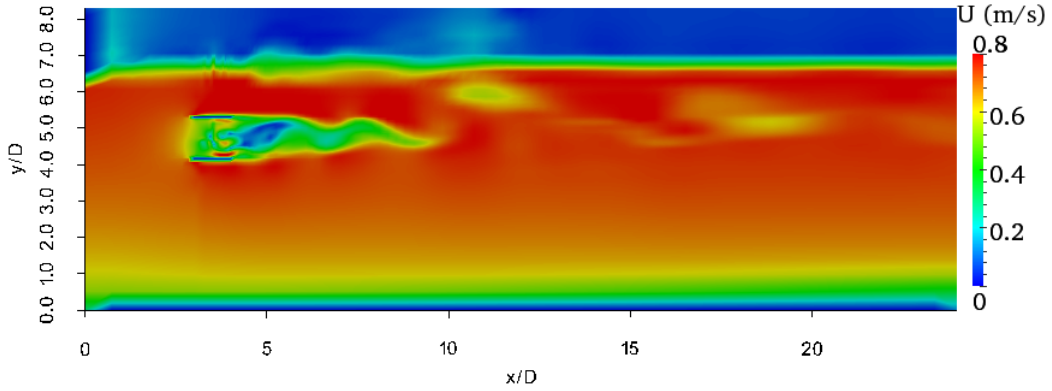

(b) One-equation eddy viscosity

Figure 2.9: Snapshots of velocity contours simulated with different sub-grid scale models

2.10 Summary

The discussions in this chapter have been focusing mainly on the literature of computational methods that have been utilized for turbulent flow simulations. After reviewing and comparing the available turbulent modelling techniques, LES has been selected for the simulation of the MRL turbine due to its fidelity compared to the other techniques. The LES modelling method was developed for solving two incompressible fluids for capturing the interface between the two phases.

A new turbine modelling method called *Immersed Body Force (IBF)* has been developed and added as a source term into the LES governing equations. The IBF model approximates the forces applied by the volume of the blades on the fluid and changes the momentum of the flow. The body force modelling method is a replacement of the actuator disc method that has been used in CFD simulations for years. The reason for changing the actuator disc method to the IBF model is to obtain more complex and sheared internal flows within

the turbine region and thus hopefully better large scale vortex patterns downstream of the turbine.

Set up of the LES modelling is also included with a review of different wall functions, inflow conditions and the methods used for geometry generation and meshing. In addition, the CFD package OpenFOAM, an open source CFD toolbox, used for the simulation is discussed in detail. This package includes geometry generation and meshing software (*blockMesh*) that was used for the generation of the computational domain used in the MRL simulations due to its simplicity.

Chapter 3

CALIBRATION OF ENERGY EXTRACTION

3.1 Introduction

A wide range of tidal stream device designs are currently under development and testing, with the aim of improving the efficiency of traditional tidal devices. One of the new generation of devices is the MRL turbine discussed in Chapter 1 section 1.3.2. The MRL device is currently in the prototype and testing phase and experimental work has been performed by Janssen and Belmont [2009] to measure its performance using a small scale model and its efficiency could reach up to 50%.

This chapter presents the results of experimental scale CFD simulations using the IBF model. The aim of this study is to investigate the performance of the turbine using an open source CFD code, OpenFOAM, and to validate the model with experimental data provided by Janssen and Belmont [2009] and a detailed CFD model. Moreover, the performance of two types of designs for the MRL turbine and two methods of CFD modelling are investigated, in order to find the best option for further development of the turbine. The long term objective is to use this body force representation IBF model in simulations of an array of turbines.

The chapter is divided into several sections. Section 3.2 details formulation of the performance metrics used as a post-processing of the data obtained from the CFD simulations using the IBF model detailed in the proceeding chapter. Section 3.4 details the comparative CFD simulations. This includes thrust and power coefficients and energy flux analysis 3.4.2, investigation of the influence of blade positions (3.4.3), and comparison of two MRL designs and two IBF models in sections 3.4.4 and 3.4.5 respectively. Section 3.5 presents details of validation of the IBF model. This includes details of the experiment of Janssen and Belmont and a comparison with vertical axis IBF model results (3.5.1), comparison of the IBF model with detailed CFD model from Berry and Tabor [2012] (3.5.2). Finally, the

chapter is concluded with a summary.

3.2 Performance metrics

Avoiding modelling the blade motions means that pressure integration over the blade surface cannot be used to directly estimate the mechanical power absorbed by the machine from the flow. Consequently published research on simplified descriptions of turbines of all kinds has focussed upon calculating the energy lost from the flow. Typical examples of this are the various developments of momentum sink models (e.g., actuator disc descriptions) or the Darcy flow based models discussed in Chapter 2 section 2.6.2 that implicitly represent the turbine by a viscous dissipation sink region. Examples of this approach are given in [MacLeod et al., 2002, Nishino and Willden, 2012a, Mikkelsen, 2003, Sanderse, 2009]. A similar approach has been undertaken in the work presented here with modifications as indicated in Chapter 2 section 2.6.3. The model is essentially based on resistances in the streamwise and vertical direction to the incoming flow. The approaches used to calculate the performance of the device are given in detail in the next sections.

3.2.1 Coefficients of Thrust and Power

In most of the actuator disc methods, the turbine is modelled using a porous disc that provides axial resistance coefficient, K_L, to the incoming flow. The thrust force is related to the dynamic head at the disc using the axial resistance coefficient, sometimes called the loss factor, as:

$$T = K_L \frac{1}{2} \rho A \overline{u_t^2} \tag{3.1}$$

where, A is the projected area of the turbine and $\overline{u_t}$ is the streamwise average velocity normal to the disc. In the MRL case, the area is not represented by a single blade but similarly by the total area swept out around the central axis. This is a function of the specific design and includes the blade width and separation of blades from the central axis. Since the blade is face on at one side of the cycle and edge on at the other side, the cross-sectional area is not symmetric about the central rotation axis. The design of

the MRL turbine includes side plates and a new cross-sectional area of the whole device (turbine + side plates), A_{Ref} , is introduced. Both areas are defined as:

$$A = LD$$
$$A_{Ref} = LD^* \tag{3.2}$$

where D^* is a combined diameter of the turbine and side plates and L is the spanwise length of the turbine. Although the cross-sectional area of the turbine, A , is used in the formulation of the equations to avoid redundancy, A_{Ref} has been used with the same equations in cases where the whole device was investigated. The power removed from the flow by the presence of the device is therefore defined using the thrust force and the average velocity as:

$$P = T\overline{u_t} \tag{3.3}$$

Eqn. (3.1) and Eqn. (2.22), which are defined in different forms, have been used to calculate the thrust force by several researchers working on tidal turbines as documented here [Giles et al., 2011, Sun, 2008, Harrison et al., 2010b, Shives and Crawford, 2010, Belloni and Willden, 2011, Bai et al., 2009, Fleming et al., 2011]. Myers et al. [2011] has also studied the performance of the turbine by directly measuring the dynamic force experienced by the disc from the flow instead of using the resistance coefficient. The thrust coefficient is defined using the thrust experienced by the turbine and the thrust force available in the upstream flow as:

$$C_T = \frac{T}{\frac{1}{2}\rho A u_\infty^2} \tag{3.4}$$

Similarly, the power coefficient can be defined using the power removed from the flow by the device and the kinetic flux available in the upstream flow as:

$$C_P = \frac{P}{\frac{1}{2}\rho A u_\infty^3} \tag{3.5}$$

The operating point of the disc is obtained by varying the value of K_L. However, in the IBF model the parameter,F_b, is varied to obtain the operating points for the MRL tidal turbine, where this force is applied in the axial and vertical direction giving a complex energy removal. Thus a direct use of these equations for post-processing the IBF model results is incorrect due to the absence of the resistance coefficient K_L in the model.

Therefore, the total thrust force can be properly evaluated by calculating the change in flux across the turbine region. A route to assess the total thrust force experienced by the device is therefore to employ a Conservation of Linear Momentum (COLM) through a control volume. The turbine is enclosed in a rectangular control volume shown in Fig. 3.1 and the momentum flux on each face of the control volume was calculated. Recent

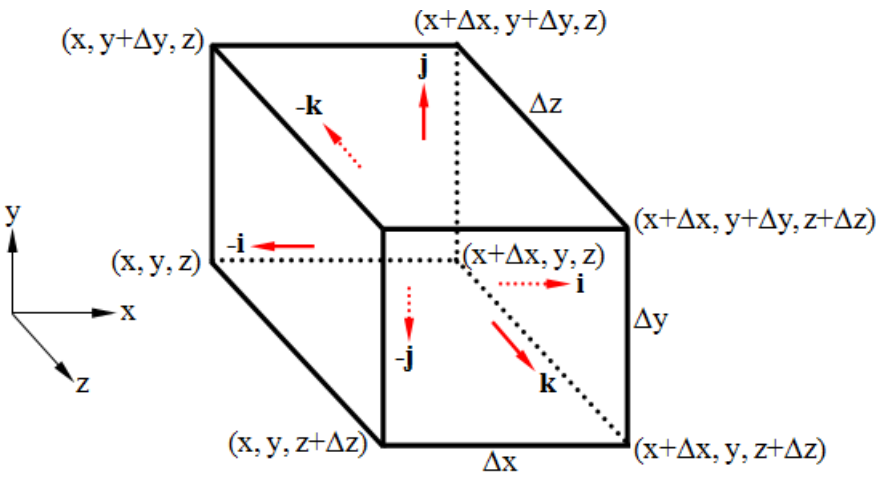

Figure 3.1: 3-D representation of the control volume

studies showed that turbines in a constrained flow have better performance compared to those in unconstrained flow due to an additional power contribution by the static pressure gradient in the streamwise direction as documented in [Houlsby et al., 2008, Garrett and Cummins, 2007, Whelan et al., 2009, Myers and Bahaj, 2007]. Thus the power available to the device is a contribution by the static pressure and dynamic heads. A new definition of thrust , C_T^*, and power ,C_P^*, coefficients was then introduced. Applying conservation of linear momentum through the rectangular control volume, the thrust force acting on the

device can be defined as:

$$\begin{aligned} T^* = & \int_{A_{yz}} [(p)|_x - (p)|_{x+\triangle x}]\, dA \\ & + \int_{A_{yz}} [(\rho u_x u_x)|_x - (\rho u_x u_x)|_{x+\triangle x}]\, dA \\ & + \int_{A_{xz}} [(\rho u_y u_x)|_y - (\rho u_y u_x)|_{y+\triangle y}]\, dA \\ & + \int_{A_{xy}} [(\rho u_z u_x)|_z - (\rho u_z u_x)|_{z+\triangle z}]\, dA \end{aligned} \tag{3.6}$$

The velocity of the mass at -**i** boundary face located at point x is given by $u_x|_x$. The mass flux entering into the face of -**i** boundary is only due to the velocity component normal to the face (i.e., u_x) which is given by $(\rho u_x)|_x$. This results a linear momentum flux of $(\rho u_x u_x)|_x$ at the -**i** boundary. The linear momentum flux for the rest of the boundary faces is defined in a similar manner.

The integration was performed over the combined cross-sectional area of the turbine and side plates on all boundary faces to calculate the thrust force on the whole device while the cross-sectional area of the turbine only was considered to calculate the thrust on the turbine. This analysis makes it possible to obtain the thrust force experienced by the side plates in addition to the thrust forces on the turbine. The power removed by the turbine from the flow is defined using the thrust force as:

$$P^* = T^* \overline{u_t} \tag{3.7}$$

In the actuator disc method, the average velocity, $\overline{u_t}$, is commonly calculated by averaging the velocity over the area of the disc. However, in this study the velocity is averaged over the volume occupied by the turbine as:

$$\overline{u_t} = \frac{1}{V} \int_V u_x dV \tag{3.8}$$

where V is the total volume of the turbine region. This average velocity value is a good representative of the fluid flow within the turbine housing. The total thrust force calculated

using the control volume is a combination of the static and dynamic heads as discussed before. Thus, the thrust and power coefficients must be calculated relative to these two components. The thrust coefficient is therefore defined as:

$$C_T^* = \frac{T^*}{A\left(\frac{1}{2}\rho u_\infty^2 + \triangle p\right)} \tag{3.9}$$

Similarly, the power coefficient can be defined as:

$$C_P^* = \frac{P^*}{Au_\infty\left(\frac{1}{2}\rho u_\infty^2 + \triangle p\right)} \tag{3.10}$$

Note that the flow velocity at the inlet boundary, u_∞, varies along the depth of the computational domain in cases were the simulation was performed using the power law inlet velocity. In such cases, the inlet velocity was averaged over the required cross-sectional area. The power available due to the static pressure head can be obtained from the difference in pressure, $\triangle p$, at the inflow and outflow of a streamtube containing the fluid passed through the turbine region as shown in Fig. 3.2. Thus the head difference was

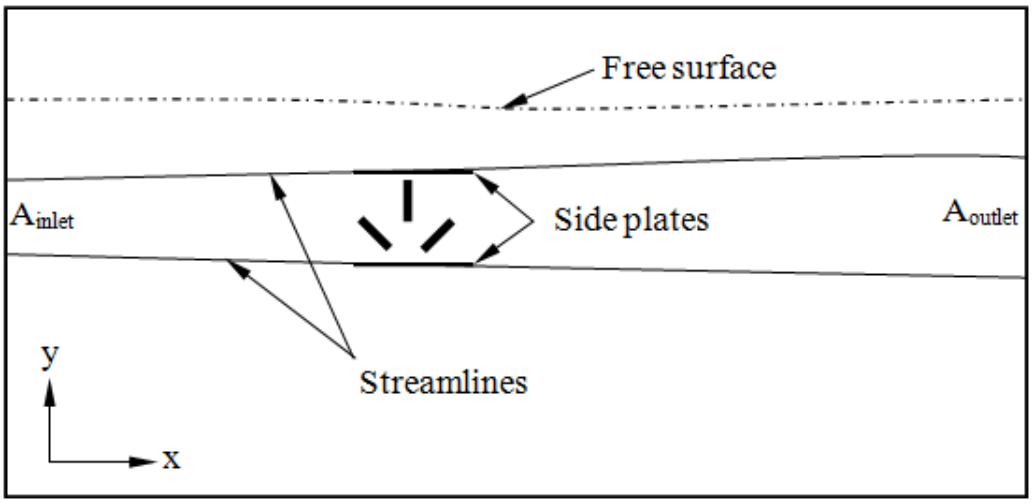

Figure 3.2: Vertical plane schematic representation of a streamtube

calculated as:

$$\triangle p = \frac{1}{A_{inlet}}\int_{A_{inlet}}(p)|_{inflow}dA - \frac{1}{A_{outlet}}\int_{A_{outlet}}(p)|_{outflow}dA \tag{3.11}$$

where $(p)|_{inflow}$ is the static pressure at the inlet boundary and $(p)|_{outflow}$ is the static

pressure at the outlet boundary. The axial induction factor can be defined as:

$$a = (1 - (\overline{u_t}/u_\infty)) \tag{3.12}$$

The blockage ratio of the channel is given as:

$$B = \frac{\sum_{n=0}^{n} nA}{A_{channel}} \tag{3.13}$$

where n is the number of devices configured in a row (spanwise direction). Note that the blockage ratio is calculated using the cross-sectional area of the turbine only , A , throughout the thesis.

3.2.2 Energy Flux

The principle of Bernoulli's theorem states that in steady, frictionless, incompressible flow, the energy is constant along a streamline which is defined as:

$$p + \rho g y + \frac{1}{2}\rho \overrightarrow{u}^2 = constant \tag{3.14}$$

where: $\overrightarrow{u}^2 = u_x^2 + u_y^2 + u_z^2$. In open channel flows, the velocity near the boundaries is smaller than in the rest of the region resulting a different energy across the section of the channel [Fenton, 2005]. In this case, the application of Bernoulli's theorem across streamlines fails to provide full picture of the energy across the channel section. The appropriate way is therefore to use the integral form of the energy equation. The integration of energy over a cross-section of a channel considers only the velocity along the stream direction and neglects any transverse velocities [Fenton, 2005]. Thus the energy flux, $E(x)$, across the channel cross-section is calculated by integrating the product of the total pressure, p_0, and the stream velocity, u_x, as:

$$E(x) = \int_{A_{yz}} p_0 u_x dA \tag{3.15}$$

This equation has been successfully applied to calculate the energy flux in several applications such as the study of tidal energy extraction. Some examples of numerical and experimental studies using this approach are given in [Shives and Crawford, 2010, Belloni and Willden, 2011, Fleming et al., 2011]. In applications where the elevation is constant the potential head is excluded from the calculations. However, in open channels where energy is removed from the flow, the dynamics of the free surface or elevation varies along the channel resulting a different potential head which must be included in the energy flux calculation. In this study, the free surface varies along the channel and the total pressure is defined by the sum of static, potential and dynamic pressures of the flow as:

$$p_0 = p + \rho g y + \frac{1}{2}\rho \overrightarrow{u}^2 \tag{3.16}$$

Note that the calculation of the potential head is performed using the height of water above, meaning the potential head is zero at the free surface and maximum at the channel floor. Investigating the energy flux within the computational domain provides full picture of the energy lost from the stream flow in the presence of devices such as tidal turbines. The power removed from the flow includes, the useful power removed by the turbine, viscous and shear losses, and the losses that are further introduced due to the remixing of the wake. In addition, there is friction loss in a channel flow which is commonly termed as head loss as explained by Jain [2000]. Houlsby et al. [2008] developed a parametrised equation to estimate the energy loss in the mixing zone by extending the knowledge of Linear Momentum Actuator Disc Theory (LMADT), which is further evidence of the inevitable energy loss during the remixing process.

3.3 Computational Set-Up

The computational domain and boundary conditions discussed in chapter 2 sections 2.9.1.1 and 2.9.1.2 have been used for the simulations. Based on the dimensions of the device and the computational domain, the blockage ratio is , B = 0.016. Most of the single turbine simulations are based on this blockage ratio. Note that the blockage ratio is calculated

based on the water level excluding the air body in the computational domain.

The main parameters used as an input to the CFD model are the IBF parameter or resistance and the velocity. The resistance forces can be calculated using the known radius,$R = 0.0525$ m, and the experimentally measured torques because of the reasons discussed in detail in Chapter 2 section 2.6.3.2. The calculated body forces and the velocity are given in table 3.1. Six trials were performed to obtain the operating points of the MRL turbine.

Tests	Torque (Nm)	Resistance Forces (N)
test 1	0.700	13.33
test 2	0.610	11.62
test 3	0.565	10.76
test 4	0.490	9.33
test 5	0.40	7.62
test 6	0.275	5.24
test 7	0.138	2.62

Table 3.1: Experimentally measured torques and the corresponding calculated resistance forces

3.4 CFD Results and Discussions

3.4.1 Preliminary Analysis

Experimental and CFD studies have proved that the streamlines downstream of an energy extraction zone expands to fulfil the mass conservation [Whelan et al., 2009, Myers and Bahaj, 2007, Houlsby et al., 2008]. This phenomenon has also been observed in this study immediately downstream of the turbine as shown in Fig. 3.3. However, as the downstream distance increases, the cross-section of the streamtube created by the streamlines reduces again. The flow is complex making it difficult to trace the streamlines for calculating the exact area of the streamtube at the outlet as shown in Fig. 3.3. Thus the cross-sectional area of the streamtube at the inflow and outflow of the computational domain was taken

constant and equal to the cross-sectional area of the device, $A = A_{inlet} = A_{outlet}$ in order to calculate the power available due to the static pressure difference at the inlet and outlet of the computational domain using Eqn. (3.11).

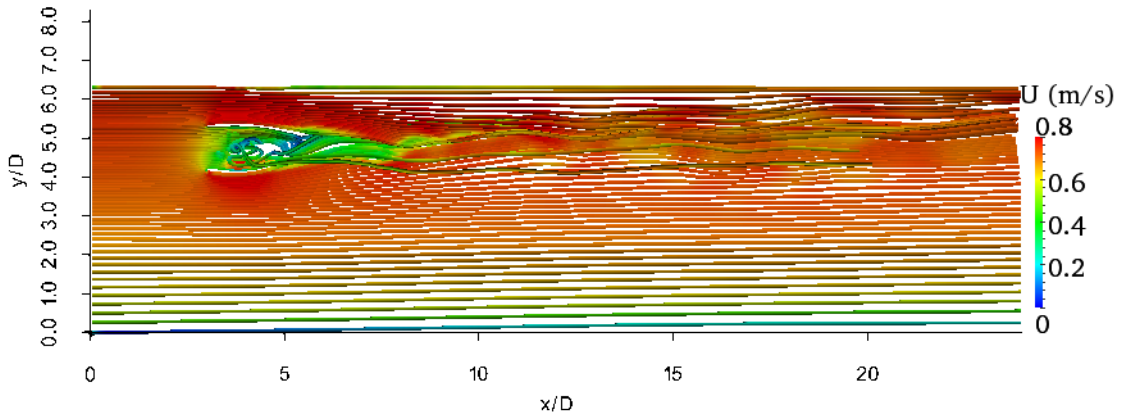

Figure 3.3: Illustration of streamlines

3.4.1.1 Mesh resolution and convergence

To evaluate convergence and mesh dependency of the solutions, a structured hex-mesh was developed with three mesh densities of 736448, 156848, and 44744 elements. The power coefficient was monitored to evaluate convergence of the solutions. Assuming that the highest mesh resolution provides the most accurate indicator of the performance of the turbine, the power was observed to vary between 1.9% and 5% among these mesh resolutions. Thus the medium mesh, 156848 elements, which has an error of 1.9% was selected for the rest of the simulations with a minimum mesh size of 0.05D (1cm) around the zone of interest and a maximum size of 0.25D (5cm) far field. The computational time taken for these simulations was also taken into consideration to select the appropriate mesh. A further flow field analysis is conducted with these three mesh densities in Chapter 4 section 4.3.2.1.

3.4.1.2 Dynamics of free surface

In open channel flow, Froude number is commonly used to classify the flow as tranquil (sub-critical), critical, and rapid (super-critical) as shown in Fig. 3.4. The Froude number , F_r , represents the ratio of inertia to gravitational forces as [Finnemore et al., Cengel and

Cimbala, 2010]:

$$F_r = \frac{u_\infty}{\sqrt{gh}} \tag{3.17}$$

If the Froude number is less than 1, the flow is tranquil and a value higher than 1 indicates rapid flow. At $F_r = 1$ when $h = h_c$, the flow becomes critical. With depth averaged upstream velocity, $u_\infty = 0.627$ m/s, and the water level at, $h = 1.2625$ m, the upstream Froude number is $F_r = 0.178$. Based on the given velocity, the critical depth is, $h_c = 0.04$ m but the position of the turbine is above this depth which indicates that the MRL turbine is operating in the tranquil region. In cases where there is energy removal from the flow such as using tidal turbines, the head downstream of the turbine drops in the tranquil flow region from h_1 to h_2 ($\Delta h = h_1 - h_2$) as shown in Fig. 3.4. This has been proved both theoretically and experimentally as documented in [Whelan et al., 2009, Myers and Bahaj, 2007, Houlsby et al., 2008].

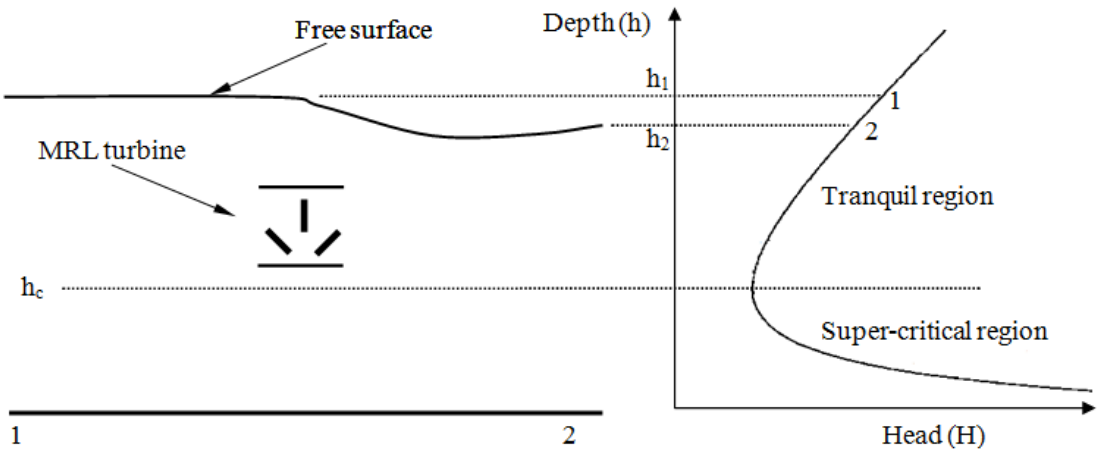

Figure 3.4: Illustration of open channel flow containing energy extraction zone

Fig. 3.5 presents the head difference at the inlet and outlet of the computational domain. An erroneous energy wave can be observed close to the inlet boundary as shown in Fig. 3.5b, which is probably due to incorrect outlet boundary condition. This led to a fixed water level at the outlet, which is counter intuitive to the principle of energy removal from a stream flow. Thus, the error appears to be as a result of an automatic correction of the flow by increasing the head of water upstream of the turbine to counter and correct the fixed water level at the outlet as shown in Figs. 3.5a and 3.6. As a result, the water level at the inlet is increased by almost 0.0017 m from the initial condition and remains constant at

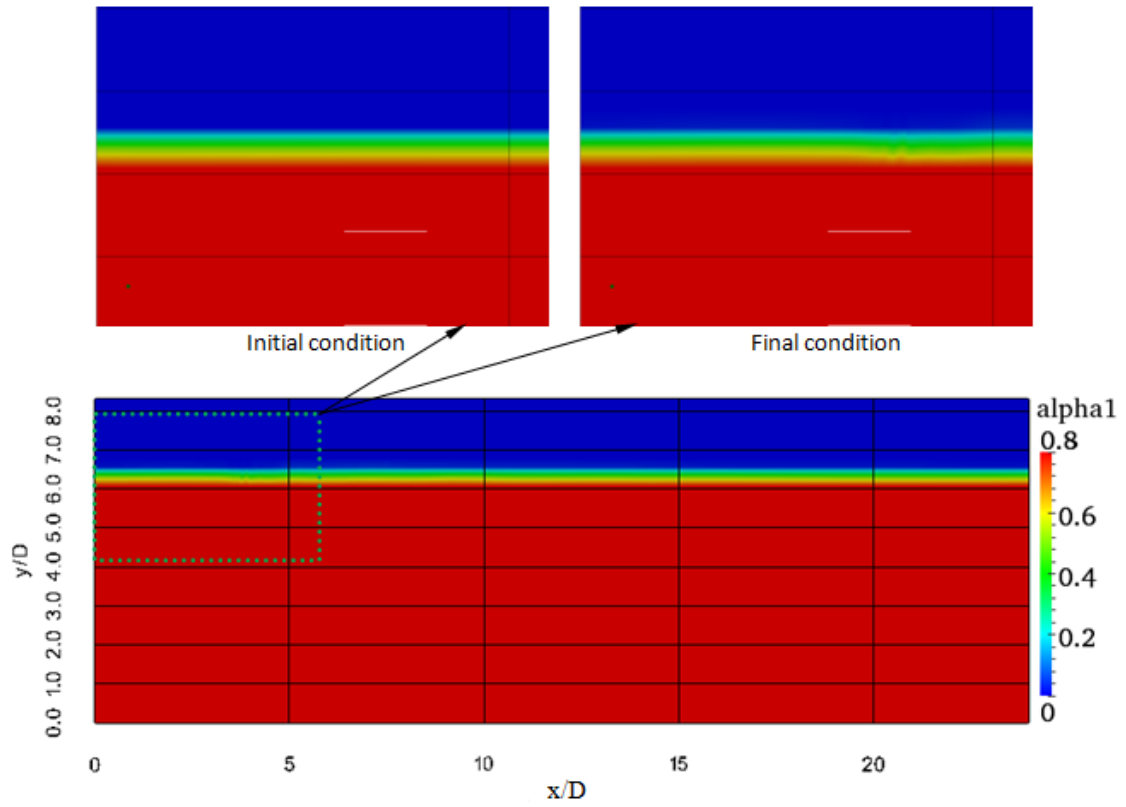

(a) Phase fraction

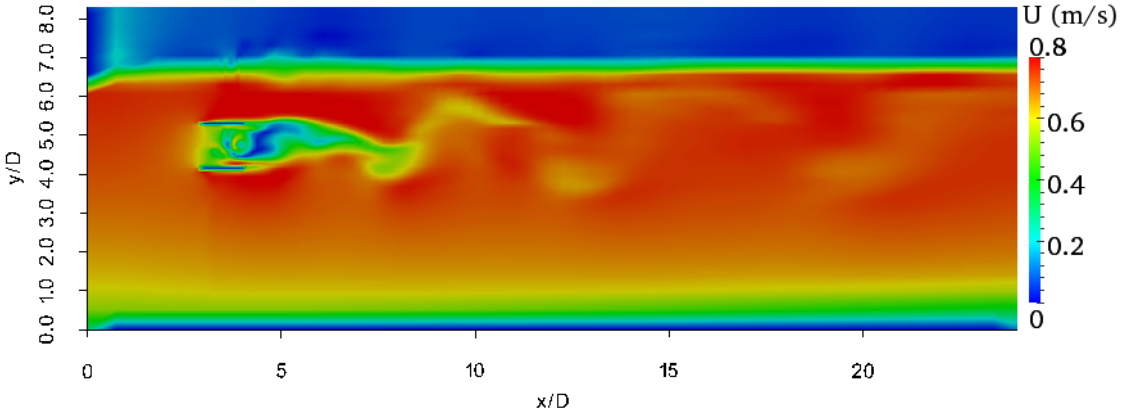

(b) Velocity contour

Figure 3.5: Dynamics of the free surface for the maximum resistance force

the outlet.

The effect of this error on the investigation of the turbine characteristics may be minimal but it is worth of calculating the expected change of the water level by using one-dimensional (1-D) theoretical analysis. A recent development of the extension of LMADT [Betz, 1920] analysis to tidal turbines is presented by Garrett and Cummins [2007], Whelan et al. [2009], Myers and Bahaj [2007], Houlsby et al. [2008] to understand the blockage effect on the limit of power extraction and the free surface deformation. Houlsby et al.

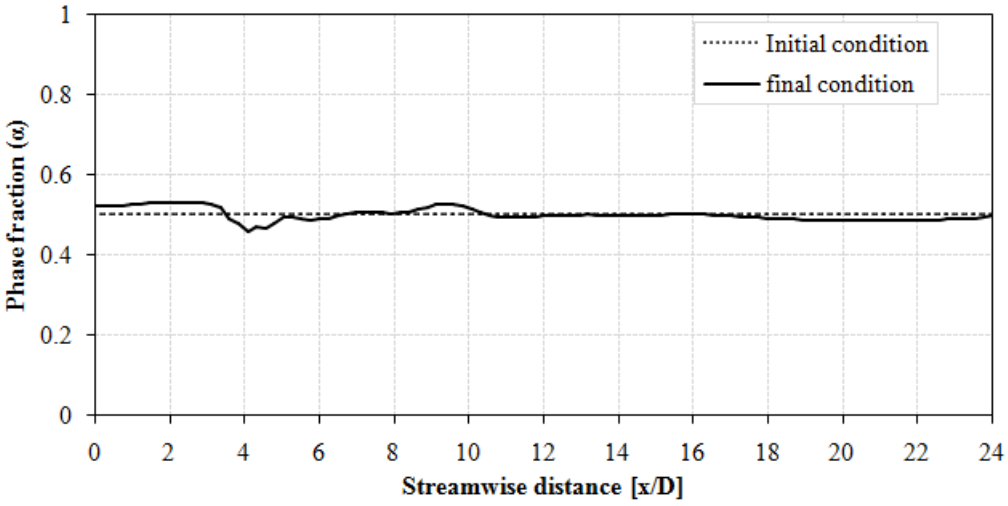

Figure 3.6: Phase fraction illustration for the deformation of free surface

[2008] has particularly expanded the analysis to take into consideration the inevitable downstream mixing effect and successfully developed parametrised analytic equations to estimate the energy loss in the mixing zone and the downstream head drop. These equations have been directly employed and the downstream head drop can be calculated by solving (Refer to Houlsby et al. [2008] for detailed derivations):

$$\frac{1}{2}\left(\frac{\Delta h}{h}\right)^3 - \frac{3}{2}\left(\frac{\Delta h}{h}\right)^2 + \left(1 - F_r^2 + \frac{C_T B F_r^2}{2}\right)\frac{\Delta h}{h} - \frac{C_T B F_r^2}{2} = 0 \qquad (3.18)$$

Fig. 3.7 shows the change of water level at the outlet against the thrust coefficient. The result clearly shows the impact of different resistance forces on the downstream head drop. As the resistance force against the flow increases, the downstream head drop increases because of the high energy removal from the flow, although this does not mean that an increased useful power removal from the stream flow. At the maximum thrust coefficient, the downstream head drops by about, $\Delta h = 0.00114$ m which is less than the increased water level at the inlet but not very significant considering the difference of the methodologies used for the calculations. This is a clear indication that the water level was increased at the inlet in order to balance the would have been expected head drop if a correct boundary condition had been used at the outlet. Thus the impact of the incorrect boundary condition on the general investigation of several issues of the MRL turbine appears to be minimal because of the increased water level at the inlet which added

additional energy to the system.

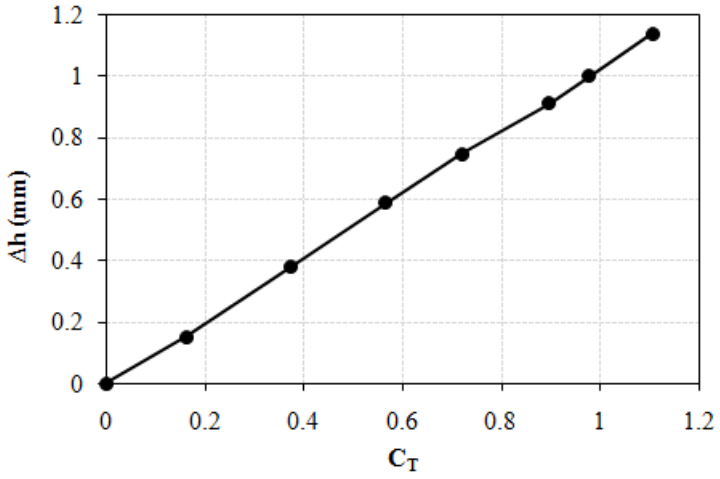

Figure 3.7: Phase fraction illustration for the deformation of free surface

3.4.2 Performance of the MRL Turbine

Fig. 3.8 shows the velocity contours on a vertical plane across the centre of the turbine at $F_b = 13.33$ N and $F_b = 7.62$ N. The flow characteristics at the wake region is quite different as expected due to the difference of the resistances. The large resistance caused a large velocity deficit on the wake of the turbine and starts to recover back further downstream, though the domain length scale used was not enough for full recovery. There are two distinct observations from these flow fields:

- At low resistances (Fig. 3.8a), there is no vortex generation downstream of the turbine and the wake recovery is slow.

- At high resistance (Fig. 3.8b), there is a huge velocity deficit immediately downstream of the turbine and faster wake recovery with sustained large scale vortices. Fast wake recovery was also observed due to high resistance coefficients by several researchers in the aforementioned references which may be advantageous to minimise the influence of wake interaction with any downstream devices in tidal stream farms. However, there is always a limit to how much resistance the turbine should apply against the flow due to its range of operating points and the need to operate around its maximum power point.

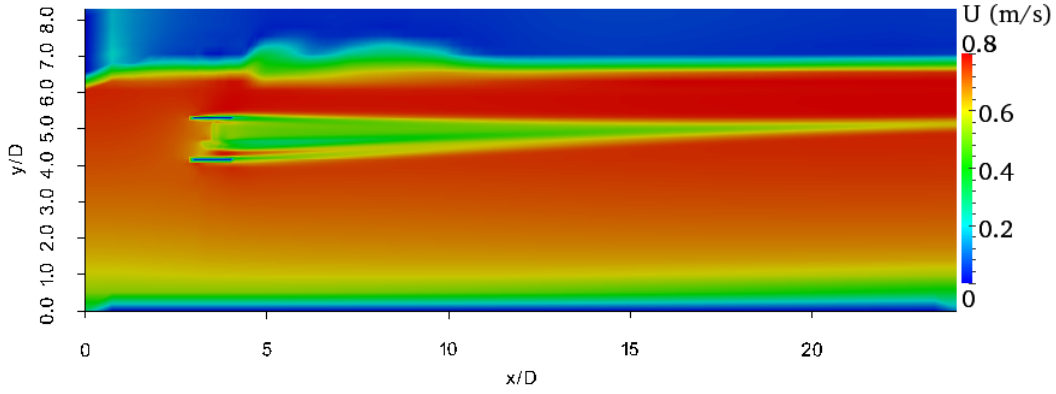

(a) $F_b = 7.62$

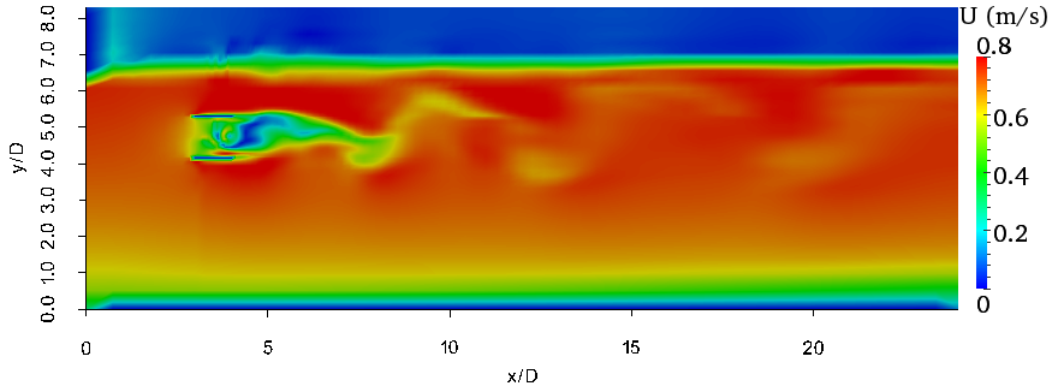

(b) $F_b = 13.33$

Figure 3.8: Velocity contours on the vertical plane across the centre of the turbine

3.4.2.1 Thrust Analysis

Fig. 3.9 shows plots of the thrust coefficients of the turbine, side plates and the whole device (turbine and side plates). $C_{T,turbine}$ represents the thrust coefficient based on the thrust on the turbine, $C_{T,plate}$ represents the thrust coefficient based on the thrust on the side plates, and $C_{T,total}$ represents the sum of thrust coefficients based on the thrust force on the whole device. From Fig. 3.9 it is clear that the thrust coefficient of the turbine is much larger than the thrust coefficient of the side plates especially at high induction factors. At $F_b = 0$, the thrust coefficient is contributed only by the side plates so as the induction factor reduces (at small resistance forces), the difference between the thrust coefficients of the turbine and side plates was reduced as expected. The thrust on the side plates slightly increases as the resistance by the turbine increases, in contrast the thrust on the turbine showed very large increase. Thus, the thrust coefficient, $C_{T,turbine} = C_T$, of the turbine and its associated power coefficient, $C_{P,turbine} = C_P$, have been used

to analyse the performance of the turbine in the subsequent sections and Chapters. This will effectively exclude the thrust/resistance force applied by the side plates against the flow. Note that the induction factor calculated using the flow through the turbine region is used to compare the results. As the resistance (thrust) force by the turbine decreases,

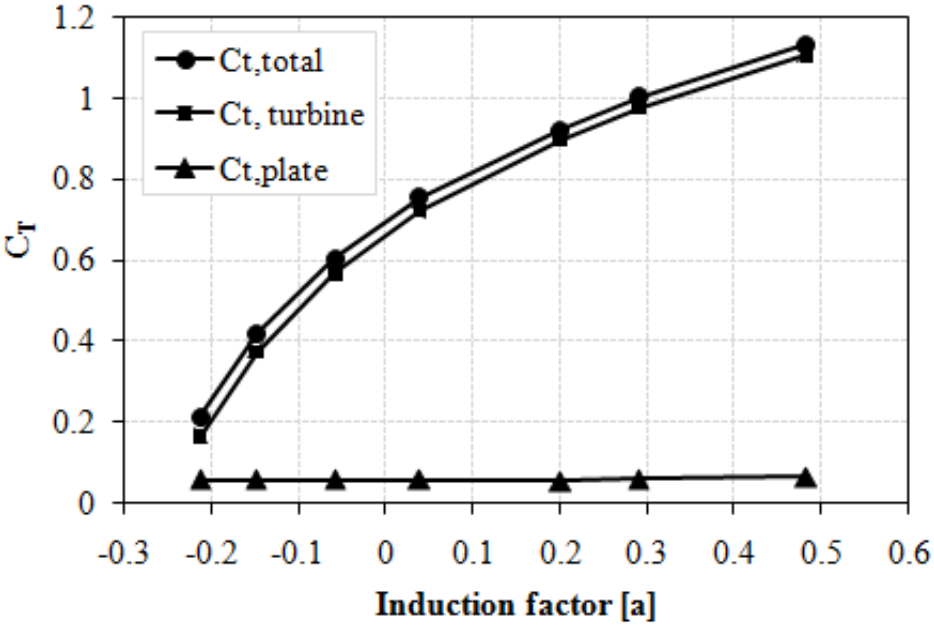

Figure 3.9: Thrust Coefficients for the turbine and side plates

the velocity through the turbine region increases and becomes greater than the upstream velocity due to the venturi flow created by the side plates resulting a negative induction factor as shown in Fig. 3.9.

3.4.2.2 Power Analysis

A full range of operating points of the MRL turbine were obtained by varying the resistance forces applied by the turbine. Fig. 3.10 shows a plot of the power coefficient of the turbine against the induction factor. The peak power coefficient of the turbine is $C_{P,turbine} = C_P = 0.717$ at $C_{T,turbine} = C_T = 0.898$. Before and after the peak power coefficient, the values keep decreasing establishing a full range of operating points of the device.

One interesting observation from the power coefficient is that the maximum power point occurs within the resistances that have been calculated using the fluid generated torque measured during the experiment as discussed in section 3.3. However, the maximum

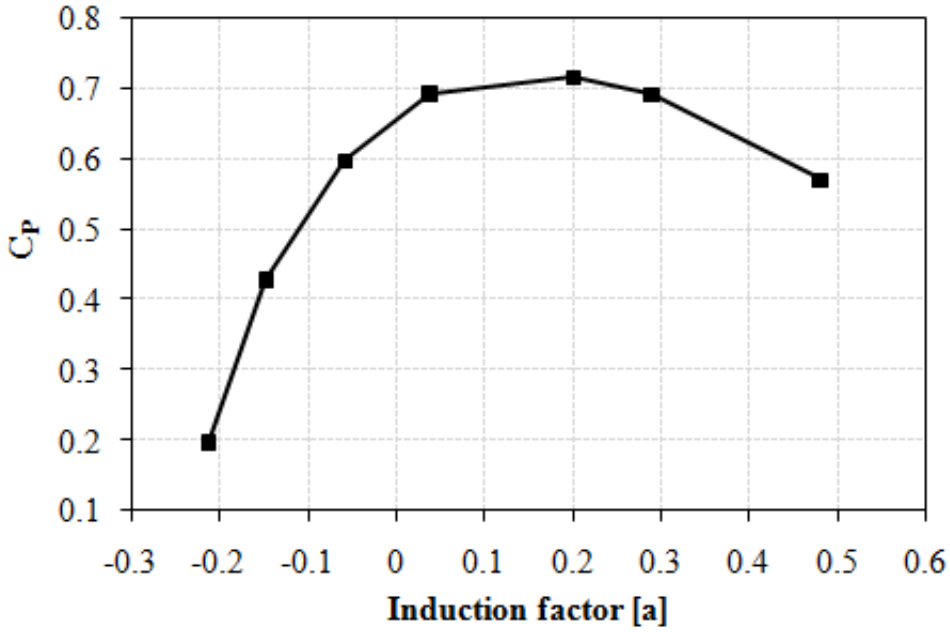

Figure 3.10: Power coefficient of the MRL turbine

power point may not be necessarily at the same torque and its associated resistance force both for the experiment and the CFD model. This is a significant indication that the IBF parameter (resistance) can be calculated using the second approach discussed in Chapter 2 section 2.6.3.2 in order to establish the MRL turbine's full range of operating points. This also allows a comparison of the power coefficients from both the IBF model and the experiments at the same torque in order to understand the useful power extracted by the turbine from the flow and the associated losses within the turbine region, which is discussed in detail in section 3.5.1. In addition, the use of experimental data to calculate the IBF parameter minimises the time and cost of doing trial and error to obtain the appropriate values.

The performance of the turbine through its power coefficient does not provide a full picture of the total power removed from the flow field. There is additional loss of power from the flow during the remixing of the wake behind the device and the bypass flows. This additional loss of energy can be fully analysed by calculating the energy flux ($E(x)$) at different cross-section of the domain. The energy flux is calculated using the total pressure as discussed in section 3.2.2.

Fig. 3.11 shows relative energy flux along the computational domain as a function of

the streamwise distance for the turbine thrust coefficient, $C_T = 0.977$. The energy flux slowly decreases upstream of the turbine (0.5 to 3D) probably due to a combination of the normal head loss due to friction in a channel flow and due to the static forces of the IBF model which can affect still some distance upstream of their position. There is a large drop between 3D and 4D (through the device), which is associated with the useful power removed from the flow by the device and other losses within the turbine region. The drop of energy flux still continues further downstream of the turbine which is associated with the energy loss in the remixing zone in addition to the friction losses occurred in a channel flow.

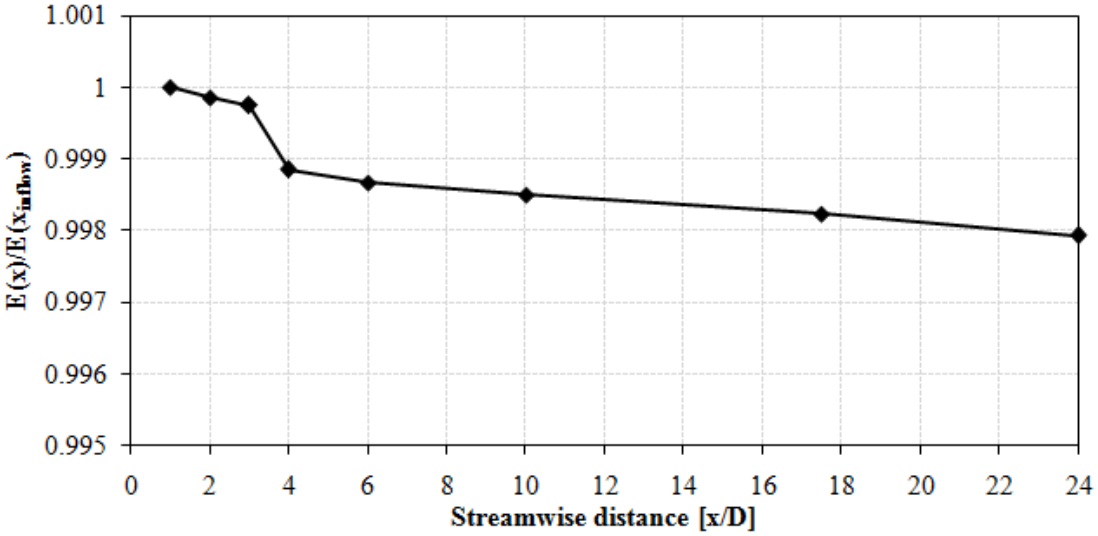

Figure 3.11: Streamwise variation of relative energy flux at $F_b = 11.62N$, $C_T = 0.977$

3.4.3 Blade Positions

So far the CFD simulations have been carried out with the blades at specified positions. Therefore, it is crucial to investigate the effect of different blade positions on the calculation of the power removal from the flow. The turbine is constructed with a three bladed system as discussed before and Fig. 3.12 shows the second blade arrangement in addition to the blade arrangement shown in Fig. 2.2 that has been used in the previous simulations. In principle, the blades can have infinite number of positions and therefore simulations with rotating blades may seem to be the best option. However, due to the reasons discussed in chapter 2, the blades are modelled in a stationary conditions, but it is important to test a

limited number of blade positions to investigate its effect on the results.

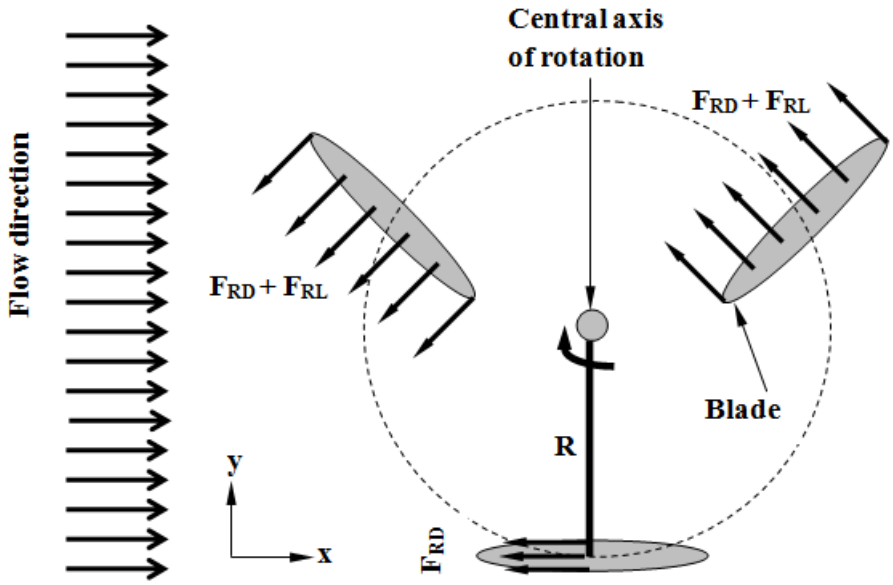

Figure 3.12: Illustration of position 2 blade arrangement

The same computational set-up was used for the two blade positions with a resistance, $F_b = 11.62N$. Fig. 3.13 shows snapshots of velocity contours both in a vertical and horizontal plane across the centre of the turbine. The results showed some differences in the internal shear flows created within the turbine region resulting a different wake structures downstream of the turbine. In addition, the free surface appears to be affected in different ways as can be seen in Figs. 3.13a and 3.13c.

The thrust coefficient, $C_T = 0.977$, of the turbine with blade position 1 is slightly lower than the thrust coefficient, $C_T = 0.985$, of the turbine in position 2. However, the power coefficient, $C_P = 0.693$, of the turbine with position 1 is greater than the power coefficient, $C_P = 0.658$, in position 2. This was mainly due to a lower average velocity at the turbine region in position 2. One of the factors which may affect the average velocity at the two blade positions is due to the position of blades where they encounter different vertical velocity profiles. Thus considering the challenges of modelling detailed blade motions and the fact that the error between the performances is not significant, modelling the MRL turbine with fixed blade configuration appears to be appropriate. Thus the CFD simulations in the subsequent sections and chapters were therefore considered position 1 blade configuration.

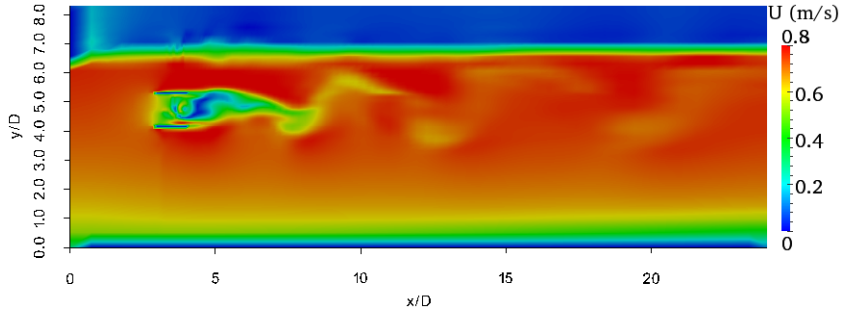

(a) Vertical plane position 1

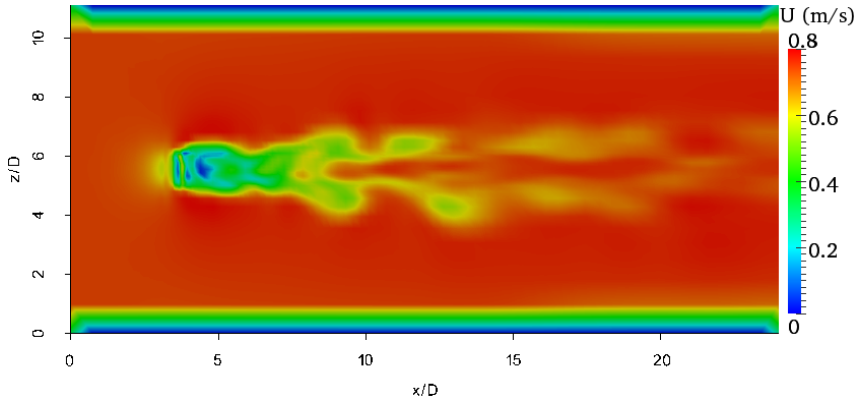

(b) Horizontal plane position 1

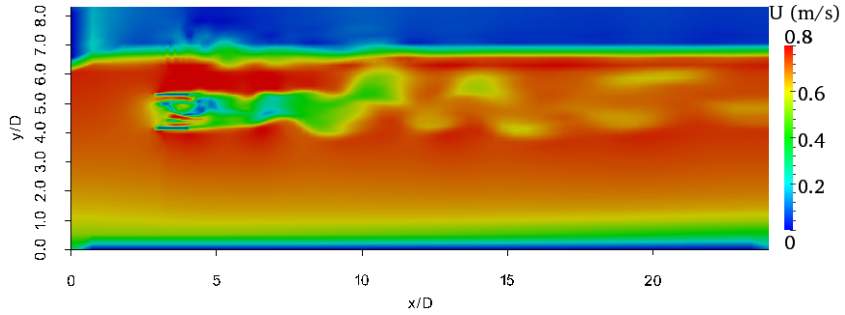

(c) Vertical plane position 2

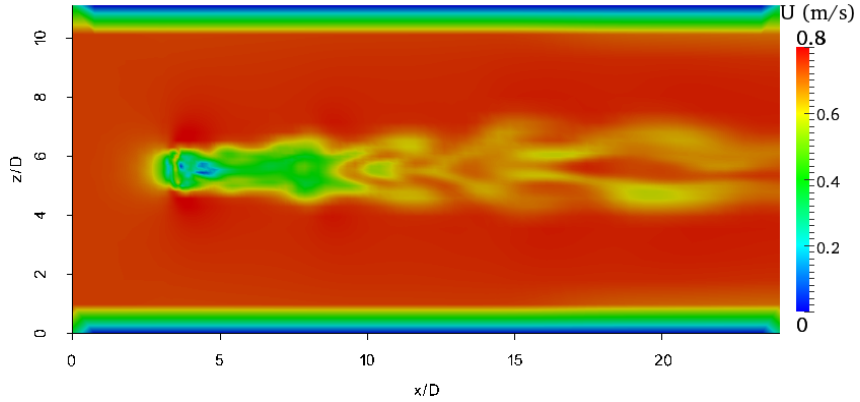

(d) Horizontal plane position 2

Figure 3.13: Velocity contours for two blade positions

3.4.4 Side Plates

It has been shown experimentally that the turbine's performance could be increased by adding a side plate on the top and bottom. In practical conditions, the bottom plate serves as a ground effect, which increases the lift force on the blades. The upper plate guides the water jet impacted on the blade to make a U-turn and decelerates the flow speed to create high pressure to be exerted on the blade. This process is similar to the working principle of the Pelton turbine. Preliminary experimental results showed that the presence of the side plates increases the performance of the turbine by up to 25% [Janssen and Belmont, 2009]. A CFD simulation was carried out with a resistance, $F_b = 11.62N$ to investigate the effect of these plates.

Fig. 3.14 shows snapshots of the velocity contours simulated with and without side plates. The results from the turbine with side plates produced physically large wake (Fig. 3.14a) compared with the same turbine but without side plate as shown in Fig. 3.14c. This difference obviously shows the amount of energy dissipated from the stream flow by both designs. This is an indication that the additional thrust/resistance force by the side plates against the flow contributes to the large velocity deficit behind the device. The design without side plates appears to affect the free surface as shown in Fig. 3.14c mainly due to the vertical velocity flow created by the thrust of the turbine which was forced to flow in the stream direction by the side plates as shown in Fig. 3.14a.

The power coefficient, $C_p = 0.693$, of the turbine with side plates is higher by 3.4% compared to the same turbine without side plates. This is qualitatively consistent with the experimental results although the increment is small in the CFD model. Note that the thrust and power coefficients are calculated considering the thrust force on the turbine only excluding the thrust force on the side plates in order to properly compare the two turbine performances. The improved performance of the turbine is solely due to the venturi flow created by the side plates which increases the flow through the turbine resulting a higher average velocity in the streamwise direction.

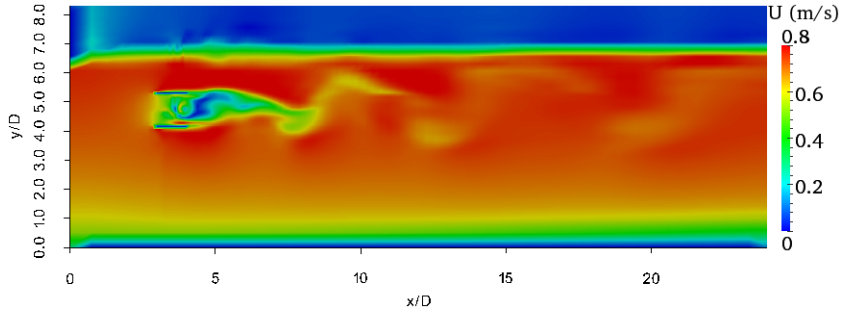

(a) Vertical plane with plate

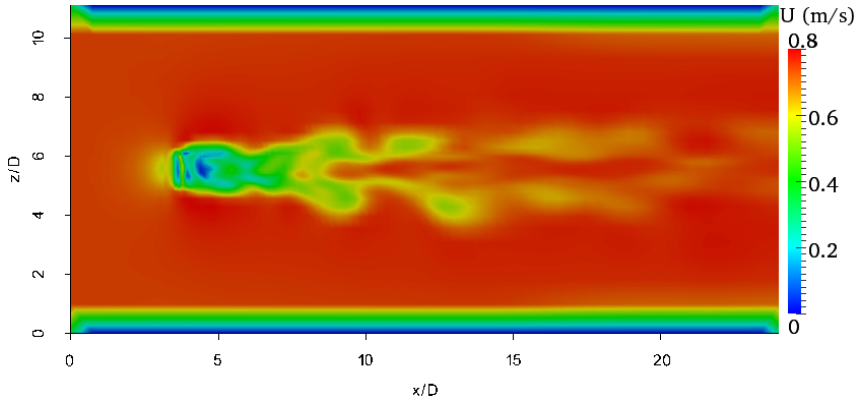

(b) Horizontal plane With plate

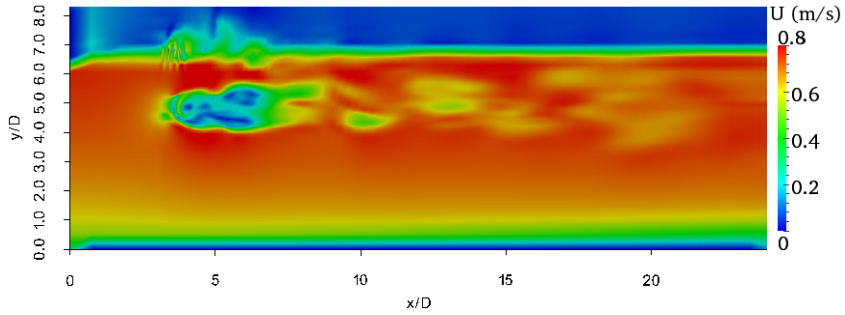

(c) Vertical plane without plate

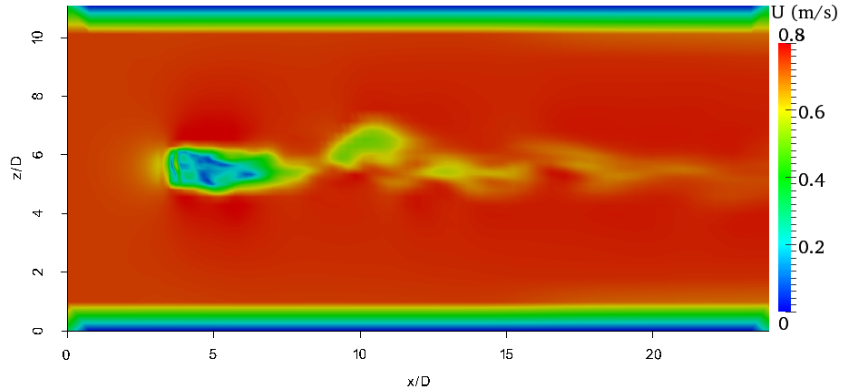

(d) Horizontal plane without plate

Figure 3.14: Velocity contours of the MRL turbine with and without side plates at the maximum applied body force

3.4.5 Comparison of the *Annular* and *Blade* approaches of the IBF model

The simulations reported up to this point were performed using the *blade* approach. However, another IBF approach with few modification to the *blade* approach, was developed for the reasons given in Chapter 2. In this section, comparison of the performance of the MRL turbine simulated using the two approaches is presented using identical computational set-up with the same body force per unit volume. Fig. 3.15 shows snapshots of the velocity contours both in vertical and horizontal planes.

Fig. 3.16 shows a comparison of the power coefficients of the turbine simulated by the two approaches. The result clearly shows some difference on the individual power coefficients and more importantly, the induction factors of the two approaches is different. This was mainly due to the difference in thrust coefficient between the two approaches. The maximum power coefficient of the *annular* approach is, $C_P = 0.665$, at a thrust force of $C_T = 0.833$ compared to the power coefficient, $C_P = 0.717$, of the *blade* approach at a resistance coefficient of, $C_T = 0.898$. Note that the maximum power coefficient of the *annular* and *blade* approaches did not occur at the same resistance force per unit volume.

The above was mainly concerned on energy extraction however it is also important to understand the overall effects of power extraction such as the downstream wake structures, and the free surface dynamics which are discussed in Chapter 4 section 4.3.1. In addition, the body forces imposed on the annular section tend to affect the flow in a manner similar to those that the real turbines do although there are no detailed experimental data at this stage to compare with, a factor which is important to be considered in future works.

3.4.6 Blockage effect

The blockage effect on the performance of the MRL tidal turbine was investigated by using three blockage ratios, $B = 0.008$, $B = 0.016$, and $B = 0.029$. Fig. 3.17 shows comparison of the performance of a single turbine simulated using these three blockage ratios. The result clearly shows that the higher the blockage ratio, the higher the performance of

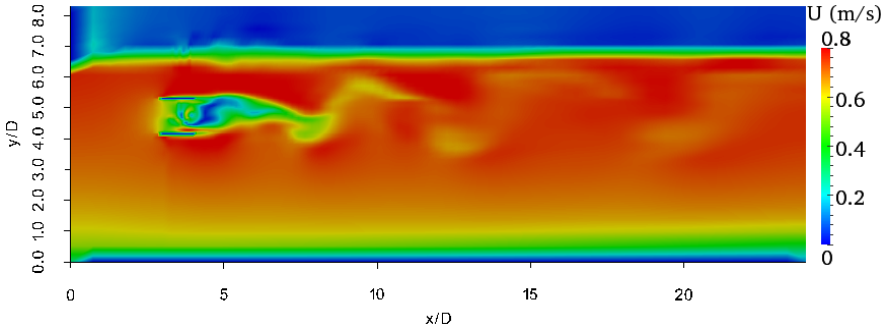

(a) *Blade* Method vertical plane

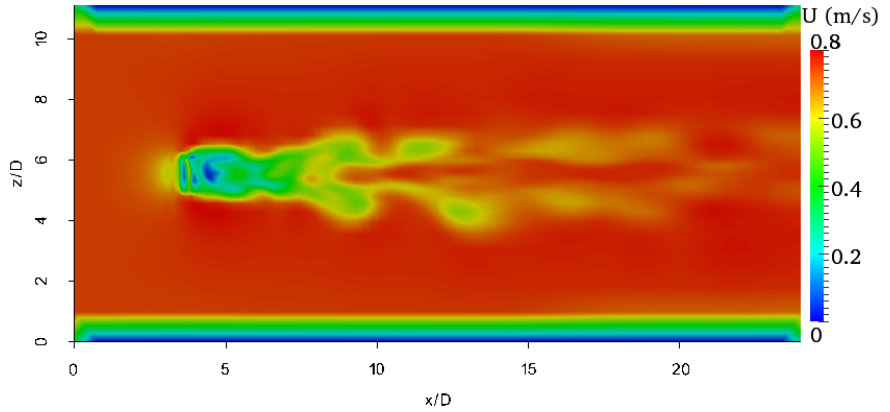

(b) *Blade* method horizontal plane

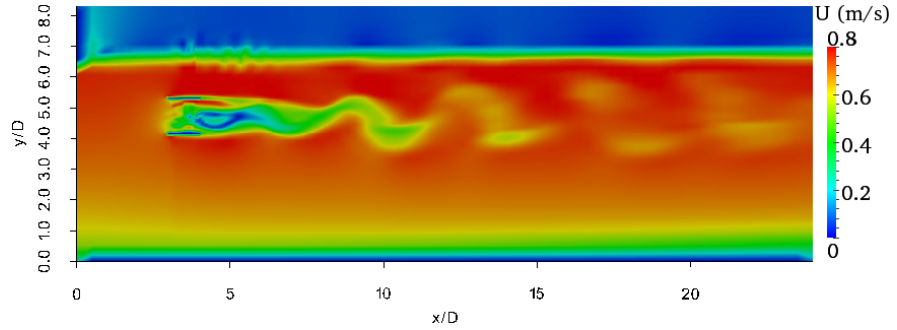

(c) *Annular* Method vertical plane

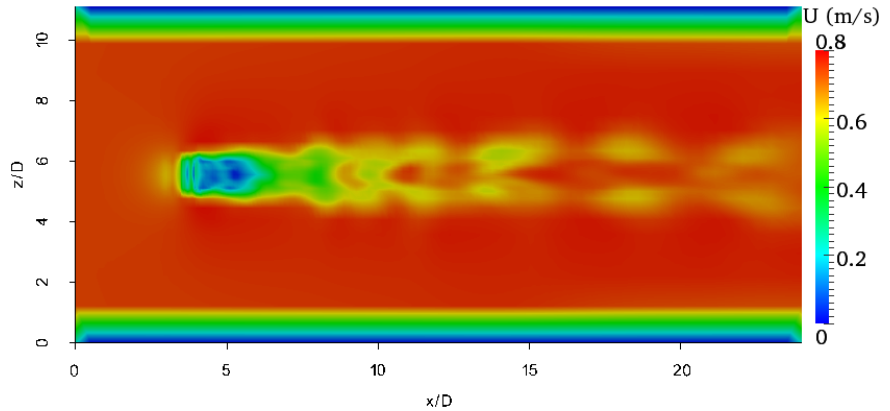

(d) *Annular* Method horizontal plane

Figure 3.15: Velocity contours on a vertical and horizontal plane simulated using both methods

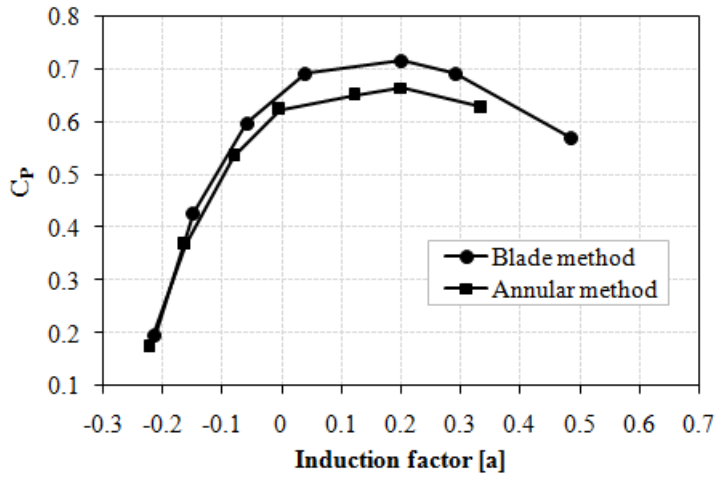

Figure 3.16: Comparisons of the performance of the MRL turbine simulated using the *annular* and *blade* approaches

the turbine. This results is consistent with other extensive studies carried out using both analytical and computational methods which shows that the performance of tidal turbines can be increased with high blockage ratio.

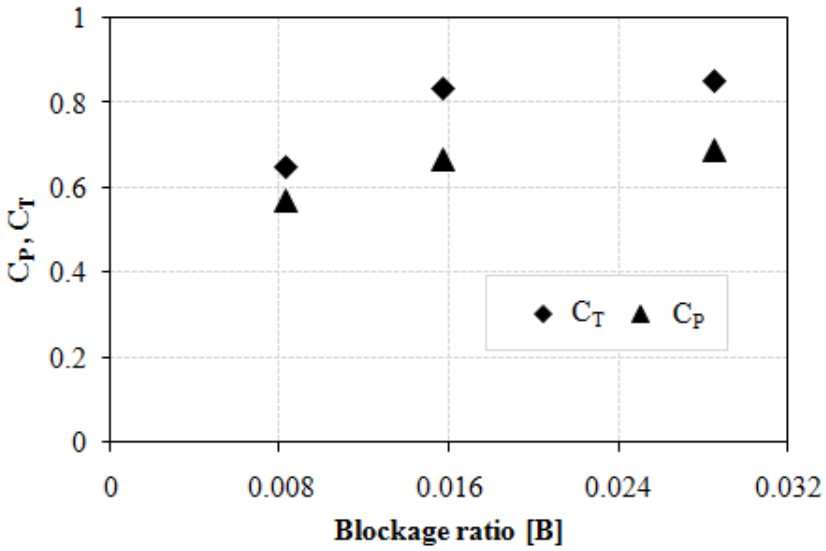

Figure 3.17: Blockage effect on the performance of tidal turbines

3.5 Validation of the IBF Model

3.5.1 Comparison with Experiments

3.5.1.1 Experimental set-up

An experimental study has been undertaken by Janssen and Belmont [2009] to determine the loading characteristics of the MRL turbine shown in Fig. 1.5. The primary aim of the work was to establish the turbine efficiency under a range of operating conditions and to obtain the optimum configurations. The data obtained from the experiments was used for validation of the IBF model. A water flow tunnel was used for the experimental study where the flow was provided using a water pump. The tests consisted of measurements of flow rates and the rate of turbine rotation under a range of mechanical torque conditions. The flow rate was varied using a controlled water pump and measured using a Rotameter.

The torque output of the turbine was calculated from the forces recorded using a belt and pulley dynamometer. The pulley was rigidly attached using grub-screws to the central axis of the turbine. A belt was then wrapped around half of the pulley, with one free end being connected directly to a force meter, and the other free end being connected to a force meter via a small spring, designed to ensure that the belt was held tight against the pulley over a wide range of tensions. As the turbine and hence the pulley rotated, the force was recorded, from which the torque was calculated using the known radius of the pulley. Several controlled torques were applied by differential forces on a bobbin of known radius and for a given flow rate in order to obtain the efficiency of the turbine at different torques.

The rate of turbine rotation was measured using a light-gate connected to a data recorder. A disc with 32 holes was connected to the turbine central axis, and as this disc rotated the light-gate recorded the number of holes that passed through its beam, displaying the results as a frequency with units (holes per minute). The uniformity of the flows was first measured across and along the tunnel. The velocity profile at different sections across the tunnel showed fairly uniform velocity except near the walls where the velocities were lower due to the boundary layer interaction with the walls.

The aim of the experiment was to obtain the necessary parameters used to define the performance of the turbine, in-terms of the power coefficient or power output. The important parameters were the torque and the rate of turbine rotation and the power output of the turbine was calculated using these parameters as:

$$P_{exp} = \tau\omega \tag{3.19}$$

from which the power coefficient can be calculated as the ratio of the power generated to the available energy of the stream flow as:

$$C_p = \frac{P_{exp}}{\frac{1}{2}\rho A u_\infty^3} \tag{3.20}$$

where, A is the projected area of the turbine defined in Eqn. (3.2). Tip Speed Ratio (TSR) is a term commonly used for conventional turbines to define the ratio of the tip speed of the blade to the upstream fluid flow. However, in the MRL turbine the blade rotates relative to the main shaft as discussed before which is quite different to the way the conventional tidal turbine blade rotates. Thus a new term called Blade Speed Ratio (BSR) is used to define the velocity ratio of the MRL turbine. The BSR is defined as the ratio of the average velocity of the blade (commonly measured at the centre of the blades) to the upstream fluid flow as:

$$BSR = \frac{\omega R}{u_\infty} \tag{3.21}$$

3.5.1.2 Computational set-up

The experimental study was carried out in a blockage ratio, $B = 0.513$. Thus, the computational domain dimensions used in the previous sections were changed according to table 3.2, which has similar blockage ratio to the experiment test tunnel. The small scale dimension of the tidal turbine shown in Fig. 1.5 was represented by the IBF model in the centre of the computational domain. It was designed to replicate the uniform flow conditions in the test tunnel. The dimensions of the domain were matched with the fluid test tunnel used for the experimental work to account for any blockage effects that can

occur. The diameter of the turbine remains constant and the turbine is submerged at 0.35D from the free surface to the top of the turbine. The computational dimensions given in the

Label	Original dimension	New dimension
Diameter	D = 0.2m	D = 0.2m
Upstream	3D	3.125D
Downstream	20D	3.125D
Width	11.1D	1.3D
Water level	6.3125D	1.65D
Air level	2D	0.85D

Table 3.2: Computational domain dimension changes

table gives the same blockage ratio as the experimental test tunnel, which is much bigger than the blockage ratio, $B = 0.016$, used in the previous simulations. The boundary conditions discussed in chapter 2 section 2.9.1.2 have been used for the simulations except the inlet velocity. The experimental study has been carried out in a tunnel where the velocity profile was nearly uniform as discussed in section 3.5.1.1. In order to match the experimental conditions a uniform inlet velocity of 0.746 m/s was used for this particular simulation.

3.5.1.3 Discussions

This experiment was carried out with the MRL turbine in a vertical axis though the device is designed to operate in a horizontal axis configuration. The turbine has been tested with different flow rates and the results indicate the device's ability to operate in water with a wide range of flow rates which would be encountered in any tidal stream situation. The power coefficient peaks at a measured blade speed ratio, $BSR = 0.5$, as shown in Fig. 3.18. This shows that the MRL model can extract maximum energy from the flow when it is rotating at a rate that gives its blades a tangential velocity close to 0.5 of the flow rate but this is a preliminary result and with a more rigorous work the results may be subjected to some changes. It was clear from the results that the maximum power coefficient occurred at the same BSR for most of the flow rates tested although the values were slightly different

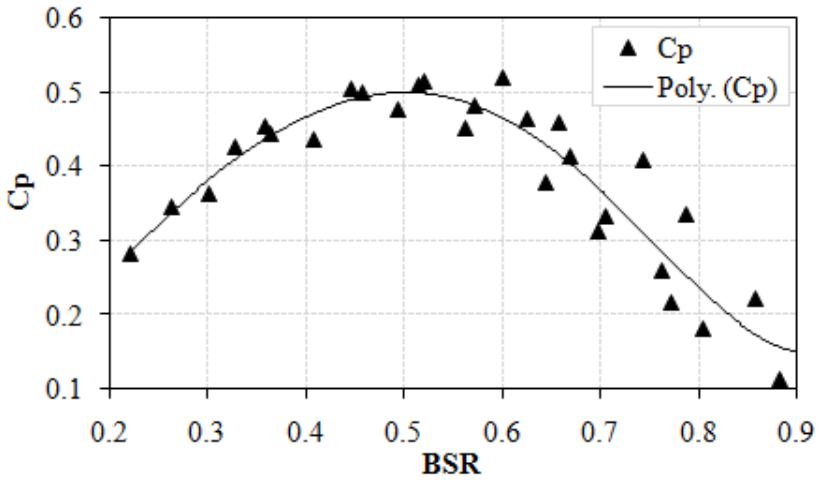

Figure 3.18: C_p **Vs. BSR for different flow rates**

which could be due to measurement errors. These measurements demonstrate the cubic relationship of the power to the fluid flow velocity.

Fig. 3.19 shows the a plot of the velocity contours simulated at the minimum and maximum resistance applied by the turbine. The momentum of the flow was reduced as it passed through the absorption zone created by the presence of the resistance forces by the turbine and to some extent by the side plates. The velocity contour clearly shows the magnitude of the impact of different values of resistance forces on the momentum change. At the minimum resistance, the flow between the side plates was undisturbed due to unbalanced operating conditions and most of the flow was forced through this region. Fig. 3.19b shows a large reduction of momentum in the downstream flow compared with Fig. 3.19a, which was caused by the maximum resistance.

Fig. 3.20 shows the power coefficient of the experimental and CFD results against the BSR and induction factor respectively. The power removed from the flow by the turbine in the IBF model is consistently higher than the power calculated due to the fluid generated torque in the experiments for all the resistance forces tested. The main reason for this difference is that the power removed from the flow is calculated using the COLM method discussed in section 3.2.1, which may include additional losses due to viscosity, shear etc. In contrast, the power measured from the experimental work is mainly due to the torque and angular speed generated by the fluid flow which in principle does not include the additional losses within the turbine region. These additional losses of power from the

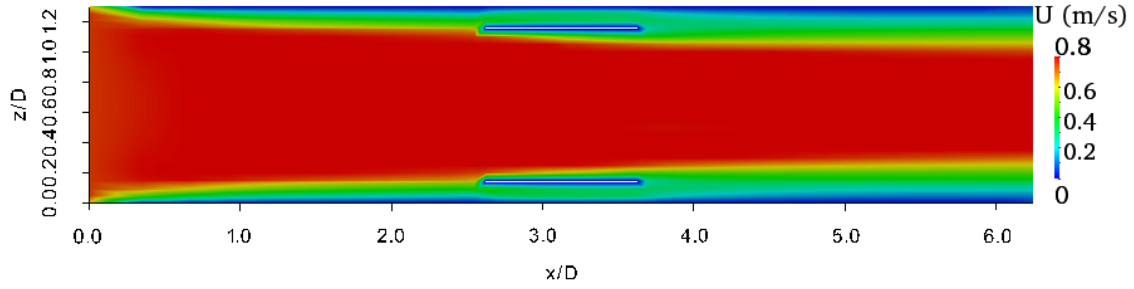

(a) At minimum resistance , $C_T = 0.141$

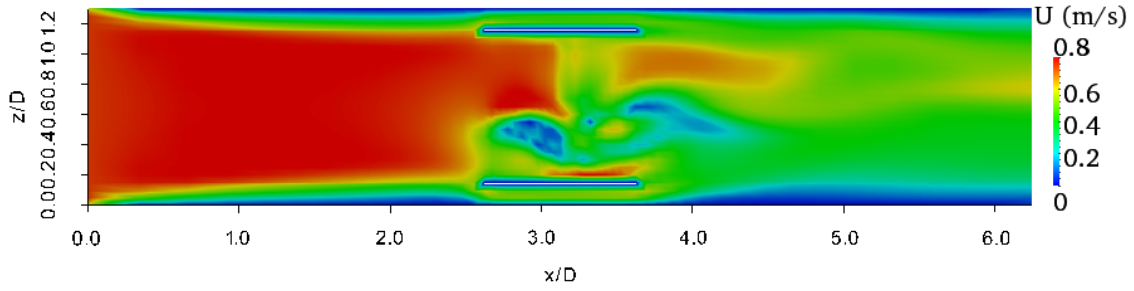

(b) At maximum resistance , $C_T = 1.125$

Figure 3.19: Velocity contours on horizontal plane across the centre of the turbine

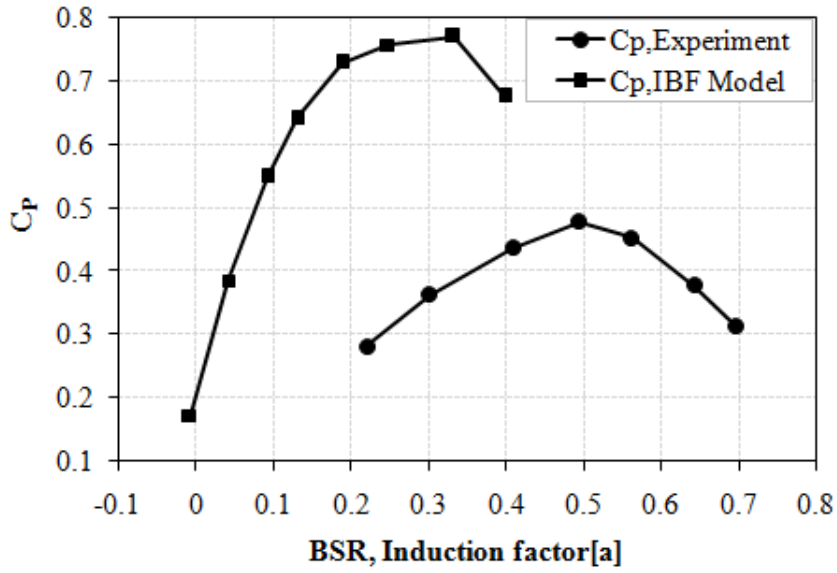

Figure 3.20: Comparison of power coefficients of the experimental and IBF model results

flow can be calculated using a simple empirical relationship as:

$$P = P_{exp} + P_{loss} \tag{3.22}$$

Eqn. (3.22) can be re-written using the necessary parameters as:

$$T\overline{u}_t = \tau\omega + C_{PL}\frac{1}{2}\rho A u_\infty^3 \tag{3.23}$$

where C_{PL} is the power loss coefficient which accounts all losses within the turbine region. In order to obtain the value of C_{PL} using Eqn. (3.23), the power coefficients of the turbine both by the IBF model and the experiments should be taken at the same operating point. The definitions of BSR and the induction factor, a, are different making it difficult to obtain a common operating points from the power curve. In such cases the appropriate way would be to compare the maximum power points from the two power curves. However, the resistance forces were calculated using the measured torque from the experiments as discussed before and the power coefficient from the IBF model can be directly compared to the power calculated in the experiment by that corresponding torque in order to obtain the value of C_{PL}. Using this approach, the power coefficient of the experiment calculated from the measured torque, $\tau = 0.61$ Nm, is $C_P = 0.437$ and the power coefficient of the IBF model obtained from the corresponding resistance force, $F_b = 11.62$, is $C_p = 0.728$. Thus the loss factor is, $C_{PL} = 0.291$, which accounts around 39.98% of the total power removed from the flow. Note that this power loss is excluding the power losses further downstream of the turbine due to remixing and any other mechanical/cable losses during transmission to the power grid. This result proves that the power calculated using the COLM is not necessarily the useful power but includes other associated losses within the turbine region.

3.5.2 Comparison with Detailed CFD model

In the case of traditional horizontal axis turbines, it has been realistic to undertake reasonably detailed analytic modelling of such devices incorporating loss mechanisms such as tip vortex losses that can not be included readily into simplified momentum sink models such as actuator disc descriptions. Thus the simple flow energy extraction models can be compared to those more realistic calculations where the actual power extracted by the turbine can be directly evaluated. This provides a link to actual experimental data for developing calibration procedures. There is also clearly the detailed CFD route available for such purposes. In the present case the flow structures in the class of turbine of interest are far more complex, particularly for systems such as the Momentum Reversal Lift device

where complex blade motions occur. This makes the detailed analytical modelling unrealistic leaving only the detailed CFD route open as a way to exploring the same comparison process.

A detailed CFD modelling of the blade motions (rotating blade) using sliding mesh methods (General Grid Interface (GGI)) is the subject of another PhD project currently underway in Exeter. preleminary results from this have been provided (personal communication M. Berry) and have been published in various recent conferences [Berry and Tabor, 2012]. Here, these results were compared with the results from the IBF model. This kind of comparison allows a link between the IBF model and experiments through the detailed CFD model as the power calculated using the fluid generated torque is the closest way of making a direct comparison with the experimental values.

3.5.2.1 Computational set-up

The detailed CFD simulations are currently under-way using a two dimensional (2D) domain to minimise the significant computational demand of three dimensional simulations induced by the dynamic sliding mesh. The blade of the MRL turbine has a chord length of $C = 0.095$ m as discussed in section 2.9.1.1 resulting a combined diameter of, $D = 0.20m$. However, the rotation of the blades with the same dimension overlaps on each other making it difficult to use the same chord length. Thus a short chord length of, $C = 0.05$ m, with a combined diameter of, $D = 0.14$ m, has been used in order to avoid the overlapping. A similar 2D computational domain (Fig. 3.21) was developed for the IBF model with identical blade dimensions and boundary conditions. The following boundary conditions were employed:

- Uniform velocity inlet ($u_\infty = 0.875$ m/s)
- Zero gradient pressure outlet
- Flow symmetry on the top and bottom of the domain
- Empty on the back and front of the domain

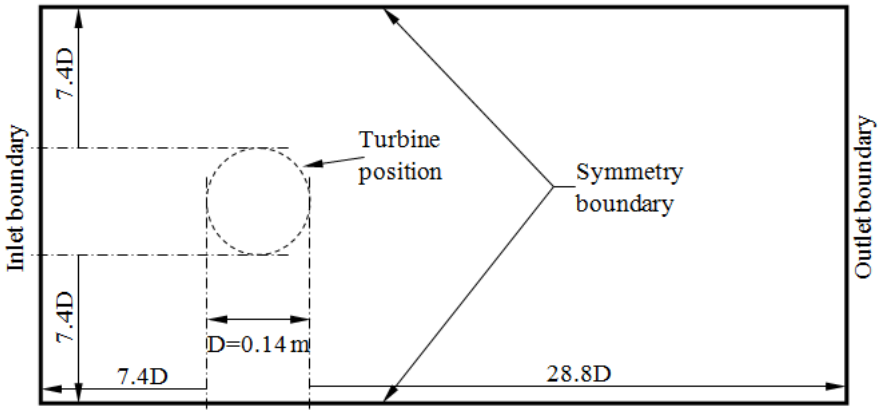

Figure 3.21: 2D computational domain

The RANS approach has been used in the detailed CFD model and the same technique was utilised for this section together with the IBF model as the LES approach is meaningless to apply in 2D simulations. The $k - \omega SST$ turbulence model has been used because of its capability of modelling separated flows.

3.5.2.2 Flow field analysis

Fig. 3.22 show a plot of the velocity contours from the two CFD models. The two models have generated similar wake structures between 0.5D and 10D. However, they have quite different wake structures from 10D onwards with the detailed CFD model (Fig. 3.22a) generating large vortex structures. One of the main reasons for this difference may be due to the effect of rotating blades although the vortex structures are generated starting from almost 10D away from the turbine. Vortex structures were not generated by the IBF model even in the 3D simulations using the RANS technique as discussed previously which was one of the reasons of using the LES technique in this study. In Fig. 3.22b a high velocity can be observed within the turbine region between the blades compared to the velocity in the detailed CFD model which is probably due to no rotational effect of the blades around that region.

3.5.2.3 Power analysis

The maximum power coefficient calculated using the fluid generated torque in the detailed CFD model is, $C_p = 0.46$, at $BSR = 0.3$. The power coefficient of the IBF model was

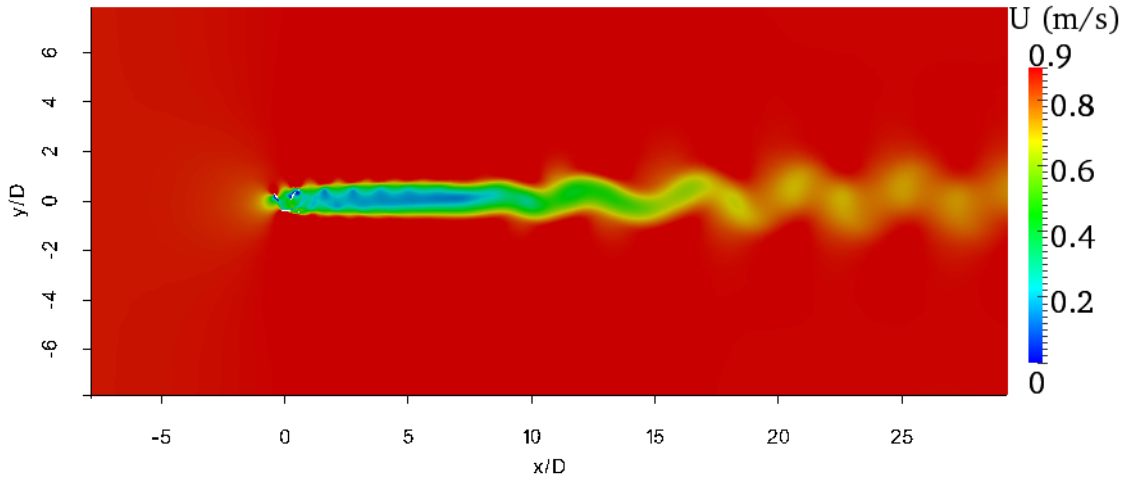

(a) GGI method

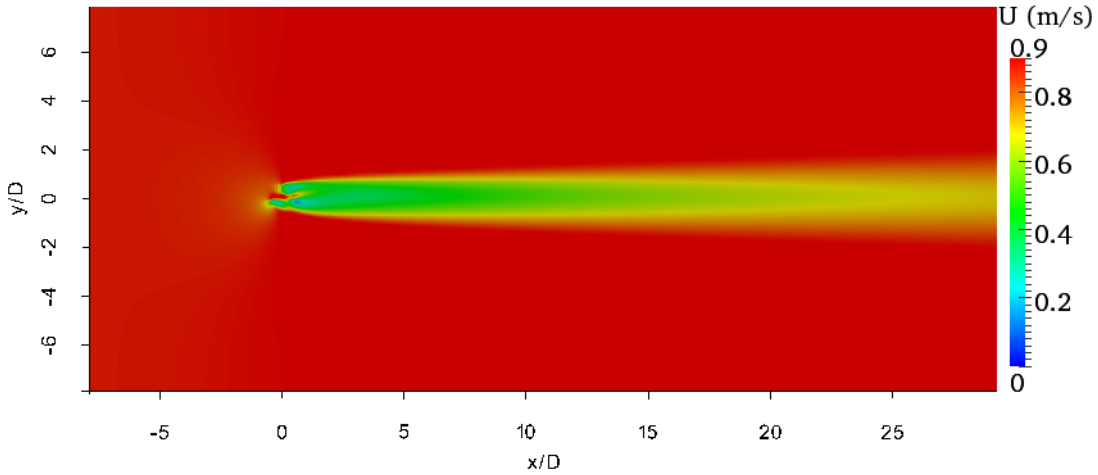

(b) IBF method, $C_T = 0.93$

Figure 3.22: Snapshots of velocity contours simulated by GGI and IBF methods

calculated using the COLM approach with little modification to the equations to exclude the Z-components of the velocities in order to match to the 2D simulation in this section. A full range of operating points were established with resistance forces,F_b, ranging from 0.01-0.13 N as shown in Fig. 3.23. Those forces are much lower than the ones used in the 3D simulations because of a small volume of blades used in the 2D simulations. A maximum power coefficient of, $C_P = 0.58$, at $C_T = 0.93$ was achieved within the given range of resistance forces. From these results, the total power loss within the turbine region can be calculated in a similar approach to the experimental comparison made in section 3.5.1.3 using Eqn. (3.23). Based on the maximum power point from the two methods, the power loss is 20.7% of the total power removed by the turbine from the flow excluding the power loss during the remixing.

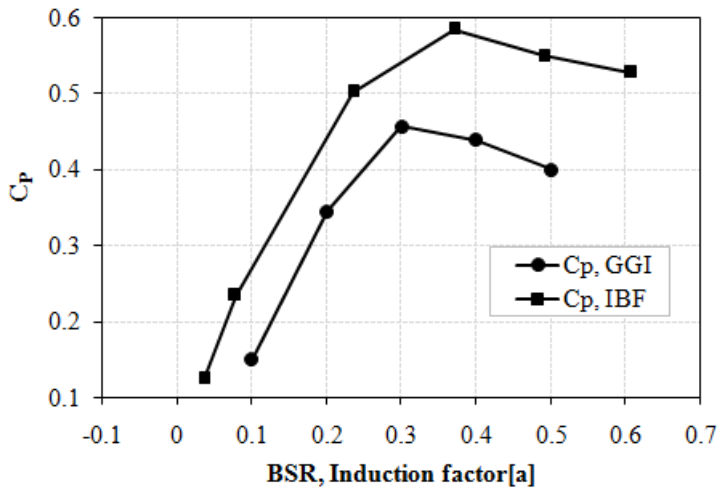

Figure 3.23: Comparison of the power coefficients of the IBF and GGI simulations

Fig. 3.24 shows a comparison of the streamwise relative energy flux for the IBF and detailed CFD models. Unlike the energy flux discussed in the open channel flow, the energy flux from this simulation is calculated without the contribution of the potential head as there is no free surface deformation. Thus the potential head component of Eqn. (3.15) is excluded and considers only the static and dynamic pressure heads to calculate the energy flux for this specific case.

The energy flux between -6.4D and -0.5D showed constant value for both models. However, they have different energy flux values between -0.5D to 0.5D even though they both showed a steep drop within the device region. In both cases, the energy loss continues from 0.5D onwards due to the downstream remixing although the energy loss from the IBF model is higher throughout the domain. The evolution of the energy loss between the two models also showed some difference between 0.5D and 7D where the energy loss in the remixing zone from the GGI model appears to be constant for unknown reason.

3.6 Summary

The main objective of this chapter was to investigate the performance and to establish the full range of operating points of a single MRL tidal turbine. A full range of operating points was formulated with resistance forces,F_b, ranging from 2.62 to 13.33 N and the maximum power coefficient occurs at $F_b = 10.76$ N resulting a thrust coefficient of $C_T = 0.898$.

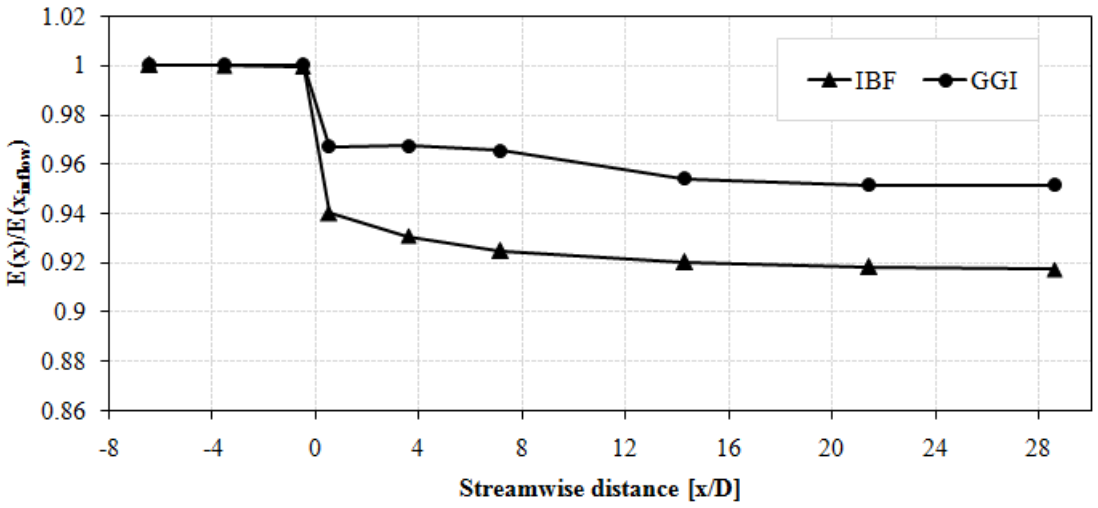

Figure 3.24: Comparison of streamwise relative energy flux between the IBF and GGI simulations

The corresponding power coefficient of the turbine was, $C_p = 0.717$. However, the power coefficient from the *annular* approach showed lower value, $C_p = 0.665$, at a thrust coefficient of, $C_T = 0.833$. The power coefficient of the IBF model showed higher values compared to the experimental and detailed CFD model results. This is an indication that the power coefficient calculated using the IBF model contains some losses within the turbine region and the comparison allowed the estimation of this power loss in addition to the useful power extracted by the turbine.

The energy flux along the streamwise direction also shows the unavoidable energy loss during remixing of the flows and provides important information to understand the influence on any downstream devices due to operating in the wake of upstream turbines. A high blockage ratio improved the performance of the turbine and this could have a positive impact on the performance of individual turbines in a tidal stream farm deployed in a closely packed configuration along the spanwise direction.

The CFD simulation results of two MRL turbine designs showed that the performance can be improved using side plates due to their ability to create venturi flow. In addition, the effect of blade positions on the performance of the turbine was investigated to understand if the blade positions have significant impact on the results. This was important due to the fact that the CFD simulations have to be carried out at arbitrary blade positions. The result showed no significant difference in the performance of the turbine, meaning the CFD

simulation can be carried out with any blade positions in order to investigate the issues surrounding tidal turbines.

Chapter 4

THE WAKE CHARACTERISTICS OF A SINGLE MRL TURBINE

4.1 Introduction

The discussions in Chapter 3 have been mainly focused on the investigation of the performance of the MRL turbine. However, a study of the flow filed characteristics is equally crucial to understand the effect of energy extraction to the free surface, wake structure, and the length of the wake downstream of the turbine.

This chapter presents the result of CFD simulations using the same MRL turbine and CFD model used in Chapter 3 and investigates the wake states created due to energy extraction from the stream flow and the effects it has on the free surface. A comparison of two MRL designs and two CFD modelling methods were also investigated based on the way the flow behaves and their effect on the dynamics of the free surface. Moreover, a sensitivity analysis was carried out to understand the influence of particular parameters on the wake recovery and free surface. These parameters include body force loading, ambient turbulence intensity, width proximity to the turbine, and the position of the turbine relative to the free surface.

The chapter is divided into several sections with section 4.2 presenting the computational domain set up and implementation of boundary conditions. In section 4.3, a comparison of two CFD modelling methods is discussed followed by a sensitivity analysis, which investigates the effects of width proximity, body force loading changes and the ambient turbulence intensity values on the flow features. A subsequent section includes the comparison of two MRL turbine designs and the effect of turbine submerging relative to the free surface. Finally, a discussion on the wake recovery is included and the chapter is concluded with a summary.

4.2 Computational Set-Up

The computational domain and boundary conditions discussed and used in Chapter 2 sections 2.9.1.1, 2.9.1.2, and 2.7.3.1 have been used in most of the simulations carried out in this chapter. However, the width has been subjected to some changes in the investigation of width proximity in section 4.3.2.2.

4.3 Results and Discussions

4.3.1 Comparison of the Two IBF Modelling Approaches

The two IBF modelling approaches (*annular* and *blade*) discussed in chapter 3 showed no significant difference during the calibration of energy extraction by the MRL turbine. However, an additional investigation of the flow features in and around the turbine, when simulated using the two approaches, is necessary in order to draw conclusions about their advantages and disadvantages and to select the best option of the IBF modelling approach for further study.

The velocity contours of the simulation results using the two approaches are shown both in vertical and horizontal planes in Fig. 4.1. The *annular* approach generated large vortex structures (Figs. 4.1a and 4.1b) as would be expected from the real turbines compared to the results shown from the *blade* approach in Figs. 4.1c and 4.1d. The possible reason for the large vortex structures from the *annular* approach is that the body forces on the *annular* section tend to impose rotational flows, as the main shaft does, whereas the forces on the blades are creating blockage effects in different directions. A combination of both forces create rotational flows both within and on the peripheral of the turbine which brings the idea of relative motion of the blades with respect to the shaft rotation, which is the basic working principle of the MRL turbine.

Fig. 4.2 shows instantaneous and time averaged horizontal velocity profiles along the centre of the turbine. There is irregular evolution of the velocity profiles downstream of the turbine where the wake is faster for the *annular* approach between 3.5D and 14D.

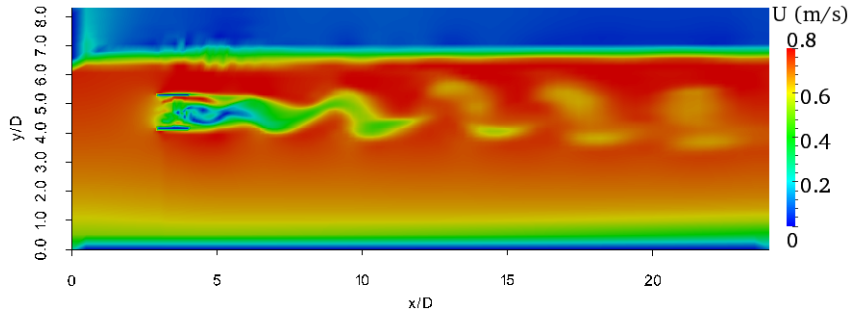

(a) *Annular* approach vertical plane

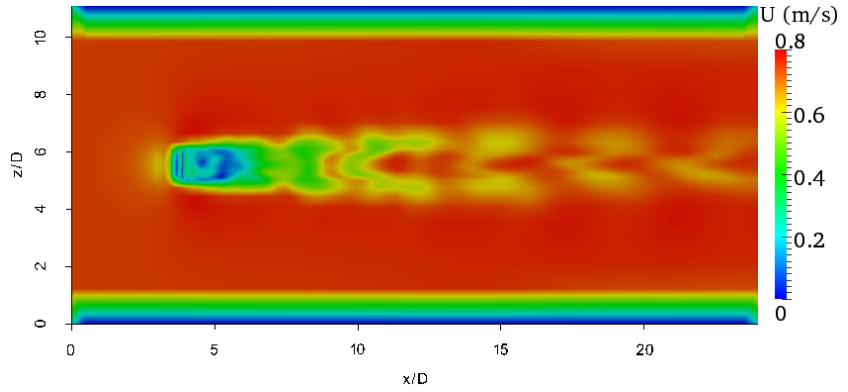

(b) *Annular* approach horizontal plane

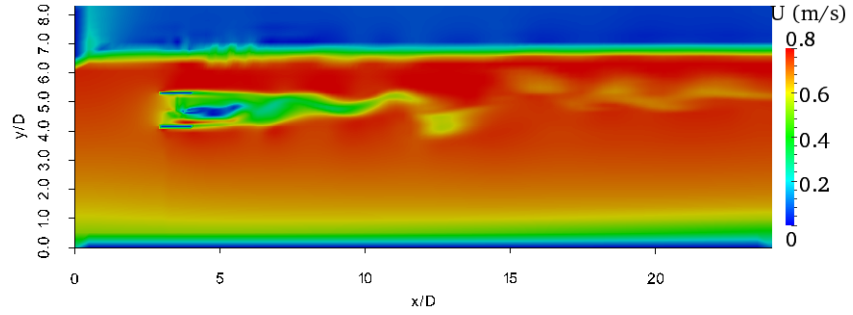

(c) *Blade* method vertical plane

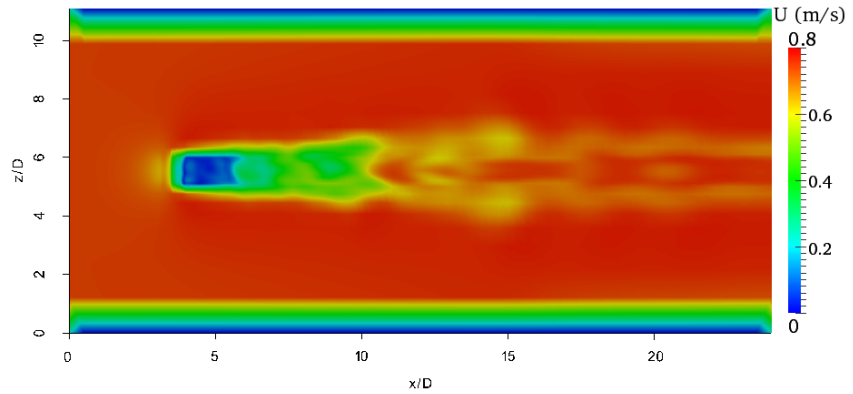

(d) *Blade* method horizontal plane

Figure 4.1: Velocity contours across the centre of the turbine

However, the result from the *blade* approach showed faster wake recovery in the rest of the velocity profiles in both figures. At the end of the domain, the velocity from the *blade* approach is higher, which is the reverse of what was expected due to the fact that a faster wake recovery was expected by observing the velocity contours given in Fig. 4.1. However, calculating the time averaged vertical velocity values at the end of the domain (24D), the wake recovers to 91% of the stream flow in both approaches. The main reason for this discrepancy could be that the dataset was extracted along the centreline through the turbine, which appears to be accelerating after 14D as shown in Fig. 4.1d. Thus, the fact that there is a faster wake recovery between 3.5D and 14D in the *annular* approach makes it a better option.

Fig. 4.3 illustrates the difference of the pressure profiles between the *annular* and *blade* approaches. The time averaged pressure profile (Fig. 4.3b) showed that the pressure drop across the turbine is higher in the *blade* approach in contrast to the instantaneous pressure profile where the pressure drop is higher in the *annular* approach. However, the instantaneous values does not represent the actual conditions as they are extracted at arbitrary time steps where the data is expected to fluctuate from time step to time step although it provides good information on the fluctuating behaviour of the flow. The high pressure drop in the *blade* is another indication to the fact that the power extracted by the *blade* approach was slightly higher as discussed in Chapter 3.

Investigations of the wake characteristics showed that the *annular* approach generates large scale vortexes, which is normally expected in the actual bladed turbine, and it has better wake recovery. The fact that the wake recovery in the *annular* approach is faster than in the *blade* approach makes it a better choice for the study of tidal stream farm modelling because it reduces the spacing between turbines which in turn minimises the possibility of influencing the performance of any downstream turbines by the wake interaction. Furthermore, a faster wake recovery minimises the area of a tidal stream farm and optimises the power extraction capability of turbines in a specified size of tidal stream farm. There is no additional computational cost or any other side effects that can be incurred which may prevent us from using either of the two approaches. Therefore, the

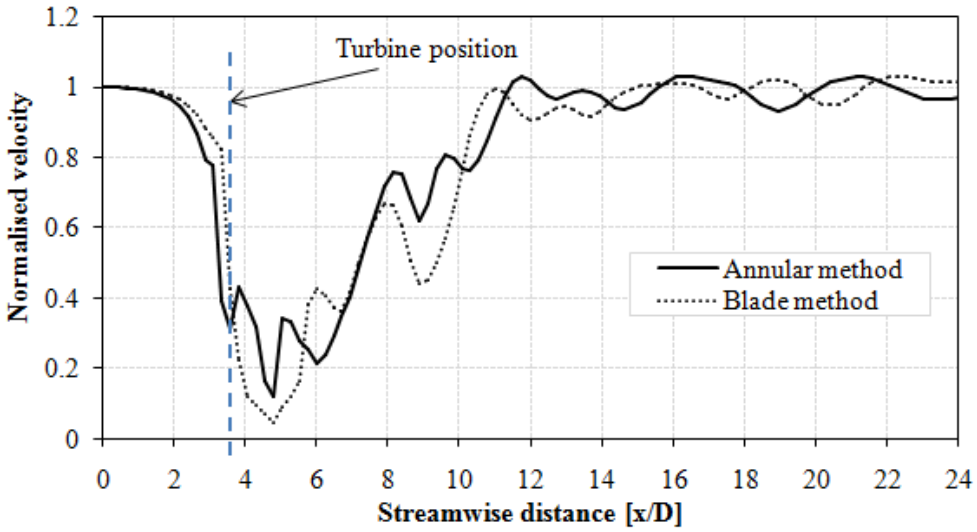

(a) Instantaneous velocity profile

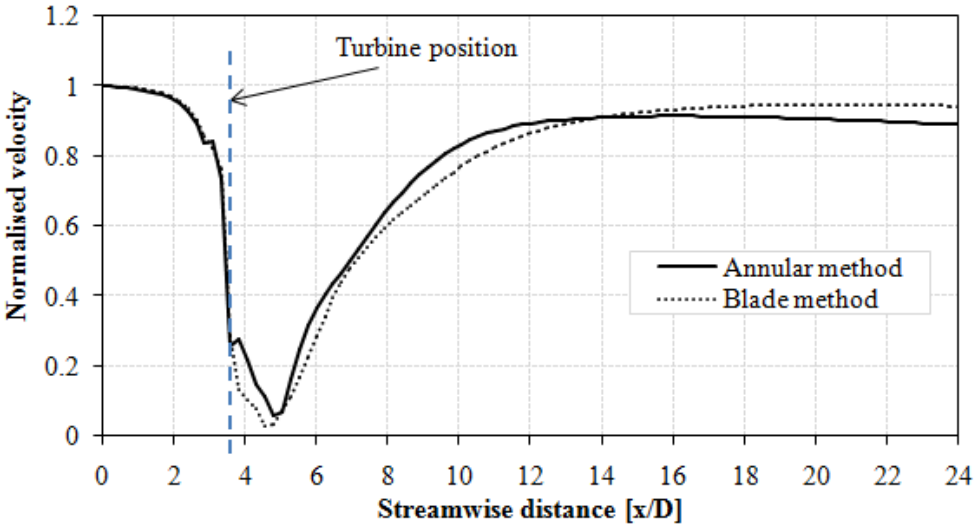

(b) Time averaged velocity profile

Figure 4.2: Stream-wise velocity profile along the centreline of the turbine for the two IBF models

annular approach has been selected for the study of the MRL turbine and will be used in the rest of this study.

4.3.2 Sensitivity Analysis

4.3.2.1 Mesh sensitivity

Mesh grid size is an important factor in numerical simulations because the accurate resolving of the flow motions depends significantly up on it. Thus, finding or developing a suitable model that can satisfy the engineering solution without the need of a fine grid

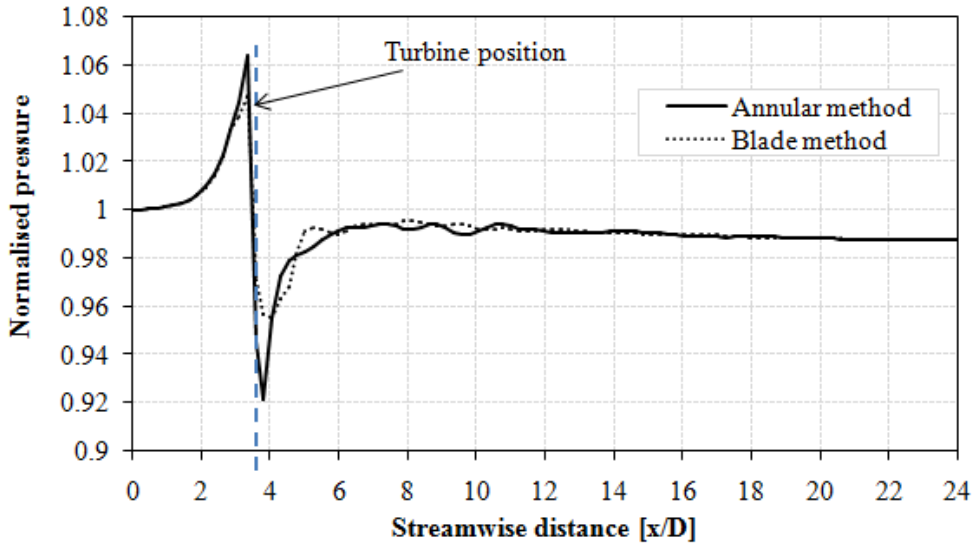

(a) Instantaneous pressure profile

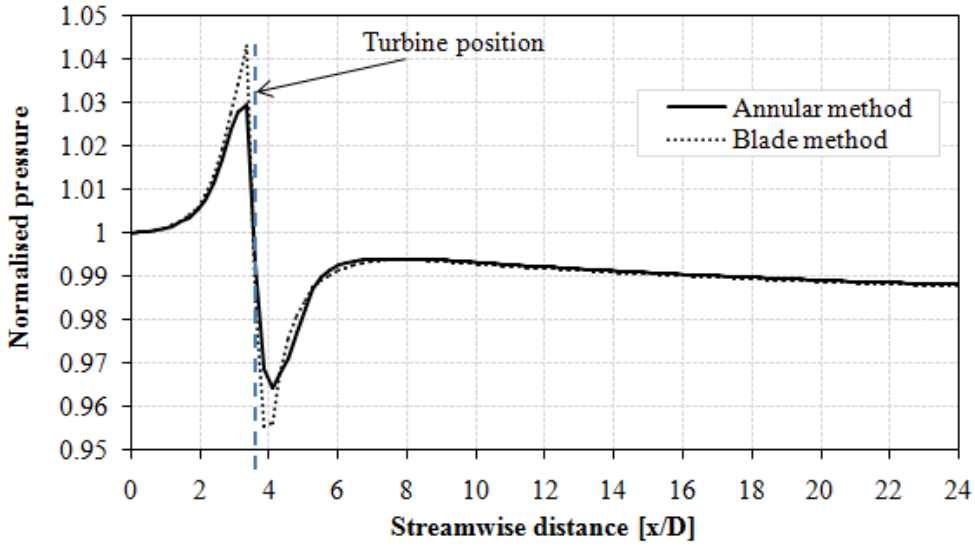

(b) Time averaged pressure profile

Figure 4.3: Stream-wise pressure profile along the centreline of the turbine for the two IBF models

size (i.e. cheap computational cost) is one of the biggest challenges engineers are facing nowadays. As the grid size gets finer, it inflicts a high computational cost because of the type of models used, such as the direct numerical simulation (DNS). In contrast, if the grid size gets coarser, this leads to the use of models developed by approximations such as the Reynolds Average Navier-Stokes (RANS) models, which can result in a poor description of the flow, especially for the simulation of turbulent flows. Therefore, using an appropriate grid size is always crucial.

Three grid size samples (fine, medium, and coarse) as shown in table 4.1, have been

selected to investigate the effect of grid size on the results . The grid size was refined in the zone of interest around the turbine region and a larger grid size was towards both end of the domain to reduce the computational cost in the three cases.

Grid size Type	X-axis (N_x)	Y-axis (N_y)	Z-axis (N_z)	number of cells
Fine	204	86	42	736448
Medium	112	54	26	156848
Coarse	66	38	18	44744

Table 4.1: Number of cells for the three different grid sizes

Figs. 4.4, 4.5, and 4.6 show the velocity contours simulated with the three grid size samples. The results from the fine mesh (Fig. 4.4a) showed a clear distinction between the water and air body, which suggests a fine grid size is required in order to adequately resolve the flow at the interface of the two phases. The boundary layer sizes are 2.3D, 1.2D, and 0.65D for the coarse, medium and fine grids respectively. The results showed different flow characteristics as expected. This shows that the fine grid also reduced the boundary layer size as shown in Fig. 4.4b, which minimises the effect of width proximity (see detail discussion about width proximity effect on section 4.3.2.2). However, the computational time was significantly increased by almost 443% compared with the medium grid, which is not feasible for large scale and/or array of turbine simulations, considering the currently available computing resources.

In contrast, the results using the coarse grid size showed poor flow descriptions (Fig. 4.6a) and a large boundary layer size (2.3D). More importantly, the result showed massive disturbances to the air body and makes it difficult to see a clear interface between the two phases, though the computational time was decreased by almost 115% compared to the medium grid size. Thus, the CFD model is incapable of resolving the flow motions with a coarse grid and requires a fine grid to get accurate description of the flows. However, the simulation result with the medium grid size produces satisfactory flow descriptions as shown in Figs. 4.5a and 4.5b. Therefore, the medium grid size is a good compromise between the fine and coarse grid sizes and so it is important to use the medium grid size

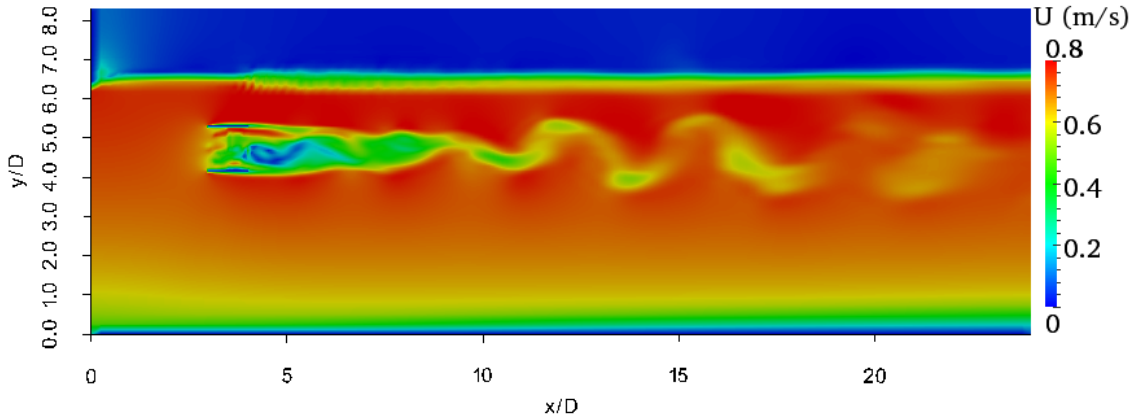

(a) Vertical plane

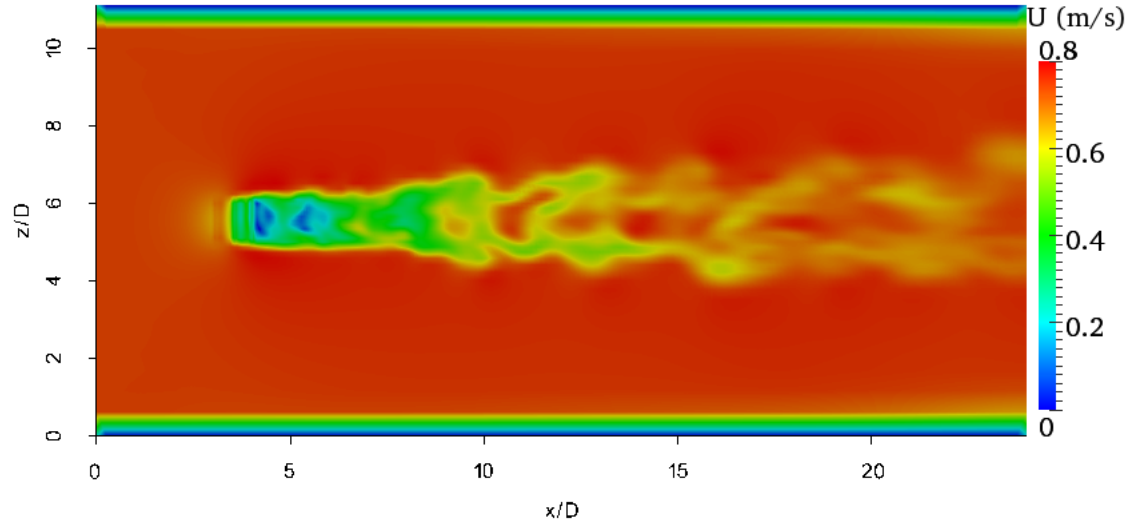

(b) Horizontal plane

Figure 4.4: Velocity contours for fine grid size

throughout this study to minimise the long computational time inflicted by the fine grid size as it satisfies the engineering solution required. Thus, the medium grid size mesh has been used in the subsequent studies but changed proportionately according to any change of the computational domain dimensions.

The velocity profiles in the stream-wise direction shown in Fig. 4.7 have different evolutions downstream of the turbine both in the instantaneous and time averaged values. The difference of the results from the three grid sizes is clearer in the time averaged velocity profile and it appears that the wake recovery is faster with the coarse grid size compared with the other two cases, though it is not consistent throughout the profile. However, the velocity profile does not represent the actual fact because the velocity dataset represents only a line along the centre of the turbine. The main reason for the faster wake recovery

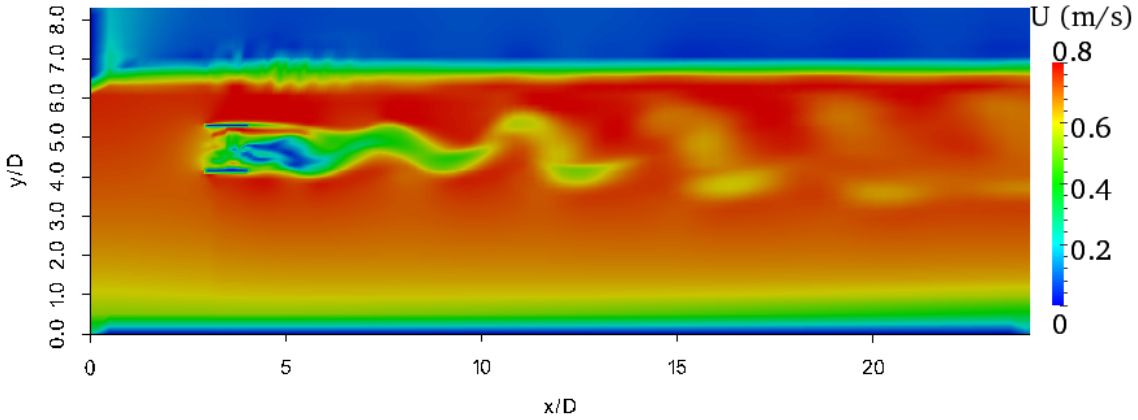

(a) Vertical plane

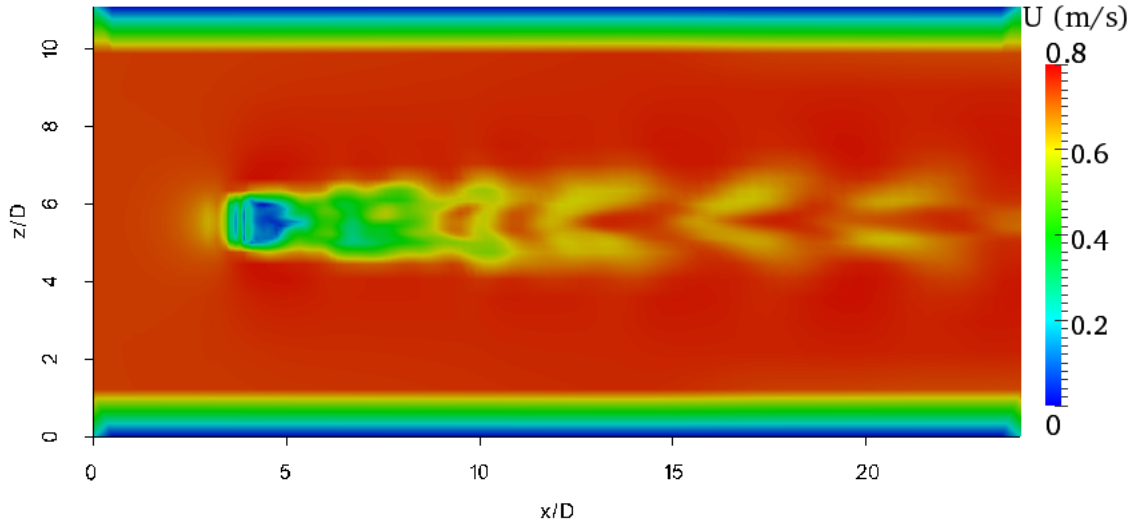

(b) Horizontal plane

Figure 4.5: Velocity contours for medium grid size

with the coarse grid is that the wake does not form along this centreline but rises above it. Therefore, the velocity value is high downstream of the turbine as shown in the horizontal plane in Fig. 4.6b. However, the velocity is lower above the centreline towards the end of the domain as shown on the vertical plane in Fig. 4.6a.

4.3.2.2 Wall boundary proximity to the turbine

The effect of different blockage ratio ($B = 0.008$, $B = 0.016$, and $B = 0.029$ which corresponds to three width dimensions of 1.22 m, 2.22 m, and 4.22 m respectively) on the performance of tidal turbines was discussed in Chapter 3. It has been proved that the higher the blockage ratio, the higher the performance of the turbine. However, a further analysis is necessary to understand the effect of different blockage ratios on the general

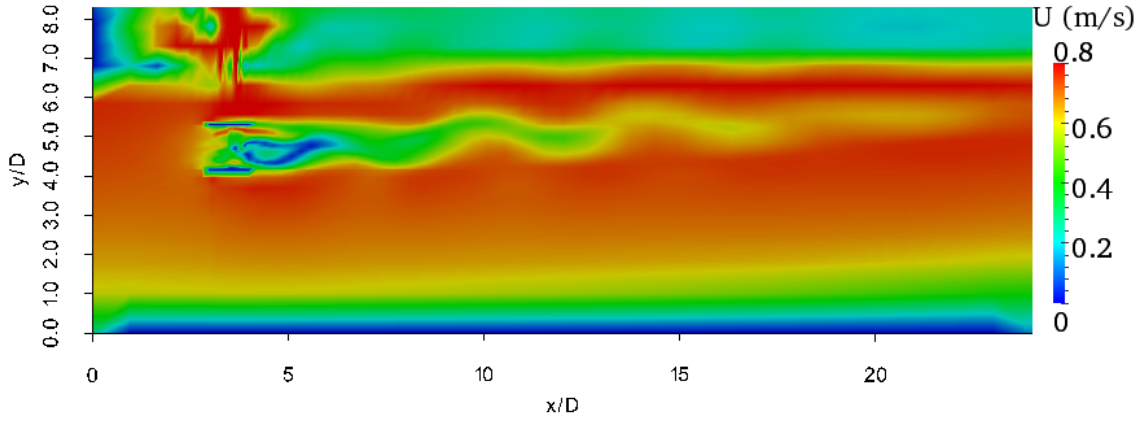

(a) Vertical plane

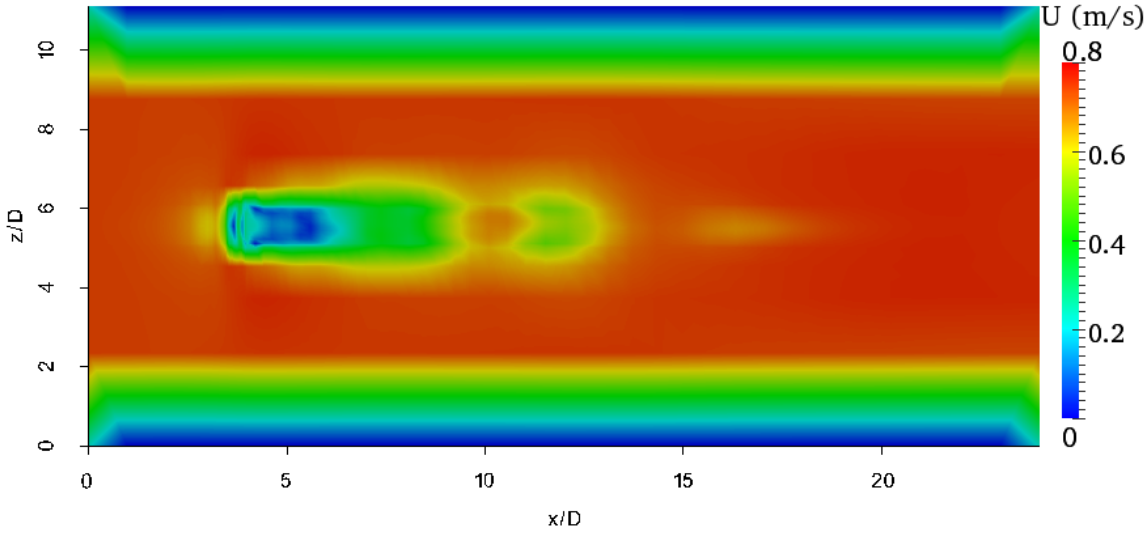

(b) Horizontal plane

Figure 4.6: Velocity contours for coarse grid size

flow features.

Figs. 4.8, 4.9, and 4.10 show the velocity contours both on the vertical and horizontal plane across the centre of the turbine. These results gave an insight of what happens to the flow features within and downstream of the turbine when the computational domain width and/or the blockage ratio is different. The simulation results showed different flow characteristics for the three domain widths used and these discrepancies were more visible on the vertical planes (Figs. 4.8a, 4.9a, 4.10a) at the interface between the two phases and on the air body. The air body in the smaller width (W = 1.22m) was severely affected leading to high velocity flow, which is not expected as the initial condition provided is zero velocity. The results from the other two width dimensions (W= 2.22m and W = 4.22m) showed a clear difference between the two phases and the interface can be easily identified

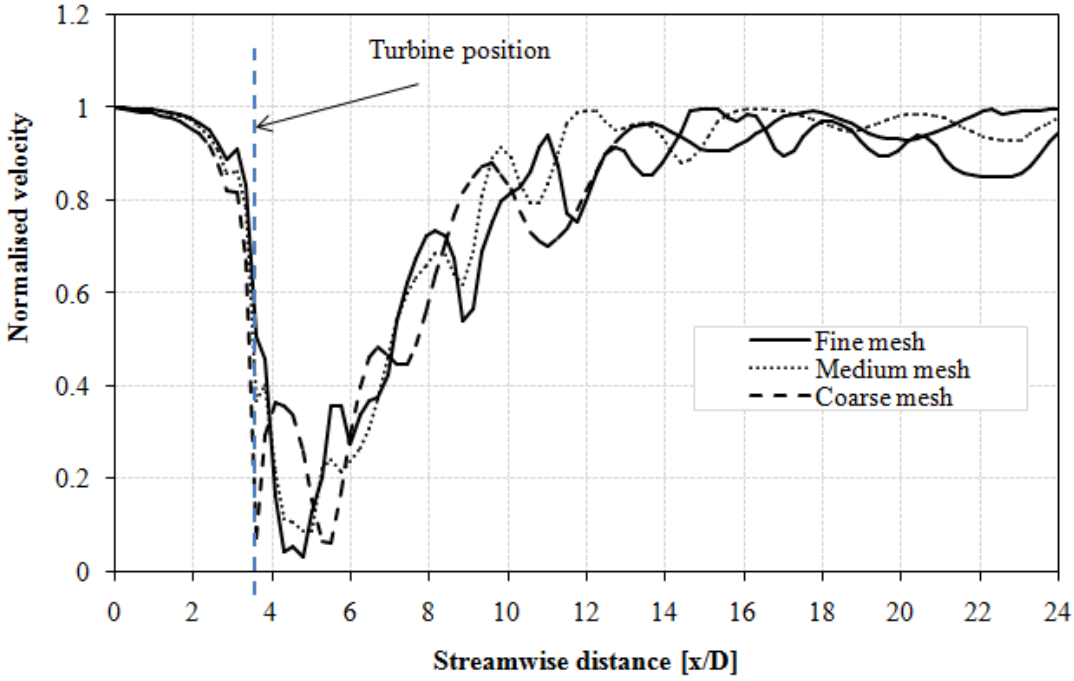

(a) Instantaneous velocity profile

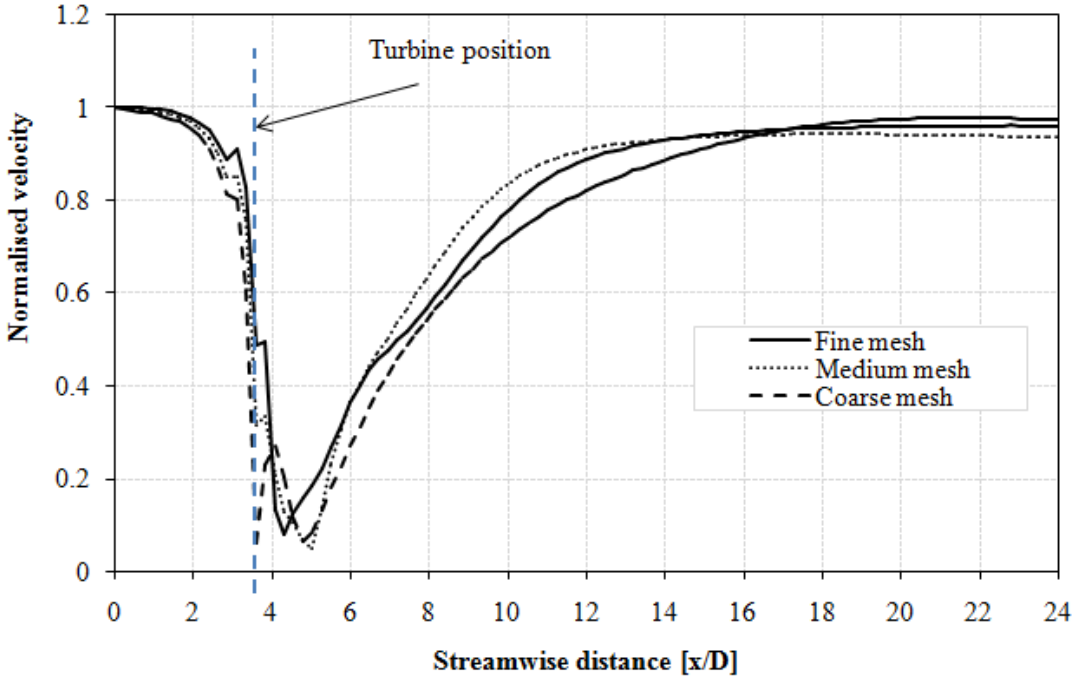

(b) Time averaged velocity profile

Figure 4.7: Stream-wise velocity profile along the centreline of the turbine for the three mesh grid sizes

except a small free surface disturbance above the energy extraction zone of the larger width. However, the larger width incurred massive computational cost compared to the other two dimensions.

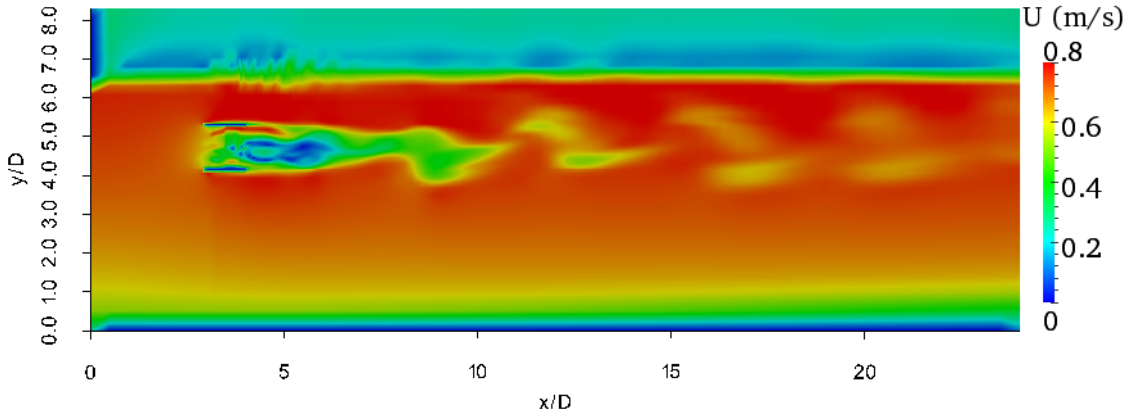

(a) Vertical plane

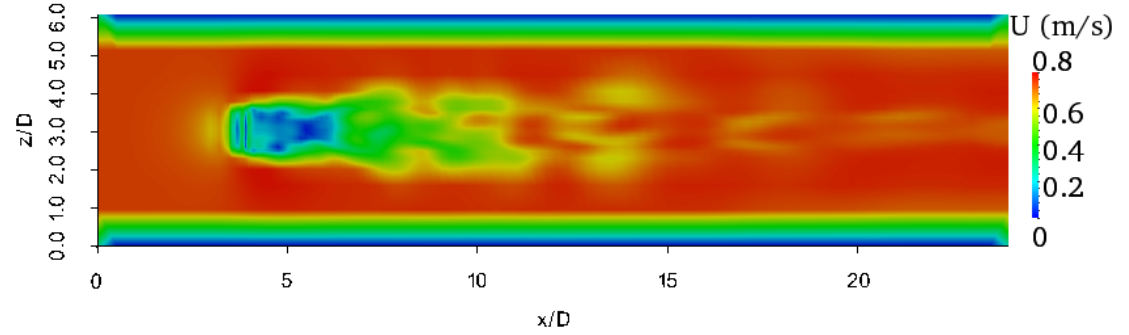

(b) Horizontal plane

Figure 4.8: Velocity contours, W = 1.22m

Fig. 4.11a shows an instantaneous velocity profile extracted from the velocity contours given in Figs. 4.8, 4.9 and 4.10. The graph demonstrates that the velocity fluctuates immediately downstream of the turbine during the recovery process and sustains upto the end of the domain. It seems difficult to differentiate the velocity profiles for the three width dimensions from this instantaneous velocity except a small difference observed between 4D and 9D, where it showed slow wake recovery in the smaller width. However, this is not always true as the velocity profile represents an instantaneous value.

A time averaged velocity was then calculated in order to understand the difference of the actual wake recovery in the three domains, as shown in Fig. 4.11b. The fluctuations disappeared in the time averaged velocity profile and clearly showed the difference of the wake recovery among the three cases. The large width (W=4.22m) showed slower wake recovery compared to the other widths throughout the downstream velocity profile. This is mainly due to the reduction of the venturi effect of the computational domain's wall boundary, which often accelerates the flow rate if a small width is used.

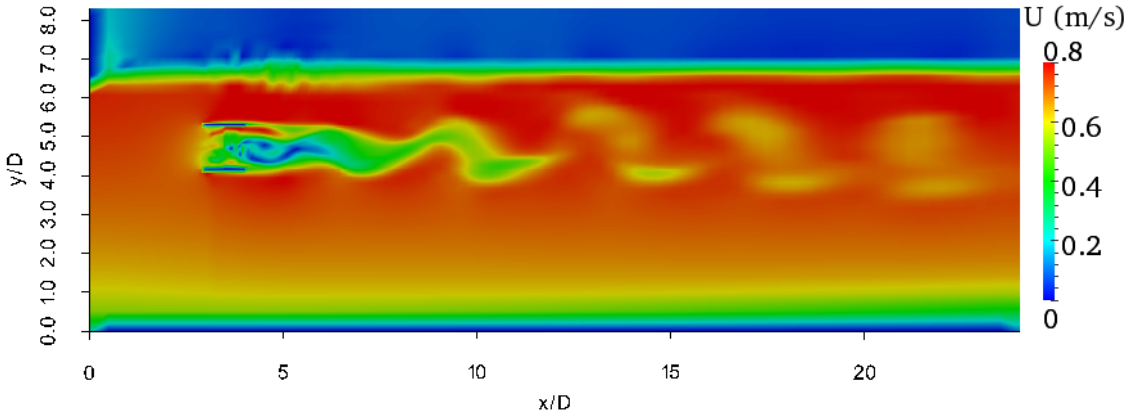

(a) Vertical plane

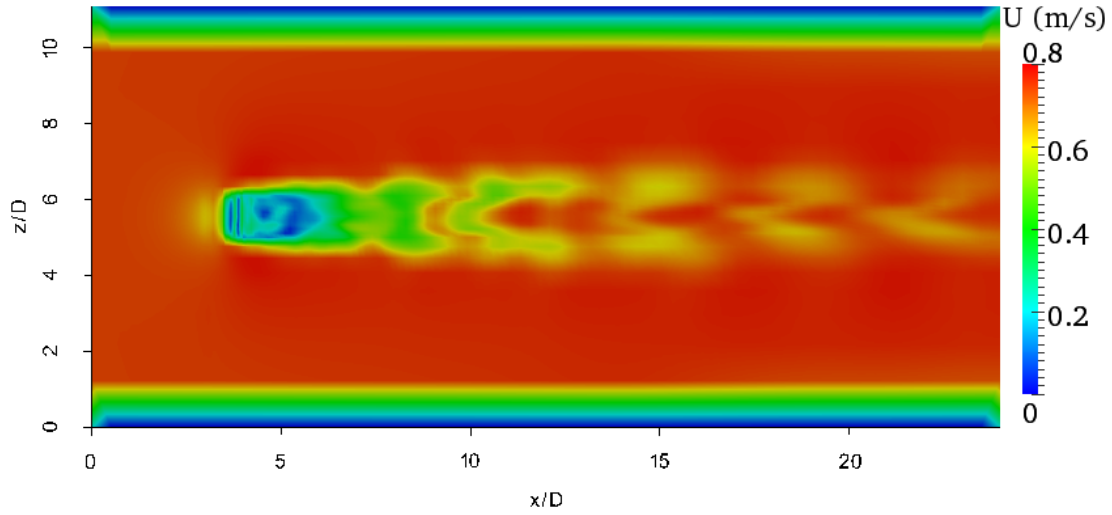

(b) Horizontal plane

Figure 4.9: Velocity contours, W = 2.22m

The pressure profile is another way of analysing the effect of the domain width, as shown in Fig. 4.12. The results showed a different pressure drop across the turbine using both the instantaneous and time averaged pressure profiles. However, in the case of the instantaneous pressure profile, there is still a pressure fluctuation, which reflects the velocity fluctuation discussed previously. The turbine in the small width (W = 1.22m) showed a high pressure drop across the turbine region compared with the other two widths because of the venturi effect, which also increased the power extraction by the turbine.

However, as the width increases the pressure drop decreases but at a slower rate. This indicates that with a very large width, the venturi effect is minimal and the power extraction by the turbine also reduces as discussed previously. Considering all the pros and cons, the turbine simulated in the medium domain width (2.22m) would satisfy the necessary

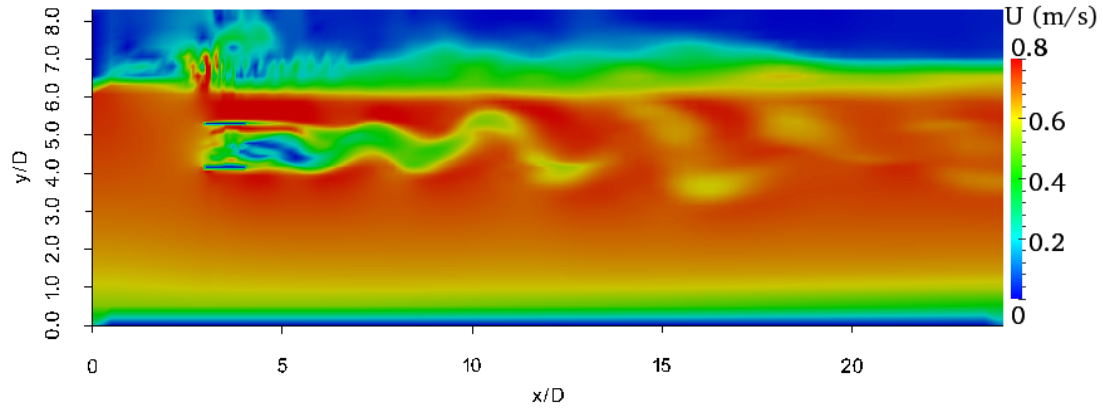

(a) Vertical plane

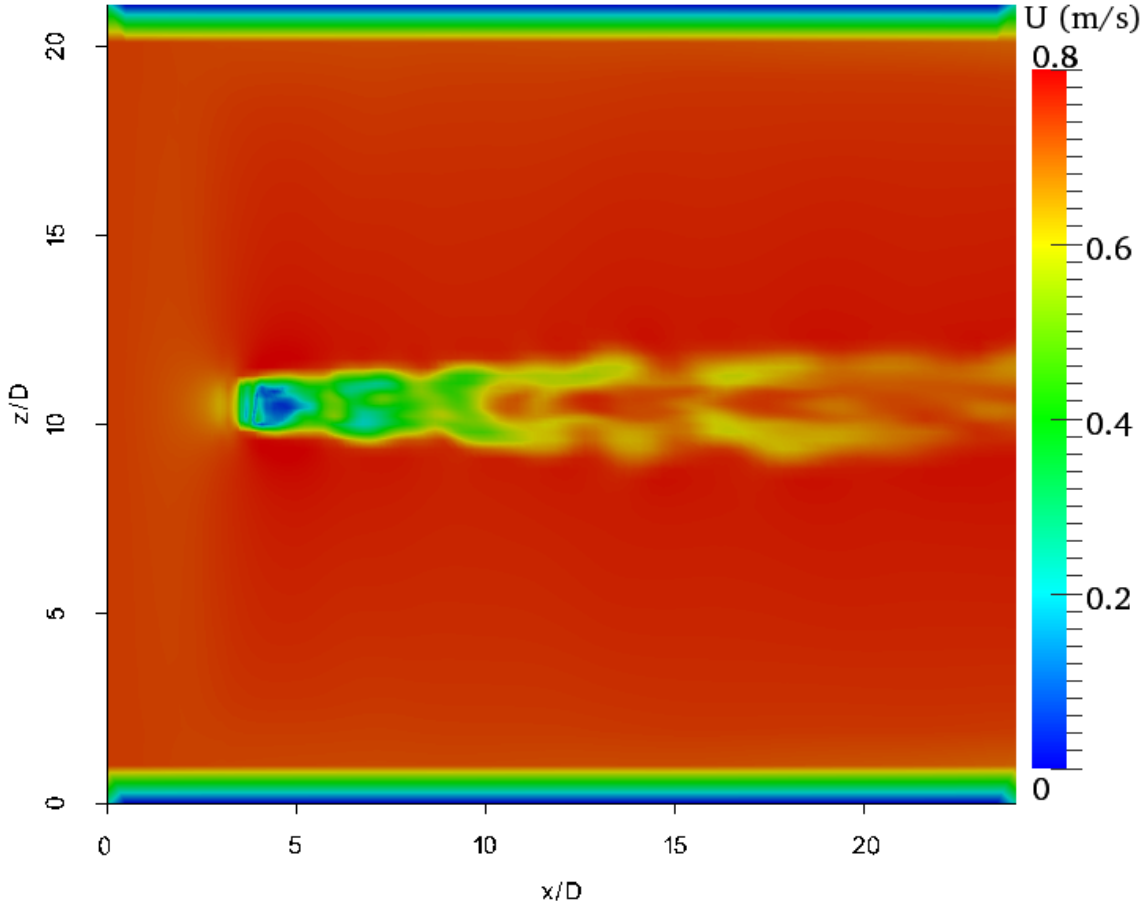

(b) Horizontal plane

Figure 4.10: Velocity contours W = 4.22m

requirements of the simulation results. Thus, a computational domain which satisfies a domain width of 2.22m, which is equivalent to around 5D spacing between the wall boundary and the turbine would be a potential choice.

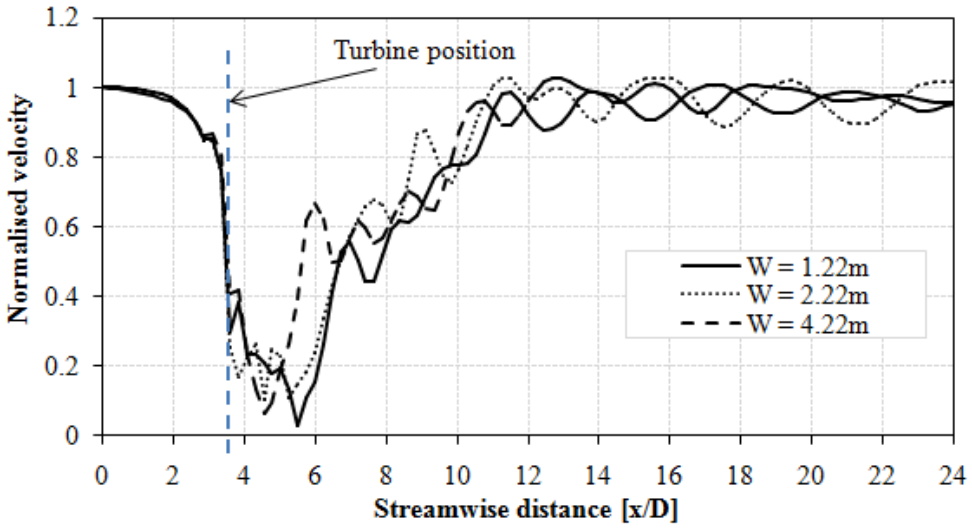

(a) Instantaneous velocity profile

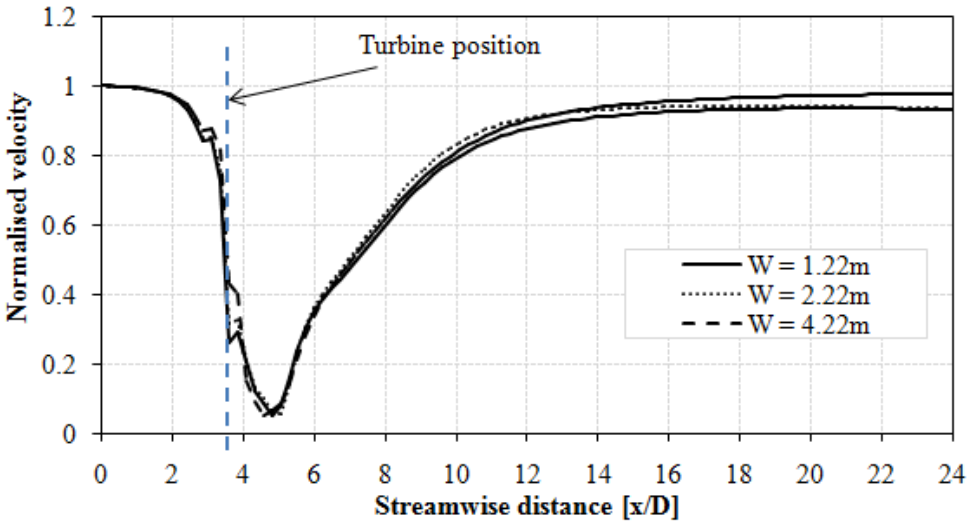

(b) Time averaged velocity profile

Figure 4.11: Stream-wise velocity profile along the centreline of the turbine for the three domain width

4.3.2.3 Body force loading

A calibration of the power extraction by the turbine carried out in chapter 3 with several body force loadings, showed that there is a body force where a peak power extraction occurs for a given turbine size, meaning there is no possibility to obtain a higher power extraction with a higher body force. This is an indication that different values of body force would have several consequences on the wake states and the free surface, and needs investigating. Table 4.2 shows a sample of three arbitrary chosen body forces used in the analysis.

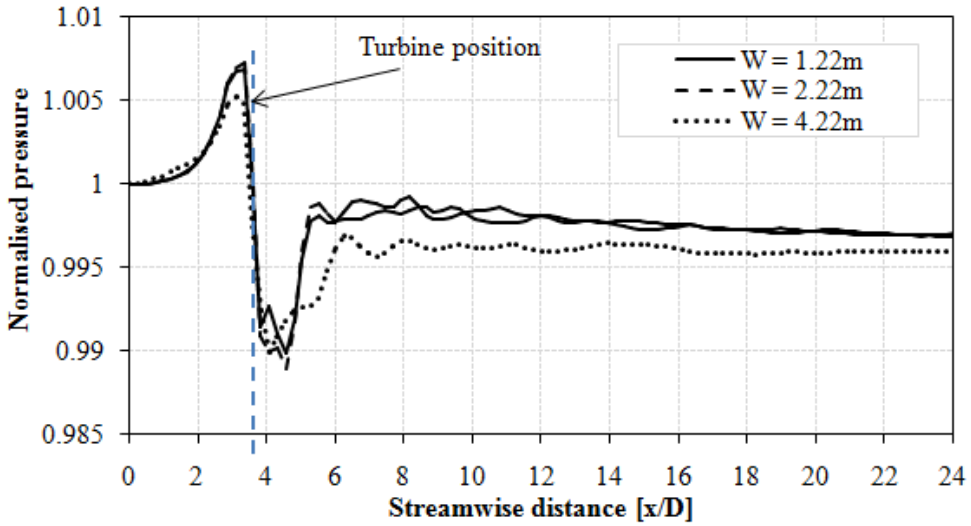

(a) Instantaneous pressure profile

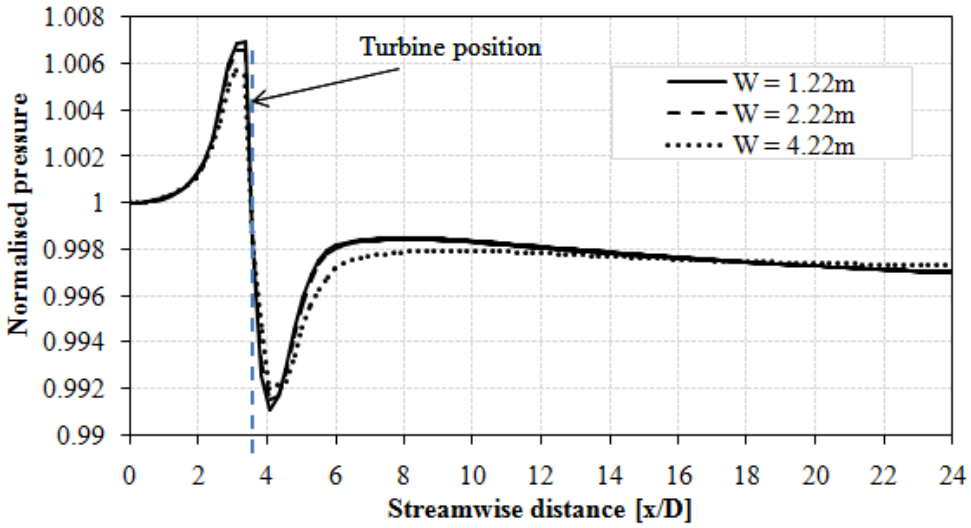

(b) Time averaged pressure profile

Figure 4.12: Stream-wise pressure profile along the centreline of the turbine for the three domain width

Velocity (m/s)	body Force (N)	
0.746	trial 1	14.5
	trial 2	16
	trial 3	17.5

Table 4.2: Velocity and body forces for CFD input

Figs. 4.13, 4.14, and 4.15 show the vertical and horizontal plane views of the velocity contours simulated with the three body forces. The velocity contours illustrate that there is a significant difference in the downstream flow characteristics of the turbine due to the different loading on the turbine blades. The downstream wake simulated with the highest

body force (Fig. 4.15a) showed larger scale vortices compared with the downstream flow simulated with the smallest body force (Fig. 4.13a). A larger scale vortex could be generated if the body force used was to be increased beyond 17.5 N. However, there is always a limit of the body force that can be applied due to the size of the blades and its associated power extraction capability. Therefore, it is not feasible to increase the body force beyond a specified range of the design parameters of the turbine.

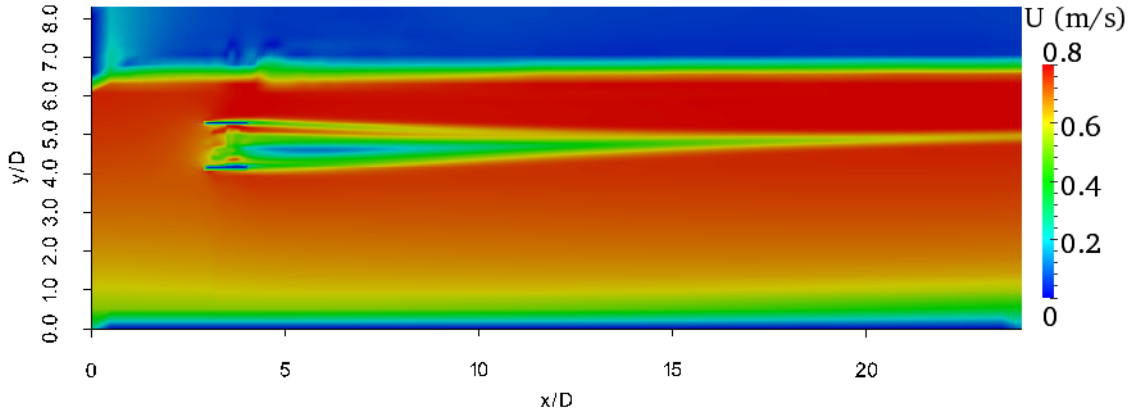

(a) Vertical plane

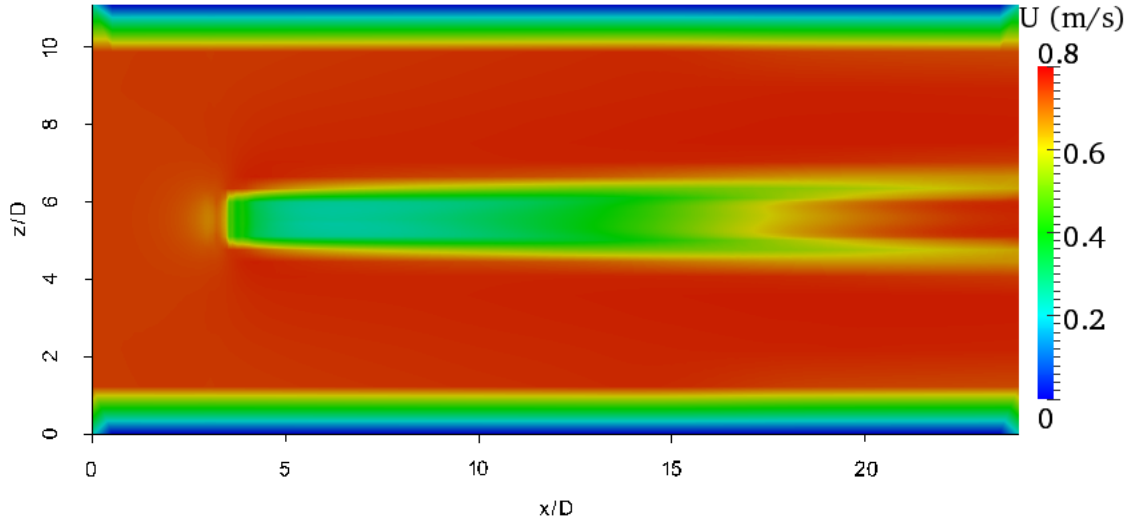

(b) Horizontal plane

Figure 4.13: Velocity contours at $F_b = 14.5N$

Fig. 4.16 shows a horizontal velocity profile extracted along the centre of the turbine from the simulation results obtained by applying the three body forces. The results show that the wake recovers faster downstream of the turbine between 5D and 17D using the highest body force (17.5N). However, calculating the averaged value of the vertical velocity at the end of the domain, the wake recovery is faster with the highest body force. The main

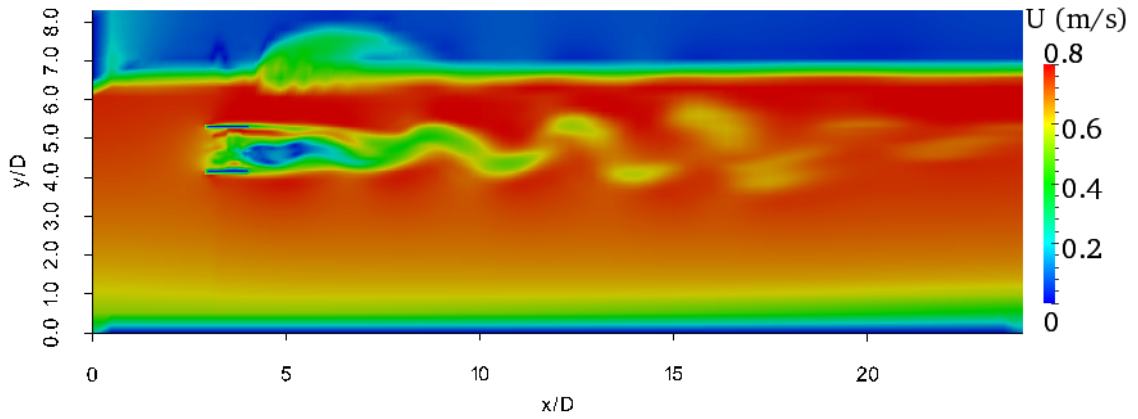

(a) Vertical plane

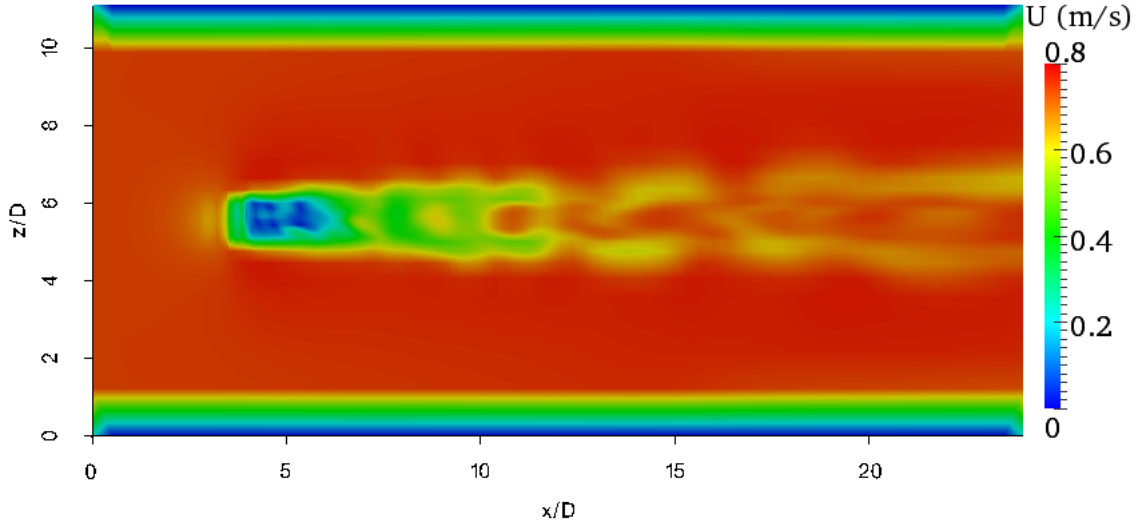

(b) Horizontal plane

Figure 4.14: Velocity contours at $F_b = 16N$

reason of this contradicting observation of the horizontal velocity profile and the averaged vertical velocity profile at the end of the domain is that, the horizontal velocity profile shown in Fig. 4.16 represents only a dataset along the centreline of the turbine. This can in fact be proved by looking at the velocity contours produced by the lower body forces (14.5N and 16N) shown in the horizontal plane of Figs. 4.13b and 4.14b, compared to the velocity contour shown in Fig. 4.15b, which shows a high velocity through the centre (the lower velocity splits into two) for the former two, from 17D downstream towards the end of the domain.

The velocity deficit immediately downstream of the turbine is also high for the highest body forces, as shown in Fig. 4.16, which in turn produces a high rate of momentum change along the stream-wise direction through the turbine. However, a high rate of momentum

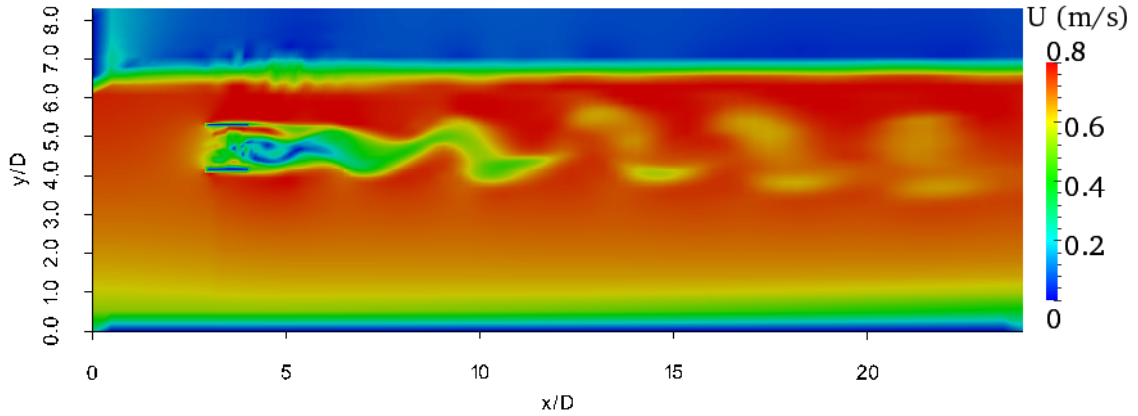

(a) Vertical plane

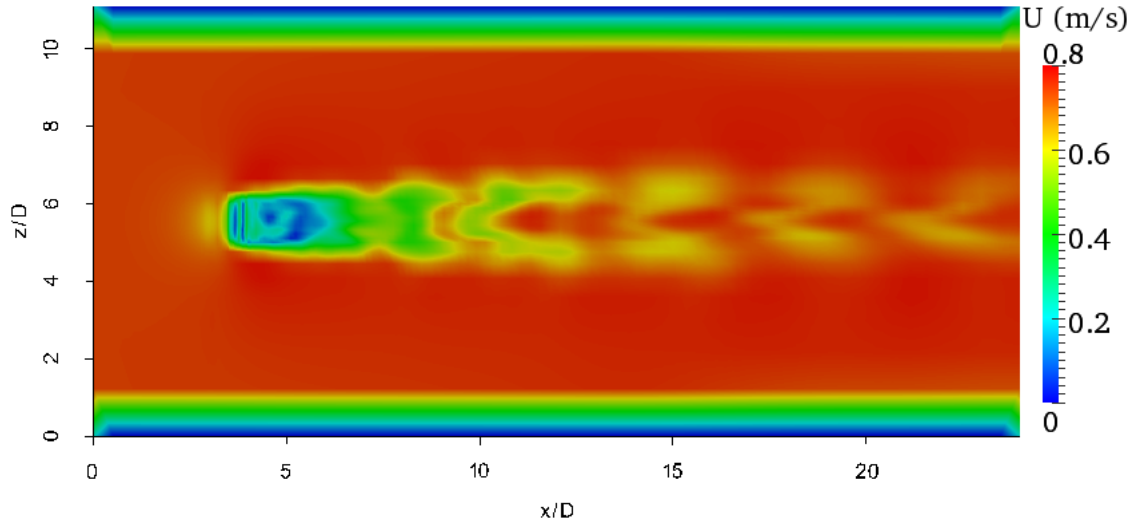

(b) Horizontal plane

Figure 4.15: Velocity contours at $F_b = 17.5N$

change does not necessarily mean an increased useful power extraction because of the cubic relationship between the power extracted and the stream flow rate. The other significant effect which modifies the above argument is that as long as the body force increases, there is a high velocity deficit immediately downstream of the turbine because it tends to act as a solid body, but this does not necessarily mean a high useful energy extraction from the stream flow.

The effect of the three body force loadings on the pressure drop across the turbine was examined and the horizontal pressure profiles are shown in Fig. 4.17. High force density is expected to inflict a massive pressure drop across the turbine and the results shown both in the instantaneous and time averaged pressure profiles proved this philosophy. The difference is only observed across the turbine region, but the pressure profile on the rest of

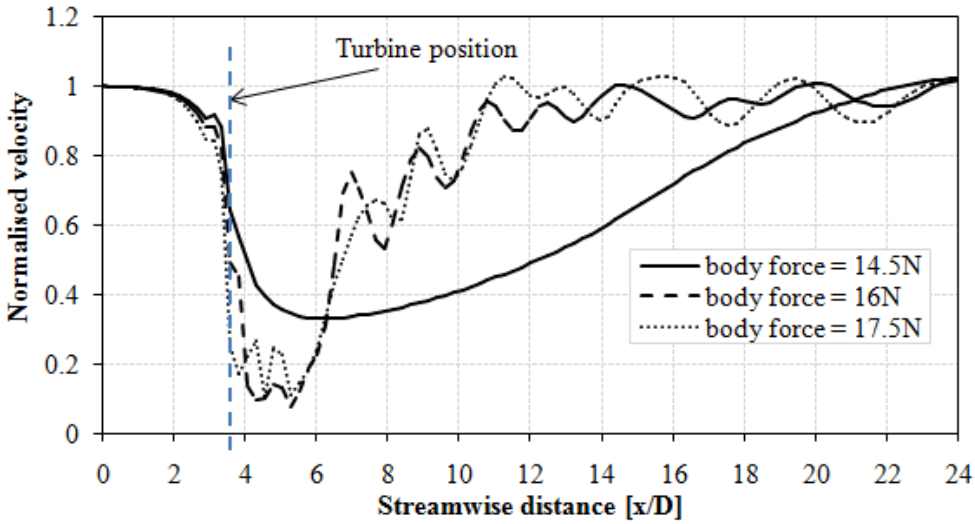

(a) Instantaneous velocity profile

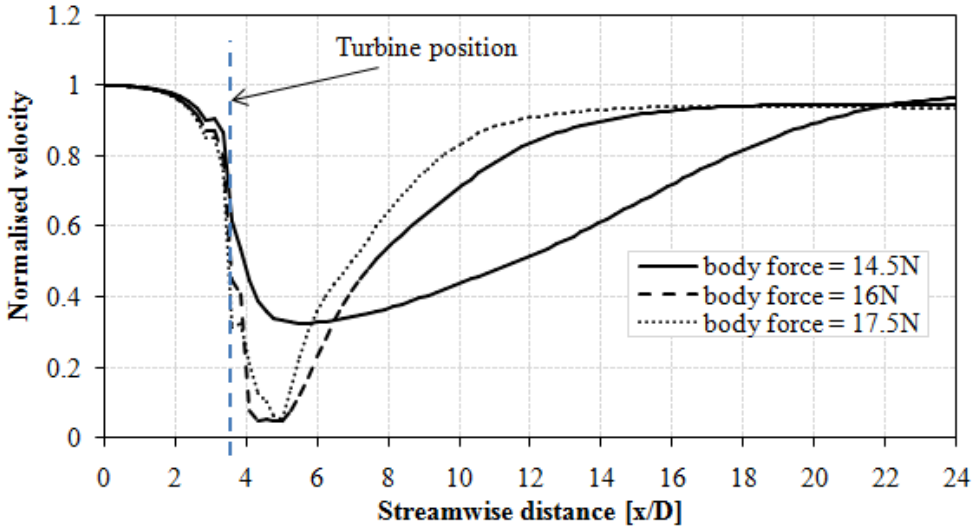

(b) Time averaged velocity profile

Figure 4.16: Stream-wise velocity profile along the centreline of the turbine for different force loading

the domain showed similar values especially in the time averaged velocity profile.

4.3.2.4 Ambient turbulence intensity

Turbulence kinetic energy is a fundamental flow property that must be calculated in order to model the fluid turbulence, and it depends on the assumption made about the inlet ambient turbulence intensity. This assumption will have an important effect on the simulation results, because experience and knowledge of the level of turbulence expected from the application is needed. A study by MacLeod et al. [2002] shows that the wake recovers

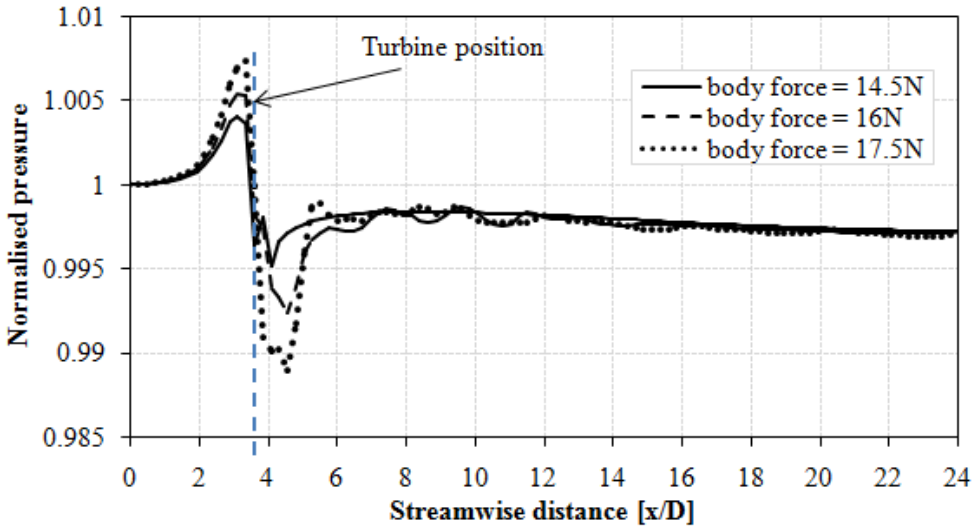

(a) Instantaneous pressure profile

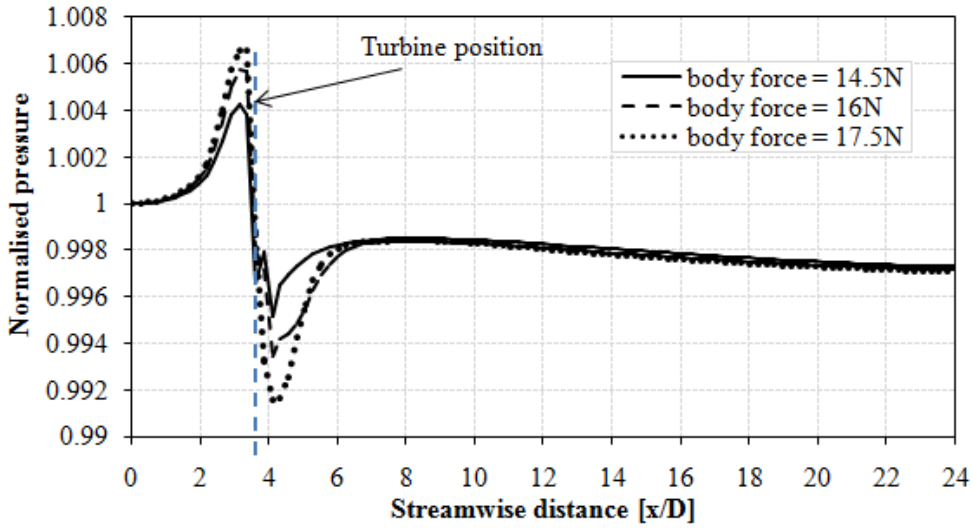

(b) Time averaged pressure profile

Figure 4.17: Stream-wise pressure profile along the centreline of the turbine for different force loading

faster as the inlet ambient turbulence intensity increases and it is important to investigate this influence in the MRL turbine simulations. Inlet values of 5% and 15% turbulence intensities were assumed to make the analysis. Fig. 4.18 shows a velocity contour of the simulated results with the two turbulence intensities. The results from the high turbulence appears to have fast vortex shedding. The flow is also disturbed in the air body above the turbine region in the case of the high turbulence intensity. Apart from these differences, the rest of the flow characteristics are more or less similar for both cases.

Fig. 4.19 shows the instantaneous and time averaged horizontal velocity profiles

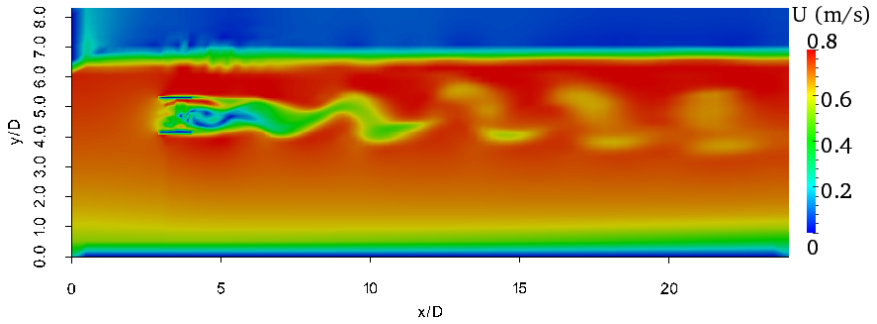

(a) 5% turbulence intensity vertical plane

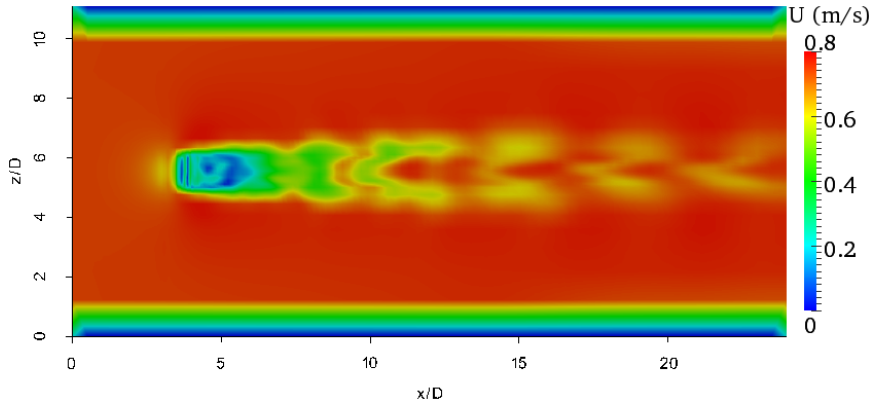

(b) 5% turbulence intensity horizontal plane

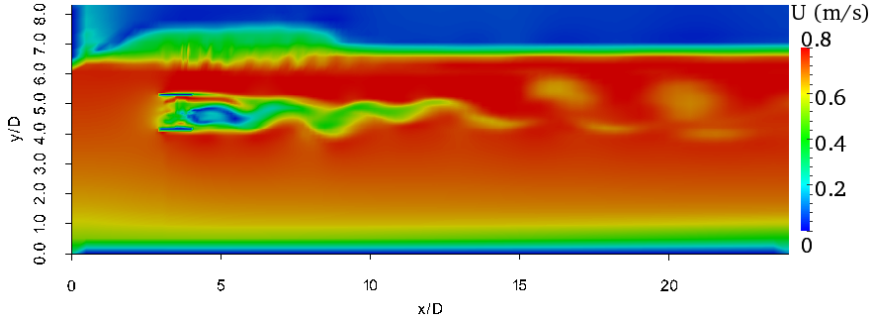

(c) 15% turbulence intensity vertical plane

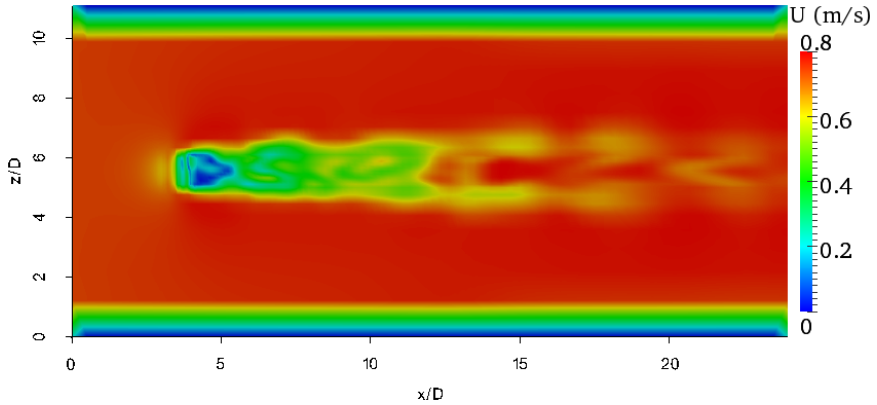

(d) 15% turbulence intensity horizontal plane

Figure 4.18: Velocity contours along the central line of the turbine

simulated using both turbulence intensities. The profiles showed a small difference in Fig. 4.19a but that profile shows an instant velocity value, where the regions which show velocity fluctuations can be easily identified. However, using the time averaged velocity profile the actual picture of the wake recovery can be obtained and looking on Fig. 4.19b, the wake recovery between 5D and 12D is almost similar. However, the result from the high turbulence intensity showed faster wake recovery from 12D onwards which is similar to the study carried out by MacLeod et al. [2002].

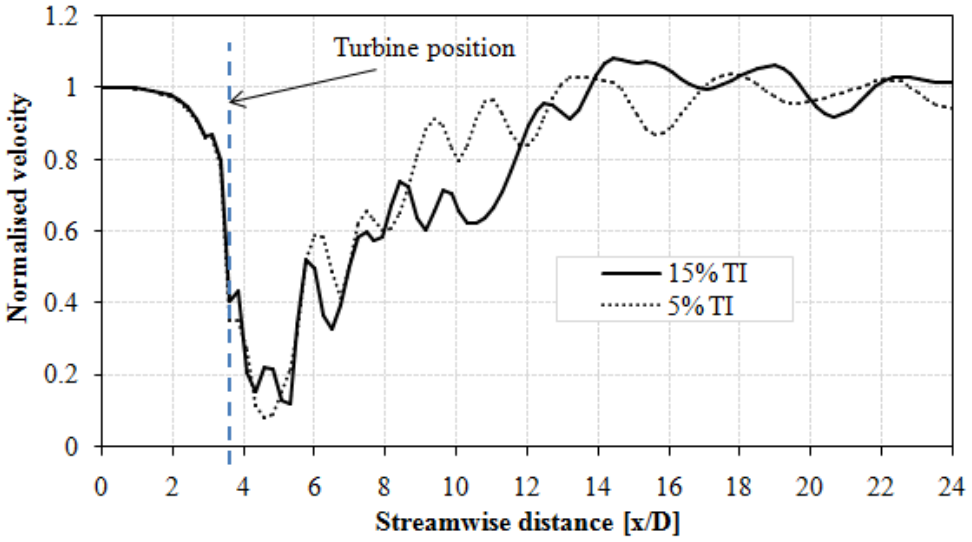

(a) Instantaneous velocity

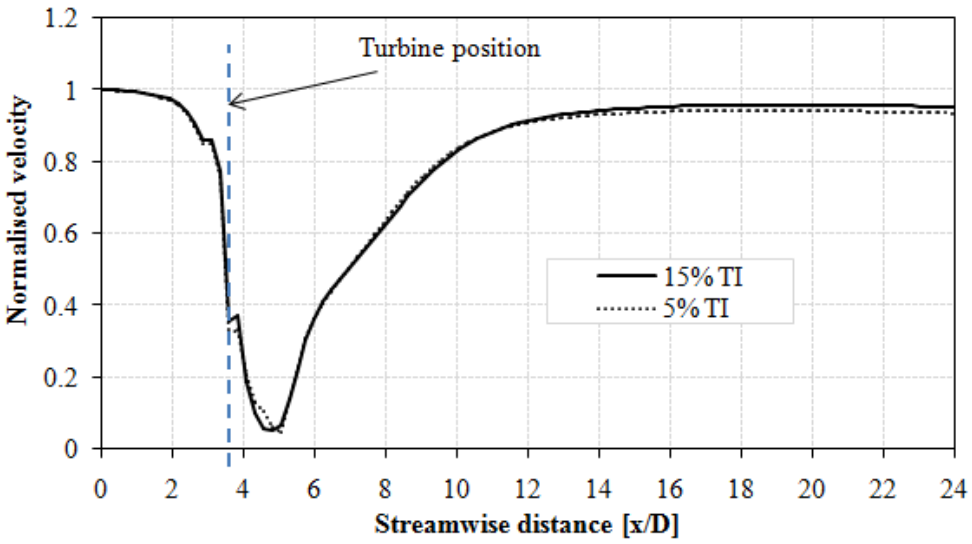

(b) Time averaged velocity

Figure 4.19: Stream-wise velocity deficit along the central line of the turbine

Unlike the velocity profiles, the pressure profiles showed a big difference between

the two turbulence intensities as shown in Fig. 4.20. The simulation results from the lower turbulence intensity showed large pressure drop across the turbine and the result is consistent in both the instantaneous and time averaged pressure profiles. Moreover, the result with the lower turbulence intensity (5%) showed high pressure values throughout the computational domain.

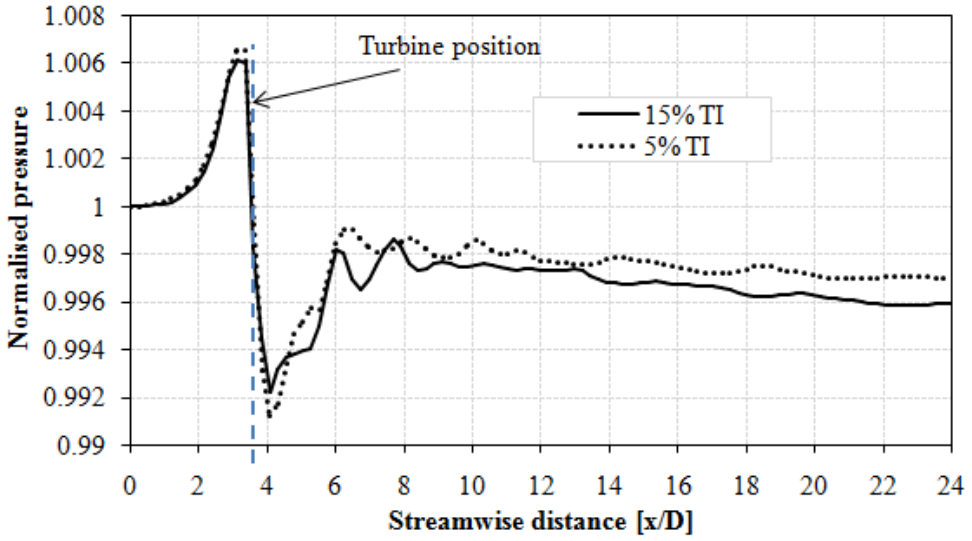

(a) Instantaneous velocity

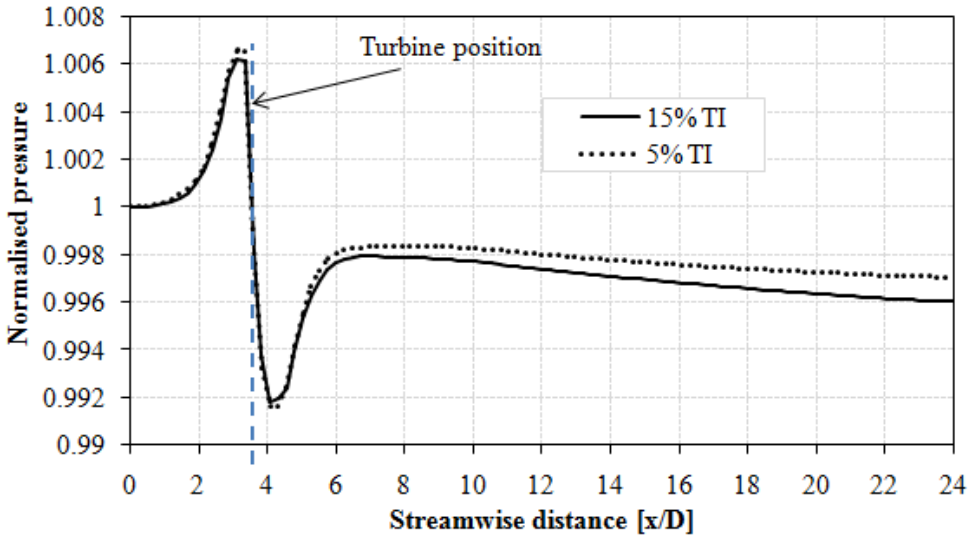

(b) Time averaged velocity

Figure 4.20: Stream-wise pressure deficit along the central line of the turbine

4.3.3 Turbine Designs With and Without Side Plates

A CFD simulation was carried out in Chapter 3 to calculate the energy extraction using the MRL tidal turbine designed with and without side plates. The results showed that the design with side plates has removed higher power from the stream flow. However, it is also important to understand the flow characteristics of these two designs in order to obtain a complete understanding of the differences, using all the necessary parameters.

Fig. 4.21 shows the vertical and horizontal plane views of the velocity contours simulated with the two designs. The results showed that the design with side plates generated large scale vortices downstream of the turbine (Fig. 4.21a). In contrast, the velocity contours shown in Fig. 4.21c indicates a different flow features and generated small scale vortices. When the real turbine is in operation, large scale vortices would be expected due to the effect of the blade rotation and the MRL design with side plates is showing a similar flow feature, which makes it a better choice for further development although a detailed experimental data is required for validation.

Vertical velocity profiles were extracted from different sections in order to understand the wake recovery, as shown in Figs. 4.22 and 4.23. The results showed that the profiles are similar upstream of the turbine (Figs. 4.22a and Fig.4.23a) using both the instantaneous and time averaged velocity profiles, which is normally expected as the flow is more or less undisturbed by the turbine. At the centre of the turbine (Fig. 4.22b and 4.23b), the velocity profiles show almost similar evolution except a small spike from the design without side plates at the height of 5.2D.

However, the velocity profiles show a large difference downstream of the turbine which is a direct reflection of the difference discussed in the velocity contours in Fig. 4.21. At every section downstream of the turbine, the velocity value from the turbine without side plates was lower, which can be seen from the samples taken at 5D and 20D in both the instantaneous and time averaged velocity profiles. Interestingly, both the instantaneous and time averaged velocities show consistent evolutions of velocity profiles from both turbine designs except at 20D where the time averaged velocity is higher for the design without plate for unknown reason as it was expected to show lower velocity profile based on the

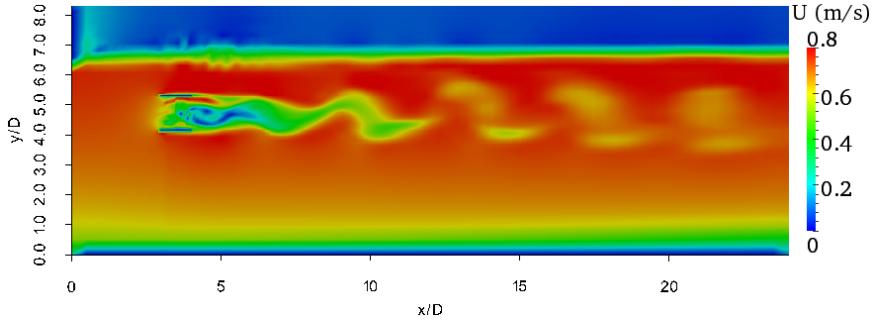

(a) With plate vertical plane

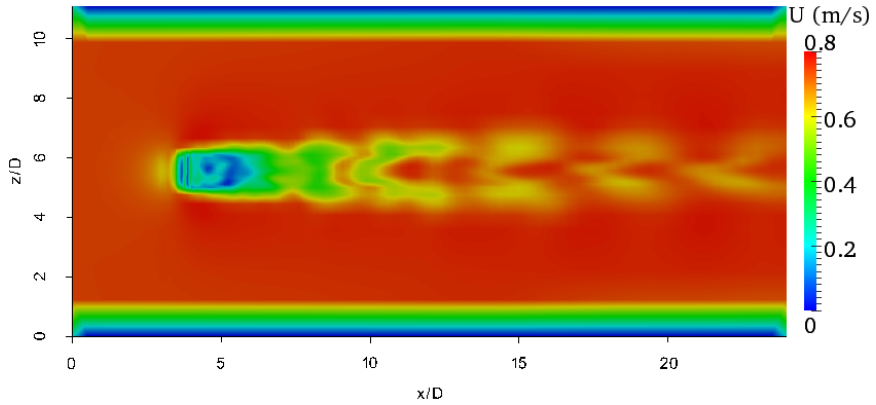

(b) With plate horizontal plane

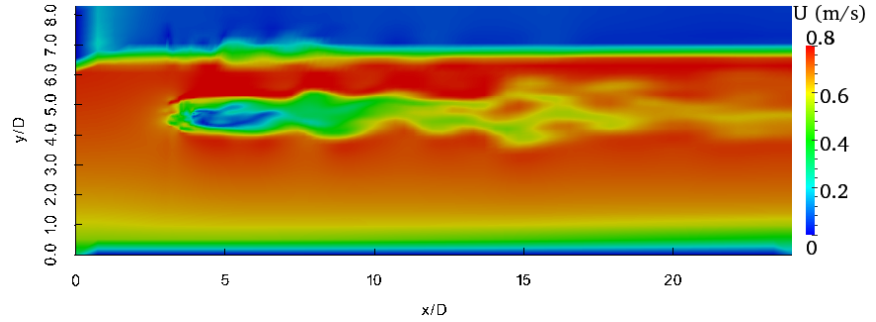

(c) Without plate vertical plane

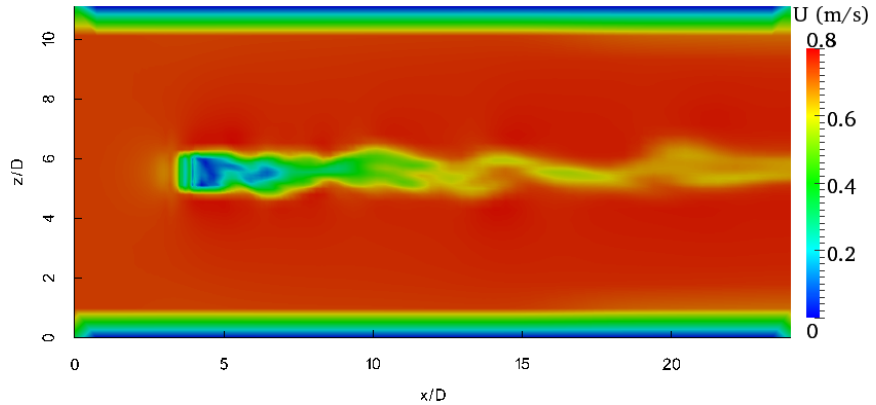

(d) Without plate horizontal plane

Figure 4.21: Velocity contours with and without side plate

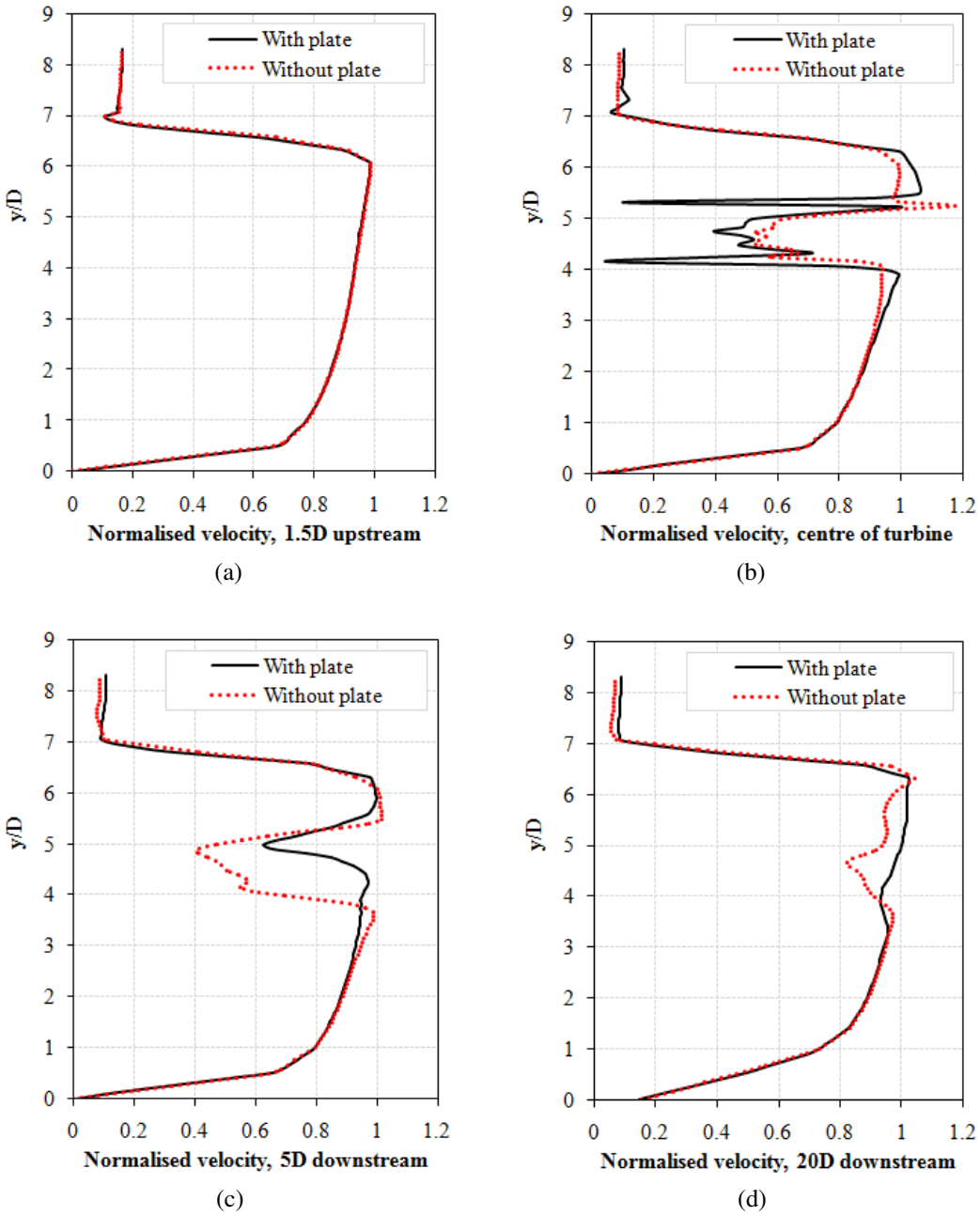

Figure 4.22: Instantaneous vertical velocity profiles with and without side plates

velocity contours shown in Fig. 4.21.

The difference between the two designs was more visible in the horizontal velocity profiles extracted along the centreline of the turbine in the stream-wise direction. The wake quickly recovers in the case of the turbine with side plates as shown in Fig. 4.24. The fact that the wake recovers faster in the case of the turbine with side plates has a significant implication on the study of turbine to turbine interactions. A faster wake recovery means less energy shadowing between devices in a tidal stream farm, which could significantly

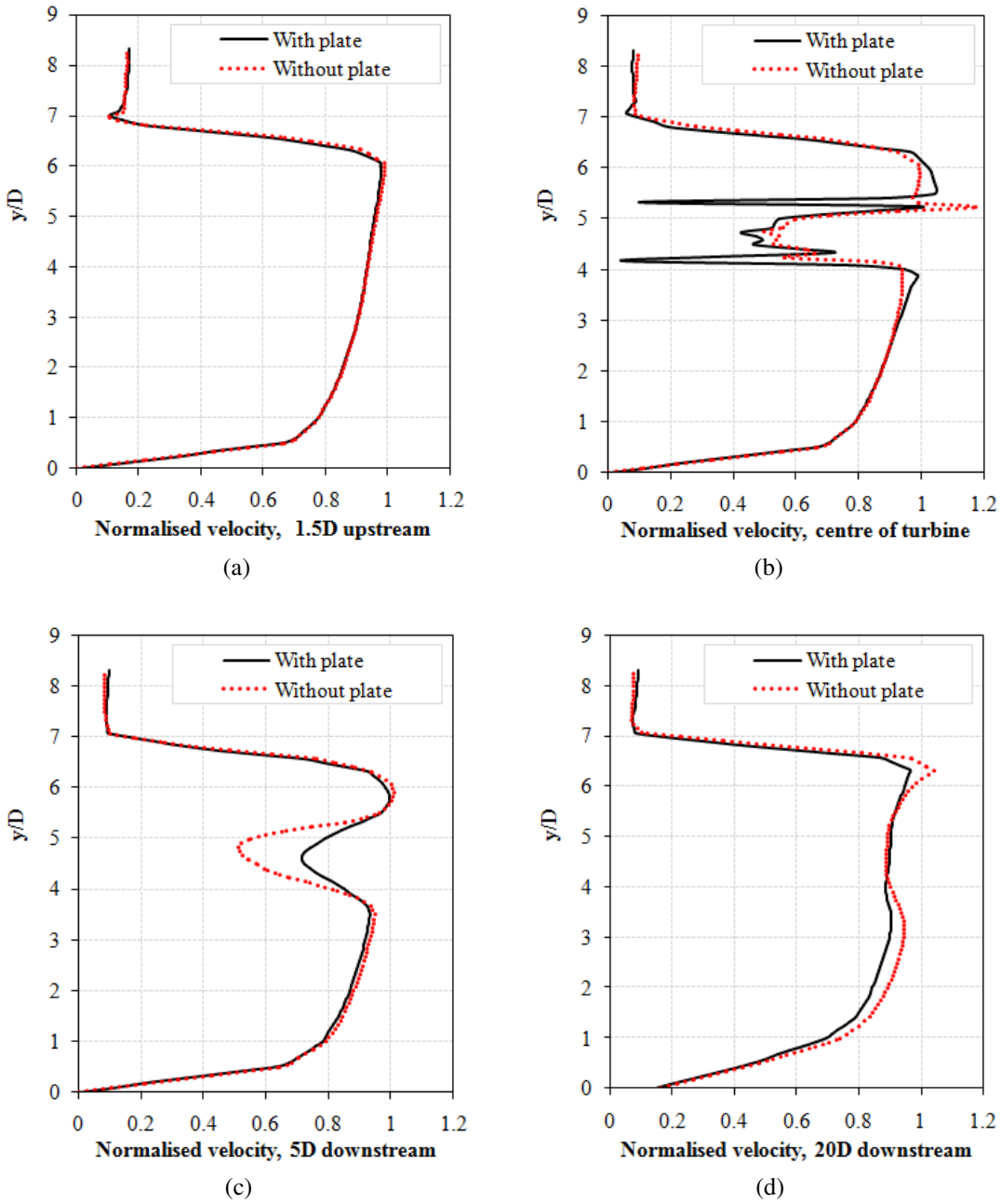

Figure 4.23: Time averaged vertical velocity profiles with and without side plates

reduce the spacing required between turbines. This in turn improves the efficiency of individual devices and boosts the overall power output of the farm. Therefore, having faster wake recovery is always preferable in the design of a tidal stream farm, though it needs a validation against experimental data to make sure that the wake recovery from the CFD simulations is not overestimated in order to minimise the risk of deviating from the reality.

Observation of the streamlines can provide some information on the way the body force

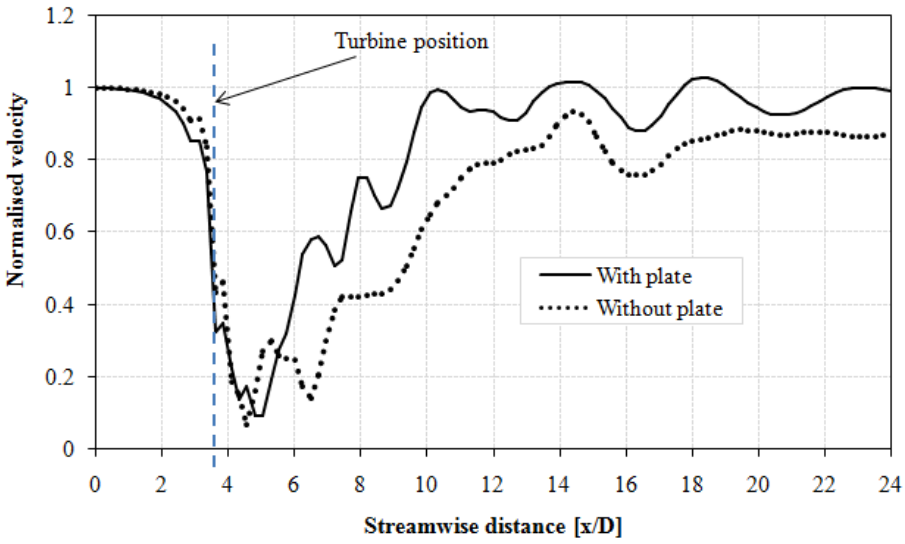

(a) Instantaneous velocity

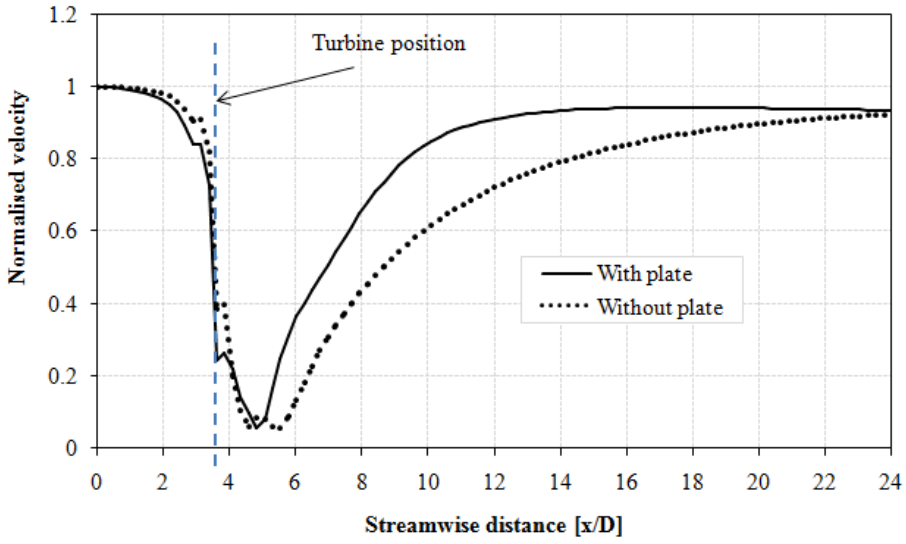

(b) Time averaged velocity

Figure 4.24: Comparison of centreline horizontal velocity profiles of the turbine with and without side plates

affects the flow features within and downstream of the turbine. The streamlines shown in Fig. 4.25 demonstrate a clear distinction of local wake expansion for the two designs. The wake expansion produced using the turbine with side plates (Fig. 4.25a) quickly converged downstream of the device, which is another proof of the faster wake recovery discussed before for this design. However, the local wake expansion from the turbine without side plates was sustained further downstream as shown in Fig. 4.25b.

The vectors shown in Fig. 4.26 represent velocity directions within and around the turbine region. The information from this vector representation can prove the theory of the

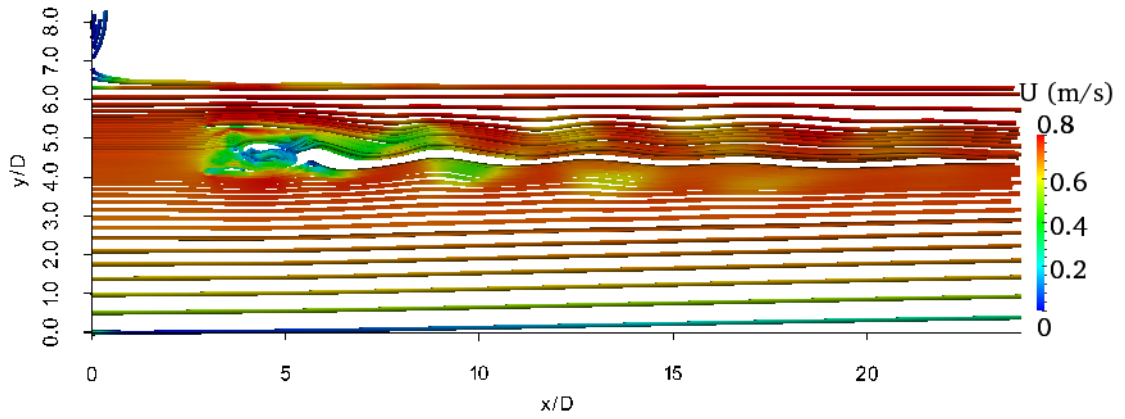

(a) With plate

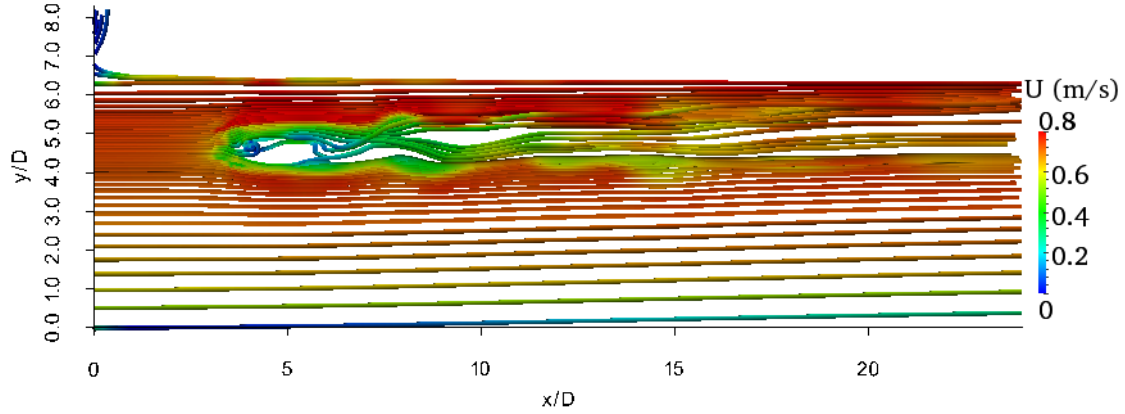

(b) Without plate

Figure 4.25: Contours of streamlines

wake recovery process. The vectors immediately downstream of the turbine are weaker in the case of turbine without side plates (Fig.4.26b) and is sustained further downstream creating free space compared to the turbine with side plates (Fig. 4.26a). This is a sign of the wake recovery differences between the two designs which proves that the turbine with side plates still has faster wake recovery. Therefore, it can be concluded that the velocity contours, velocity profiles, the streamlines and the velocity vector analysis all showed similar results and, therefore, this is an indication that the turbine with side plates is the best option for further development.

4.3.4 Free Surface Deformation

The MRL turbine is designed to operate relatively close to the water surface and it is important to investigate the dynamics of the free surface at different positions of the turbine across the depth of the water. The analysis was carried out in two stages. The first stage

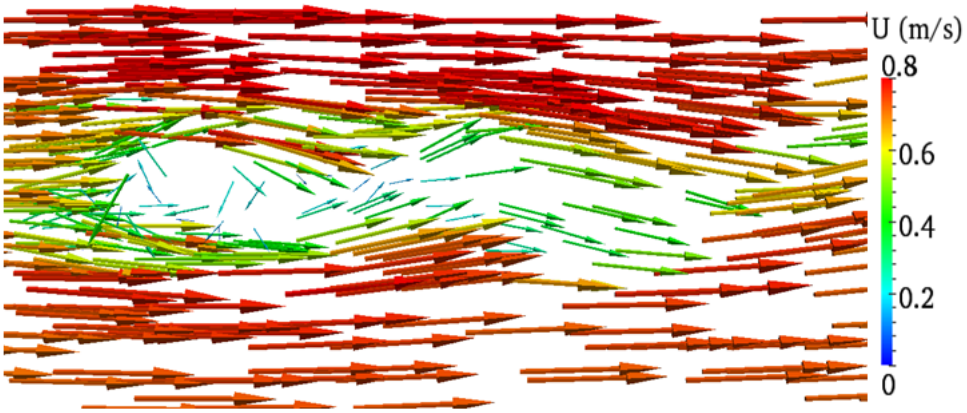

(a) With side plate

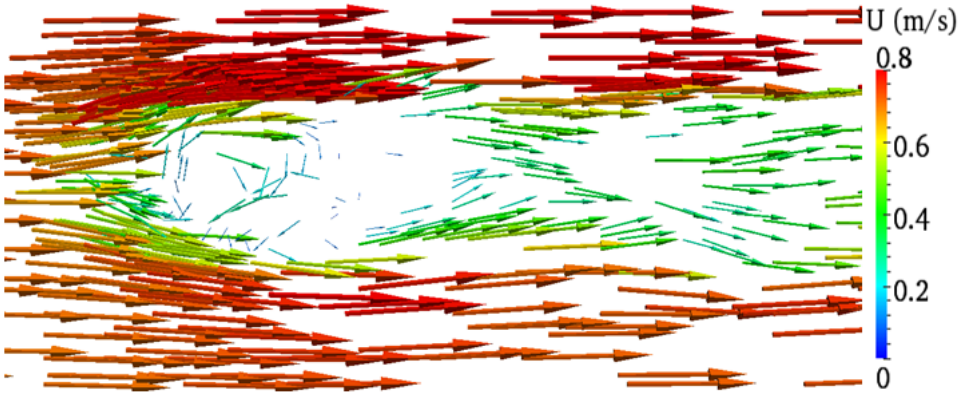

(b) Without side plate

Figure 4.26: Velocity vectors

compares the effect of using the two MRL designs (with and without side plates) on the dynamics of the free surface. In the second stage, it examines the effect of the turbine with side plates on the dynamics of the free surface considering three turbine positions (0.25D, 1D, and 2D) relative to the free surface.

Uniform inlet velocity profile across the domain was implemented to obtain constant kinetic energy in order to minimise its impact on the comparison of different turbine positions across the depth of the channel. Otherwise, if the power law velocity profile is used, the variation of kinetic energy available throughout the depth of the domain would have its own effect on the results, making it difficult to compare the effect of energy extraction by the turbine on the dynamics of the free surface.

4.3.4.1 Comparison of the surface deformation by the two designs

The two designs simulated at a depth of 0.25D showed noticeable variation of surface deformation, though its magnitude is not clear from the snapshots of the phase shown in Fig. 4.27.

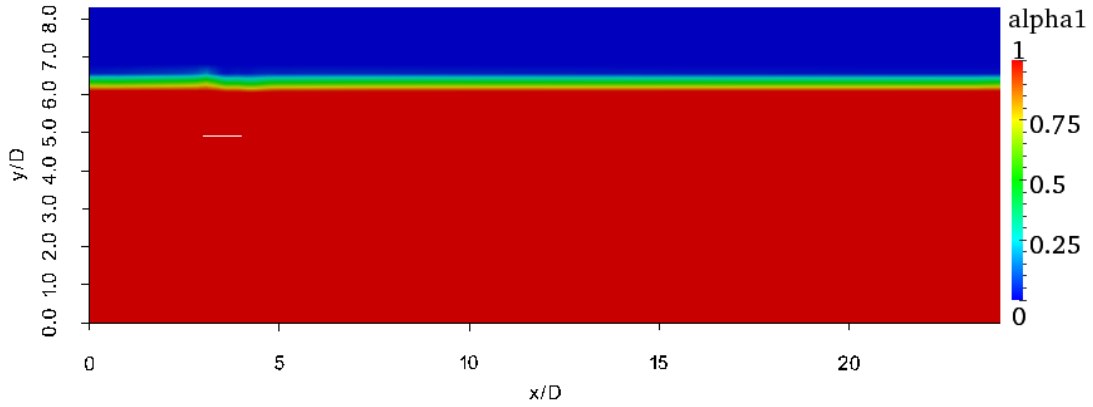

(a) With plate at 0.25D

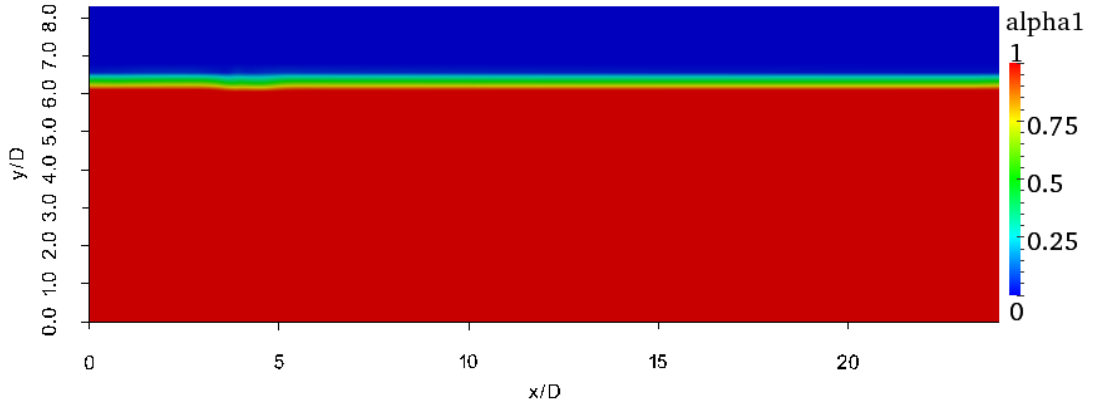

(b) Without plate at 0.25D

Figure 4.27: Snapshots of the phase showing the free surface deformation for the two designs

To obtain a clear picture of the magnitude of the surface deformation, a phase fraction plot was extracted from the two designs as shown in Fig. 4.28. The phase fraction at the interface showed an increased head upstream of the turbine compared to the initial water head and drops immediately above the turbine and recovers further downstream to its original head as shown in Fig. 4.28. This finding is in line with the investigations carried out using CFD by Sun et al. [2008] and experiments by Myers and Bahaj [2007] to understand the effect of energy extraction on the free surface. The laboratory work with a small size horizontal axis turbine of 40cm in diameter proves that if the flow is sub-critical, then there is a free surface deformation immediately downstream of the device with the

CFD simulation confirming similar findings.

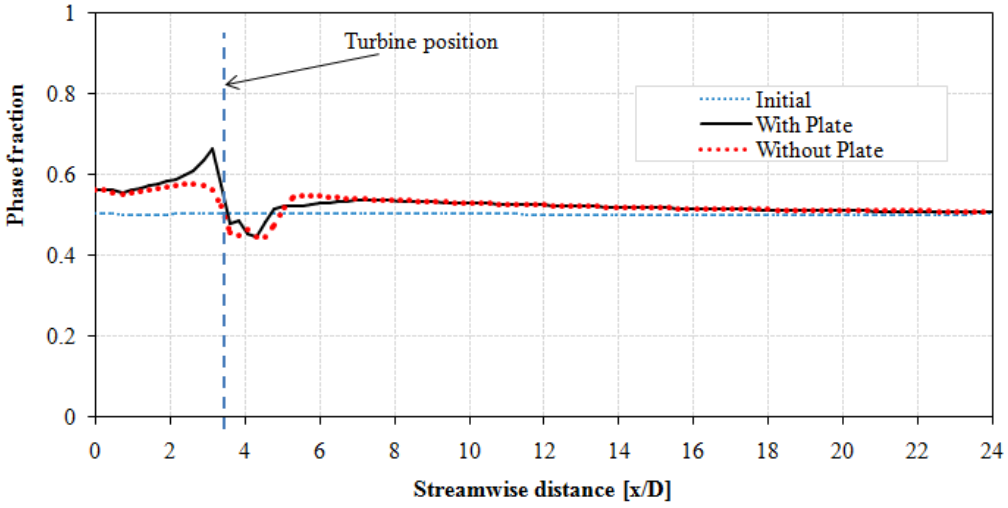

Figure 4.28: Comparison of free surface deformation for the two designs at 0.25D

However, comparing the phase fraction for the two designs shows different profiles. The head of water showed a higher value as the water approaches the turbine in the case of the design with side plates. One of reasons is that the water flow direction reverses due to the plates, which increases the blockage effect compared to the design without side plates. The additional thrust force applied by the presence of the side plates may also contribute to an increased head upstream of the turbine. On the other hand, the phase fraction showed a higher head immediately downstream of the turbine for the design without side plates because the water has the chance to flow upwards at 90^o, which creates a high local wake expansion that contributes to the increase of the head.

Several parameters related to the two MRL designs have been discussed so far, such as the efficiency, the flow characteristics, and surface deformation. The results obtained from the comparison of the two designs can be summarised as follows:

1. The efficiency of the design with side plates is better than the design without side plates as proved in chapter 3.

2. The simulation results showed that the wake recovers faster in the case of the turbine with side plates.

3. The design without side plates showed a high impact on the dynamics of the free

surface, which may have dire environmental consequences such as flooding, due to a tidal stream farm using large scale turbines.

Therefore, it is clear that the design with side plates has a lot of advantages and is the best option for further development of the turbine. Thus, the rest of the study in this chapter and other chapters will focus on the turbine with side plates.

4.3.4.2 Comparison of the surface deformation at different turbine positions relative to the free surface

The snapshots of the phases simulated with the turbine at three depth positions indicate different surface deformation as shown in Fig. 4.29. The impact of the turbine reduced as the turbine moved deeper towards the floor. However, it is always important to keep the device well above the floor to avoid the effect of the interaction of the floor wall boundary and the flow rate, which in turn affects the performance of the turbine.

The impact of the turbine on the dynamics of the free surface shown in Fig. 4.29 can be clearly visualised using the phase fraction at the interface of the two phases. As the turbine moves closer to the free surface (0.25D), that turbine has more influence on the free surface deformation and drops larger than the turbines deeper in the domain (1D and 2D) as shown in Fig. 4.30. The other differences observed from the phase fraction graph is that the turbine closer to the free surface has more blockage effect resulting a bigger head increase upstream of the turbine, while the turbine deeper on the domain (2D) shows less upstream head elevation.

4.3.5 Velocity Deficit at Different Cross-Sections

The discussions in the previous sections have been focused on the comparisons of two types of MRL design, sensitivity analysis and other related issues based on the differences in the flow characteristics. In this section, the wake recovery of the turbine, which has been selected for further development, was investigated. This was examined by comparing the vertical velocity profiles at the inlet and different sections of the domain. The vertical and horizontal planes of the velocity contours, which have been discussed in different

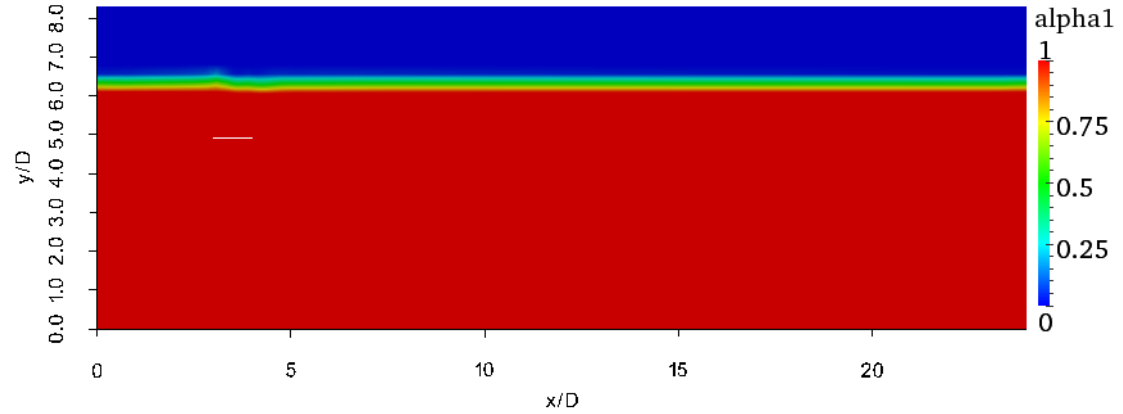

(a) Turbine position at 0.25D

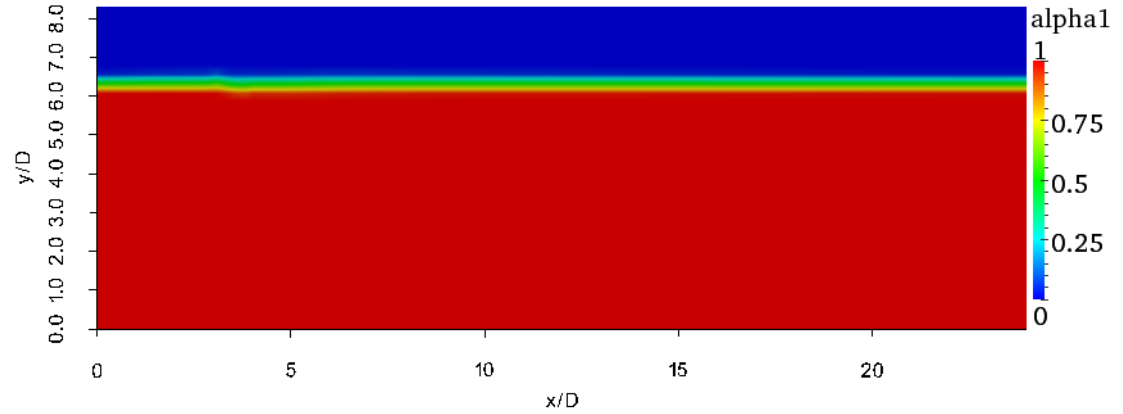

(b) Turbine position at 1D

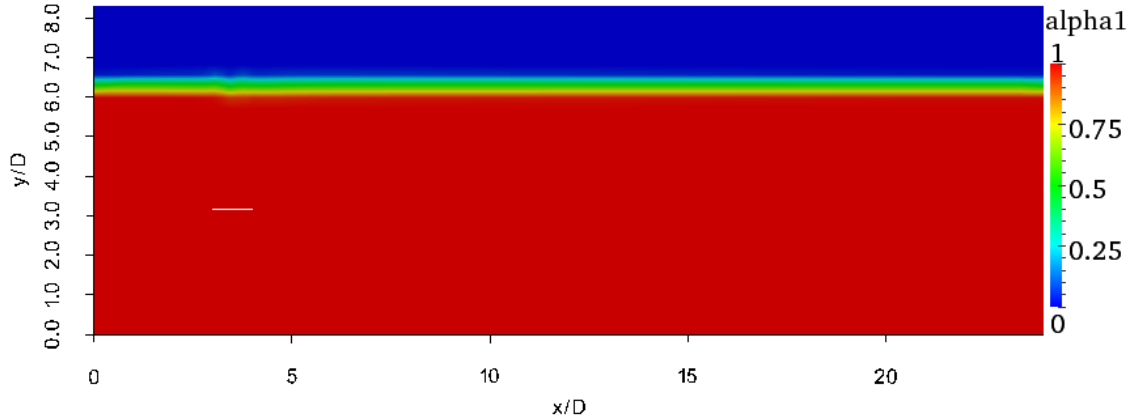

(c) Turbine position at 2D

Figure 4.29: Snapshots of the phase for the turbine with side plates at three positions

occasions in the previous sections, are shown in Fig. 4.31.

The instantaneous and time averaged vertical velocity profiles shown in Figs. 4.32 and 4.33 were extracted from 6 different cross-sections and were compared with the vertical velocity profile at the inlet of the domain. The velocity profiles both in the form of instantaneous and time averaged values show similar trend, but the magnitude of their

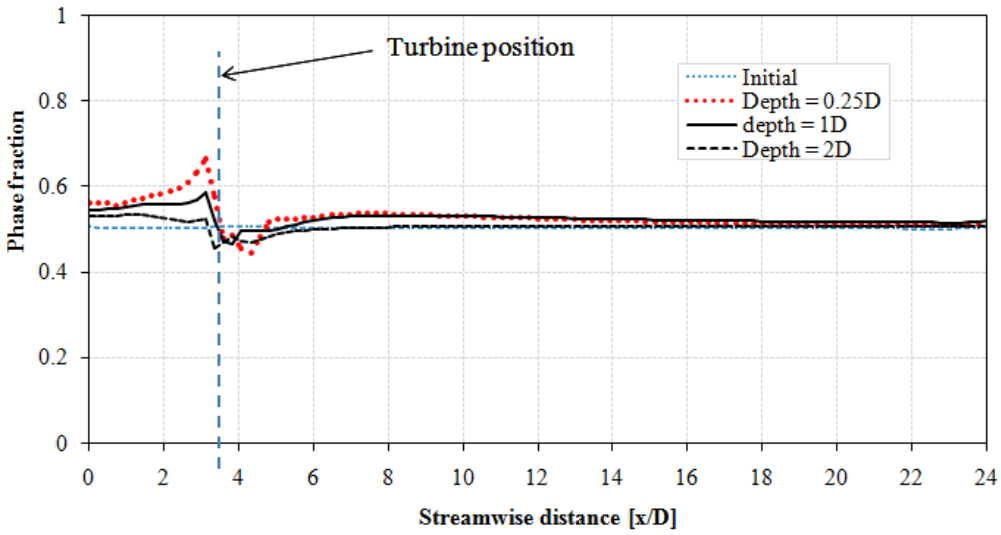

Figure 4.30: Comparison of free surface deformation at different depths

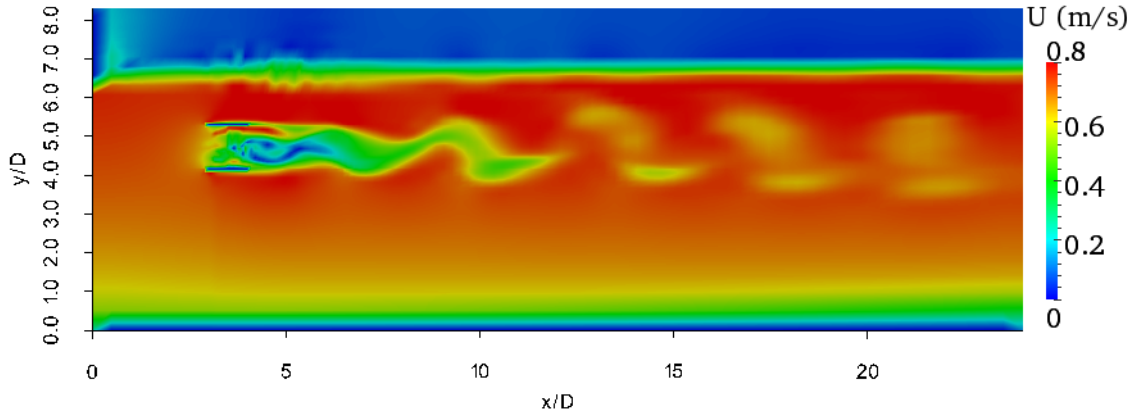

(a) Vertical plane

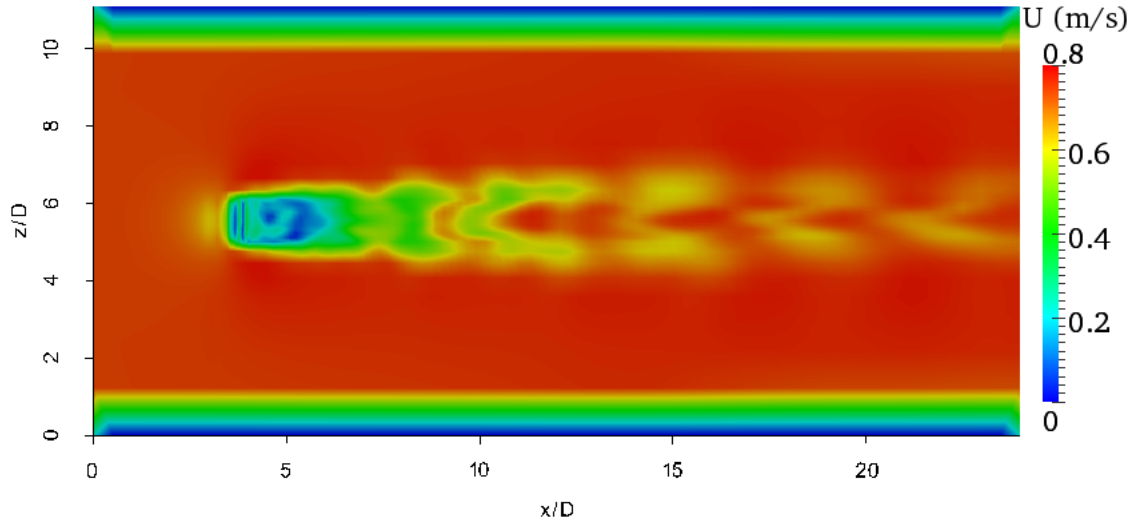

(b) Horizontal plane

Figure 4.31: Velocity contour of a single turbine sliced through the centre of the turbine both in vertical and horizontal planes

velocity deficit compared to the inlet velocity profile is different.

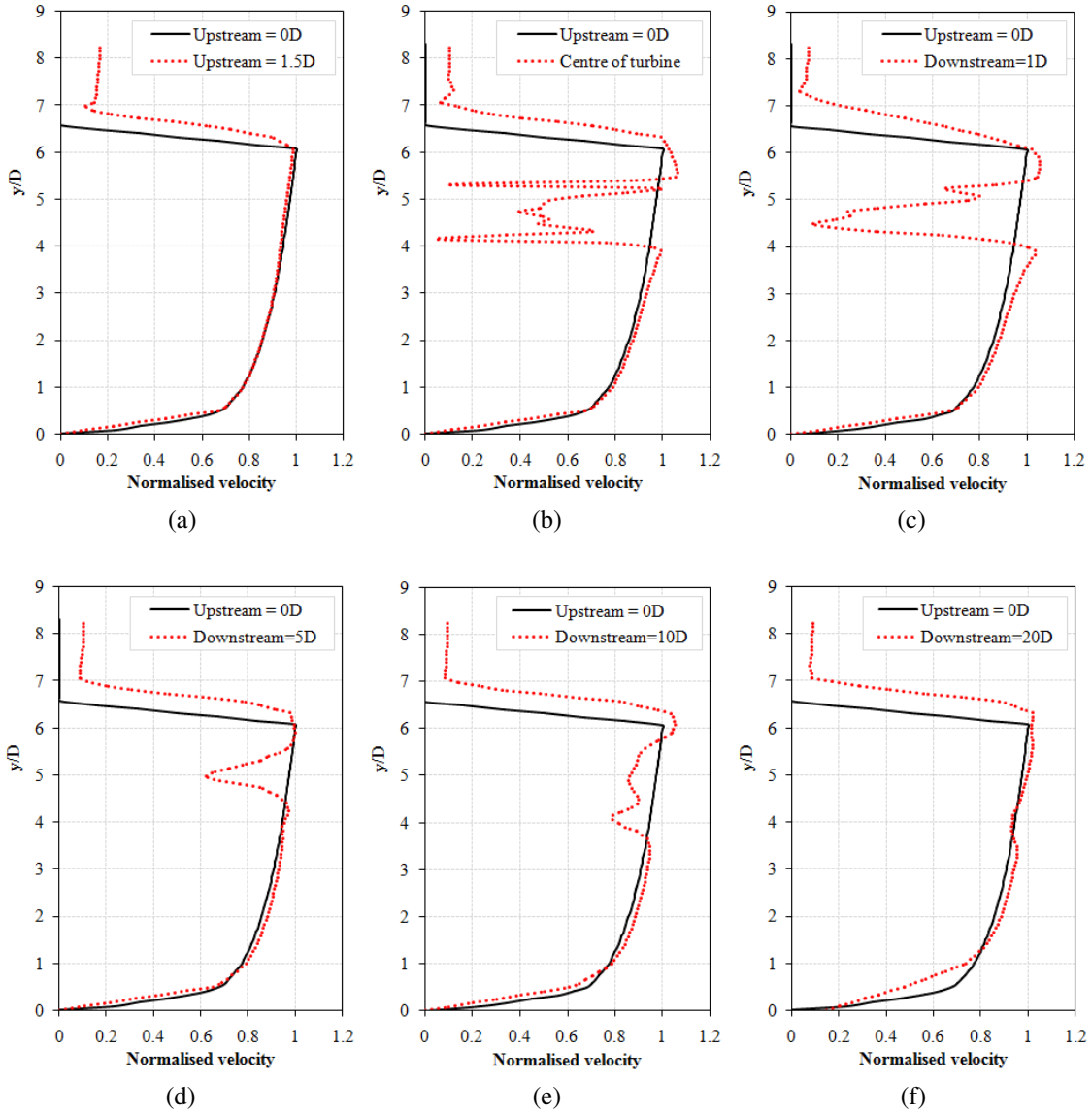

Figure 4.32: Instantaneous vertical velocity profiles at different sections of the velocity contours given in Fig. 4.31

The flow at the turbine region showed a massive velocity deficit and the flow is very complex, as expected due to the complexity of the drag and lift forces applied to the fluid. The high velocities observed within the turbine region are due to the venturi flow created through the bypass between the body forces, while the lower velocities are due to the blockage of the flow by the body forces as shown in Fig. 4.33b. There are also zero velocity values due to the presence of the side plates, where there is no fluid flow through them due to their solidity. As the fluid flows away from the turbine region towards the

end of the domain, the wake recovers slowly to its initial condition. At 10D (Fig. 4.33e) and 20D (Fig. 4.33f) downstream of the turbine, the flow recovers to 88% and 92% of its initial condition respectively. This shows an increase of 4% recovery as the downstream distance doubled, which is a very slow recovery. The wake recovers quickly in the region between 5D and 10D and is almost flat till the end of the domain (20D).

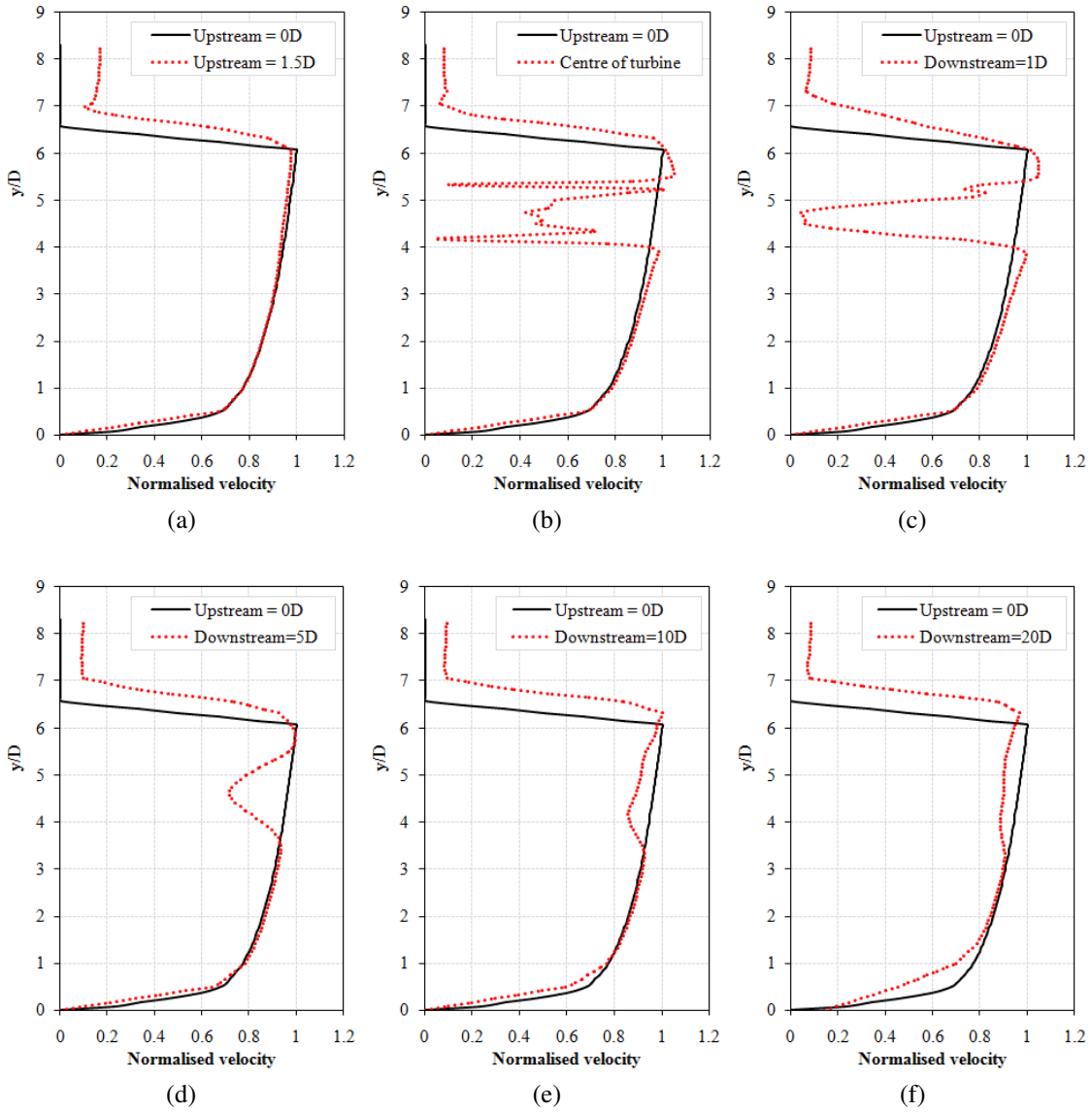

Figure 4.33: Time averaged vertical velocity profiles at different sections of the velocity contours given in Fig. 4.31

However, the information given about the wake recovery can not be the same for any simulation because it heavily depends on the loading of the turbine as discussed in section 4.3.2.3, but can be compared with a data obtained using same loading and gives

important information about the mixing length scale downstream of the turbine. There is no experimental data, to date, about the wake recovery of the MRL turbine that can be used for validation of the CFD model results, but this result should be helpful to compare with any experimental data that may be available in the future. The other observation from these results is that, the velocity profiles above 6D in the air body have no similar evolution compared to the base velocity profile (upstream = 0D) as shown in Figs. 4.32 and 4.33. The possible reason is that the air body may have been affected by the wave created at the sharp interface between the air and water as the water flows along the domain, which increases the velocity of the air body beyond the expected value.

4.4 Summary

Many of the studies on this chapter were focused on the flow characteristics of energy extraction by the MRL turbines. The flow features were used as a factor for comparison of two turbine designs and the quality of the two alternative IBF approaches. The analysis indicates that the *annular* approach showed faster wake recovery and produces large vortex structures downstream of the turbine compared to the *blade* method and is considered the best option to use for further numerical simulations.

The CFD model was also used to examine the flow characteristics of the two MRL turbine designs (with and without side plates), and the results simulated using the turbine with side plates showed the expected flow characteristics, with faster wake recovery and high performance, making it a better option for further large scale development. It shows a wake recovery of around 92% of the stream flow at 20D downstream of the turbine. In addition, the influence of energy extraction by the turbine to the dynamics of the free surface was investigated by simulating the turbine at three different turbine positions. The result showed that the turbine close to the free surface has a massive impact on the surface deformation and showed large head drop immediately downstream of the turbine compared with the same turbine simulated at a deeper position.

The CFD model also successfully examines the sensitivity of flow characteristics within and around the turbine to the change of force loading, geometry width, mesh grid size, and

turbulence intensity. These results proved the capability of the developed IBF model in analysing several issues relating to this design of tidal turbine.

Chapter 5

INVESTIGATING THE WAKE INTERACTION OF MULTI-TIDAL TURBINES

5.1 Introduction

The study of turbine to turbine interaction is crucial to understand how energy shadowing of an array of devices influences energy extraction by the individual devices. The turbine to turbine interaction can be investigated using small scale experiments but the feasibility of experimental studies with several devices in a tidal stream farm is challenging due to the high investment required to cover the associated expenses. Consequently, researchers are focusing on exploring alternative methods to investigate the flow features around tidal turbines and computational fluid mechanics (CFD) software packages are currently the best options available to utilize for these kinds of studies.

The aim of this study is therefore to demonstrate the capability of the new CFD based IBF model in investigating turbine to turbine interactions. The investigation has been conducted in two stages. The first stage examined the performance and wake characteristics of a single turbine, which was considered as a base case for the analysis of turbine to turbine interaction in tidal stream farm. In the second stage, a small tidal stream farm model containing three, two, and seven turbines, where one of the devices was taken to be the base case, were developed. The influence of the additional turbines on the performance of the base case was then investigated. In addition, a different lateral and longitudinal inter-turbine spacing was used to examine its influence on the base case relative to an initially assumed spacing.

The details of the simulation results of the turbine to turbine interaction will be described in several sections in this Chapter . In section 5.3 the computational domain set up and the detail turbine configurations are described. Investigation of the performance and wake characteristics of a single turbine is presented in section 5.4. The comparison of

the influence of turbine to turbine interaction of a farm containing three, two and seven turbines relative to the performance of a base case and on individual turbines are given in sections 5.5, 5.6, 5.7 respectively. Finally, a summary is given in section 5.9.

5.2 Related Studies

The study of wake interactions of wind turbines using both analytical and CFD techniques is well documented as this technology has been in the forefront for many years [Calaf et al., 2010, Méchali et al., 2006, Barthelmie et al., 2006, Schlez et al., 2001, Barthelmie et al., 2007, 2009, Rathmann et al., 2007, Barthelmie et al., 2004, Ainslie, 1988, Troldborg et al., 2011]. Recently there have been different efforts to investigate the wake interactions of turbines in tidal stream farms where the knowledge acquired from the study of wind technology is often utilised with the appreciation of the fundamental differences of the working environments of the two technologies. The methodologies used in wind technologies are often adjusted and modified in order to employ in the study of tidal turbines. The computational cost always comes in to play when CFD techniques are used to study the flow features of turbines and this depends on the type of problems to be solved. For a single turbine simulations either in wind or tidal turbines, it could be possible to employ more detailed modelling techniques as the computational demand is manageable with the current computational resources. As the number of devices increases, such as the study of arrays of devices, the computational cost significantly increases.

Thus most researchers employ moderate cost techniques such as the actuator disc method to investigate the wake interactions in arrays of turbines. Harrison et al. [2010a] used a blade element and actuator disc method to study the wake interaction of a tidal stream farm with 5 rows of turbines configured in the streamwise direction. This study showed that the power coefficient of the second row was lower than the rest of the devices due to huge wake interaction from the first row but the turbines from the third row onwards showed better power coefficients due to high wake recovery within the array. Those comparisons have been made based on a single resistance coefficient. Study of a staggered configuration of arrays of devices by Bai et al. [2009] and Batten and Bahaj [2006]showed

an acceleration of the bypass flows due to the venturi created by the turbines which is important to improve the performance of any downstream devices.

[Churchfield et al., 2011] has studied the wake propagations and power production by modelling the turbine using rotating actuator lines and they observed that a staggered configurations of turbines with a small longitudinal spacing offers high efficiency. Similarly, Myers et al. [2011] and Daly et al. [2011] have carried out experimental study of arrays of devices and they also showed that with a particular inter-turbine spacing there is a potential of accelerated flow regions which can be used for high power production by deploying turbines on those regions. Daly et al. [2011] particularly indicated that a flow acceleration of up to 14% can be achieved due to the presence of arrays of devices. The experimental work also gives an insight of less wake propagation downstream of single row of turbines if the lateral spacing is increased otherwise a laterally closely spaced turbines would produce a huge plug flow of slow water which can affect the performance of downstream devices. They have suggested that an off-set or staggered configuration would provide a better option and allows a longitudinally closely packed devices to be deployed with less wake interaction and possibly higher power extraction due to accelerated bypass flows.

Different configurations of devices were also studied by Jo et al. [2012b] using CFD and experiments and the results showed high influence of wake interaction on downstream devices if an appropriate longitudinal spacing between the rows is not used. Those studies indicate that there is a surge of interest to study the influence of turbine to turbine interactions of arrays of devices in order to optimize the power extraction by minimising any environmental impacts.

A direct comparison of the results from this study with the results from the literature might be difficult for the following reasons:

- The MRL turbine is a new design and there has not been any documented CFD work on this device as most of the previous CFD studies have focussed on the conventional tidal turbines such as the horizontal axis propeller devices.

- The flow features around the turbine are expected to be different to the propeller devices due to the fact that the MRL turbine has highly complex internal shear flows

and the IBF model is developed to generate similar flow features within the turbine region.

- Unlike most of the studies mentioned so far, a free surface is introduced in this study which is expected to have some effect compared to modelling the tidal turbine without free surface. It also impacts upon possible pitch resonances for pontoon supported turbines.

However, these studies could be used to compare the common issues such as the blockage effect, the acceleration of bypass flows etc.

In most of the studies mentioned above, the turbine is modelled using the actuator disc approach by which the thrust applied by the turbine against the flow is represented by a resistance coefficient, K_L, as discussed in Chapter 3 section 3.2. The actuator disc method is slightly modified in this study and the IBF model is used to represent the MRL tidal turbine for the reasons discussed in Chapter 2. As a result, it was challenging to employ the equations of the actuator disc method to calculate the performance of the MRL turbine because of the absence of the resistance coefficient. For this reason, the COLM approach has been used so far to calculate the thrust and power coefficients of a single MRL tidal turbine. However, it is difficult to calculate the performance of individual devices in a tidal stream farm using the COLM approach due to the complexity of the flow features involved especially to calculate the available power due to the pressure gradient along the streamtube. Thus the simplest and most appropriate way of solving this difficulty appears to be to formulate an empirical relationship between the resistance force, F_b, and the resistance coefficient, K_L , using the calculated thrust or power coefficients by the COLM approach. The turbines in this Chapter have been represented and simulated using the annular IBF model approach and the power coefficients calculated using this approach at different resistance forces presented in Chapter 3 section 3.4.5 were used to find the relationship between the two model parameters. Those power coefficients were used as known values and Eqn. (3.3) was used to calculate the value of the resistance coefficient, K_L , for each corresponding resistance force applied in the IBF model.

Fig. 5.1 shows the resistance coefficients plotted against the resistance forces. An

exponential fitting curve was used in the standard Excel to formulate the relationship between the two parameters and based on the fitting curve, the resistance coefficient can be defined as:

$$K_L = 0.48e^{0.187F_b} \tag{5.1}$$

For the single and upstream turbines in the tidal stream farm, the resistance force equivalent to the maximum power point in the single turbine simulations was applied. The resistance coefficient, $K_L = 1.304$, calculated from the maximum power point was directly used in the calculation of thrust and power coefficients of the upstream turbines so there was no need to use Eqn. (5.1).

Calibration of the energy extraction inevitably depends upon the inflow conditions. Given that the turbines interact with each other these inlet conditions are themselves unknown at the start of the calculation which makes it difficult to apply the correct resistance force to each of the downstream row of turbines. One possible way of solving this problem is to fix the power extracted by each turbine in advance and employ an iterative scheme to adapt the resistances until the scheme converges to a self consistent flow field although this has its own drawbacks as the power extracted from each turbines is unknown in advance. Even if the power extracted is known in advance, the iterative scheme requires several evaluations of the farm model to converge and is thus proportionately more expensive and is beyond the scope of this thesis. The best option at this stage is therefore to apply different resistance forces for each row of turbines. Thus the resistance force applied to the downstream turbines was successively reduced by 10% from the resistance force of the upstream turbine due to operating on the wake of upstream turbines. In such cases, Eqn. (5.1) was used to calculate the resistance coefficients, K_L , of these turbines. With the resistance coefficient known, it was possible to employ the rather simple equations (Eqns. (3.1), (3.3), (3.4), and (3.5)) of the actuator disc method discussed in Chapter 3 to calculate the performance of individual devices in the tidal stream farms. Note that a further verification might be necessary before using the above formulated relationship for using in perhaps large scale simulations. However, for this particular study there are no risks as the MRL turbines used are the same size throughout the investigations.

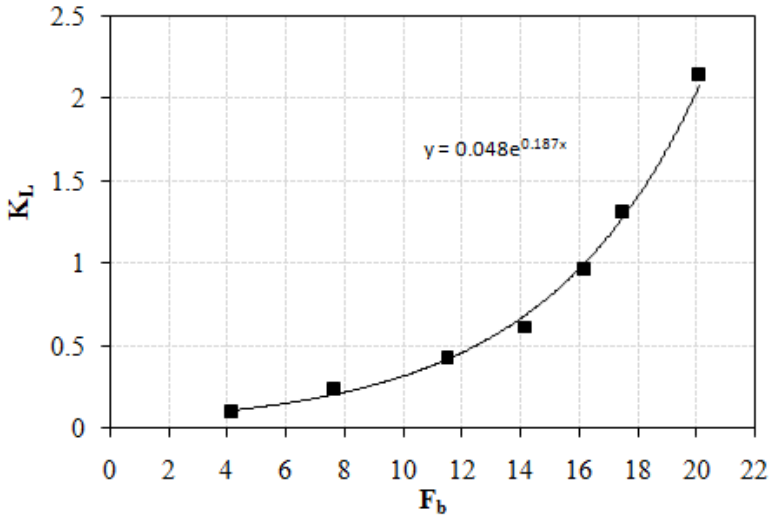

Figure 5.1: Exponential relationship between the resistance force and resistance coefficient

5.3 Computational Set-Up

The CFD simulations were performed using several turbine configurations. The computational domain used in the previous Chapters has been used while changing the dimensions to accommodate the number of turbines in the tidal stream farm. The boundary conditions described in Chapter 2 sections 2.9.1.2 and 2.7.3.1 were also used for all of the simulations carried out in this Chapter. There are four main turbine configurations containing one, two, three, and seven turbines and sub configurations with the change of inter-turbine longitudinal and lateral spacing to examine the effect of blockage on the performance of the base turbine and on individual turbines. The development of the configurations are discussed step by step in the next sub-sections. The turbines are represented as a line to show their layout on the tidal farm.

5.3.1 Base Turbine Computational Domain

Fig. 5.2 shows the computational domain of single turbine configuration in a a horizontal plane across the centre of turbine and has a blockage ratio of $B = 0.016$. This turbine is considered as the base turbine for the analysis of the rest of the configurations. The base turbine is labelled as 1 to distinguish from the rest of the turbines in all of the configurations described in the subsequent sections.

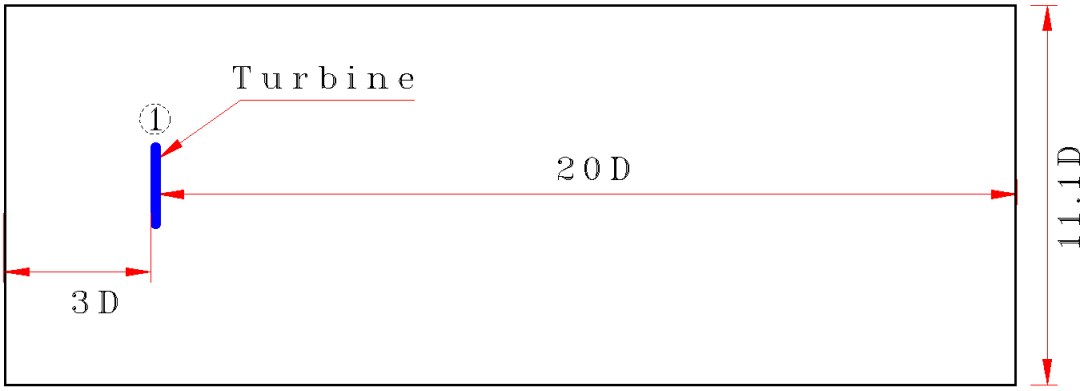

Figure 5.2: Single turbine configuration

5.3.2 Two Turbine Configuration

The development of a tidal stream farm starts in this section with the addition of a single upstream turbine (turbine 2) as shown in Fig. 5.3. Two configurations were used for the inter-turbine interaction analysis by changing the longitudinal spacing between the turbines denoted as Upstream Spacing (US) while keeping the Outlet Spacing (OS) constant at 20D as shown in table 5.1. The configuration numbers were given based on the number of MRL turbines in the farm. The first number represents the number of turbines in the farm, and the second number represents the configurations of the inter-turbine spacing changes. The changes were only due to the longitudinal spacing with the same lateral spacing as the base case keeping the blockage ratio constant as the turbines are configured in the same streamtube blocking the same stream flow.

No of devices	Configuration	Spacing			Blockage ratio
		US	OS	W	B
2	21	15D	20D	11.1D	0.016
	22	20D	20D	11.1D	0.016

Table 5.1: Change of longitudinal spacing of the two turbine configuration

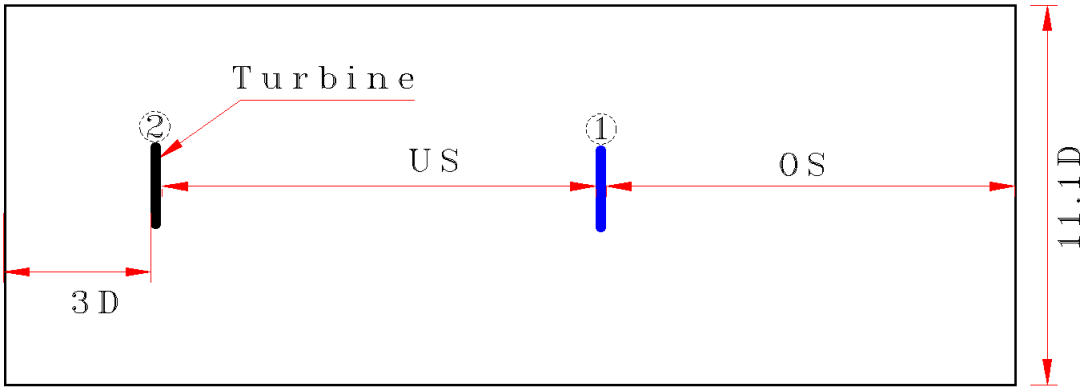

Figure 5.3: Two turbine configuration

5.3.3 Three Turbine Configuration

The computational domain shown in Fig. 5.4 contains three turbines configured laterally across the flow direction. The Lateral Spacing (LS) values were changed according table 5.2 to obtain two configurations to analyse the proximity effect of those additional turbines on the performance of both the base turbine and individual turbines. The width (W) of the domain is changed to accommodate the three turbines based on the lateral spacing and gives a different blockage ratio compared to the single turbine as shown in table 5.2. The blockage ratios are calculated using the combined area of individual turbines to get a global blockage ratio of the channel.

No of devices	Configuration	Spacing			Blockage ratio
		LS	OS	W	B
3	31	3D	20D	19.3D	0.027
	32	6D	20D	25.3D	0.021

Table 5.2: Lateral spacing changes of the three turbine configuration

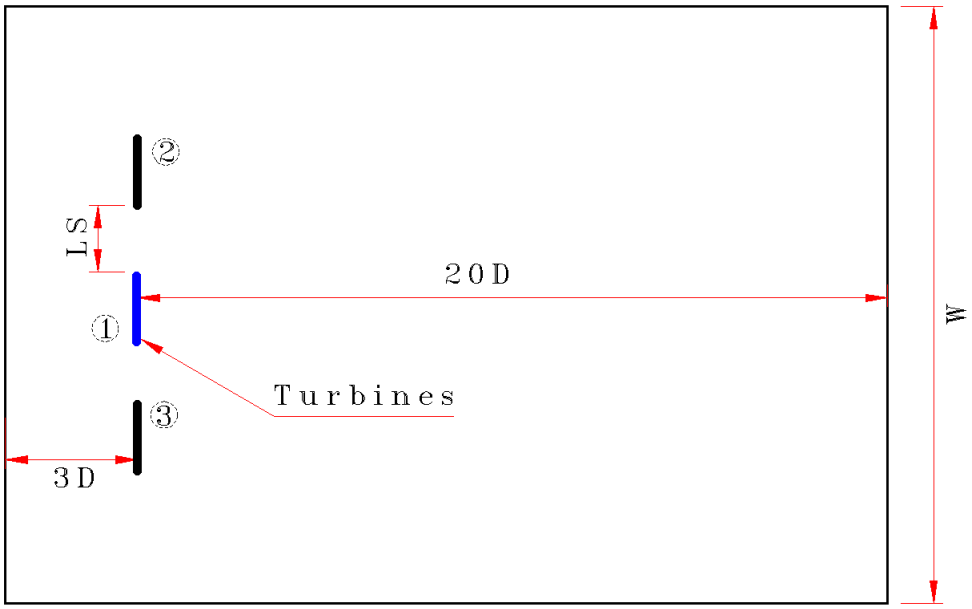

Figure 5.4: Three turbine configuration

5.3.4 Seven Turbine Configuration

Fig. 5.5 shows simple schematic diagram representation of seven turbine configuration. The effects of the surrounding turbines on the base turbine were analysed using four configurations by varying the lateral and longitudinal spacing. In addition to the spacing names given in the previous sections, downstream spacing (DS) is added to vary the longitudinal spacing between the middle and downstream row as shown in Fig. 5.5.

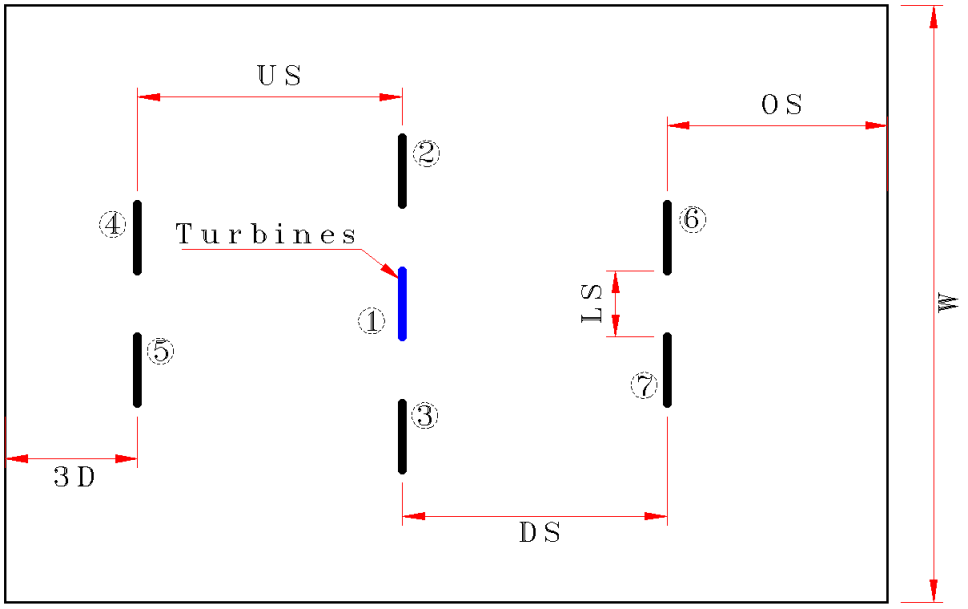

Figure 5.5: Seven turbine configuration

No of devices	Configuration	Spacing					Blockage ratio
		US	DS	OS	LS	W	B
7	71	10D	10D	10D	3D	19.3D	0.045
	72	10D	10D	10D	6D	25.3D	0.034
	73	15D	15D	15D	3D	19.3D	0.045
	74	15D	15D	15D	6D	25.3D	0.034

Table 5.3: Longitudinal and lateral spacing change of seven turbine configuration

The depth of water is kept constant with the previous configurations but the changes of lateral spacing have an effect on the value of the blockage ratio where configurations 71 and 73 have the same blockage ratio of $B = 0.045$ and configurations 72 and 74 have a blockage ratio of $B = 0.034$. The changes in longitudinal spacing have no effect on the blockage ratio as the blockage ratio is calculated using the total area of the turbines to the cross-sectional area of the channel. Note that the blockage ratios are calculated considering the combined area of individual turbines which block different stream flows because of an off-set configuration of some of the turbine unlike the two turbine configurations discussed in section 5.3.2. Thus, turbines 4 and 6 blocks the same stream flow and similarly turbines 5 and 7 blocks the same stream flow. These four turbines are considered as a combined area of two turbines which gave total number of turbines in the tidal stream farm which blocks different stream flows to 5 instead of 7 devices.

5.4 Base Case Turbine

The discussions in the previous chapters have been focusing on the power extraction, the wake characteristics and other related parameters of a single MRL turbine. Therefore, it is essential to compile some of the main points in this section to be used as a basis for the analysis of the influence of wake interactions on the performance and flow characteristics of the MRL turbine. The blockage ratio, $B = 0.016$, used in the previous Chapters remains the same for the single turbine simulations. The influence of the turbine to turbine interactions in a farm containing two, three, and seven turbines of different blockage ratio were examined relative to the results discussed in this section.

5.4.1 Flow Field Analysis

The simulation was carried out with a resistance coefficient of, $K_L = 1.304$, which gave the maximum power point during the investigation of the performance of a single turbine in Chapter 3. Fig. 5.6 shows the velocity contours both in vertical and horizontal plane across the centre of the single turbine. A physically large wake (lower flow rate) can be seen immediately downstream of the turbine due to the momentum change created by the immersed body forces.

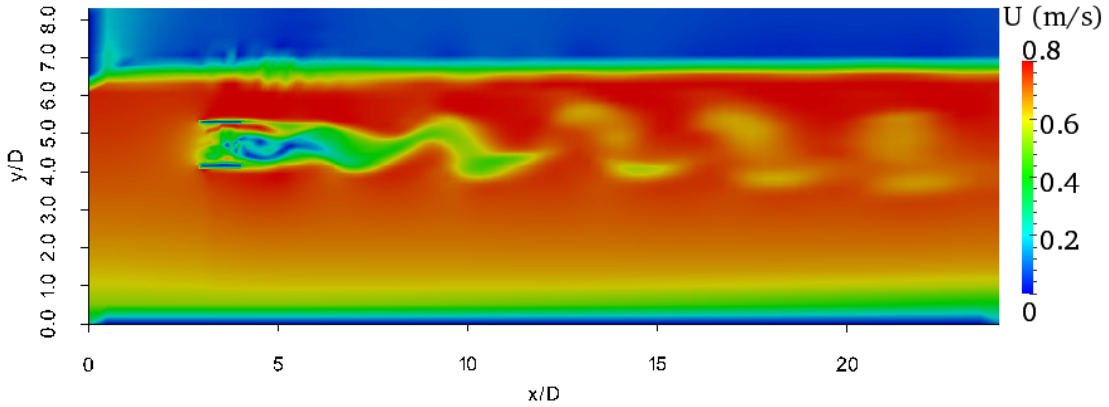

(a) Vertical plane

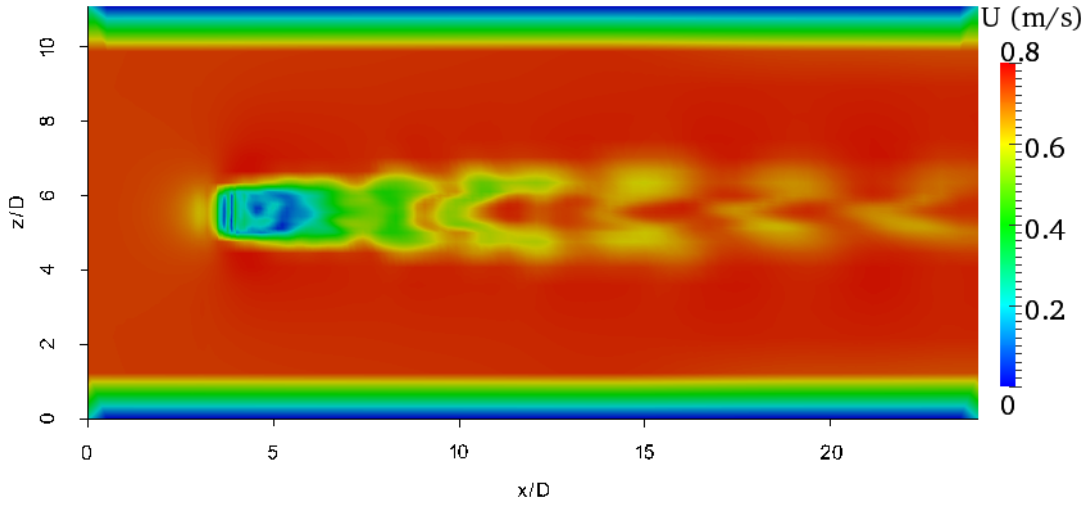

(b) Horizontal plane

Figure 5.6: Vertical and horizontal plane velocity contours of the base case

The wake characteristics was examined using both horizontal and vertical velocity profiles. Fig. 5.7 shows the instantaneous and time averaged velocity profiles along the stream direction through the centre of the turbine. It is clear from the graph that the flow rate decreases as the fluid passed through the turbine and starts to recover back further

downstream. It shows particularly large velocity deficit immediately downstream of the turbine. The wake was not fully recovered to its initial flow rate at the end of the domain as shown in the graph probably due to insufficient length of the domain.

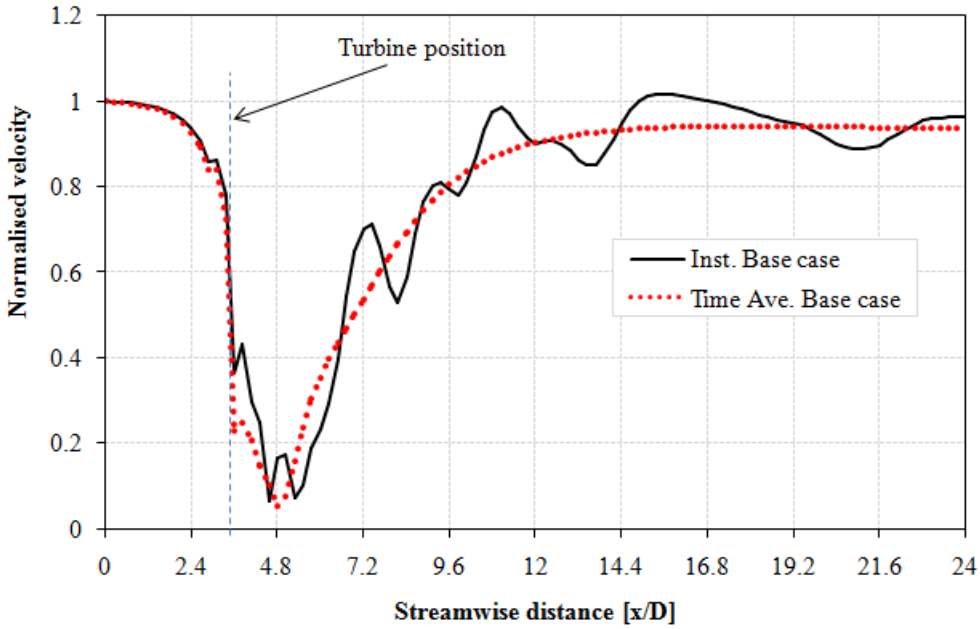

Figure 5.7: Instantaneous and time averaged centreline velocity profiles of the base case along the streamwise direction

The vertical velocity profiles was examined at the end of the domain to obtain the downstream length required for full recovery of the wake to the initial flow rate. The flow rate recovered to 92% of the stream flow at the end of the domain (20D), which indicates that the downstream length of the domain was not enough for full wake recovery. The result shows that a 20D longitudinal spacing between turbines will create a wake interaction consequently affecting the performance of downstream turbines. Therefore, a more detailed investigation of the inevitable turbine to turbine interactions in a tidal stream farm is vital to obtain a knowledge of its influence on the performance of individual turbines and is discussed in the subsequent sections.

To gain better understanding of the velocity fluctuations downstream of the turbine, the instantaneous velocity signal shown in Fig. 5.7 has been analysed using the wavelet transform method. Fig. 5.9 shows the analysed signal and the corresponding linearly decomposed signal at 3 levels of detail coefficients and one approximation. These coefficients give a representation of the energy distribution among different scales and how it

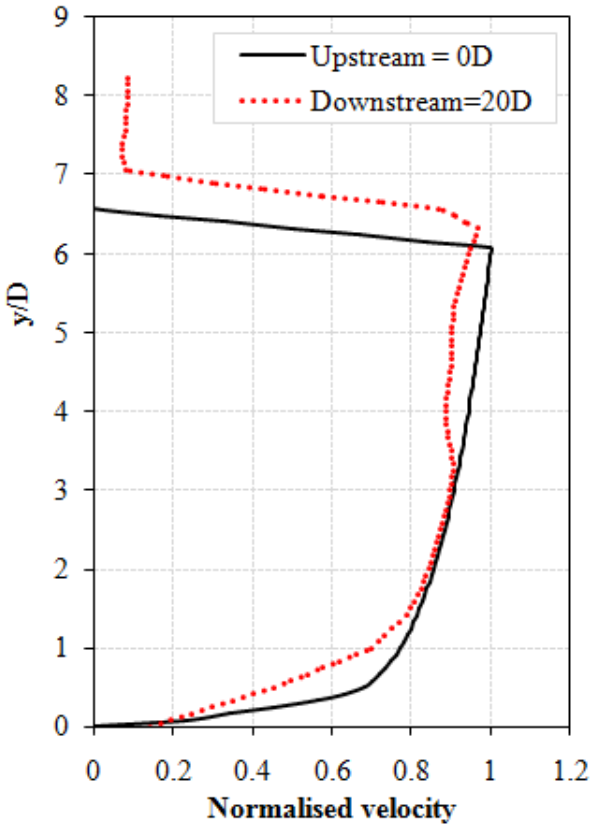

Figure 5.8: Comparison of vertical velocity profiles at the inlet and outlet of the computational domain

varies with position in the domain.

The amplitudes of the detailed coefficients of d1, d2 and d3 are higher within and downstream of the turbine (from 2.4D - 16.8D) and vanish afterwards. The details show zero amplitude before 2.4D and after 16.8D especially on the fine scale d1, which indicates negligible velocity fluctuations. The wavelet decomposition analysis improved in detecting the velocity fluctuations in the stream-wise direction, which is crucial to know the downstream length where the fluctuations reduce. However, it should be noted that a reduced fluctuation is not to mean the wake is recovered back to its initial conditions, but it gives valuable information on the variant extent of the velocity fluctuations that could reach any downstream turbine which can affect its performance and life cycle.

A comparison of the detailed coefficients between the levels indicate that the amplitude was higher at d3 than d1 considering similar positions though the fluctuation was almost zero at the end of the domain in all of the levels. The high amplitude was probably due to high contribution of large length scales to the detailed coefficients.

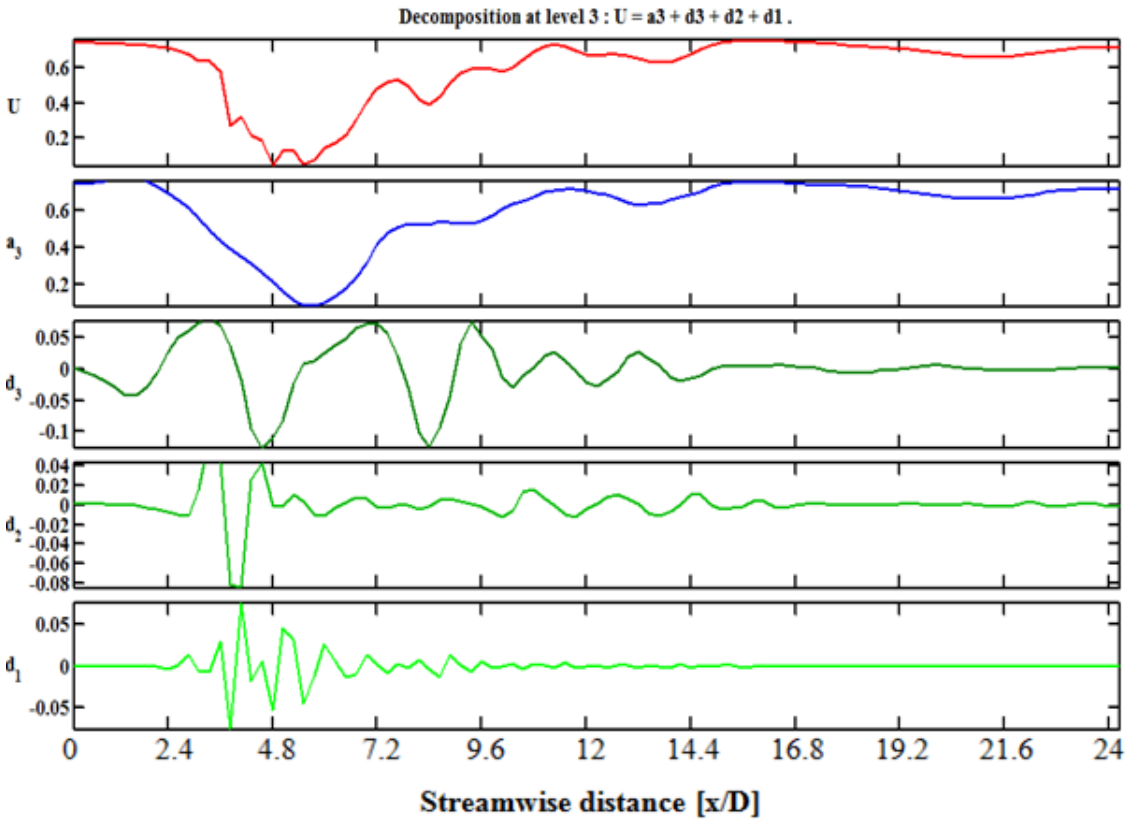

Figure 5.9: Detailed coefficients of the instantaneous velocity profiles

The pressure has been equally affected due to the body forces and can be used in some of the investigations of the wake characteristics. The three parameters, power coefficient, velocity, and pressure are expected to be affected similarly due to the proximity of the turbines because of their inter-relation. The instantaneous and time averaged pressure profiles are shown in Fig. 5.10. The pressure builds up upstream of the turbine due to the blockage by the body forces and drops across the turbine region and recovers further downstream of the turbine to its initial condition.

5.4.2 Thrust and Power Analysis

From the detailed investigation of the performance of a single turbine carried out in Chapter 3, both the thrust and power coefficients at its maximum power point are given in table 5.4. These values represents the thrust force experienced by turbine 1 and its performance when simulated in an isolated condition.

The velocity and pressure profiles, and the thrust and power coefficients of the same turbine simulated in a tidal stream farm with additional turbines at different configurations

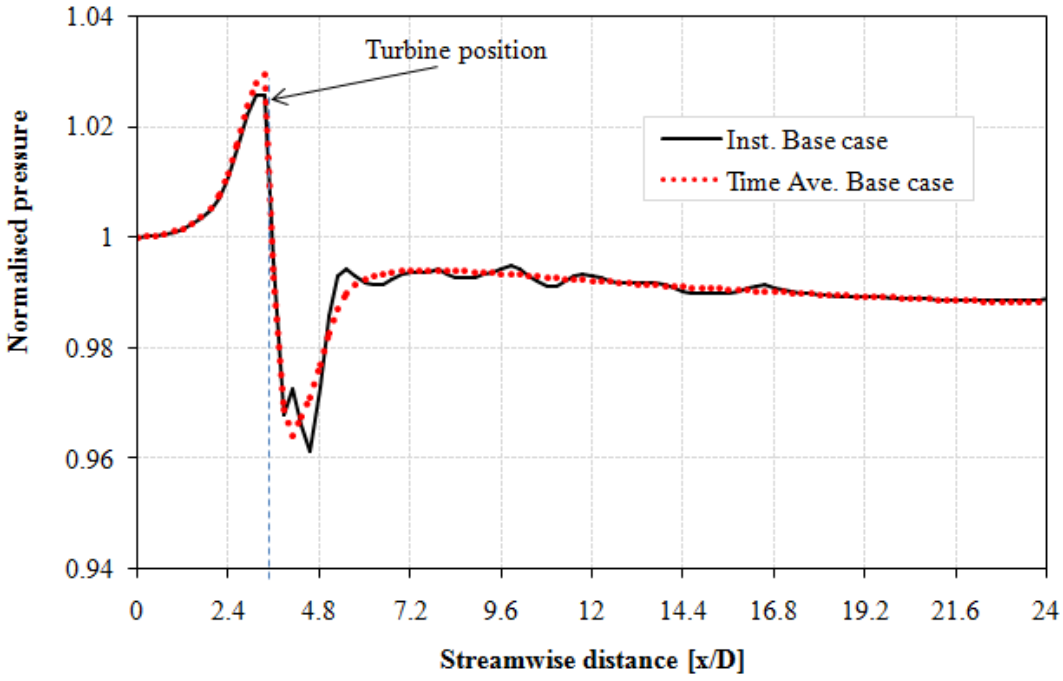

Figure 5.10: Centreline pressure profile of the base turbine along the streamwise direction

No of turbines	C_T	C_P
Base case	0.833	0.665

Table 5.4: Thrust and power coefficients of the base case turbine

were compared with the results discussed in this section. These results were labelled as a base case in the subsequent sections.

5.5 The Influence of Lateral Turbines

Turbines configured in a spanwise direction across a channel are part of a tidal stream farm, which requires a detail investigation on the effect the change of lateral inter-turbine spacing on the performance of individual devices. A sample of three MRL turbines with arbitrary selected lateral spacing of 3D (configuration 31) was simulated and the results were compared relative to other configuration by changing the lateral spacing to 6D (configuration 32). The change of lateral spacing has a direct effect on the blockage of the channel, which would in-turn provide information on the blockage effect to the performance of individual turbines. The same resistance coefficient, $K_L = 1.304$, was equally applied to three of the turbines as they are operating at the same row. This is the

point where maximum power point is obtained based on the investigations in section 5.4 and Chapter 3.

5.5.1 Flow Field Analysis

Fig. 5.11 shows a horizontal plane of the velocity contours for the two configurations. It is clear from Fig. 5.11a that there is a high chance of wake mixing at the end of the domain due to the small spacing (3D) used between the turbines in configuration 31. The mixing might lead to high energy loss which could affect the performance of any downstream turbines. This arrangement might not allow the inclusion of another downstream turbine that could use the advantage of the accelerated bypass flow between the turbines. The spacing between the turbines was increased to 6D (configuration 32) to minimise the mixing of the wake, and the result showed in Fig. 5.11b proved that increased spacing avoided the mixing problem. This configuration allows more space for deployment of additional turbines in a staggered layout, which may reduce the downstream length required in Fig. 5.11a to avoid the wake interaction. This kind of configuration can help to maximise the energy extraction from tidal stream farms in a small plot of area.

Clearer information about the flow characteristics can be presented using the velocity profiles extracted from the velocity contours. Fig. 5.12 shows the instantaneous and time averaged velocity profiles through turbine 1 in the two configurations (31 and 32) and the base case turbine discussed in section 5.4. The velocity profiles of turbine 1 in configurations 31 and 32 showed slower wake recovery compared with the base except beyond 18D near the end of the domain. There is no obvious reason for this result as the wake recovery of the velocity from turbine 1 in the two configurations was expected to be faster than in the base case due to increased blockage that accelerates the flow through this turbine.

The instantaneous and time averaged velocity profiles through each of the turbines in the two configurations are shown in Figs. 5.13 and 5.14. The velocity profile from turbine 1 in configuration 31 has a faster wake recovery compared to the other turbines in the same configuration due to a high turbine scale blockage compared to the turbine scale blockage

of turbines 2 and 3. Note that the turbine scale blockage is evaluated by considering the width of the bypass flows (lateral spacings) between the turbines and the side walls where their combined value is the global blockage ratio of the two configurations given in table 5.2. However, the results from the turbines in configuration 32 showed almost similar profiles throughout the domain except a small difference between 4D and 16D where turbine 3 showed a higher value for unknown reason as turbines 2 and 3 were expected to show a similar profile due to their symmetrical position in the domain.

The effect of the wake of each turbine and their proximity on the bypass flow has been investigated using the velocity profiles through the centre of the bypass between turbines 1 and 2 and turbines 1 and 3 as shown in Fig. 5.15. The bypass flow is accelerated in both configurations due to the venturi flow created by the presence of the devices although the magnitude is different. The velocity is higher between 3D and 14D in configuration 31 due to small lateral spacing (3D) however it falls below the velocity in configuration 32 due to the wake mixing beyond 16D. The velocity of the bypass flow remains higher than the velocity at the inlet of the domain which could have a positive impact on the performance of downstream turbines deployed along the bypass flows.

Velocity data has been extracted in the span-wise direction through the centre of the three turbines in the two configurations to investigate the profiles in different directions to the ones discussed before as shown in Fig. 5.16. The profiles showed slightly higher velocity values in configuration 31 through the bypass regions between turbines 1 and 2 and 1 and 3 which is another way of looking at the venturi flow created by the proximity of the devices. The velocity deficit across the turbines are higher in configuration 32 which is again due to a lower blockage ratio compared to the velocity deficits in configuration 31. However, the velocity deficit across turbine 1 showed a smaller value compared to the other two turbines in both configurations which is probably due to the device scale blockage effect that increases the flow through this turbine.

Fig. 5.17 shows the pressure profiles along the centreline of turbine 1 in the two configurations and the base case. The pressure drop across turbine 1 in configurations 31 and 32 is almost similar but the pressure drop in the base case is higher than in the

two configurations. These difference are mainly due to the blockage effect of the laterally configured turbines and the results showed that the proximity of the turbines showed some influence on the pressure drops and this has direct consequences on the power extraction from each of the turbines in the farm.

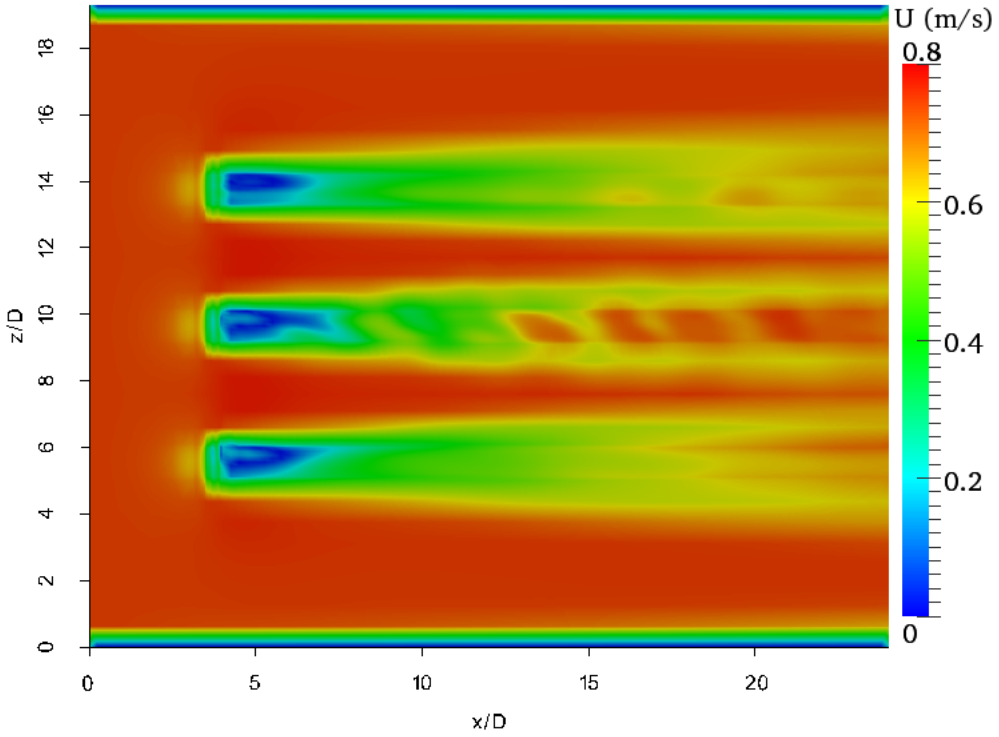

(a) Configuration 31

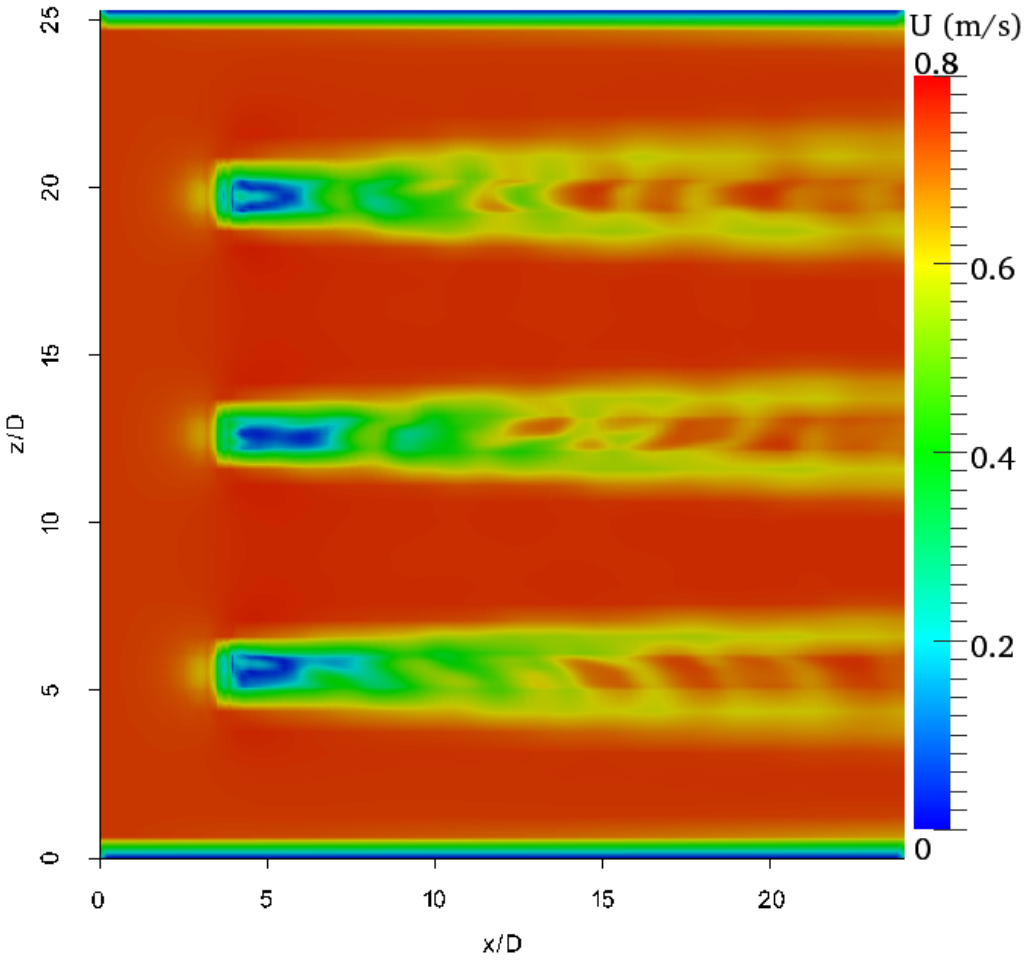

(b) Configuration 32

Figure 5.11: Horizontal plane velocity contours of the three turbines

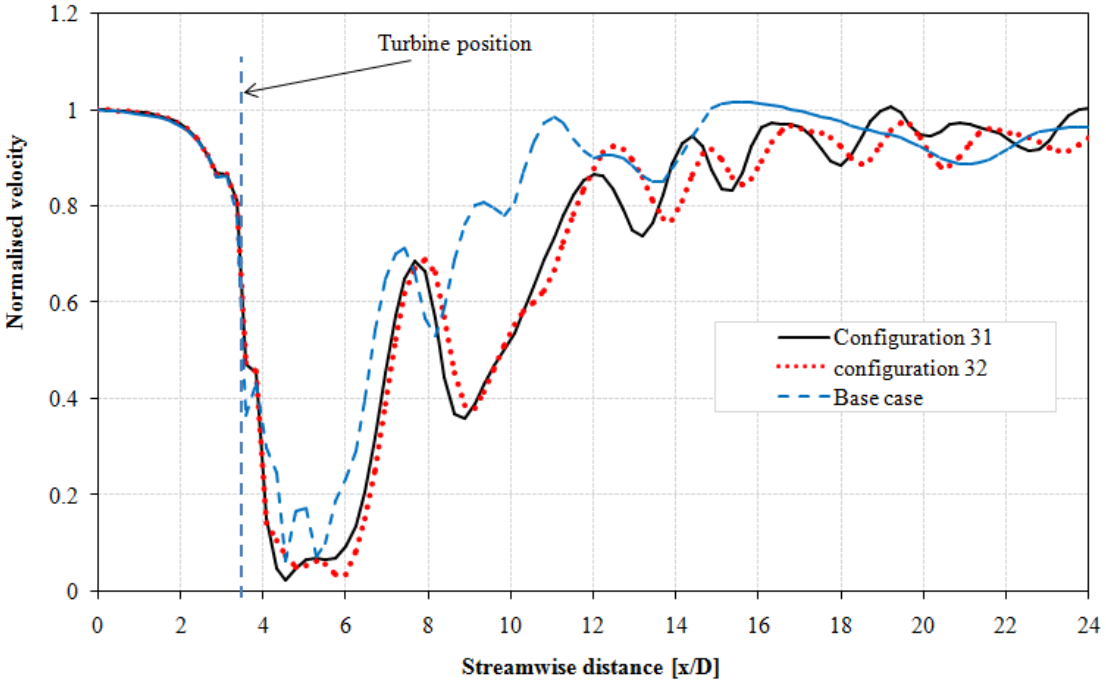

(a) Instantaneous

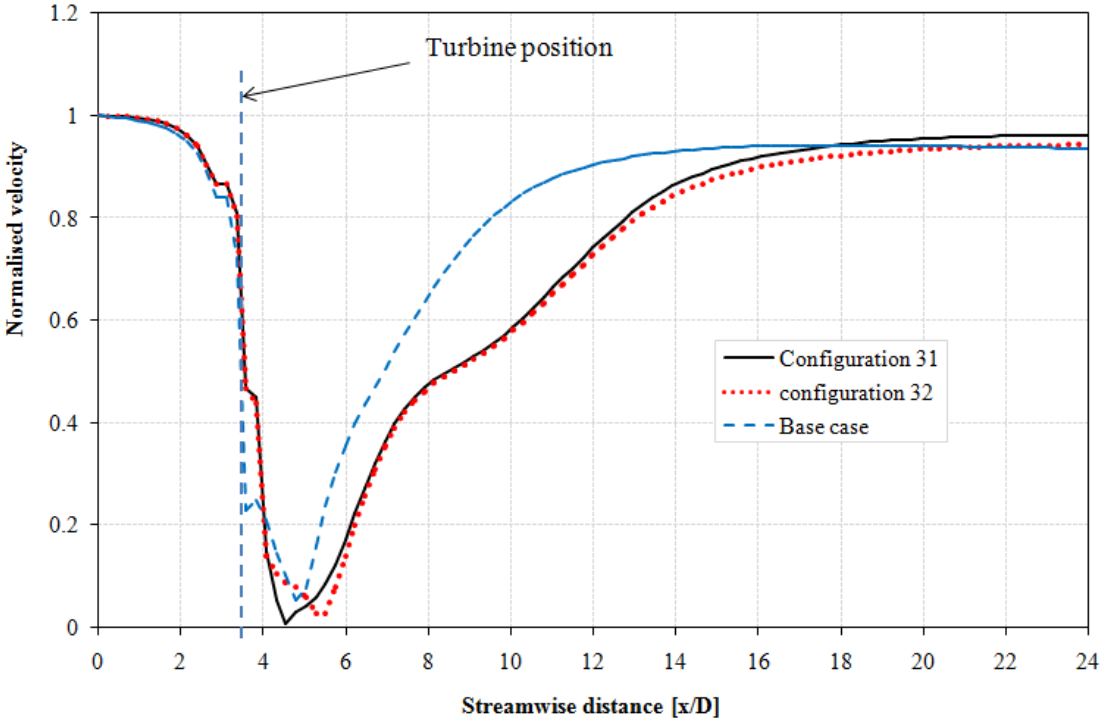

(b) Time averaged

Figure 5.12: Comparison of the centreline velocity profiles of the base case and turbine 1 in the two configurations

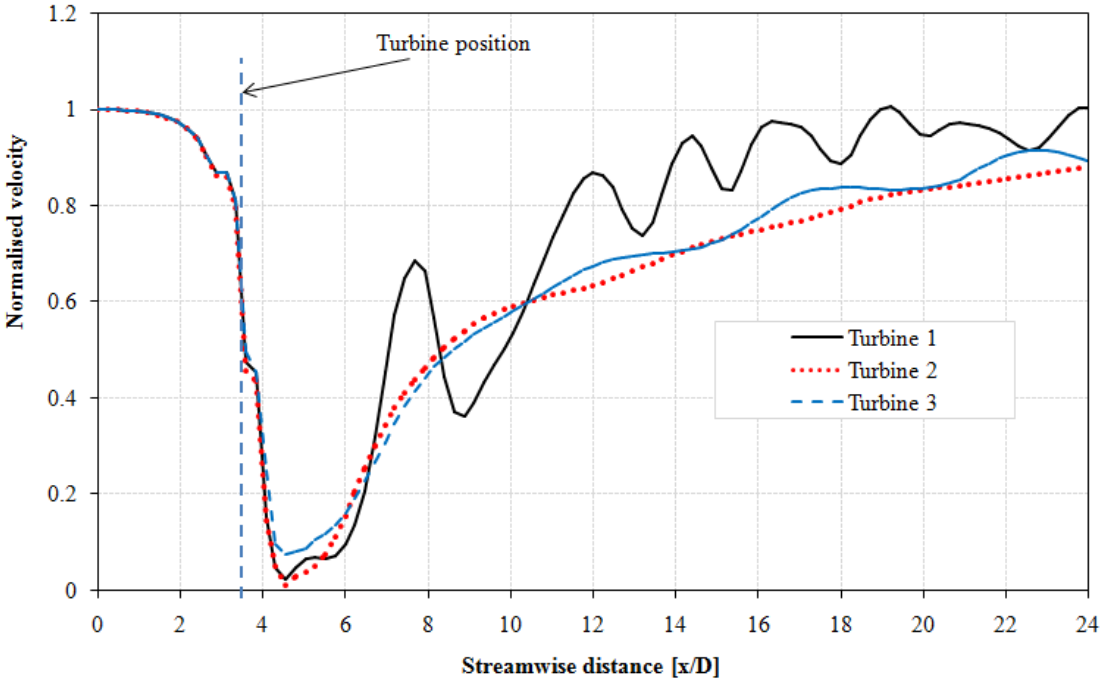

(a) Configuration 31

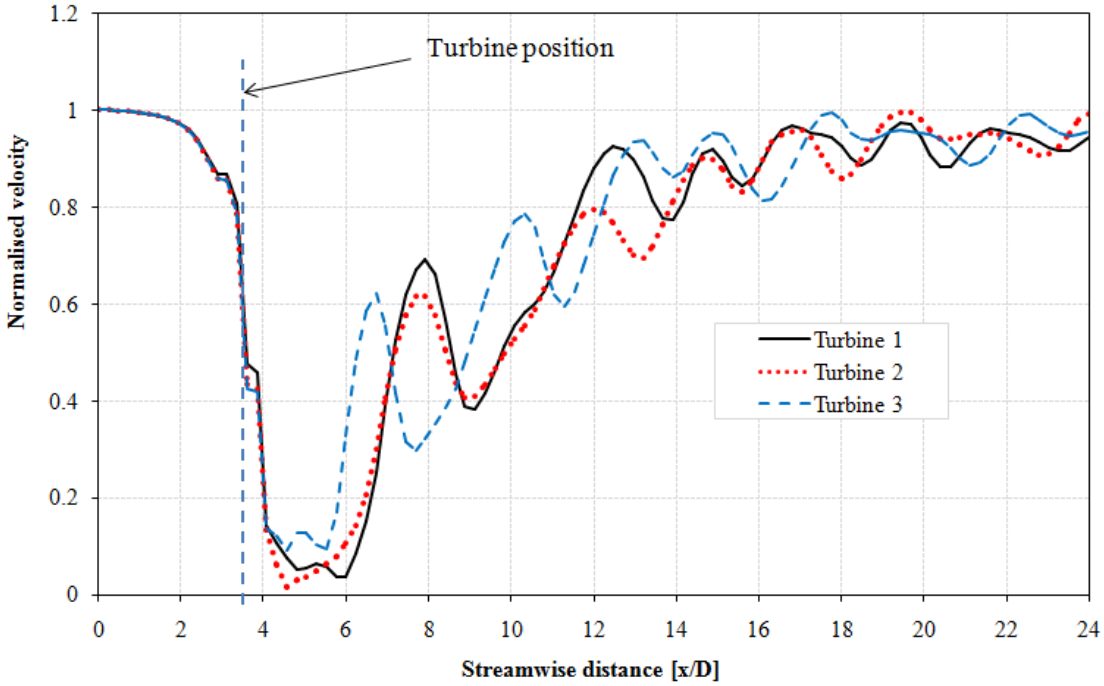

(b) Configuration 32

Figure 5.13: Comparison of the instantaneous centreline velocity profiles of the three turbines along the streamwise direction

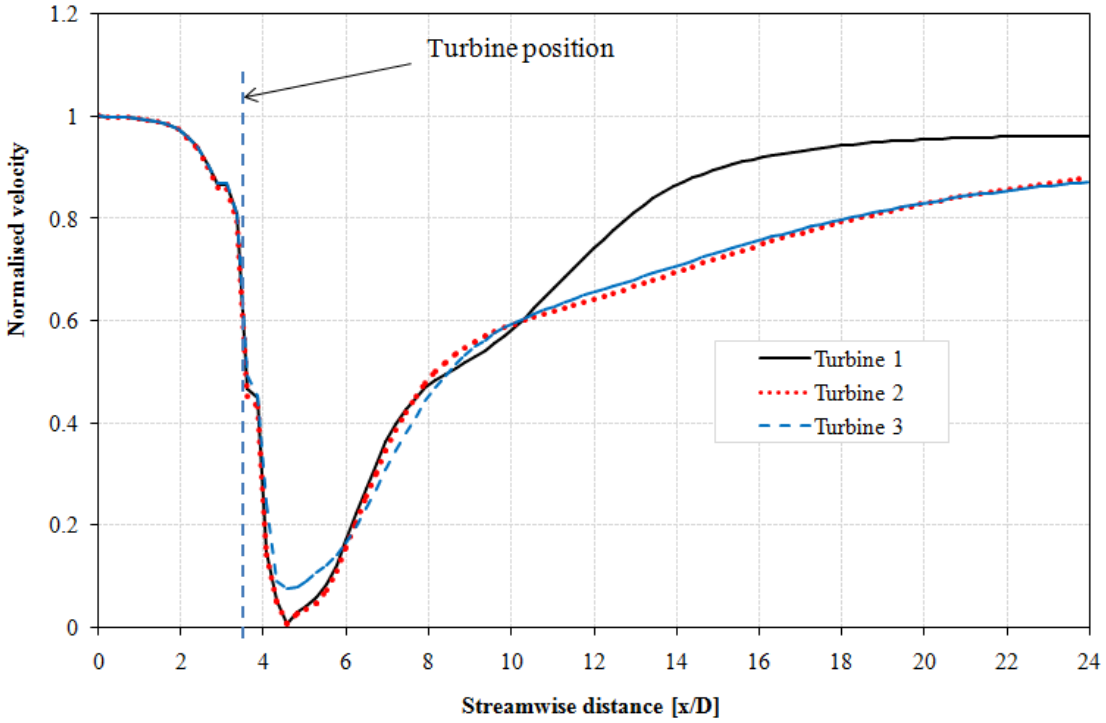

(a) Configuration 31

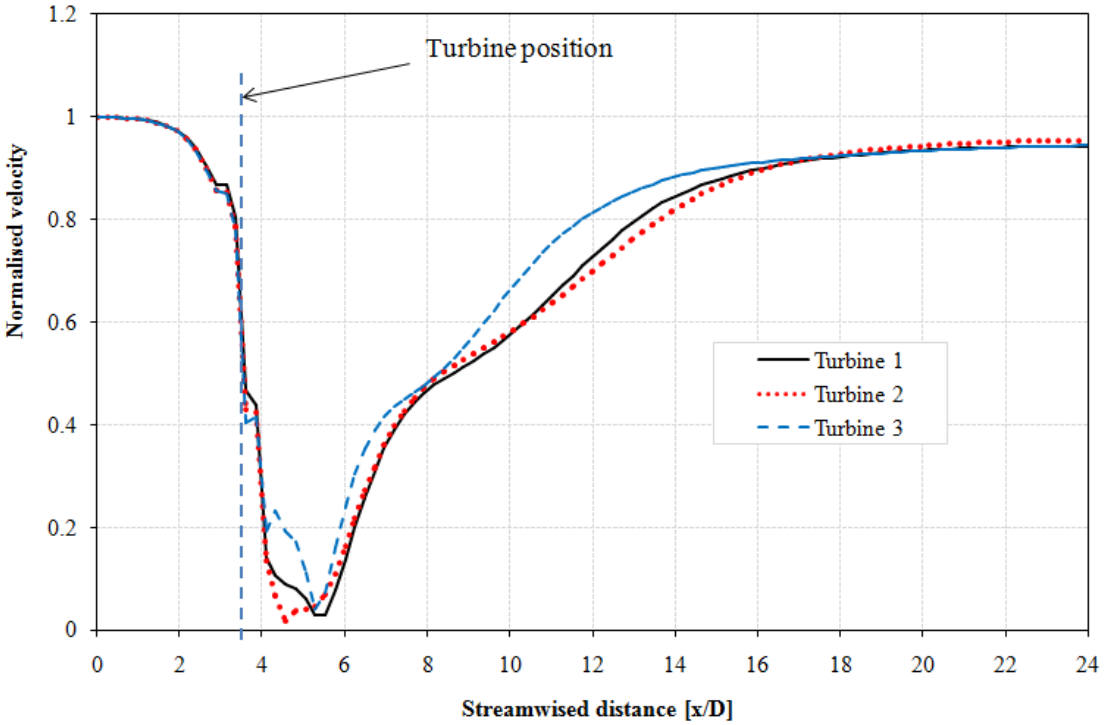

(b) Configuration 32

Figure 5.14: Comparison of the time averaged centreline velocity profiles of the three turbines along the streamwise direction

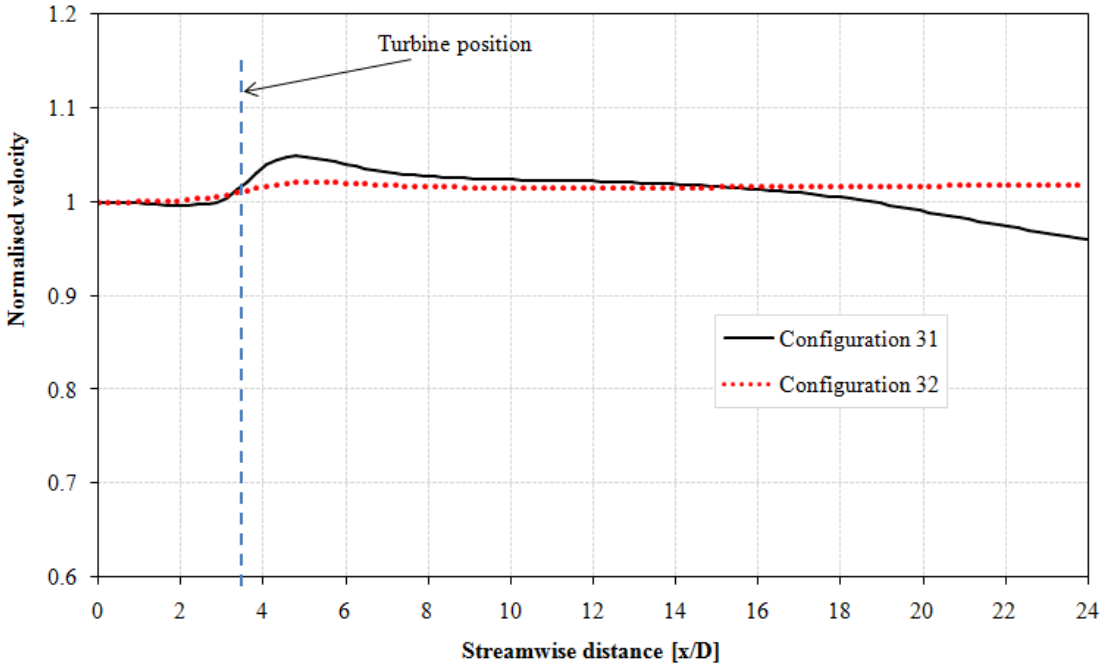

(a) Bypass flow between turbines 1 and 2

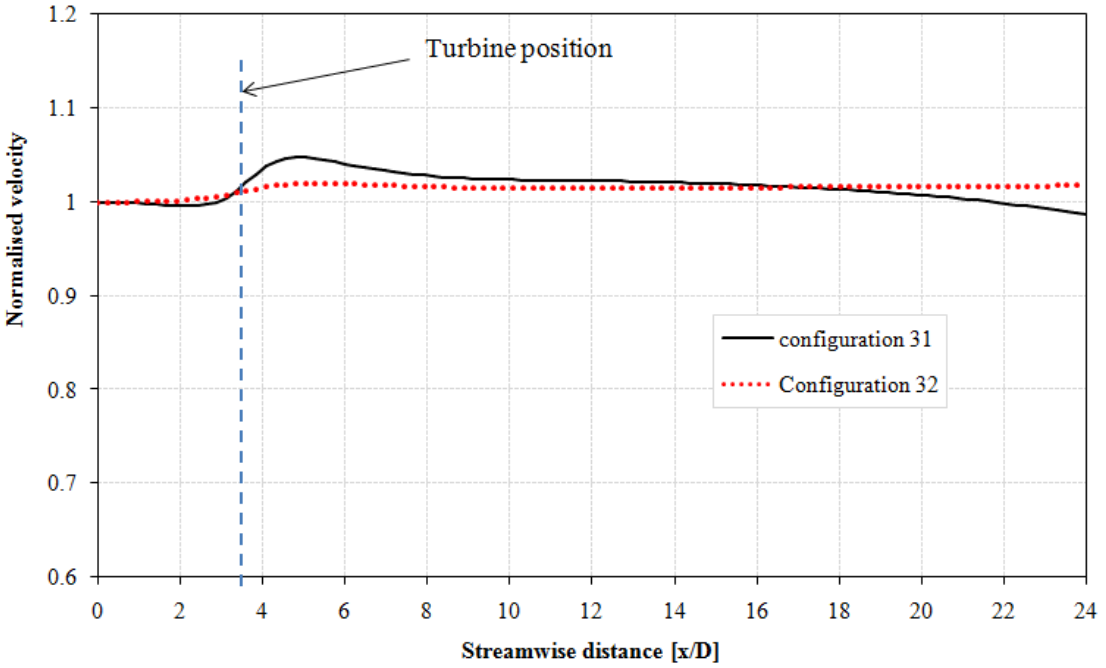

(b) Bypass flow between turbines 1 and 3

Figure 5.15: Comparison of the velocity profiles through the bypass flow of the three turbines along the streamwise direction

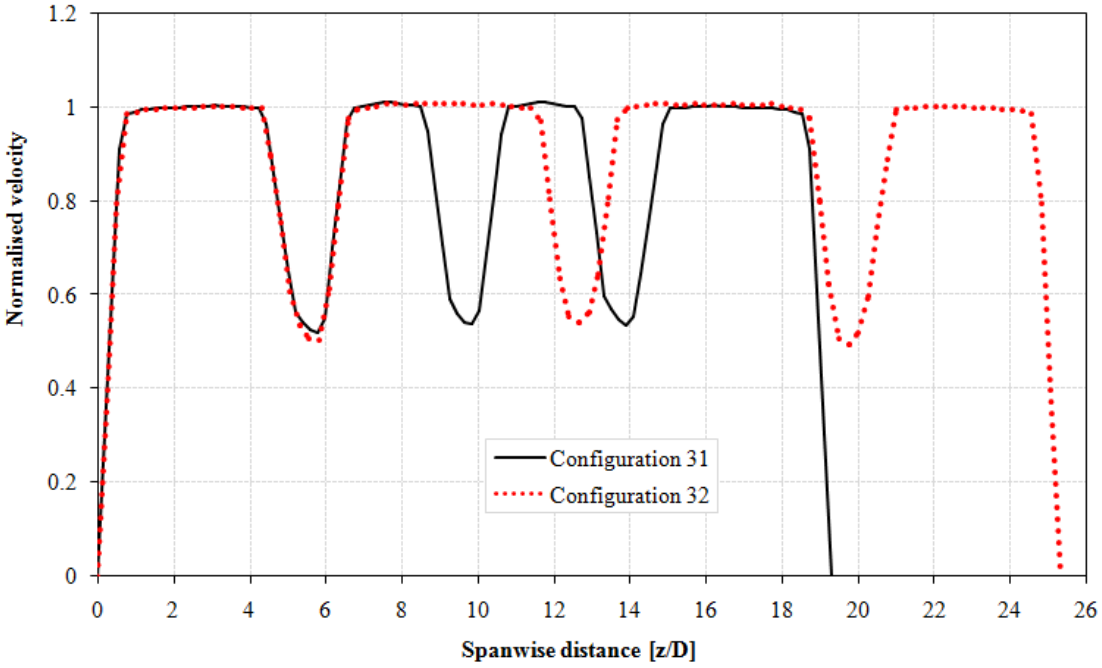

Figure 5.16: Comparison of the centreline velocity profiles of the two configurations along the spanwise direction

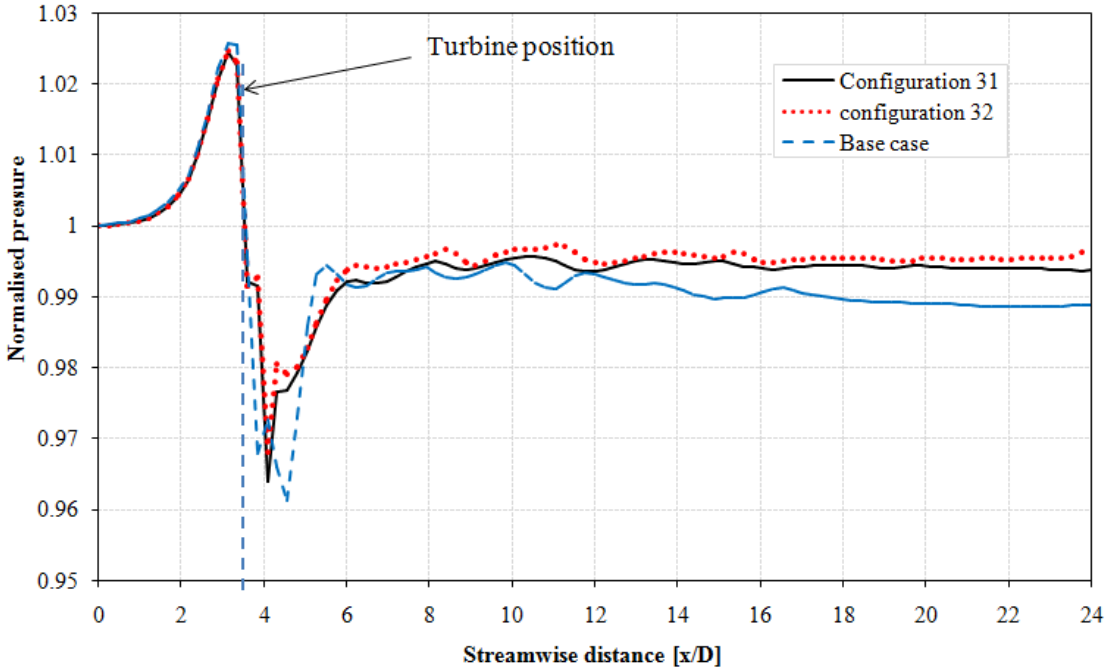

(a) Instantaneous pressure profile

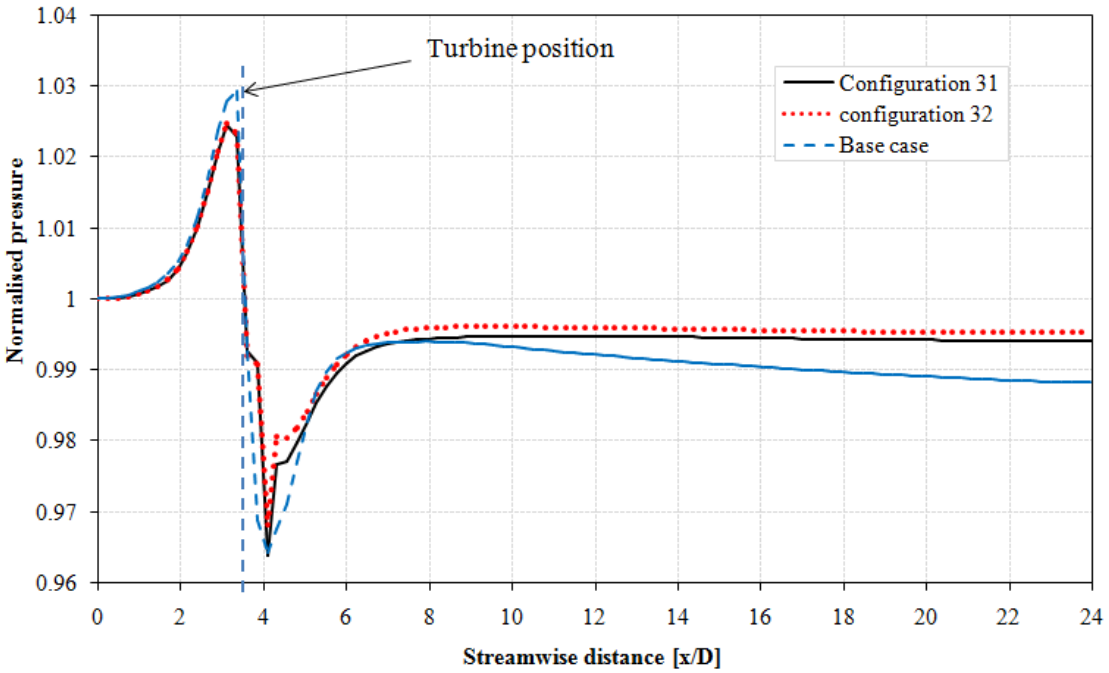

(b) Time averaged pressure profile

Figure 5.17: Comparison of the centreline pressure profiles of the base case and turbine 1 in the two configurations

5.5.2 Thrust and Power Analysis

Fig. 5.18 shows a comparison of the thrust forces of the base case and the three turbines in the two configurations. The result clearly showed significant differences both with the base case and between the turbines in configurations 31 and 32. The thrust force, $C_T = 0.911$, showed in Fig. 5.19 of turbine 1 and its power coefficient of $C_p = 0.761$ in configuration 31 is higher than the values in the base case and in configuration 32. This is mainly due to high blockage ratio of, $B = 0.027$, compared to the blockage ratio, $B = 0.021$, of configuration 32 and $B = 0.016$ of the base case. Note that a different resistance coefficient would be expected to affect the operating point of the turbine and possibly operate away from its maximum power point as already seen in the single turbine investigations in Chapter 3. The thrust and power coefficient values of the base case are included in the tables shown within the figures for the purpose of comparison only but note that these values are obtained from the simulation of an isolated turbine.

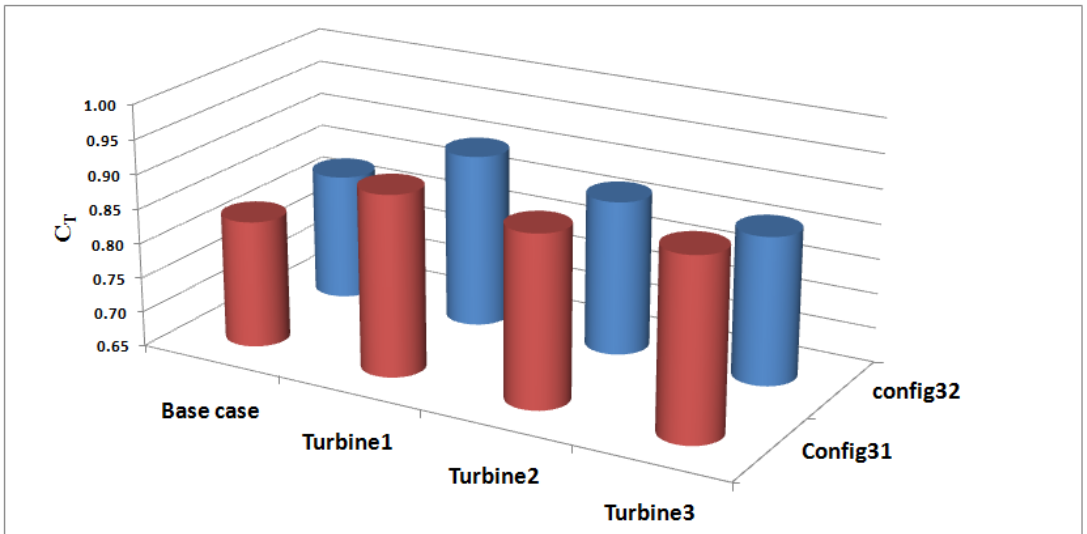

	Base case	Turbine1	Turbine2	Turbine3
Config31	0.833	0.911	0.897	0.909
config32	0.833	0.900	0.872	0.863

Figure 5.18: Comparison of thrust coefficient by the turbines in the base case and the two configurations

The thrust and power coefficient of turbine 1 in configuration 32 is still higher than the values of the base case because of its higher blockage ratio but the trend shows that with a further increase of the inter-turbine spacing, a decrease of the blockage ratio, the values

would be expected to be similar to the base case. However, the thrust and power coefficient of the three turbines in configuration 32 are lower than the same turbines simulated in configuration 31 as can be seen from the bar graphs and tables. These results showed that the performance of individual turbines in a farm can be improved by decreasing the lateral spacing or increasing the blockage ratio. However, due to the proximity of the turbines there is a possibility of wake mixing, which could inflict significant energy shadowing to other turbines deployed downstream unless appropriate longitudinal spacing is used. An optimised location of the devices in a tidal stream farm could be therefore obtained by adding upstream and downstream rows of turbines.

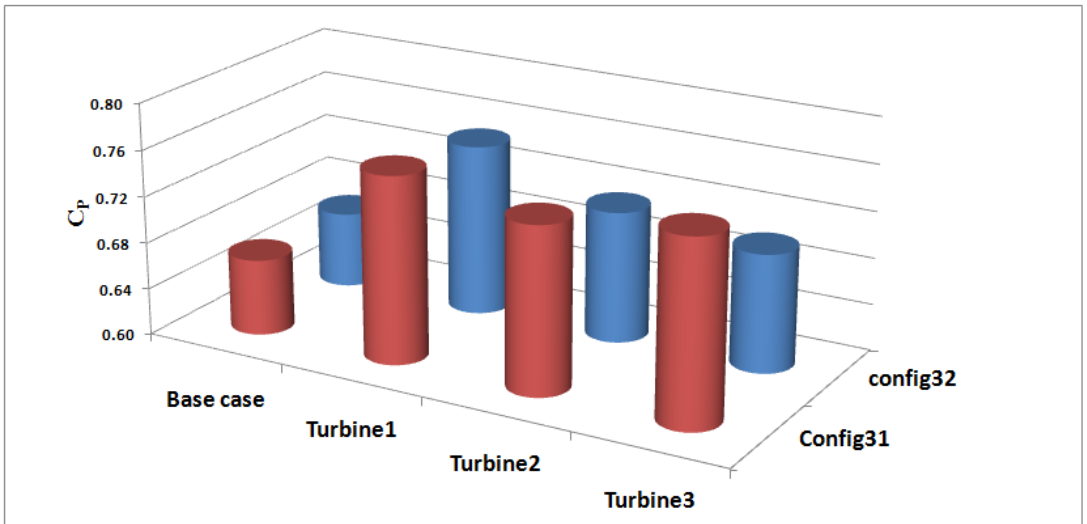

	Base case	Turbine1	Turbine2	Turbine3
Config31	0.665	0.761	0.744	0.758
config32	0.665	0.748	0.713	0.702

Figure 5.19: Comparison of power coefficients by the turbines in the base case and the two configurations

These results are consistent with other analytical and CFD studies [Houlsby et al., 2008, Bai et al., 2009, Nishino and Willden, 2012b] which showed that a high blockage can improve the performance of individual turbines, though the modelling methods and the type and scale of the turbines used were different. The results also strengthen the novelty of the MRL turbine which is designed to have high aspect ratio in order to utilize the blockage effect to increase its efficiency when stretches across a stream flow. Therefore, deployment of several turbines across a channel will have a positive impact on the performance of individual turbines as they collectively act as a blockage.

5.6 The Influence of Upstream Turbine

Unlike the spanwise configurations discussed in the previous section, several turbines can be configured in the streamwise direction blocking the same streamtube with a constant blockage ratio. However, there are possibilities of staggered layout by which the blockage ratio could be different. For this section, two turbines were configured in the streamwise direction blocking the same streamtube resulting a constant blockage ratio, $B = 0.016$, as the single turbine configuration even with the change of longitudinal spacing. Note that unlike the lateral spacing, any change of longitudinal spacing has no effect on the blockage ratio. To investigate the influence of the wake interaction, two MRL turbines configured with 15D and 20D longitudinal spacing have been considered. The resistance force of the upstream turbine is equivalent to the resistance force used in the single turbine simulations, which is equivalent to the resistance coefficient, $K_L = 1.304$. However, the resistance force of the downstream turbine was reduced by 10% compared to the resistance of the upstream turbine in both configurations, which is equivalent to a resistance coefficient, $K_L = 0.913$, based on the exponential relationship developed between the resistance force and the resistance coefficient in section 5.2.

5.6.1 Flow Field Analysis

Fig. 5.20 shows the velocity contours for the two configurations. A small turbine spacing in configuration 21 (15D) created massive wake interaction between the two turbines as shown in the vertical and horizontal planes of the velocity contours. As the spacing between the turbines increased to 20D (configuration 22), the wake interaction was decreased as shown in Fig. 5.20b resulting in a small velocity deficit downstream of the turbine.

The instantaneous and time averaged centreline velocity profiles extracted from the two configurations are shown in Figs. 5.21 and 5.22 respectively. The instantaneous velocity profiles showed fluctuating behaviour and it appears that the velocity approaching to the downstream turbine is disturbed in both configurations, but it is difficult to understand the magnitude of the wake recovery from these profiles.

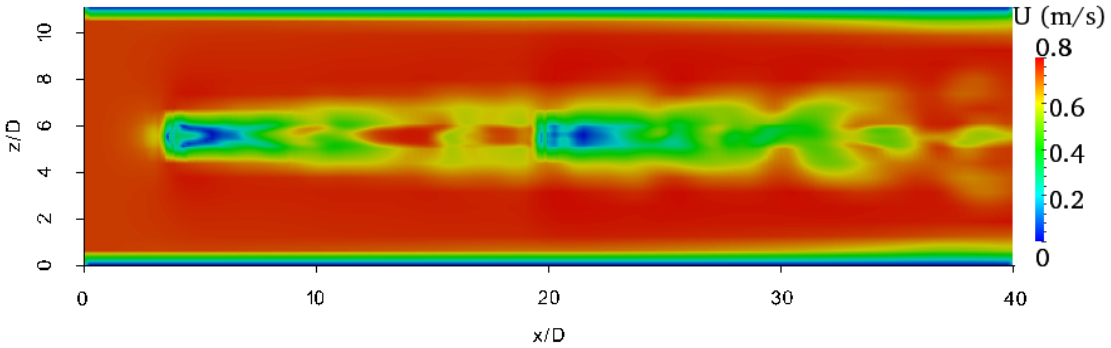

(a) Horizontal plane configuration 21

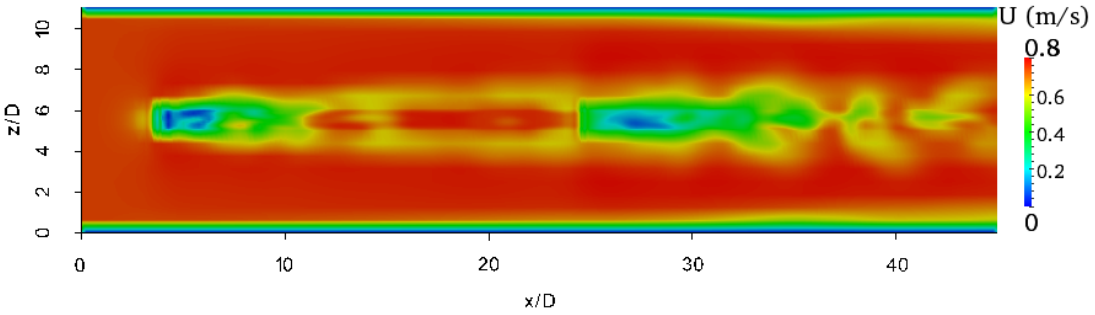

(b) Horizontal plane configuration 22

Figure 5.20: Velocity contours of two turbines in two configurations

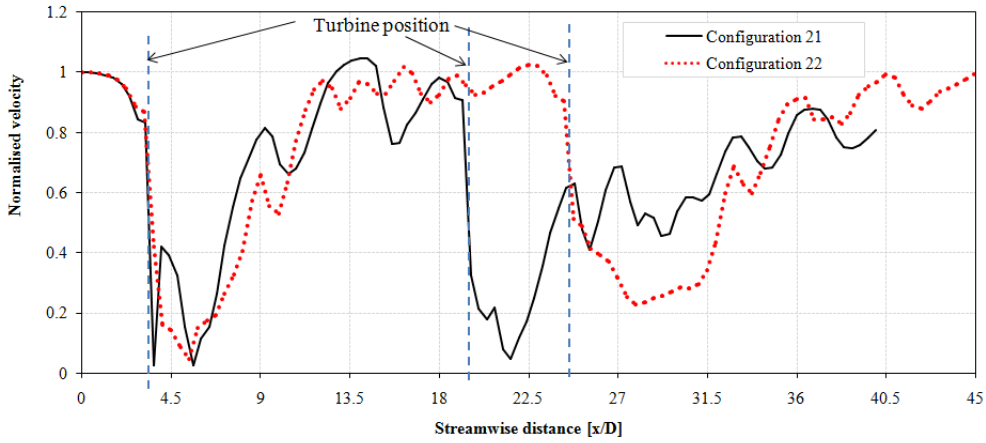

Figure 5.21: Instantaneous centreline velocity profiles along the streamwise direction

The time averaged velocity profiles given in Fig. 5.22 showed a clear difference of the velocity deficit downstream of the turbines. The turbine in configuration 21 showed high velocity deficit due to low local incident velocity because of the wake interaction from the upstream turbine. When the longitudinal spacing is increased in configuration 22, the velocity deficit is decreased because of the high local incident velocity. Note that the downstream turbines in both configurations have the same resistance coefficient which is the reason for this different output of the velocity deficit. However, the profiles around

the upstream turbines (turbine 2) are similar in both configurations as expected due to the same resistance coefficient and no wake interaction.

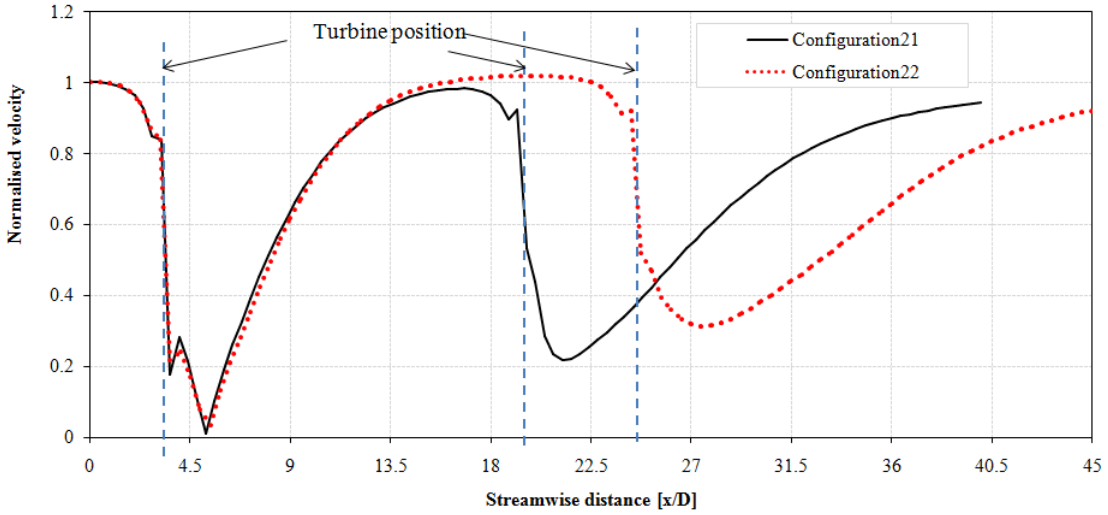

Figure 5.22: Time averaged centreline velocity profiles along the streamwise direction

To obtain a clear understanding of the influence of wake interactions, the velocity profiles from the two configurations (21 and 22) were compared to the results of the base turbine discussed in section 5.4. The instantaneous velocity profiles appears to show the same velocity deficit immediately downstream of the turbine in configuration 21 (Fig. 5.23a) and the base case though the wake recovery is different. However, the velocity deficit is higher in the base case compared to the turbine in configuration 22. Note that these are arbitrary instantaneous velocity profiles. A more appropriate way is to use the time averaged velocity profiles though showing the instantaneous values have some advantages to understand the flow fluctuations downstream of the turbines.

In the time averaged velocity profiles shown in Fig. 5.24, it is clear that the velocity deficit immediately downstream of the turbine in the base case is higher than the downstream turbine in both configurations but with different magnitudes for the reasons discussed previously. This result shows that the resistance coefficient, $K_L = 0.913$, used in the downstream turbines is small to reduce the velocity of the flow as the one in the base case and the upstream turbines where the resistance coefficient was, $K_L = 1.304$. Thus an increased resistance coefficient of the downstream turbines would be expected to increase the change of momentum of the flow by which high velocity deficit can be obtained in

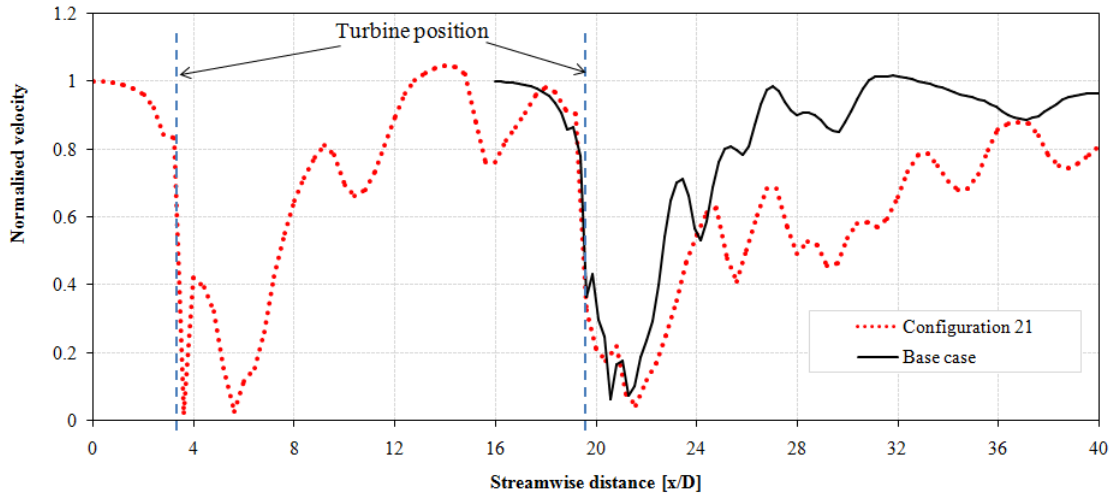

(a) Configuration 21

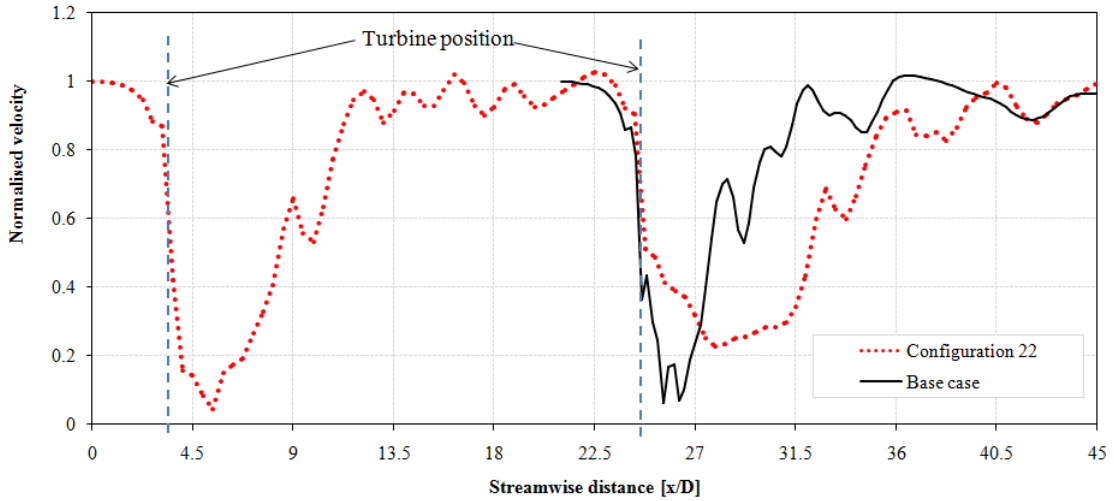

(b) Configuration 22

Figure 5.23: Comparison of the instantaneous velocity profiles of the base case and turbine 1 in the two configurations

both configuration similar to the base case and the upstream turbines.

Fig. 5.25 shows the analysed signal, the instantaneous velocity profile given in Fig. 5.23, and the corresponding linearly decomposed signals at 3 levels of detail coefficients and one approximation for the two configurations. The detail coefficients showed that the velocity fluctuations at the end of the domain in configuration 22 (Fig. 5.25b) were higher than in configuration 22.

The velocity fluctuations were higher immediately downstream of the turbine and reduced far away from the turbine region. These fluctuations observed in the two configurations are higher than the base case (Fig. 5.25) probably due to the wake interaction

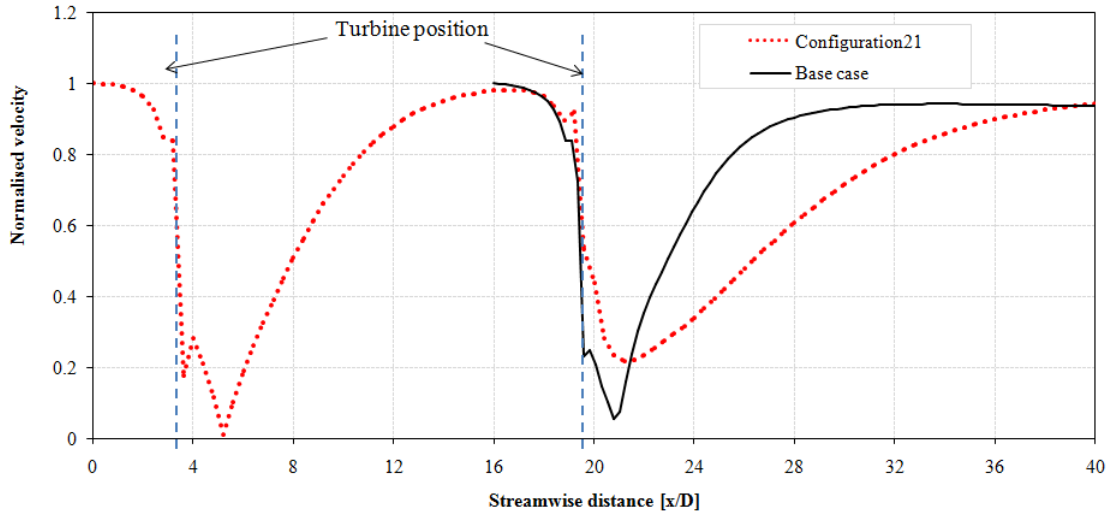

(a) Configuration 21

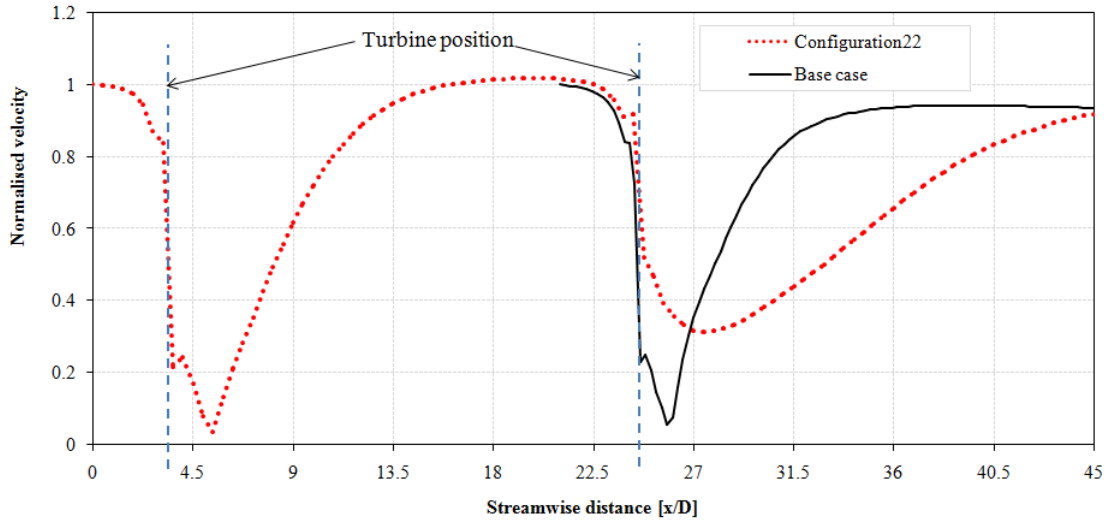

(b) Configuration 22

Figure 5.24: Comparison of the time averaged velocity profiles of the base case and turbine 1 in the two configurations

which could damage the performance of any downstream turbines.

Comparison of the instantaneous and time averaged pressure profiles of the turbines in the two configurations with the base case are shown in Figs. 5.26 and 5.27 respectively. The results are a reflection of the conditions discussed in the velocity profiles as the pressure profiles are directly related to the flow characteristics. The pressure drop across the turbine in the base case is higher than the pressure drop from the turbine in both configurations but is similar to the pressure drop from the upstream turbines.

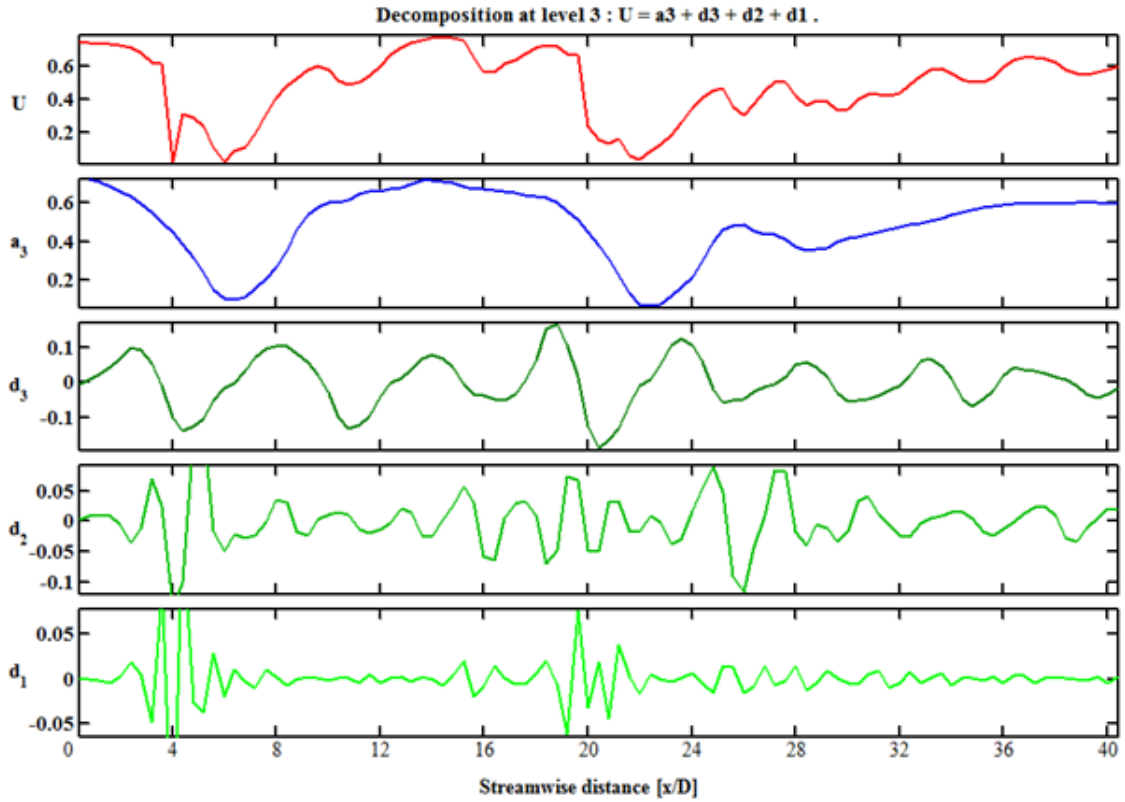

(a) Configuration 21

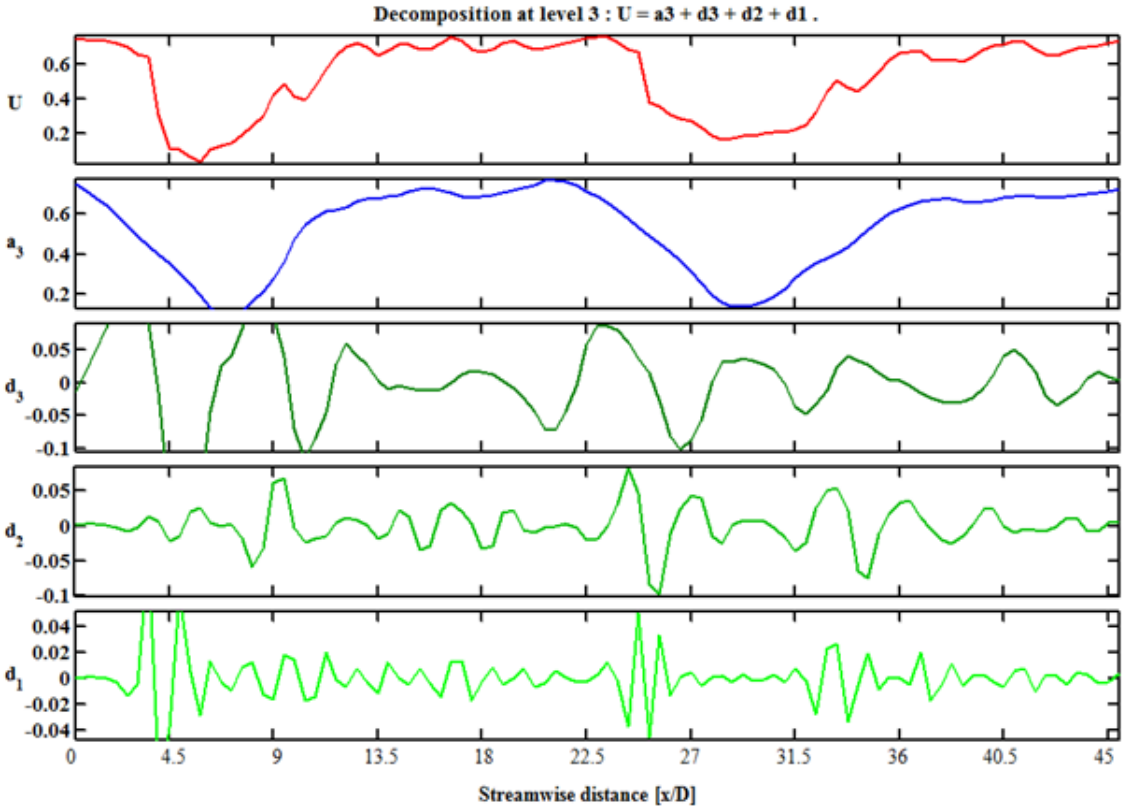

(b) Configuration 22

Figure 5.25: Detail coefficients of the instantaneous velocity profiles given in Fig. 5.23

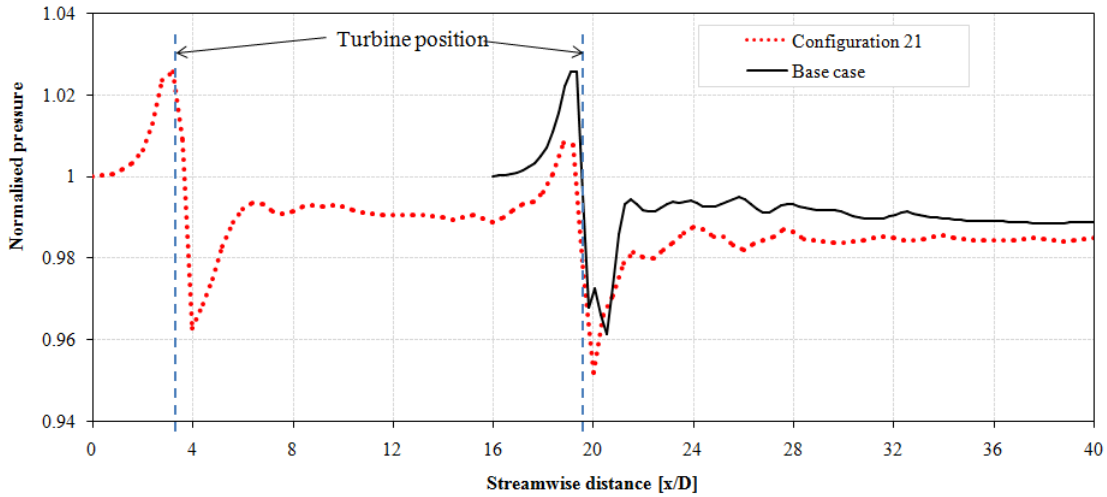

(a) Configuration 21

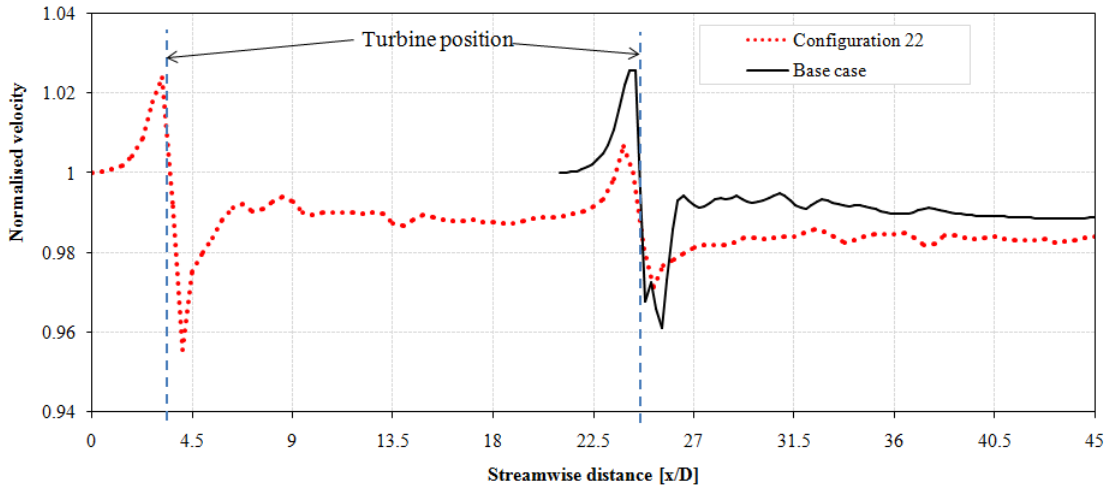

(b) Configuration 22

Figure 5.26: Comparison of the instantaneous centreline pressure profiles of the base case and turbine 1 in the two configurations

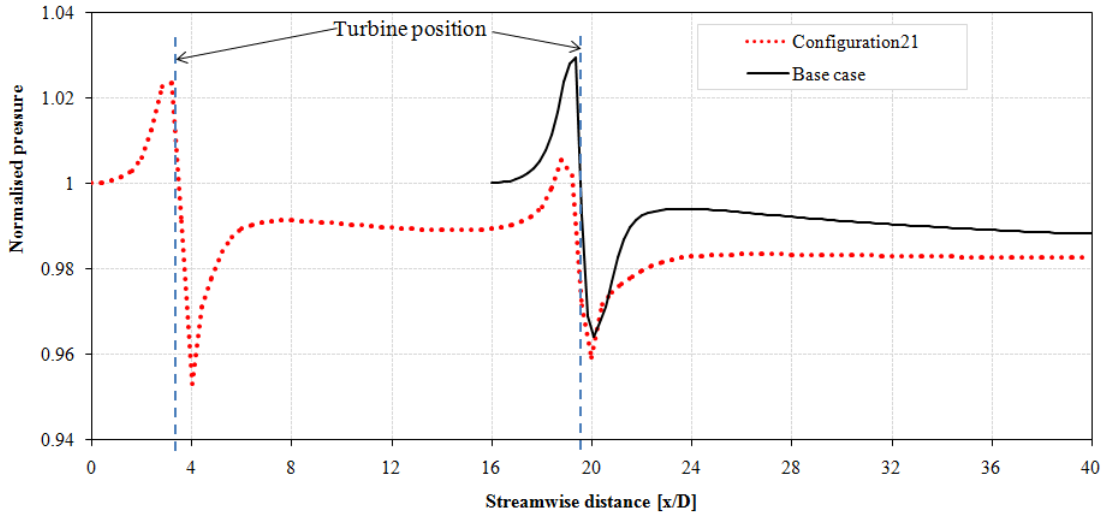

(a) Configuration 21

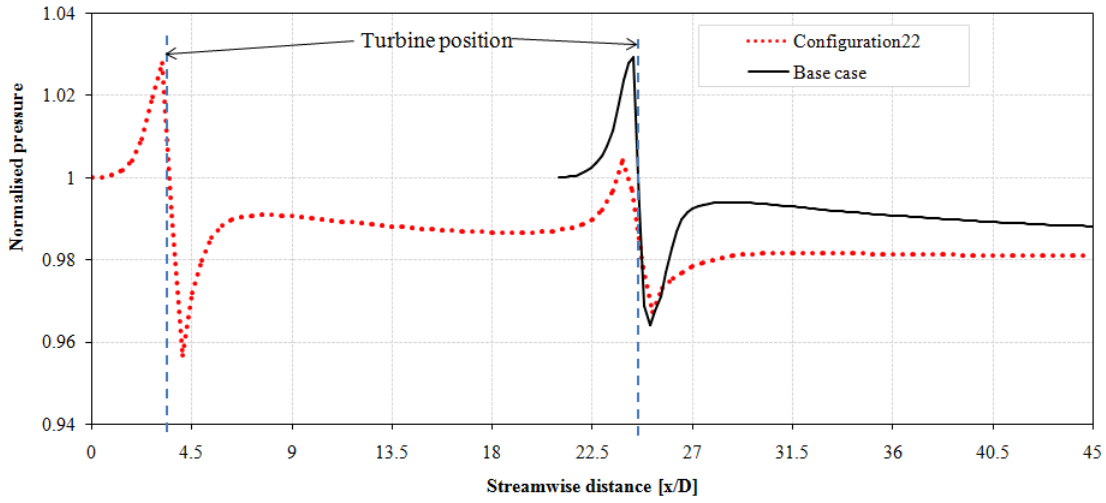

(b) Configuration 22

Figure 5.27: Comparison of the time averaged centreline pressure profiles of the base case and turbine 1 in the two configurations

5.6.2 Thrust and Power Analysis

A detail analysis was carried out to compare the thrust and power coefficients of the turbine simulated in the two configurations and the base case. Geometrically similar turbines should have the same C_p characteristics. However, the changes of the average velocity of the downstream turbine due to the wake interaction have direct influence on the value of C_p. The thrust and power coefficients of turbine 2 in both configurations was expected to be similar with the base case, but the results given in Figs. 5.28 and 5.29 showed a different value. The value was slightly improved in configuration 22 when the longitudinal spacing was increased. This is an indication that the blockage by the downstream turbine has an influence on the performance of the upstream turbine where the averaged velocity at the turbine was reduced compared to the results from the base case.

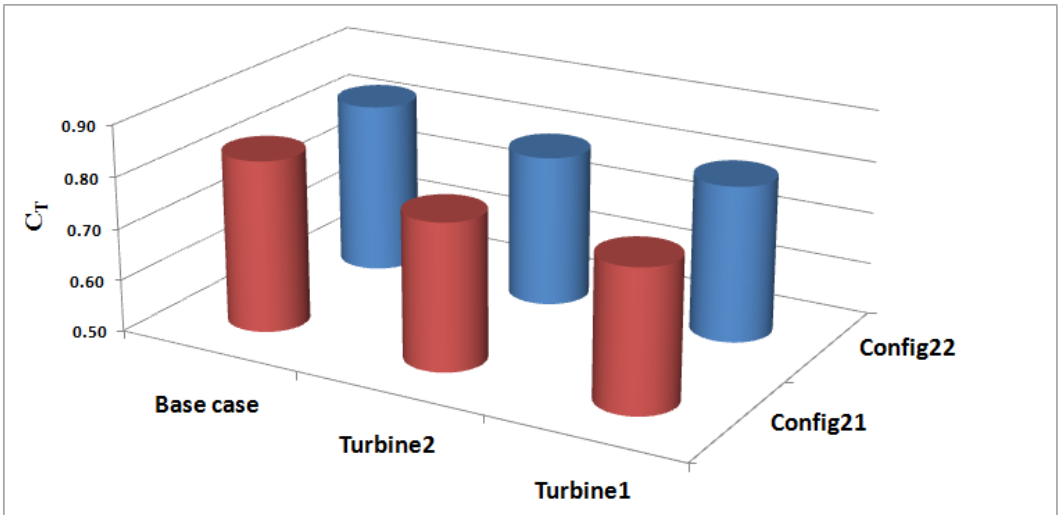

	Base case	Turbine2	Turbine1
Config21	0.833	0.784	0.773
Config22	0.833	0.792	0.802

Figure 5.28: Comparison of thrust coefficients by the turbines in the base case and the two configurations

The thrust coefficient of turbine 1 in the two configurations is less than the the thrust coefficient of the base case as shown in Fig. 5.28. In contrast, the power coefficient is higher than the base case. However, the maximum power coefficient, $C_P = 0.751$, from configuration 22 is lower than the maximum power points observed from the MRL turbine in the three turbine configurations discussed in section 5.5 although that high

power coefficient was due to a high blockage by the laterally configured turbines. In the two turbine configurations, the blockage ratio is considered to be the same as the single turbine (base case) as both turbines block the same stream flows as a result the power coefficient of any turbine in the two configurations is expected to be less than or equal to the base case. Thus there is no obvious reason why the power coefficient of turbine 1 in the two configurations is higher than the base case although it may be that the effect of blockage ratio of turbines configured in a way that blocks the same stream flows could have different effect than a single turbine. The thrust and power coefficients of the turbine in configuration 22 are higher than in configuration 21 due to increased longitudinal spacing which reduces the wake interaction from the upstream turbine.

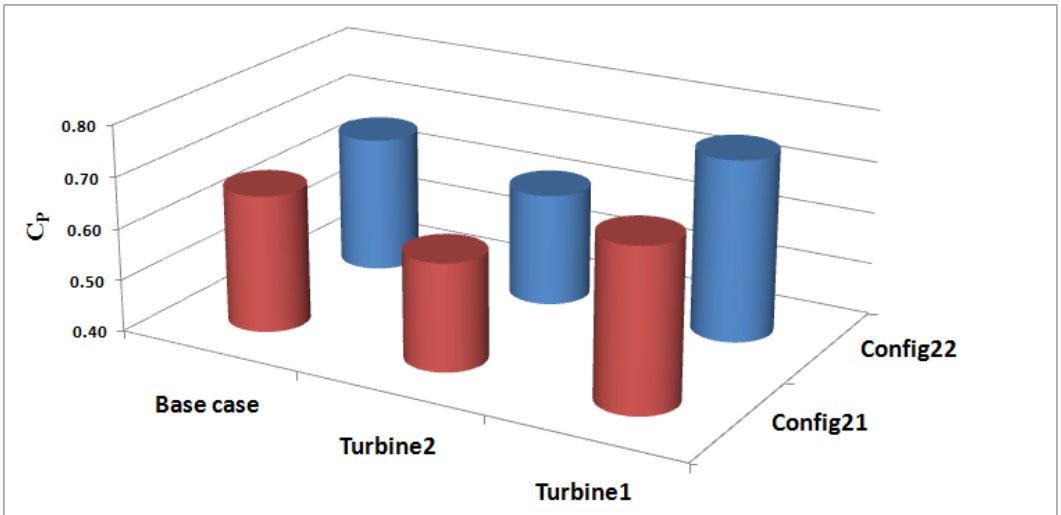

	Base case	Turbine2	Turbine1
Config21	0.665	0.608	0.711
Config22	0.665	0.618	0.751

Figure 5.29: Comparison of power coefficient by the turbines in the base case and the two configurations

5.7 The Influence of Surrounding Turbines

In this section, more turbines were added upstream, downstream, and on the side of the base turbine (turbine 1) to analyse the combined effect of the surrounding turbines. First, initially assumed longitudinal and lateral spacings were used in configuration 71. These spacings were then changed to obtain three additional configurations 72, 73 and 74 in

order to investigate the relative influence of these changes on the flow features and the performance of individual turbines in the farm containing 7 devices. The resistance force of the upstream row of turbines is equivalent to the resistance forces used in the single turbine simulations, which is equivalent to the resistance coefficient, $K_L = 1.304$. However, the resistance force of the middle and downstream rows of turbines was reduced successively by 10% compared to the resistance of the upstream turbine, which is equivalent to a resistance coefficients of $K_L = 0.913$ and $K_L = 0.658$ respectively. Note that the same resistance force was applied to each turbine in the same row due to operating at the same streamwise position.

5.7.1 Flow Field Analysis

The velocity contours from all four configurations are shown in Figs. 5.30 and 5.31. The wake of the upstream row (turbines 4 and 5) in configuration 71 interacts with the middle row (turbines 1, 2 and 3) and the mixed wake of these rows subsequently creates severe wake interactions with the downstream row (turbines 6 and 7), as shown in Fig. 5.30a. The wake interactions of the upstream row with the middle row were minimized by increasing the lateral spacing or decreasing the blockage ratio from $B = 0.045$ to $B = 0.034$ in configuration 72 as shown in Fig. 5.30b. However, the wake of the upstream row still interacted with the downstream row as it flows through the bypass of the middle row due to insufficient longitudinal spacing.

The longitudinal spacing (10D) between the rows used in configurations 71 and 72 was increased to 15D in configurations 73 and 74 while keeping the same lateral spacing of the former configurations. However, there was still a wake interaction among the turbines in configuration 73 (Fig. 5.31a) though it was improved compared with configuration 71 (Fig. 5.30a) which suggests that the longitudinal spacing was not enough for full recovery of the wake. The lateral spacing of configuration 73 was increased while maintaining the same longitudinal spacing and the interaction was minimised as shown in configuration 74 (Fig. 5.31b). The main reason for the minimal interaction in configuration 74 was that the wake of the upstream row had sufficient lateral and longitudinal spacing, which flows

through the bypass without interacting with the middle row and almost recovered back to its initial condition before it reaches the downstream row. There is a huge velocity deficit downstream of turbines 4 and 5 in four of the configurations compared to the rest of the turbines which is mainly due to the different resistance forces applied to each row.

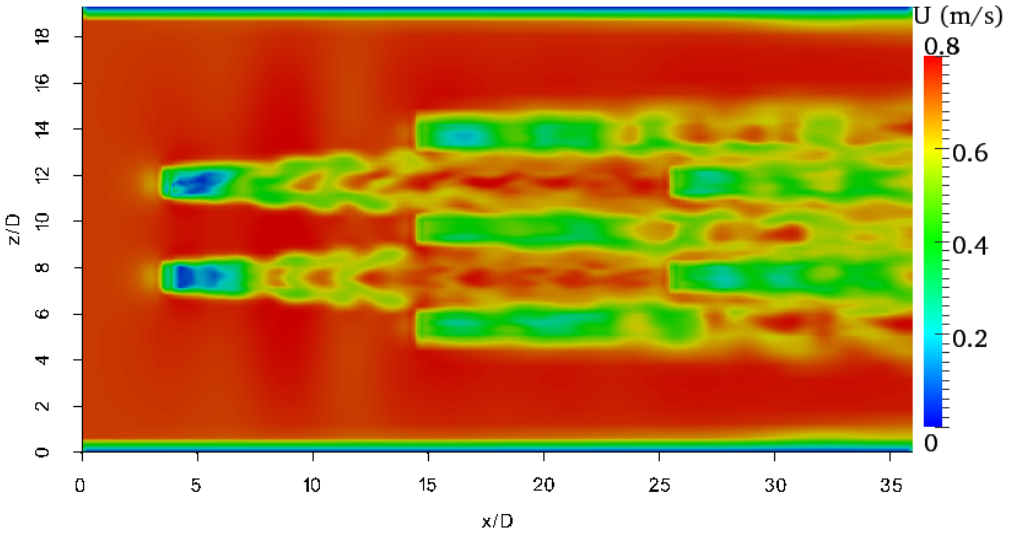

(a) Configuration 71

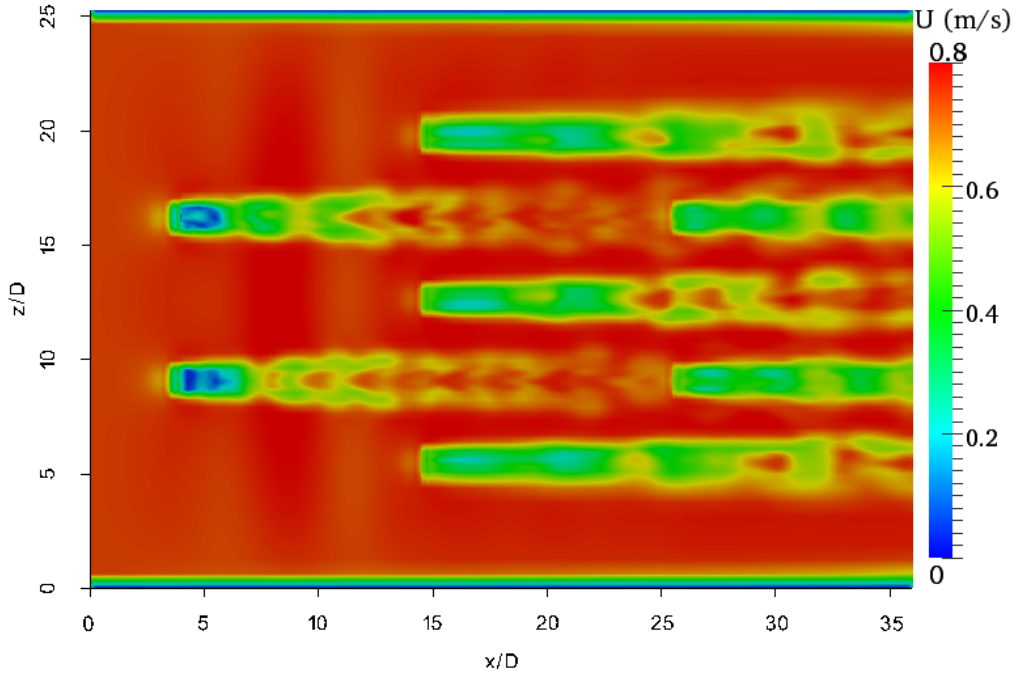

(b) Configuration 72

Figure 5.30: Velocity contours of seven MRL devices

However, there are interesting observations on the velocity deficit downstream of each turbines. A one-dimensional velocity dataset was extracted along the stream direction through the centre of turbine 1 from the four configurations to compare the velocity deficit

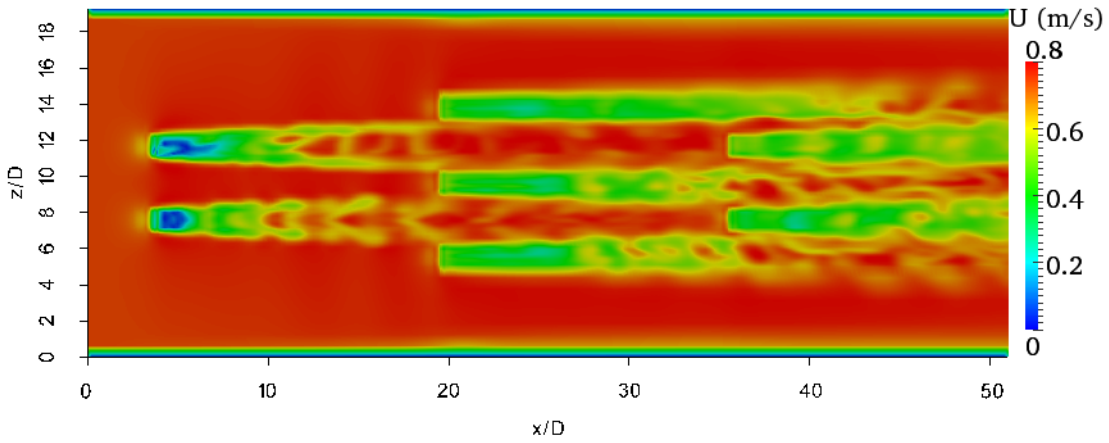

(a) Configuration 73

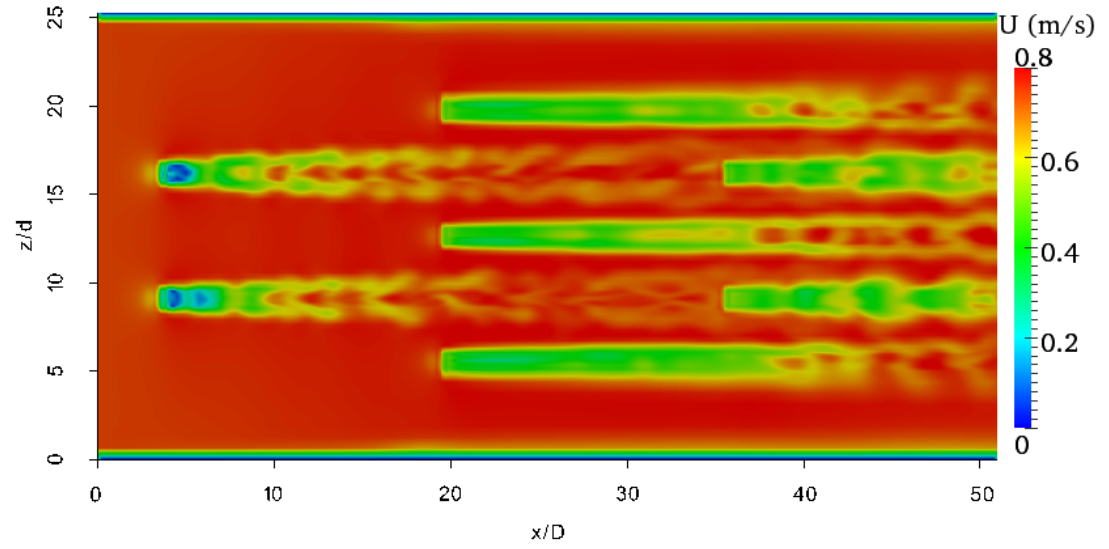

(b) Configuration 74

Figure 5.31: Velocity contours of seven MRL devices

with the base case as shown in Figs. 5.32 and 5.33. The velocity deficit of the turbine in the base case is larger than the velocity deficit of the same turbine in four of the configurations but with different magnitude. The velocity deficit of the turbine in configurations 71 is smaller than the others. The main reason for this difference is due to the venturi flow created by the upstream row turbines which accelerates the flow that reaches turbine 1 and consequently increases the flow through this turbine. Apparently, the wake interaction of the upstream turbine appears to have no effect on this turbine. The second reason is the velocity through turbine 1 can be higher due to the local blockage by turbines 2 and 3 on the same row as discussed in section 5.5.

The wake of the base case recovers faster than the wake of the same turbine simulated

in configurations 71 and 72 as shown in Figs. 5.32a. and 5.32b. This is down to the fact that a higher resistance force gives faster wake recovery compared to lower resistance forces as proved by different studies. This is an indication that the resistance force applied to turbine 1 in the two configurations is small.

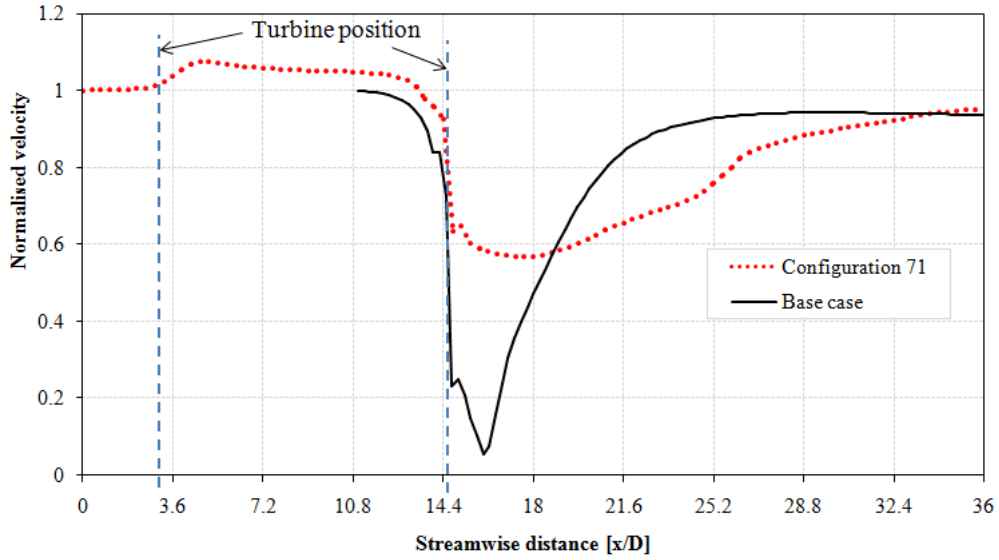

(a) Configuration 71 and base case

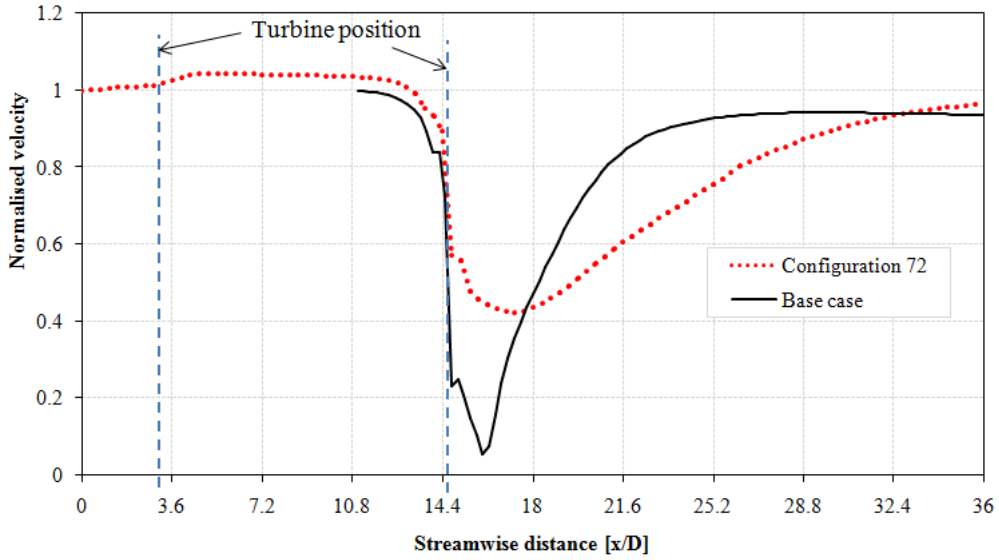

(b) Configuration 72 and base case

Figure 5.32: Comparison of the time averaged centreline velocity profiles of the base case and turbine 1 in configurations 71 and 72

In contrast, the wake of turbine 1 in configurations 73 and 74 recovers faster than the base case beyond 36D as shown in Figs. 5.33a and 5.33b though it is still less than the base case between 26D and 36D. The reason for this difference could be that the velocity

is accelerated because of the venturi flow created by the downstream row of turbines as the wake interaction with these turbines is minimised in these two configurations by increasing both the lateral and longitudinal spacings. However, the wake recovery between 26D and 36D still remains less than the base case due to the low resistance force applied to turbine 1.

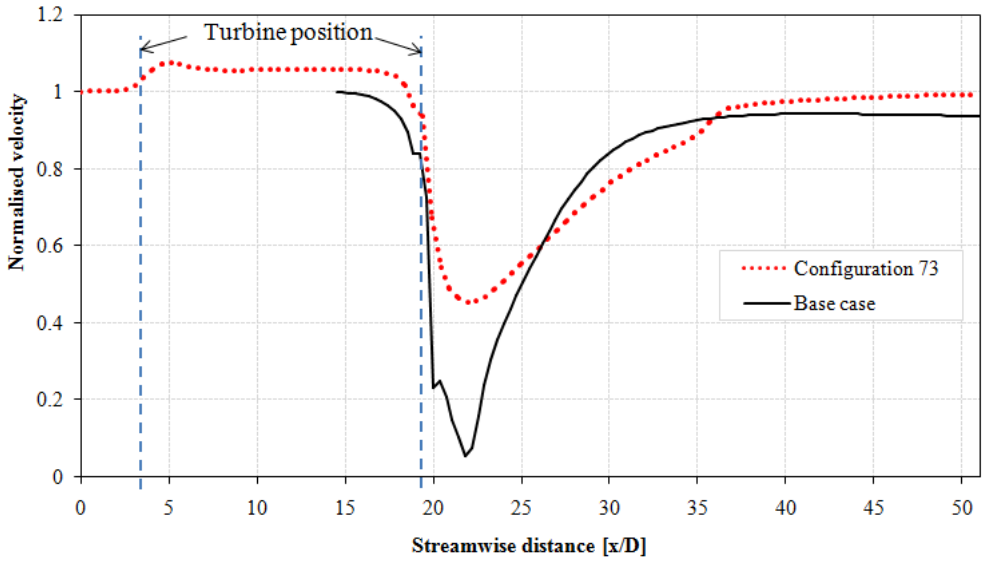

(a) Configuration 73 and base case

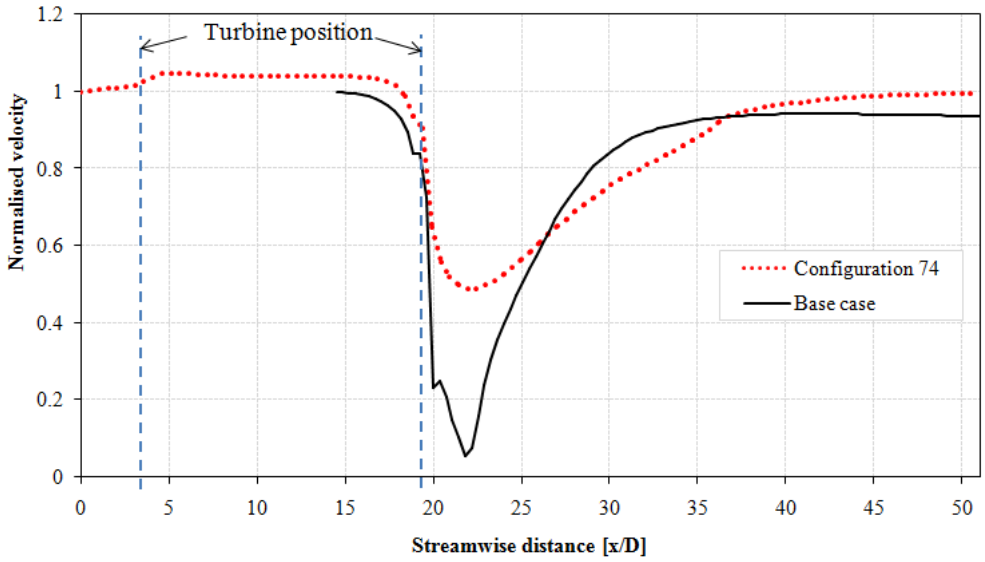

(b) Configuration 74 and base case

Figure 5.33: Comparison of the time averaged centreline velocity profiles of the base case and turbine 1 in configurations 73 and 74

Figs. Figs. 5.34 and 5.35 show an instantaneous velocity profiles extracted at arbitrary time step in order to analyse the fluctuations using the wavelet transform.

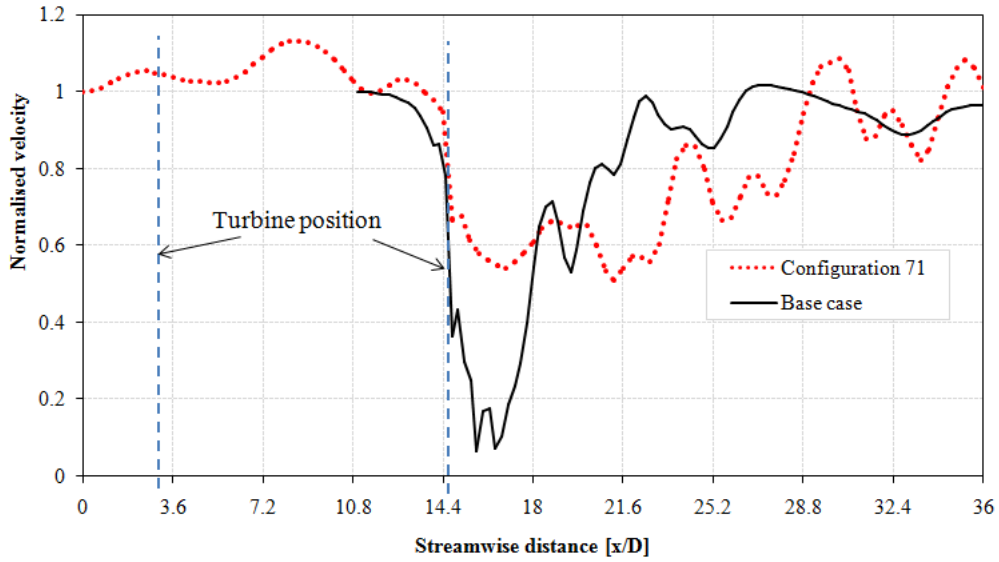

(a) Configuration 71 and base case

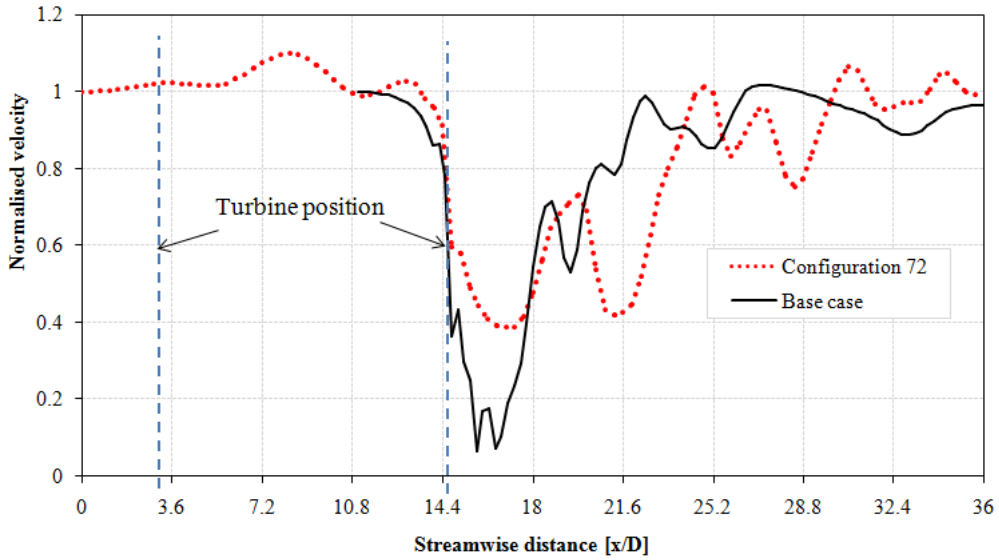

(b) Configuration 72 and base case

Figure 5.34: Comparison of the instantaneous centreline velocity profiles of the base case and turbine 1 in configurations 71 and 72

Fig. 5.36 and 5.37 show the analysed signal (the instantaneous velocity profiles shown in Figs. 5.34 and 5.35) and the corresponding linearly decomposed signals at 3 levels of detail coefficients and one approximation for the four configurations. The detailed coefficients showed that the velocity fluctuations at the end of the domain in configuration 71 (Fig. 5.36a) were higher than in configuration 72 (Fig. 5.36b). These higher fluctuations were due to the mixing of the wake that sustains beyond the end of the computational domain, which was improved in configuration 72. The magnitude of the velocity fluctuation

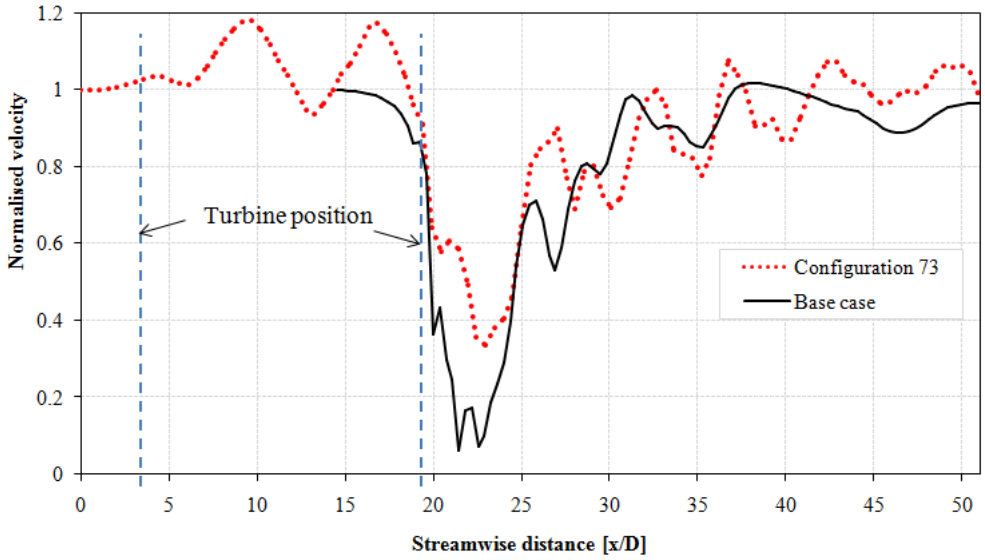

(a) Configuration 73 and base case

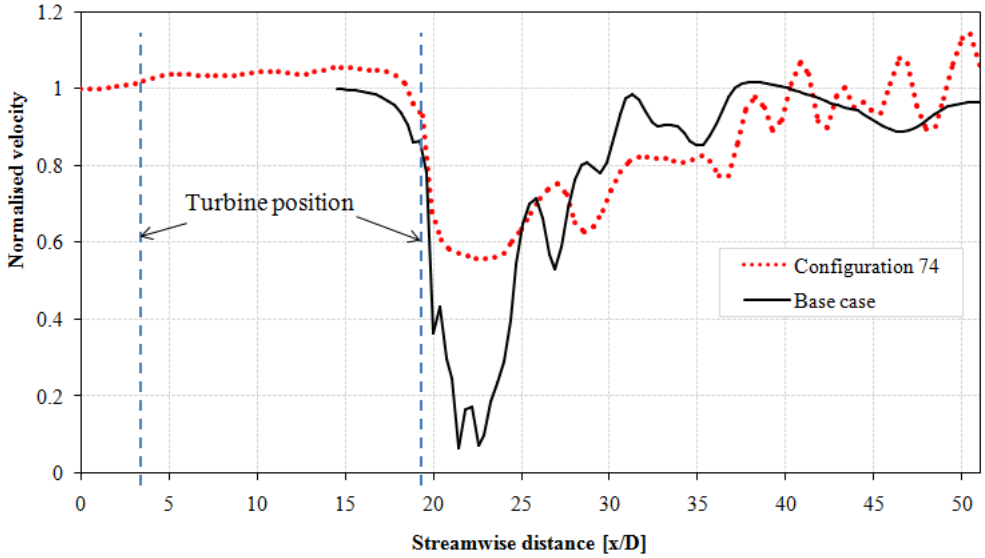

(b) Configuration 74 and base case

Figure 5.35: Comparison of the instantaneous centreline velocity profiles of the base case and turbine 1 in configurations 73 and 74

in configuration 73 (Fig. 5.37a) is smaller compared with configuration 74 (Fig. 5.37b). Thus, the results showed some differences in the four configurations relative to each other with the change of longitudinal and lateral spacing which is mainly due to the influence of wake interactions and blockage effects.

The velocity fluctuations were higher immediately downstream of the turbine and reduced further downstream in all four of the configurations. The fluctuations observed in the four configurations are higher than in the base case (Fig. 5.9).

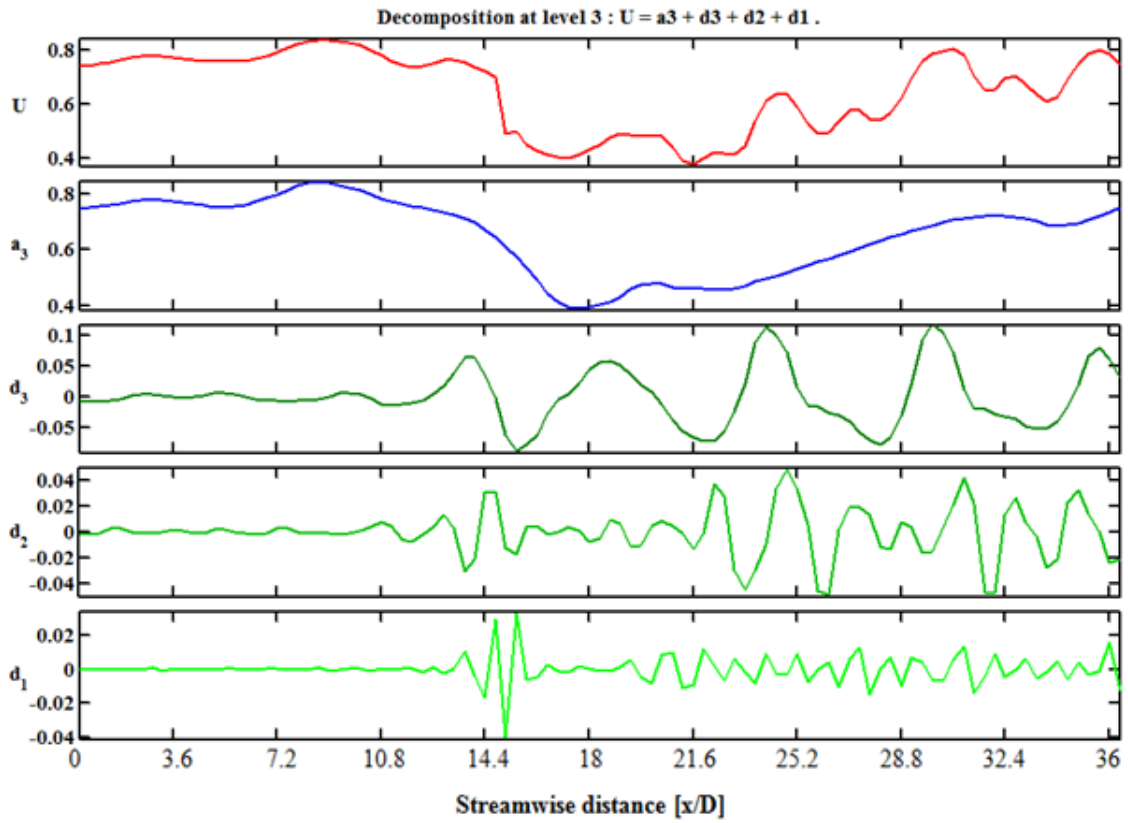

(a) Configuration 71

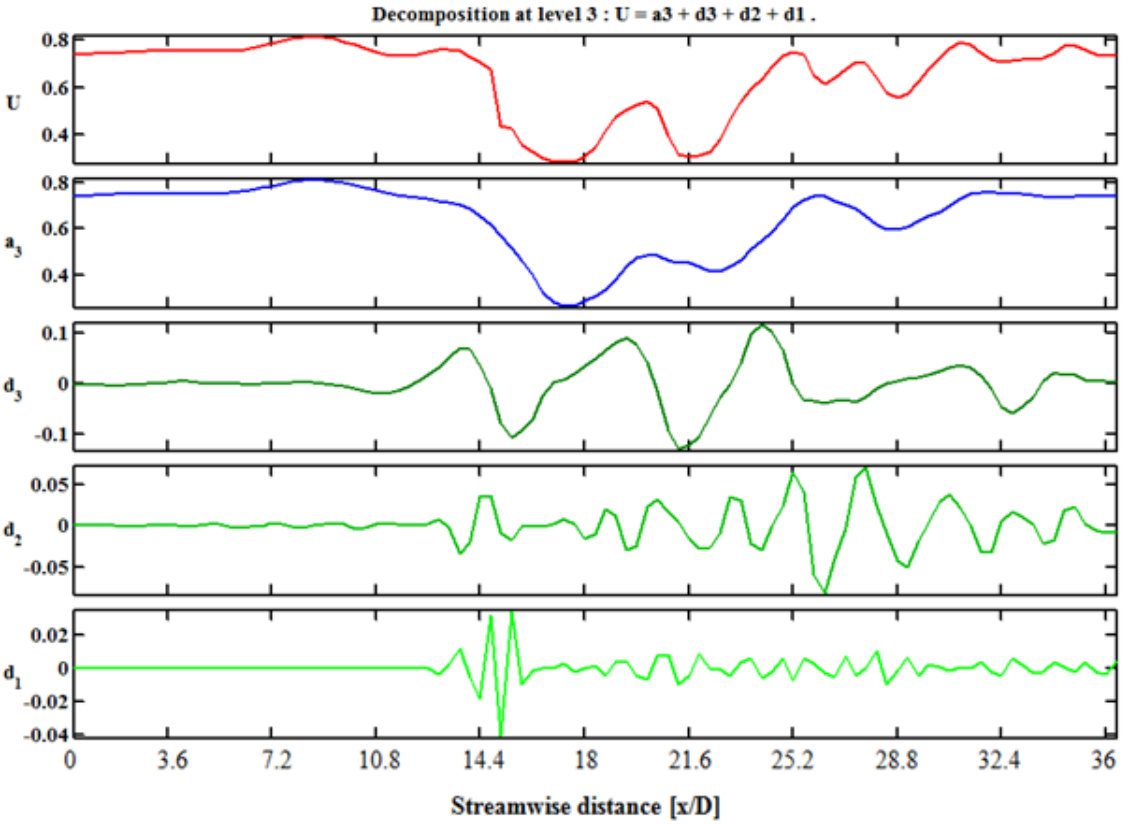

(b) Configuration 72

Figure 5.36: Wavelet coefficients of the centreline velocity through turbine 1

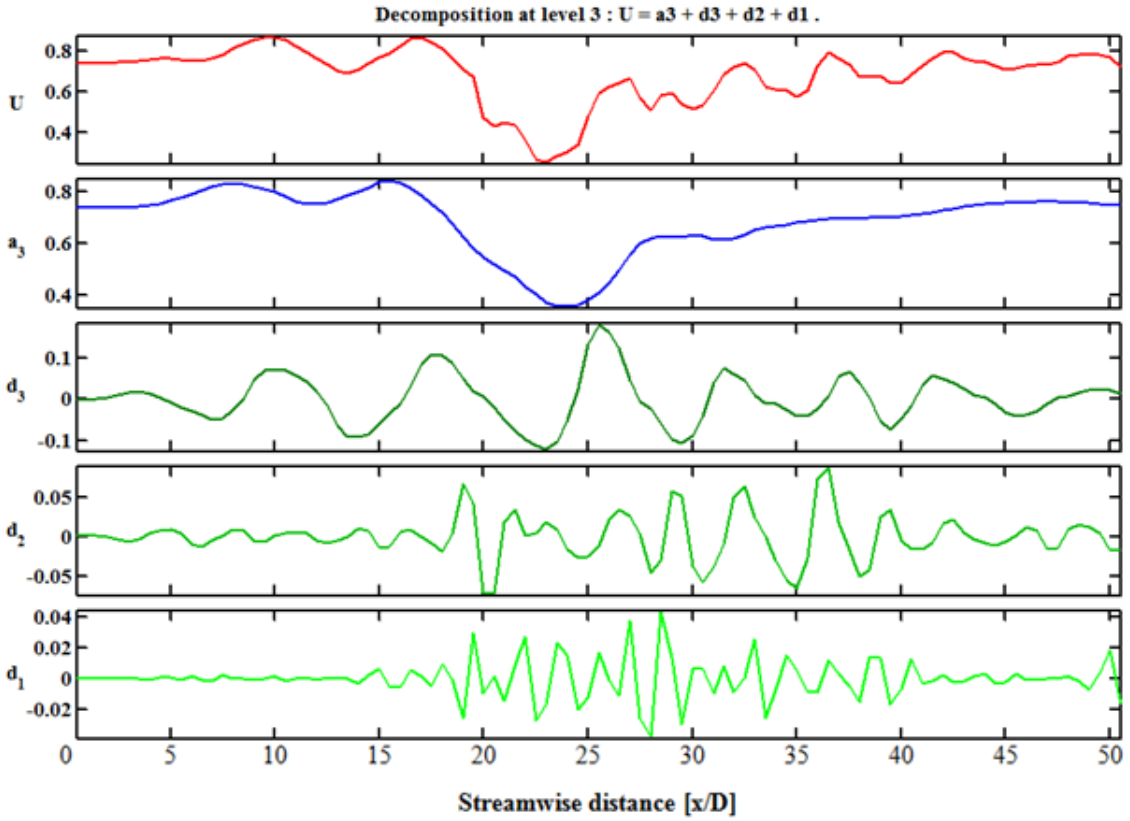

(a) Configuration 73

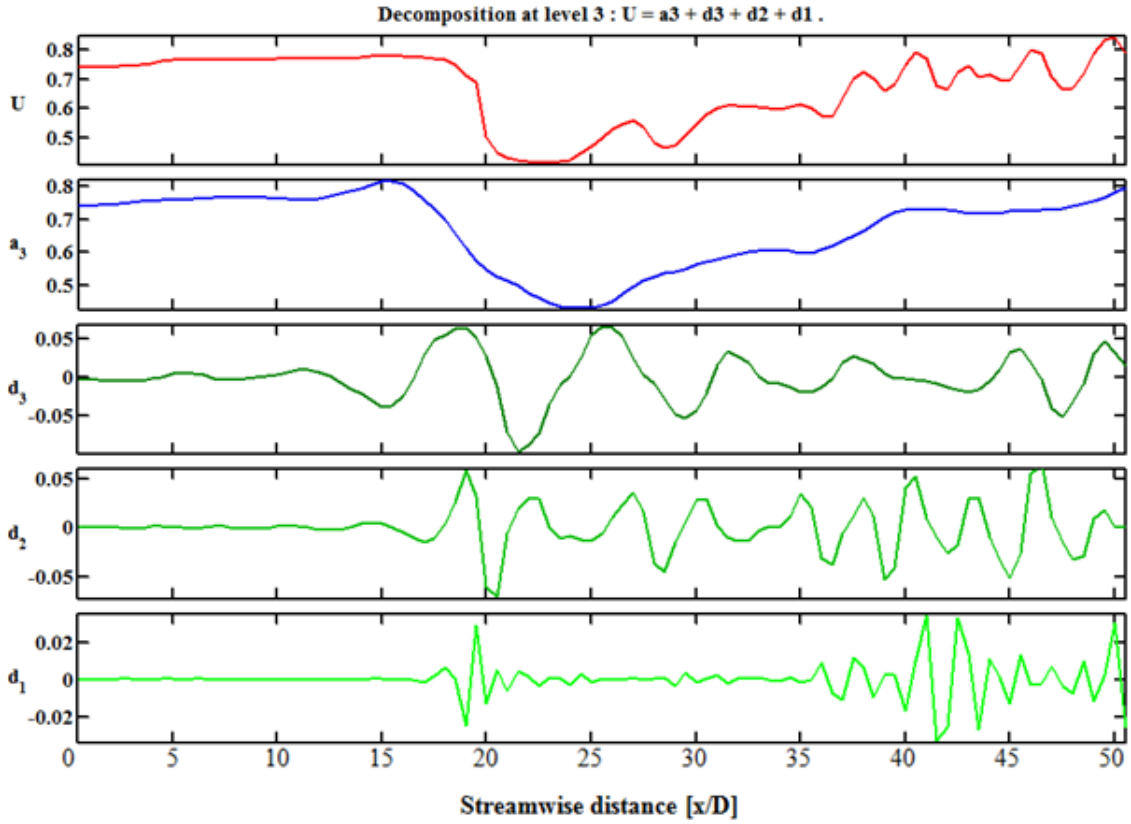

(b) Configuration 74

Figure 5.37: Wavelet coefficients of the centreline velocity through turbine 1

5.7.2 Thrust and Power Analysis

The influence of wake interactions on the performance of turbine 1 and on the individual turbines, both relative to the base case, were analysed by changing both the lateral and longitudinal inter-turbine spacing.

Figs. 5.38 and 5.39 show the thrust and power coefficients of the turbines in the four configurations and the base case. The thrust and power coefficients of turbine 1 in the four configurations are lower than the base case although the values of the same turbine in the four configurations showed some difference. This is due to a combined effect of the following reasons:

- Turbine 1 is experiencing high local incident velocity due to the venturi flow created by the upstream row of turbines.
- The resistance coefficient, $K_L = 0.913$, is lower than it would have been required by turbine 1 due to the high local incident velocity which results the turbine to operate away from its maximum operating point.

There is an indication that the local incident velocity of turbine 1 is higher than the velocity at the inlet of the domain. Thus this would require an even higher resistance coefficient than the value,$K_L = 1.304$, applied to the upstream turbines in order for the turbine to operate around its maximum operating point. The thrust and power coefficient of turbine 1 is also lower than the other two turbines (turbines 2 and 3) in the same row. However, the performance of turbine 1 was expected to be higher than the others due to a high blockage ratio as discussed in the three turbine configurations in section 5.5. The probable reason for this discrepancy may be a combination of lower resistance coefficient and wake interaction from the upstream row of turbines.

In contrast to the performance of turbine 1, the two turbines in the same row (turbines 2 and 3) showed an improved performance but this is still less than the base case. This is an indication that these two turbines are not reaching their maximum operating point either and require higher resistance coefficient than the currently applied value although it may not be the same as the resistance coefficient of the upstream row of turbines. Note that

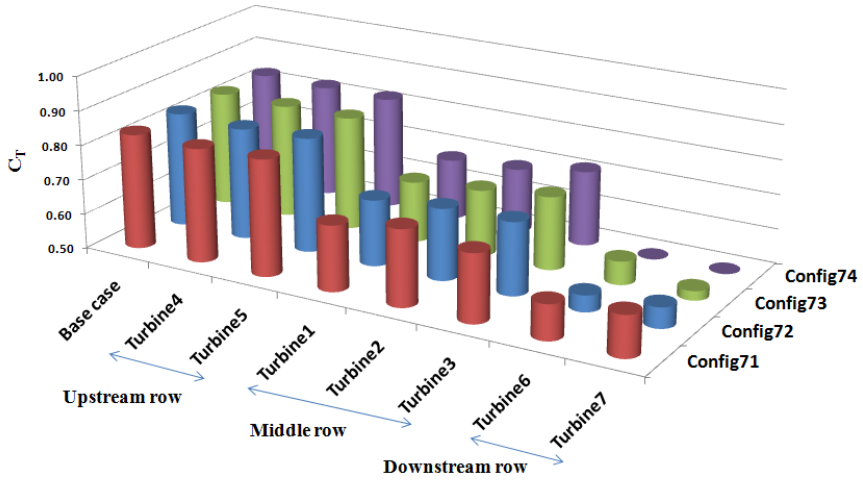

	Base case	Turbine4	Turbine5	Turbine1	Turbine2	Turbine3	Turbine6	Turbine7
Config71	0.833	0.829	0.836	0.690	0.721	0.697	0.602	0.619
Config72	0.833	0.823	0.832	0.691	0.707	0.710	0.548	0.560
Config73	0.833	0.830	0.829	0.676	0.691	0.712	0.568	0.527
Config74	0.833	0.828	0.826	0.677	0.687	0.717	0.454	0.495

Figure 5.38: Comparison of thrust coefficients of the turbines in the base case and the four configurations

the same resistance coefficient, $K_L = 0.913$, was applied to the middle row of turbines (turbines 1, 2 and 3) although the performance of turbine 1 is slightly lower for the reasons discussed.

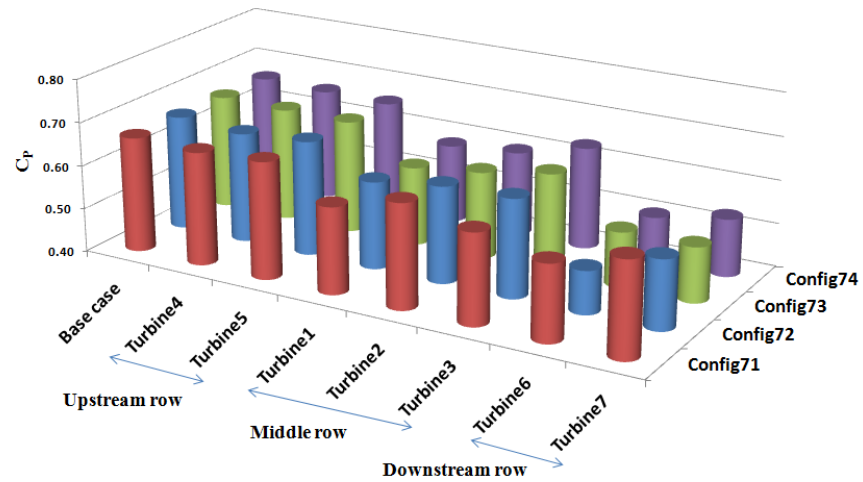

	Base case	Turbine4	Turbine5	Turbine1	Turbine2	Turbine3	Turbine6	Turbine7
Config71	0.665	0.661	0.670	0.599	0.641	0.609	0.575	0.619
Config72	0.665	0.654	0.665	0.602	0.623	0.627	0.500	0.560
Config73	0.665	0.662	0.661	0.582	0.601	0.628	0.527	0.527
Config74	0.665	0.660	0.657	0.583	0.596	0.636	0.505	0.533

Figure 5.39: Comparison of power coefficient of the turbines in the base case and the four configurations

The thrust and power coefficients of the upstream row of turbines (turbines 4 and 5) showed slightly higher values than the base case. This could be due to the local blockage effect which can increase the performance of the turbines. The thrust and power coefficients of the turbine in the configuration with high blockage ratio, $B = 0.045$, (configuration 71) showed slightly higher values compared to the configurations with lower blockage ratio, $B = 0.034$, (configurations 72). Similarly the values in configuration 73,$B = 0.045$, are higher than in configuration 74, $B = 0.034$. The blockage effect by downstream turbine on the upstream turbine observed in the two turbine configuration in section 5.6 appears to be minimal in the seven turbine configuration which could be due to the off-set layout of the upstream row of turbines with the middle row of turbines and a very large longitudinal spacing with the downstream row of turbines.

The thrust and power coefficients of the downstream row of turbines (turbines 6 and 7) are lower than the base case in four of the configurations. These values could be improved by increasing the currently applied resistance coefficient,$K_L = 0.658$. The reasons discussed so far for the low performance of the middle and downstream row of turbines is evident from the velocity contours given in Figs. 5.30 and 5.31. It showed a low velocity deficit downstream of each turbine compared to the velocity deficit of the upstream row of turbines. This shows that there is still room for improvement by changing the resistance coefficient of these turbines in order to obtain their maximum operating point.

5.8 Execution Time of the Simulations

The simulations were carried out using an 8 GB machine and the elapsed CPU time for each configuration is given in table 5.5. These elapsed CPU times are for a time step (*deltaT*) of 5 seconds. The results were compared relative to the elapsed CPU time (0.537 hours) for the simulation of a single turbine (base case). As the number of turbines increased, the computational domain size also increased resulting in a higher CPU time. Even with the same number of turbines, the elapsed CPU time is different from one configuration to the other which is a result of the different computational domain size used. Configuration

74 takes the highest CPU time (7.647 hours) compared with the others due to its large computational domain.

number of Turbines	Configuration	Time step (seconds)	Elapsed CPU time (hours)
1	Base case	5	0.537
2	21	5	0.847
	22	5	0.920
3	31	5	1.189
	32	5	1.463
7	71	5	3.350
	72	5	4.419
	73	5	5.664
	74	5	7.647

Table 5.5: Elapsed CPU time of the CFD simulations

However, based on the elapsed CPU time given in the table, it is difficult to conclude that the IBF model is computationally cheap. The main reason is that there are no other simulation results with the same domain and physical presence of the blades to compare these results, but it is known from experience that a CFD model with a physical presence of the blades can significantly increase the computational power due to the treatment involved to resolve the flow on the surface of the blades as discussed in detail in the previous chapters. In addition, a detailed 2D CFD simulations using dynamic sliding mesh can take more than 10 days for 20 revolutions of the blades (to obtain fully developed wake structure) (personal communication M. Berry). In the case of the IBF model, simulation of a single turbine takes more than 8 hours to obtain fully developed wake structures which is much cheaper than the detailed CFD model even for 3D CFD simulations although both are not directly comparable because of the different computational domains used. Therefore, the information given in this section is only to highlight the execution time taken in the simulation of each configuration.

5.9 Summary

Due to the limited availability of experimental data, the results were compared with a base case simulation to understand the relative influence of additional turbines in a tidal stream farm. This study has provided valuable information on the influence of wake interactions by changing the longitudinal and lateral spacings among the turbines. The investigation of wake interaction showed that a laterally close configuration of turbines could improve the performance of individual turbines due to the blockage effect, which is created by the array of turbines in the cross flow direction. The results also showed a small longitudinal and lateral spacing between turbines can inflict a high energy shadowing that affects the performance of downstream turbines. Therefore, a sufficient longitudinal spacing is required to minimise the wake interactions among the turbines.

However, a tidal stream farm with a staggered turbine layout requires shorter longitudinal spacing and shows an acceleration of flows through the bypass regions which could have a potential advantage in improving the performance of downstream devices by using an appropriate lateral spacing. This confirms previous studies which showed that an off-set layout of turbines have the advantage of using accelerated flows within the tidal stream farm. Thus, the work shows the capability of the IBF model in investigating the inevitable wake interactions which occurs in a tidal stream farm and other related issues.

Chapter 6

CONCLUSIONS AND FUTURE WORK

The main concerns of this study have been to understand the performance of the MRL turbine and the influence of energy extraction to the flow physics, such as the wake structures, wake interactions, free surface dynamics and other associated issues. To investigate this influence, it requires substantial computational power or high investment cost, though it depends on the methods acquired to carry out this study. Several options have arisen to achieve the objectives outlined in this thesis. First, experiments can be used with single and clusters of turbines either in a lab or in a specified site such as the Severn estuary. However, the investment cost to carry out such experiments is extremely high, and is certainly beyond the capacity of this project work. Second, numerical simulations can be performed using an open source CFD software package, OpenFOAM, which is relatively cheaper compared to the experiments though this method is still expensive to simulate several turbines in a tidal stream farm. Thirdly, a parametrised analytic models can be used to estimate the actual limit to power extraction from a stream flow and this method is the cheapest one compared to the previous two methods although it lacks providing detail information of the flow physics due to frequent assumptions made to reduce the number of parameters involved. In this study the CFD approach was used to investigate all the issues related to the MRL turbine. Three turbulent modelling CFD techniques, namely DNS, LES and RANS were reviewed and the DNS appears to be impossible to employ for the MRL simulations considering the currently available computational power. However, it was possible to employ either LES and RANS considering their computational cost, but a comparison of these two modelling techniques with the help of preliminary results and detailed literature review showed that the LES technique has the upper hand in providing a detailed flow physics. Thus the LES technique has been selected for most of the simulations. This chapter is divided into two sections, with the first section being a summary of the research findings and the second section is a recommendation for future

research works.

6.1 Conclusion

Modelling of a detailed blade rotation of tidal turbines as well as clusters of those turbines is extremely computationally expensive although the results obtained from such kind of modelling techniques are expected to be a better description of the detailed flow physics. Thus the use of a relatively cheaper CFD based turbine model was important as this thesis was dealing with a turbine design which has highly complex blade rotations and the simulation of clusters of these devices. A new CFD based IBF model which represents the MRL turbine was therefore developed to minimise the computational cost. This turbine model was thoroughly used to investigate the performance of the MRL turbine and the associated flow characteristics. In general, most of the objectives outlined for this thesis have been achieved although there have not been enough experimental and/or analytical data about the MRL turbine to validate the CFD results. A summary of the main findings of this research work are given in the following sections.

6.1.1 CFD based IBF model

The IBF model was developed based on the concept of actuator disc methodology by incorporating additional geometric features that induce energy absorption from the flow which also lead to a downstream wake structure intended to reflect more closely those of the real turbines than simple momentum sink zone models. Two IBF model approaches (*blade* and *annular*) have been developed and comparison of the results from these approaches showed that the *annular* approach provided better information on the rate of wake recovery, wake structures and other associated issues although this would require a detailed experimental data to validate its fidelity which is not yet available. Thus the conclusions of this thesis are given based on the results from the *annular* approach. In general, the developed IBF model has proved its capability in analysing several issues relating to this design of tidal turbines and achieved the purpose it has been developed for. Some of those issues are:

- The IBF model successfully extracted energy from the flow due to the lift and drag resistance forces applied against the flow.

- The representation of the MRL turbine by the IBF model approach provides enough information about the influence of energy extraction by the turbine to the dynamics of the free surface.

- The IBF model generated large scale vortex structures which would be expected from the real turbines.

- The IBF model successfully examines the sensitivity of flow characteristics within and around the turbine to the change of force loading, geometry width, mesh grid size, and turbulence intensity.

6.1.2 Performance of the MRL turbine

A full range of operating points of the MRL turbine was formulated and a maximum power coefficient of, $C_p = 0.665$, was observed with a blockage ratio of, $B = 0.016$. However, the performance of the turbine was significantly improved at a higher blockage ratio both in the single and tidal stream farm investigations. Thus the power coefficient of a single turbine in the three turbine configuration reached up to, $C_P = 0.761$, at a thrust coefficient, $C_T = 0.911$, which was mainly due to a high blockage ratio of, $B = 0.027$. These results are consistent with other studies which showed that the limit of power extraction of tidal turbines can be higher than the Lanchester-Betz limit of $C_P = 0.593$ obtained at $B = 0$, which is mainly due to the tidal turbine operating in a constrained environment, high blockage ratio, that increases the thrust force on the device.

The power coefficient of the IBF model showed consistently higher values compared to the experiments and a detailed CFD model results. This is an indication that the power coefficient calculated using the IBF model contains some other losses within the turbine region, such as losses due to viscous, shear etc. The comparison allowed to estimate the power loss in addition to the useful power extracted by the turbine. A range of issues regarding the power extraction by the turbine have been investigated and are summarised

as follows:

- The performance of the MRL turbine designed with side plates was increased due to the venturi flow created by the presence of the plates.
- The performance of single turbine simulated with a blockage ratio, $B = 0.029$, was 3% greater than the performance of the same turbine simulated with a blockage ratio, $B = 0.016$.
- A laterally close configuration of turbines also improved the performance of individual turbines due to the blockage effect, which is created by the array of turbines in the cross flow direction.
- A small longitudinal spacing between turbines inflicted a massive energy shadowing that affects the performance of downstream turbines.
- In the tidal stream farm, accelerated flow regions were observed which would have a positive influence on increasing the performance of turbines deployed on those regions.
- The effect of blade positions on the performance of the turbine was investigated to understand if the fixed blade positions have a significant impact on the results. This was important due to the fact that the CFD simulations have to be carried out at arbitrary blade positions. The result showed no significant difference in the performance of the turbine.
- The energy flux along the streamwise direction showed the unavoidable energy loss during remixing of the flows and provides important information to understand the influence on any downstream devices due to operating in the wake of upstream turbines.

6.1.3 Flow Field Features

The influence of energy extraction on the general flow features within and around the MRL turbine was thoroughly investigated at different conditions and the main findings about the

flow features are:

- The bypass flow beneath and top of a single turbine was highly affected while the influence of the turbine on the side bypass flow was minimal. However, in arrays of devices the side bypass flow heavily depends on how closely the devices are configured. A small lateral spacing created accelerated bypass flow regions.
- The investigation of the flow characteristics of the two MRL turbine designs (with and without side plates) showed that the turbine with side plates has a faster wake recovery, making it a better option for further large scale development. It shows a wake recovery of around 92% of the stream flow at 20D downstream of the turbine.
- The influence of energy extraction by the turbine to the dynamics of the free surface was analysed by simulating the turbine at three different turbine positions. The result showed that the turbine close to the free surface has a massive impact on the surface deformation and showed a large head drop immediately downstream of the turbine compared with the same turbine simulated at a deeper position.
- A sufficient longitudinal spacing is required to minimise the wake interactions among the turbines. A tidal stream farm with a staggered turbine layout can reduce the longitudinal spacing by about 50% with a minimum of 6D lateral spacing compared with a regular turbine layout due to the advantage of using bypass flows.
- A complex and sheared internal flow was observed within the turbine region.
- The rate of wake recovery was increased with a higher thrust/resistance force applied by the turbine against the flow. This was similar to other studies which showed that the performance of downstream turbines in a tidal stream farm can be improved due to a fast wake recovery because of high thrust resulting in less wake interaction.

6.1.4 Limitations of this Research

Although the research has achieved its objectives, an unavoidable limitation has been identified which could have strengthened the findings of this research. An important

limitation in this research is the absence of a detailed experimental or analytical data about the MRL turbine. An effort has been made to validate the energy extraction by the IBF model to preliminary experimental and detailed CFD modelling data provided by Janssen and by Berry however there is no data available related to the flow features of the MRL turbine, such as inlet velocity profile, wake structures, free surface dynamics etc.

Thus due to a limited availability of experimental data, the results were mostly compared with a base case simulation especially in the tidal stream farm investigations carried out to understand the relative influence of additional turbines and the change of longitudinal and lateral spacings to the general flow field and performance of the turbines. In addition, an approximate power law inlet velocity profile which is commonly used in the simulation of tidal turbines was implemented as the site for the deployment of the MRL turbine is not yet identified. In the future, a rigorous experimental study to obtain a detailed flow physics of the MRL turbine and its performance both for a single and clusters of devices could make it possible to develop stronger conclusions on the newly developed IBF model.

6.2 Future Work

The findings of this study can be improved and expanded in many ways, mainly in the areas of experiments, detailed CFD models of the blade motions, and analytical work. The recommendations proposed for future works are as follows:

6.2.1 Experiments

An experimental study was carried out by Janssen and Belmont to establish the efficiency of a single MRL turbine, which was used as a validation for the CFD results in this study. However, more experimental work is required on a single and clusters of turbines either in a small channel or in other selected sites such as the seven estuary:

- To establish a full range of operating points for a single MRL turbine in different working environments, such as in channels which have different blockage ratio.
- To understand the length scale and energy remixing downstream of a single turbine

and the general flow features through and around the turbine such as the complex and sheared internal flows, wake structures, free surface dynamics.

- To measure the energy loss in the remixing region downstream of the turbine.
- To understand the influence of wake interaction both on the performance of individual turbines and on the flow features of a cluster of turbines in a tidal stream farm.
- To establish the inlet velocity profiles in a selected site for the deployment of the MRL turbine.

The outcomes from this work can inform all aspects of numerical modelling work on this area and also provide data for validation purposes.

6.2.2 CFD Direction

The studies carried out in this thesis were mainly focused on the modelling of a cluster of turbines to understand the wake interactions by opting to use a fairly simplified CFD model to minimise the computational cost. However, it is equally important to understand the detailed blade motions though this could inflict a huge computational cost if attempted to use in the simulation of several devices. The following are the recommendations proposed for future work in the CFD directions:

- A detailed CFD description of the blade motions using either the overset meshing or the General Grid Interface (GGI) method (which is the subject of another PhD project currently under-way in Exeter). Some preliminary results have already been used for comparisons as discussed previously. The outcomes of this modelling method will be:
  - The relationship between turbine loading and momentum absorption zone and the associated turbine vortex and
  - Length scale and energy remixing distance downstream of the turbine

Detailed results of this method can be used to validate the IBF model of a single turbine to build the confidence of using this model in the simulation of tidal stream devices.

- CFD simulations of a large scale MRL turbine using the IBF model to investigate the scalability effect on the results.

- Simulation of the MRL turbine using experimentally measured inlet velocity profile from a site selected for the deployment of this device and comparing with the results obtained using the power law velocity profile.

6.2.3 Analytical Modelling

Analytical modelling can be used to understand the performance of tidal turbines and the flow features although the results that can be obtained from this method is not as reliable as the experiments and CFD methods because of the frequent assumptions employed to reduce the number of parameters involved. However, it is widely used due to its simplicity and cheaper computational cost especially in the investigation of blockage effects of clusters of devices. Thus the following analytical modelling can be carried out to understand the performance of a single and clusters of devices and to optimise their locations for maximum power output:

- Development of analytic models to establish a full range of operating points of a single MRL turbine

- Development of analytic models to estimate the total power extracted by each turbine in a tidal stream farm containing ideally for tenth and hundreds of turbines taking into consideration the influence of wake interaction on the performance of downstream devices.

- Formulation of analytic sub models to describe the wake velocity profiles of a single and individual turbines in a tidal stream farm taking into consideration the influence of wake interaction on the wake velocity profile of downstream devices.

- Development of a new approach for describing the global flow associated with a tidal stream farm containing up to several hundred separate unit based devices, incorporating bathymetry and entry/discharge conditions.

- Optimisation of the spatial distribution of tidal stream devices in a tidal stream farm subject to both economic and environmental constraints. The parametrised analytic models can be used as an input functions to the optimisation tools.

The parametrised analytic models could be used as a basis for further studies such as for validation of other numerical modellings.

Bibliography

P.S. Addison. *The illustrated wavelet transform handbook: introductory theory and applications in science, engineering, medicine and finance*. Taylor & Francis, 2002.

P.S. Addison. Wavelet transforms and the ECG: a review. *Physiological measurement*, 26: R155, 2005.

John F Ainslie. Calculating the flowfield in the wake of wind turbines. *Journal of Wind Engineering and Industrial Aerodynamics*, 27(1):213–224, 1988.

B. Andrew. Phase II Tidal Stream Energy Assessment. Technical report, Technical Report 107799/D/2200/03,Black and Veatch Ltd on behalf of Carbon Trust, 2005.

M. Asif and T. Muneer. Energy supply, its demand and security issues for developed and emerging economies. *Renewable and Sustainable Energy Reviews*, 11(7):1388–1413, 2007.

AS Bahaj and LE Myers. Fundamentals applicable to the utilisation of marine current turbines for energy production. *Renewable energy*, 28(14):2205–2211, 2003.

AS Bahaj, LE Myers, RI Rawlinson-Smith, and M. Thomson. The effect of boundary proximity upon the wake structure of horizontal axis marine current turbines. *Journal of offshore mechanics and Arctic engineering*, 134(2), 2012.

L. Bai, R.R.G. Spence, and G. Dudziak. Investigation of the influence of array arrangement and spacing on tidal energy converter (TEC) performance using a 3-dimensional CFD model. In *Proceedings of the 8th European Wave and Tidal Energy Conference, Uppsala, Sweden*, 2009.

J. Bardino, J.H. Ferziger, and W.C. Reynolds. Improved turbulence models based on large eddy simulation of homogeneous, incompressible turbulent flows. *Stanford Univ. Report*, 1, 1983.

Rebecca Barthelmie, Gunner Larsen, Sara Pryor, Hans Jørgensen, Hans Bergström, Wolfgang Schlez, Kostas Rados, Bernhard Lange, Per Vølund, Søren Neckelmann, et al.

Endow (efficient development of offshore wind farms): modelling wake and boundary layer interactions. *Wind Energy*, 7(3):225–245, 2004.

Rebecca Jane Barthelmie, Ole Rathmann, Sten Tronæs Frandsen, KS Hansen, E Politis, J Prospathopoulos, K Rados, D Cabezon, W Schlez, J Phillips, et al. Modelling and measurements of wakes in large wind farms. In *Journal of Physics: Conference Series*, volume 75, page 012049. IOP Publishing, 2007.

Rebecca Jane Barthelmie, K Hansen, Sten Tronæs Frandsen, Ole Rathmann, JG Schepers, W Schlez, J Phillips, K Rados, A Zervos, ES Politis, et al. Modelling and measuring flow and wind turbine wakes in large wind farms offshore. *Wind Energy*, 12(5):431–444, 2009.

RJ Barthelmie, GC Larsen, ST Frandsen, L Folkerts, K Rados, SC Pryor, B Lange, and G Schepers. Comparison of wake model simulations with offshore wind turbine wake profiles measured by sodar. *Journal of Atmospheric and Oceanic Technology*, 23(7): 888–901, 2006.

WMJ Batten and AS Bahaj. Cfd simulation of a small farm of horizontal axis marine current turbines. In *Proceedings World Renewable Energy Congress WREC IX*. Elsevier Science, 2006.

WMJ Batten, AS Bahaj, AF Molland, and JR Chaplin. The prediction of the hydrodynamic performance of marine current turbines. *Renewable energy*, 33(5):1085–1096, 2008.

R. Bedard, M. Previsic, O. Siddiqui, G. Hagerman, and M. Robinson. Survey and characterization tidal in stream energy conversion (TISEC) devices. *EPRI Final Report, EPRI-TP-004 NA*, 2005.

C.S.K. Belloni and R.H.J. Willden. Flow field and performance analysis of bidirectional and open-centre ducted tidal turbines. In *9th European Wave and Tidal Energy Conference*, 2011.

SE Ben Elghali, MEH Benbouzid, and JF Charpentier. Marine tidal current electric power generation technology: State of the art and current status. In *Electric Machines & Drives*

Conference, 2007. IEMDC'07. IEEE International, volume 2, pages 1407–1412. IEEE, 2007.

M. Berry and G.R. Tabor. CFD analysis of a single mrl tidal turbine. In *Proceedings of the Annual Assembly of the SuperGen UK Center*, 2012.

A. Betz. Das Maximum der theoretisch moglichen Ausnutzung des Windes durch Windmotoren. *Zeitschrift fur das gesamte Turbinenwesen*, 26:307–309, 1920.

J. Blazek. *Computational fluid dynamics: principles and applications*. Elsevier Science, 2001.

LS Blunden and AS Bahaj. Tidal energy resource assessment for tidal stream generators. *Proceedings of the Institution of Mechanical Engineers, Part A: Journal of Power and Energy*, 221(2):137–146, 2007.

J. Boussinesq. Théorie de l'écoulement tourbillant (theories of swirling flow), mém. prés. par div. savants à l'acad. *Sci. Paris*, 23, 1877.

M. Breuer, N. Jovičić, and K. Mazaev. Comparison of DES, RANS and LES for the separated flow around a flat plate at high incidence. *International journal for numerical methods in fluids*, 41(4):357–388, 2003.

Marc Calaf, Charles Meneveau, and Johan Meyers. Large eddy simulation study of fully developed wind-turbine array boundary layers. *Physics of Fluids*, 22:015110, 2010.

J. Callaghan and R. Boud. *Future marine energy: results of the marine energy challenge: cost competitiveness and growth of wave and tidal stream energy*. Carbon Trust, 2006.

I Celik. Introductory turbulence modeling. *Western Virginia University Class Notes*, 1999.

Y.A. Cengel and J.M. Cimbala. *Fluid mechanics*. Tata McGraw-Hill Education, 2010.

M.H. Chaudhry. *Open-channel flow*. Springer Verlag, 2008.

G. Chen, C. Kharif, S. Zaleski, and J. Li. Two-dimensional navier–stokes simulation of breaking waves. *Physics of fluids*, 11:121, 1999.

Y. Cheng, FS Lien, E. Yee, and R. Sinclair. A comparison of large eddy simulations with a standard¡ i¿ k¡/i¿−¡ i¿ ε¡/i¿ reynolds-averaged navier–stokes model for the prediction of a fully developed turbulent flow over a matrix of cubes. *Journal of Wind Engineering and Industrial Aerodynamics*, 91(11):1301–1328, 2003.

C.L. Chiu and N.C. Tung. Maximum velocity and regularities in open-channel flow. *Journal of hydraulic engineering*, 128(4):390–398, 2002.

M.J. Churchfield, Y. Li, and P.J. Moriarty. A large-eddy simulation study of wake propagation and power production in an array of tidal-current turbines. 2011.

P. Clark, R. Klossner, and L. Kologe. Tidal energy. *EMS PSU EDU*, 13, 2003.

JA Clarke, G. Connor, AD Grant, C. Johnstone, and D. Mackenzie. Development of a contra-rotating tidal current turbine and analysis of performance. 2007.

DP Coiro, U. Maisto, F. Scherillo, S. Melone, and F. Grasso. Horizontal axis tidal current turbine: numerical and experimental investigations. In *Proceeding of Offshore wind and other marine renewable energies in Mediterranean and European seas, European seminar, Rome, Italy*, 2006.

P. Cooper and O.C. Kennedy. Development and analysis of a novel vertical axis wind turbine. 2004.

T. Craft, S. Gant, A. Gerasimov, H. Iacovides, and B. Launder. Wall functions strategies for use in turbulent flow CFD. *Heat transfer*, 1:3–14, 2002.

TJ Craft, AV Gerasimov, BE Launder, and CME Robinson. A computational study of the near-field generation and decay of wingtip vortices. *International journal of heat and fluid flow*, 27(4):684–695, 2006.

T. Daly, L.E. Myers, and A.B.S. Bahaj. Experimental investigation of the effects of the presence and operation of tidal turbine arrays in a split tidal channel. *Volume 9 Marine and Ocean Technology*, page 2262, 2011.

L. Davidson and S.H. Peng. Hybrid les-rans modelling: a one-equation sgs model combined with ak–ω model for predicting recirculating flows. *International Journal for Numerical Methods in Fluids*, 43(9):1003–1018, 2003.

B.V. Davis. Low head tidal power: a major source of energy from the worlds oceans. In *Energy Conversion Engineering Conference, 1997. IECEC-97., Proceedings of the 32nd Intersociety*, volume 3, pages 1982–1989. IEEE, 1997.

J.W. Deardorff. A numerical study of three-dimensional turbulent channel flow at large reynolds numbers. *J. Fluid Mech*, 41(2):453–480, 1970.

A. Dejoan, JL Santiago, A. Martilli, F. Martin, and A. Pinelli. Comparison between large-eddy simulation and reynolds-averaged navier–stokes computations for the must field experiment. part ii: effects of incident wind angle deviation on the mean flow and plume dispersion. *Boundary-layer meteorology*, 135(1):133–150, 2010.

S. Donovan. Wind farm optimization. *University of Auckland, Dept. Engineering Science*, 2005.

NG Douglas, NM Robinson, EM Leeming, and SH Hall. WINDOPS: a new PC-based approach for windfarm design and optimization. In *Wind Energy Conversion 1997: Proceedings of the 19th British Wind Energy Association Conference, Heriot-Watt University, Edinburgh, UK, 16-18 July 1997*, page 51. Wiley, 1998. ISBN 1860580823.

S. Draper, GT Houlsby, MLG Oldfield, and AGL Borthwick. Modelling tidal energy extraction in a depth-averaged coastal domain. *Renewable Power Generation, IET*, 4(6): 545–554, 2010.

K. Dyer. Coastal and estuarine sediment dynamics. *JOHN WILEY AND SONS, CHICHESTER, SUSSEX(UK), 1986, 358*, 1986.

DA Egarr, T. ODoherty, S. Morris, and RG Ayre. Feasibility study using computational fluid dynamics for the use of a turbine for extracting energy from the tide. In *15th Australasian Fluid Mechanics Conference, The University of Sydney, Sydney, Australia*, 2004.

C.N. Elkinton, J.F. Manwell, and J.G. McGowan. Optimizing the Layout of Offshore Wind Energy Systems. *Marine Technology Society officers*, 42(2):19, 2008.

V. Eswaran and SB Pope. Direct numerical simulations of the turbulent mixing of a passive scalar. *Physics of Fluids*, 31(3):506–520, 1988a.

V. Eswaran and SB Pope. An examination of forcing in direct numerical simulations of turbulence. *Computers & Fluids*, 16(3):257–278, 1988b.

M. Farge. Wavelet transforms and their applications to turbulence. *Annual Review of Fluid Mechanics*, 24(1):395–458, 1992.

J. Fenton. Open channel hydraulics. *Institut für Hydromechanik, Universität Karlsruhe*, 2005.

J.H. Ferziger and M. Perić. *Computational methods for fluid dynamics*, volume 2. Springer Berlin, 1999.

EJ Finnemore, JB Franzini, and RL Daugherty. Fluid mechanics with engineering applications. 2002. *McGraw-Hill, ISBN 0*, 7:112196.

H.B. Fischer. Longitudinal dispersion and turbulent mixing in open-channel flow. *Annual Review of Fluid Mechanics*, 5(1):59–78, 1973.

C.F. Fleming, S.C. McIntosh, and R.H.J. Willden. Design and analysis of a bi-directional ducted tidal turbine. In *9th European Wave and Tidal Energy Conference*, 2011.

G.L.T. Fo. The state of art of hydrokinetic power in brazil. 2003.

Doerte Fouquet and Thomas B Johansson. European renewable energy policy at crossroadsfocus on electricity support mechanisms. *Energy Policy*, 36(11):4079–4092, 2008.

P.L. Fraenkel. Tidal current energy technologies. *Ibis*, 148:145–151, 2006.

J.P. Frau. Tidal energy: promising projects: La rance, a successful industrial-scale experiment. *Energy Conversion, IEEE Transactions on*, 8(3):552–558, 1993.

S. Gant and T. Stallard. Modelling a tidal turbine in unsteady flow. In *Proceedings of the Eighteenth (2008) International Offshore and Polar Engineering Conference*, pages 473–479, 2008.

C. Garrett and P. Cummins. The efficiency of a turbine in a tidal channel. *Journal of Fluid Mechanics*, 588:243–251, 2007. ISSN 0022-1120.

M. Germano, U. Piomelli, P. Moin, and W.H. Cabot. A dynamic subgrid-scale eddy viscosity model. *Physics of Fluids A: Fluid Dynamics*, 3:1760, 1991.

J. Giles, L. Myers, A.B. Bahaj, and B. Shelmerdine. The downstream wake response of marine current energy converters operating in shallow tidal flows. 2011.

P. Givi. Model-free simulations of turbulent reactive flows. *Progress in energy and combustion science*, 15(1):1–107, 1989.

L. Gordon. Mississippi river discharge. *RD Instruments, San Diego, Calif*, 1992.

A.M. Gorlov. The helical turbine and its applications for tidal and wave power. In *OCEANS 2003. Proceedings*, volume 4, pages 1996–Vol. IEEE, 2003.

A.M. Gorlov and V.M. Silantyev. Limits of the turbine efficiency for free fluid flow. *Journal of energy resources technology*, 123:311–317, 2001.

P Gousseau, B Blocken, T Stathopoulos, and GJF Van Heijst. Cfd simulation of near-field pollutant dispersion on a high-resolution grid: a case study by les and rans for a building group in downtown montreal. *Atmospheric Environment*, 45(2):428–438, 2011.

AS Grinspan, P. Suresh Kumar, UK Saha, P. Mahanta, DV Ratna Rao, and G. Veda Bhanu. Design, development and testing of savonius wind turbine rotor with twisted blades. *Department of Mechanical Engineering, Indian Institute of Technology. Guwahati, India*, 2001.

R. Gross, M. Leach, and A. Bauen. Progress in renewable energy. *Environment International*, 29(1):105–122, 2003.

A. Grossmann and J. Morlet. Decomposition of hardy functions into square integrable wavelets of constant shape. 1984.

G. Hagerman, B. Polagye, C.R. Bedard, and M. Previsic. Methodology for estimating tidal current energy resources and power production by tidal in-stream energy conversion (TISEC) devices. 2006.

Fujihiro Hamba. An attempt to combine large eddy simulation with the k-ε model in a channel-flow calculation. *Theoretical and computational fluid dynamics*, 14(5):323–336, 2001.

ME Harrison, WMJ Batten, and AS Bahaj. A blade element actuator disc approach applied to tidal stream turbines. In *OCEANS 2010*, pages 1–8. IEEE, 2010a.

ME Harrison, WMJ Batten, LE Myers, and AS Bahaj. Comparison between CFD simulations and experiments for predicting the far wake of horizontal axis tidal turbines. *Renewable Power Generation, IET*, 4(6):613–627, 2010b.

X. He, S. Chen, and R. Zhang. A lattice boltzmann scheme for incompressible multiphase flow and its application in simulation of rayleigh-taylor instability. *Journal of Computational Physics*, 152(2):642–663, 1999.

C. Hirsch. *Numerical computation of internal and external flows: the fundamentals of Computational Fluid Dynamics*, volume 1. Butterworth-Heinemann, 2007.

C.W. Hirt and B.D. Nichols. Volume of fluid (VOF) method for the dynamics of free boundaries. *Journal of computational physics*, 39(1):201–225, 1981.

GT Houlsby, S. Draper, and MLG Oldfield. Application of linear momentum actuator disc theory to open channel flow. Technical report, Technical Report 2296-08, OUEL, 2008.

GT Houlsby, MLG Oldfield, and MD. McCulloch. Transverse horizontal axis water turbine, tidal energy research group (oxford university), available at:. `http://www.eng.ox.ac.uk/tidal/research/thawt`, 2011.

Thomas JR Hughes, Assad A Oberai, and Luca Mazzei. Large eddy simulation of turbulent channel flows by the variational multiscale method. *Physics of Fluids*, 13:1784, 2001.

G. Iaccarino, A. Ooi, PA Durbin, and M. Behnia. Reynolds averaged simulation of unsteady separated flow. *International Journal of Heat and Fluid Flow*, 24(2):147–156, 2003.

Subhash C Jain. *Open-channel flow*. Wiley, 2000.

A.P. Janssen and M.R. Belmont. Initial research phase of MRL turbine. Technical report, Technical Report N0:MO 562L, 2009.

H. Jasak. Multi-physics simulations in continuum mechanics. In *Proceedings of 5th International Conference of Croatian Society of Mechanics, Trogir, page*, 2006.

H. Jasak, A. Jemcov, and Z. Tukovic. Openfoam: A c++ library for complex physics simulations. In *International Workshop on Coupled Methods in Numerical Dynamics, IUC, Dubrovnik, Croatia*, 2007.

C. Jo, J. Yim, K. Lee, and Y. Rho. Performance of horizontal axis tidal current turbine by blade configuration. *Renewable Energy*, 42:195–206, 2012a.

Chul Hee Jo, Kang H Lee, Jun H Lee, and Cristian Nichita. Multi-arrayed tidal current energy farm and the integration method of the power transportation. In *Power Electronics, Electrical Drives, Automation and Motion (SPEEDAM), 2012 International Symposium on*, pages 1428–1431. IEEE, 2012b.

Richard W Johnson. *Handbook of fluid dynamics*. CRC, 1998.

B. Jürgens and H.J. Heinke. Voith schneider propeller (VSP)-investigations of the cavitation behaviour. In *First International Symposium on Marine Propulsors, SMP*, volume 9, 2009.

MJ Khan, MT Iqbal, and JE Quaicoe. Design considerations of a straight bladed darrieus rotor for river current turbines. In *Industrial Electronics, 2006 IEEE International Symposium on*, volume 3, pages 1750–1755. IEEE, 2006.

MJ Khan, G. Bhuyan, MT Iqbal, and JE Quaicoe. Hydrokinetic energy conversion systems and assessment of horizontal and vertical axis turbines for river and tidal applications: A technology status review. *Applied Energy*, 86(10):1823–1835, 2009.

M.S. Kirkgoz and M. Ardiclioglu. Velocity profiles of developing and developed open channel flow. *Journal of hydraulic engineering*, 123:1099, 1997.

A. Kumar and S. Grover. ≪performance characteristics of a savonius rotor for wind power generation-a case study,≫ alternate sources of energy. In *Proc. of Ninth National Convention of Mechanical Engineers, IIT Kanpur*, 1993.

Y. Kyozuka. An experimental study on the darrieus-savonius turbine for the tidal current power generation. *Journal of Fluid Science and Technology*, 3(3):439–449, 2008.

S. Lain and C. Osorio. Simulation and evaluation of a straight-bladed darrieustype cross flow marine turbine. *Journal of scientific & industrial research*, 69(12):906–912, 2010.

M.J. Lawson, Y. Li, and D.C. Sale. Development and verification of a computational fluid dynamics model of a horizontal-axis tidal current turbine. ASME, 2011.

Ju Hyun Lee, Sunho Park, Dong Hwan Kim, Shin Hyung Rhee, and Moon-Chan Kim. Computational methods for performance analysis of horizontal axis tidal stream turbines. *Applied Energy*, 2012.

P.G. Lemarié-Rieusset and Y. Meyer. Ondelettes et bases hilbertiennes. *Revista Matematica Iberoamericana*, 2(1):1–18, 1986.

A. Leonard. Energy cascade in large-eddy simulations of turbulent fluid flows. *Adv. Geophys*, 18:237–248, 1974.

M Lesieur. Turbulence in fluids, fluid mechanics and its applications, vol. 40, 1997.

M. Lesieur and O. Metais. New trends in large-eddy simulations of turbulence. *Annual Review of Fluid Mechanics*, 28(1):45–82, 1996.

Y. Li, J.L. Barbara, and M.C. Sander. Modeling tidal turbine farm with vertical axis tidal current turbines. In *Systems, Man and Cybernetics, 2007. ISIC. IEEE International Conference on*, pages 697–702. IEEE, 2007.

H. Lübcke, S. Schmidt, T. Rung, and F. Thiele. Comparison of les and rans in bluff-body flows. *Journal of wind engineering and industrial aerodynamics*, 89(14):1471–1485, 2001.

AJ MacLeod, S. Barnes, KG Rados, and IG Bryden. Wake effects in tidal current turbine farms. In *International Conference on Marine Renewable Energy-Conference Proceedings*, pages 49–53, 2002.

A. Mason-Jones, T. O'Doherty, DM O'Doherty, PS Evans, and PS Wooldridge. Characterisation of a HATT using CFD and ADCP site data. In *ECOR Symposium 2008 and Ocean Innovation 2008 Conference and Exhibition, St Johns Newfoundland*, 2008.

RA McAdam, GT Houlsby, MLG Oldfield, and MD McCulloch. Experimental testing of the transverse horizontal axis water turbine. *Renewable Power Generation, IET*, 4(6): 510–518, 2010.

GN McCann. Tidal current turbine fatigue loading sensitivity to waves and turbulence–a parametric study. In *Proceedings of the 7th European Wave and Tidal Energy Conference*, 2007.

T. Mccombes, C. Johnstone, and A. Grant. Unsteady wake modelling for tidal current turbines. *Renewable Power Generation, IET*, 5(4):299–310, 2011.

JM McDonough. Introductory lectures on turbulence physics, mathematics and modeling. 2004.

Martin Méchali, Rebecca Barthelmie, Sten Frandsen, and PE Réthoré. Wake effects at horns rev and their influence on energy production. In *European Wind Energy Conference and Exhibition*, page 10, 2006.

S. Menon, P.K. Yeung, and W.W. Kim. Effect of subgrid models on the computed interscale energy transfer in isotropic turbulence. *Computers & fluids*, 25(2):165–180, 1996.

M. Mihaescu, S. Murugappan, M. Kalra, S. Khosla, and E. Gutmark. Large eddy simulation and reynolds-averaged navier–stokes modeling of flow in a realistic pharyngeal airway model: An investigation of obstructive sleep apnea. *Journal of biomechanics*, 41(10): 2279–2288, 2008.

R. Mikkelsen. *Actuator disc methods applied to wind turbines*. PhD thesis, Technical University of Denmark, 2003.

V.B. Miller, A.E. Landis, and L.A. Schaefer. A benchmark for life cycle air emissions and life cycle impact assessment of hydrokinetic energy extraction using life cycle assessment. *Renewable Energy*, 36(3):1040–1046, 2011.

Chin-Hoh Moeng and John C Wyngaard. Spectral analysis of large-eddy simulations of the convective boundary layer. *Journal of Atmospheric Sciences*, 45:3573–3587, 1988.

P. Moin and J. Kim. Numerical investigation of turbulent channel flow. *Journal of Fluid Mechanics*, 118:341–377, 1982.

Hukam C Mongia. Recent progress in comprehensive modeling of gas turbine combustion. *AIAA Paper*, 1445, 2008.

S. Murakami. Overview of turbulence models applied in cwe–1997. *Journal of Wind Engineering and Industrial Aerodynamics*, 74:1–24, 1998.

L. Myers and AS Bahaj. Wake studies of a 1/30th scale horizontal axis marine current turbine. *Ocean Engineering*, 34(5-6):758–762, 2007. ISSN 0029-8018.

LE Myers and AS Bahaj. Experimental analysis of the flow field around horizontal axis tidal turbines by use of scale mesh disk rotor simulators. *Ocean engineering*, 37(2-3): 218–227, 2010.

LE Myers, B. Keogh, and AS Bahaj. Experimental investigation of inter-array wake properties in early tidal turbine arrays. In *OCEANS 2011*, pages 1–8. IEEE, 2011.

A Nakayama and SN Vengadesan. On the influence of numerical schemes and subgrid–stress models on large eddy simulation of turbulent flow past a square cylinder. *International journal for numerical methods in fluids*, 38(3):227–253, 2002.

Rachel F Nicholls-Lee, Stephen R Turnock, and Stephen W Boyd. Simulation based optimisation of marine current turbine blades. 2008.

K. Nilsson, E. Segergren, and M. Leijon. Simulation of direct drive generators designed for underwater vertical axis turbines. In *Fifth European Wave Energy Conference*, 2003.

T. Nishino and R.H.J. Willden. Effects of 3-d channel blockage and turbulent wake mixing on the limit of power extraction by tidal turbines. *International Journal of Heat and Fluid Flow*, 2012a.

T. Nishino and R.H.J. Willden. The efficiency of an array of tidal turbines partially blocking a wide channel. *Journal of Fluid Mechanics*, 708:596, 2012b.

T. O'Doherty, DA Egarr, A. Mason-Jones, and DM O'Doherty. An assessment of axial loading on a five-turbine array. *Proceedings of the Institution of Civil Engineers Energy*, 162:57–65, 2009a.

T. O'Doherty, A. Mason-Jones, DM O'Doherty, and CB Byrne. Experimental and computational analysis of a model horizontal axis tidal turbine. In *Proceedings of the 8th European Wave and Tidal Energy Conference, Uppsala, Sweden*, pages 833–841, 2009b.

DM ODoherty, A. Mason-Jones, T. ODoherty, and CB Byrne. Considerations of improved tidal stream turbine performance using double rows of contra-rotating blades. In *Proceedings of the 8th European Wave and Tidal Energy Conference. Uppsala, Sweden: IET Renewable Power Generation*, pages 434–442, 2009.

N. Paget. Tradewind turbines update-April 2012, available at:. `http://www.tradewindturbines.com/turbine.php`, 2012.

I. Paraschivoiu. *Wind turbine design: with emphasis on Darrieus concept*. Presses inter Polytechnique, 2002.

U. Piomelli. Wall-layer models for large-eddy simulations. *Progress in aerospace sciences*, 44(6):437–446, 2008.

Ugo Piomelli. Large-eddy simulation: achievements and challenges. *Progress in Aerospace Sciences*, 35(4):335–362, 1999.

Ole Rathmann, Sten Tronæs Frandsen, and Rebecca Jane Barthelmie. Wake modelling for intermediate and large wind farms. 2007.

A. Rizzi and B. Engquist. Selected topics in the theory and practice of computational fluid dynamics. *Journal of Computational Physics*, 72(1):1–69, 1987.

W. Rodi. Comparison of les and rans calculations of the flow around bluff bodies. *Journal of Wind Engineering and Industrial Aerodynamics*, 69:55–75, 1997.

R.S. Rogallo and P. Moin. Numerical simulation of turbulent flows. *Annual Review of Fluid Mechanics*, 16(1):99–137, 1984.

S.M. Salim, R. Buccolieri, A. Chan, and S. Di Sabatino. Numerical simulation of atmospheric pollutant dispersion in an urban street canyon: Comparison between rans and les. *Journal of Wind Engineering and Industrial Aerodynamics*, 99(2):103–113, 2011.

B. Sanderse. Aerodynamics of wind turbine wakes. *Energy Research Center of the Netherlands (ECN), ECN-E–09-016, Petten, The Netherlands, Tech. Rep*, 2009.

JL Santiago, A. Dejoan, A. Martilli, F. Martin, and A. Pinelli. Comparison between large-eddy simulation and reynolds-averaged navier–stokes computations for the must field experiment. part i: Study of the flow for an incident wind directed perpendicularly to the front array of containers. *Boundary-layer meteorology*, 135(1):109–132, 2010.

Wolfgang Schlez, Alejandro Umaña, Rebecca Barthelmie, Gunner Larsen, Kostas Rados, Bernhard Lange, G Schepers, and T Hegberg. Endow: Improvement of wake models within offshore wind farms. *Wind Engineering*, 25(5):281–287, 2001.

H. Schlichting and K. Gersten. *Boundary-layer theory*. Springer, 2004.

S. Schmidt and F. Thiele. Comparison of numerical methods applied to the flow over wall-mounted cubes. *International journal of heat and fluid flow*, 23(3):330–339, 2002.

PN Shankar. Development of vertical axis wind turbines. In *Sadhana (Academy Proceedings in Engineering Sciences)*, volume 2, pages 49–66. Indian Academy of Sciences, 1979.

M. Shiono, K. Suzuki, and S. Kiho. An experimental study of the characteristics of a darrieus turbine for tidal power generation. *Electrical Engineering in Japan*, 132(3): 38–47, 2000.

M. Shiono, K. Suzuki, and S. Kiho. Output characteristics of darrieus water turbine with helical blades for tidal current generations. In *Proceedings of the Twelfth International Offshore and Polar Engineering Conference, Kitakyushu, Japan*, 2002.

M. Shives and C. Crawford. Overall efficiency of ducted tidal current turbines. 2010.

M. Shives and C. Crawford. Ducted turbine blade optimization using numerical simulation. 2011.

J. Smagorinsky. General circulation experiments with the primitive equations. *Monthly weather review*, 91(3):99–164, 1963.

C.G. Speziale. A combined large-eddy simulation and time-dependent rans capability for high-speed compressible flows. *Journal of scientific computing*, 13(3):253–274, 1998.

Charles G Speziale. Analytical methods for the development of reynolds stress closures in turbulence. Technical report, DTIC Document, 1990.

X. Sun. Numerical and experimental investigation of tidal current energy extraction. 2008.

X. Sun, JP Chick, and IG Bryden. Laboratory-scale simulation of energy extraction from tidal currents. *Renewable Energy*, 33(6):1267–1274, 2008.

H. Tennekes and J.L. Lumley. *A first course in turbulence*. MIT press, 1972.

J. Thomson, B. Polagye, M. Richmond, and V. Durgesh. Quantifying turbulence for tidal power applications. In *OCEANS 2010*, pages 1–8. IEEE, 2010.

Y. Tominaga and T. Stathopoulos. Cfd modeling of pollution dispersion in a street canyon: Comparison between les and rans. *Journal of Wind Engineering and Industrial Aerodynamics*, 99(4):340–348, 2011.

Yoshihide Tominaga and Ted Stathopoulos. Numerical simulation of dispersion around an isolated cubic building: model evaluation of rans and les. *Building and Environment*, 45 (10):2231–2239, 2010.

Niels Troldborg, Gunner C Larsen, Helge A Madsen, Kurt S Hansen, Jens N Sørensen, and Robert Mikkelsen. Numerical simulations of wake interaction between two wind turbines at various inflow conditions. *Wind Energy*, 14(7):859–876, 2011.

Stephen R Turnock, Alexander B Phillips, Joe Banks, and Rachel Nicholls-Lee. Modelling tidal current turbine wakes using a coupled rans-bemt approach as a tool for analysing power capture of arrays of turbines. *Ocean Engineering*, 38(11):1300–1307, 2011.

G. Tzanetakis, G. Essl, and P. Cook. Audio analysis using the discrete wavelet transform. In *Proc. Conf. in Acoustics and Music Theory Applications*, 2001.

DRIEST VAN et al. On turbulent flow near a wall. *J. Aero. Sci.*, 23:1007–1011, 1956.

R. Vennell. Tuning turbines in a tidal channel. *Journal of fluid mechanics*, 663(1):253–267, 2010.

R. Vennell. Estimating the power potential of tidal currents and the impact of power extraction on flow speeds. *Renewable Energy*, 36(12):3558–3565, 2011a.

R. Vennell. Tuning tidal turbines in-concert to maximise farm efficiency. *Journal of Fluid Mechanics*, 671(1):587–604, 2011b.

R. Vennell. The energetics of large tidal turbine arrays. *Renewable Energy*, 48:210–219, 2012.

R. Verstappen and AEP Veldman. Spectro-consistent discretization of navier-stokes: a challenge to rans and les. *Journal of Engineering Mathematics*, 34(1):163–179, 1998.

H.K. Versteeg and W. Malalasekera. *An introduction to computational fluid dynamics: the finite volume method*. Prentice Hall, 2007.

B. Wegner, A. Maltsev, C. Schneider, A. Sadiki, A. Dreizler, and J. Janicka. Assessment of unsteady rans in predicting swirl flow instability based on les and experiments. *International journal of heat and fluid flow*, 25(3):528–536, 2004.

JI Whelan, JMR Graham, and J. Peiro. A free-surface and blockage correction for tidal turbines. *Journal of Fluid Mechanics*, 624:281–291, 2009. ISSN 0022-1120.

F.M. White. *Viscous fluid flow*, volume 66. McGraw-Hill New York, 1991.

David C Wilcox. *Turbulence Modelin for CFD*. DCW Industries, Inc, 1998.

AJ Williams, TN Croft, I. Masters, MR Willis, and M. Cross. Combined bem-cfd modelling of tidal stream turbines using site data. In *International Conference on Renewable Energies and Power Quality (ICREPQ10)*, 2010.

Z. Xie and I.P. Castro. LES and RANS for turbulent flow over arrays of wall-mounted obstacles. *Flow, turbulence and combustion*, 76(3):291–312, 2006.

C. Yang, R. Lohner, and S.C. Yim. Development of a CFD simulation method for extreme wave and structure interactions. In *Proceeding of 24th Int. Conference on Offshore Mech. and Arctic Eng.(OMAE2005), Halkidiki, Greece*, pages 12–17, 2005.

C. Yang, R. LOHNER, and H. Lu. An unstructured-grid based volume-of-fluid method for extreme wave and freely-floating structure interactions. *Journal of Hydrodynamics, Ser. B*, 18(3):415–422, 2006.

S.Q. Yang, S.K. Tan, and S.Y. Lim. Velocity distribution and dip-phenomenon in smooth uniform open channel flows. *Journal of hydraulic engineering*, 130:1179, 2004.

A. Yoshizawa and K. Horiuti. A statistically-derived subgrid-scale kinetic energy model for the large-eddy simulation of turbulent flows. *Journal of the Physical Society of Japan*, 54(8):2834–2839, 1985.

Akira Yoshizawa. Eddy-viscosity-type subgrid-scale model with a variable smagorinsky coefficient and its relationship with the one-equation model in large eddy simulation. *Physics of Fluids A: Fluid Dynamics*, 3:2007, 1991.

Wei Zhang and Qingyan Chen. Large eddy simulation of indoor airflow with a filtered dynamic subgrid scale model. *International journal of heat and mass transfer*, 43(17): 3219–3231, 2000.

Appendix A

List of Publications

A.1 Journal Papers

1. M.G. Gebreslassie, G.R. Tabor, and M.R. Belmont. Numerical simulation of a new type of cross flow tidal turbine using OpenFOAM - Part I: Calibration of energy extraction, *Renewable Energy Journal*, 50:994-1004, 2013

2. M.G. Gebreslassie, G.R. Tabor, and M.R. Belmont. Numerical simulation of a new type of cross flow tidal turbine using OpenFOAM - Part II: Investigation of turbine-to-turbine interaction. *Renewable Energy Journal*, 50:1005-1013,2013

3. M.G. Gebreslassie, G.R. Tabor, and M.R. Belmont. CFD Simulations for Sensitivity Analysis of Different Parameters to the Wake Characteristics of Tidal Turbine . *Open Journal of Fluid Dynamics*,2(3):56-64, 2012

4. M.G. Gebreslassie, G.R. Tabor, and M.R. Belmont. CFD simulations for investigating the wake states of a new class of tidal turbine. *Renewable Energy and Power Quality Journal*, presented at the International Conference on Renewable Energies and Power quality (ICREPQ'12), No. 10, paper No. 241, 2012

A.2 Conference Proceedings

1. G.R. Tabor, M.G. Gebreslassie, M.R. Belmont. Investigation of the influence of turbine to turbine interaction on their performance using OpenFOAM, *In Proceedings of the Oxford Tidal Energy Workshop*, 29-30 March 2012, Oxford, UK,
   pp 11-12,2012